A CONTACTLESS AND NON-INTRUSIVE CURRENT MEASUREMENT TECHNIQUE FOR LOW AND MEDIUM VOLTAGE AC POWER SYSTEMS

by

Prasad Shrawane

A thesis submitted to the
School of Graduate and Postdoctoral Studies in partial
fulfillment of the requirements for the degree of

Doctor of Philosophy

in

Electrical and Computer Engineering

Department of Electrical, Computer and Software Engineering

School of Graduate and Postdoctoral Studies

Faculty of Engineering and Applied Sciences

University of Ontario Institute of Technology (Ontario Tech University)

Oshawa, Ontario, Canada

August 2023

THESIS EXAMINATION INFORMATION

Submitted by: **Prasad Shrawane**

PhD in **Electrical, Computer and Software Engineering**

Thesis title: **A Contactless and Non-intrusive Current Measurement Technique for Low and Medium Voltage AC Power Systems**

An oral defense of this thesis took place on June 26, 2023 in front of the following examining committee:

Examining Committee:

Chair of Examining Committee	Dr. Khalid Elgazzar
Research Supervisor	Dr. Tarlochan S. Sidhu
Examining Committee Member	Dr. Sheldon Williamson
Examining Committee Member	Dr. Akramul Azim
University Examiner	Dr. Bale Reddy, Ontario Tech University - FEAS
External Examiner	Dr. Yuan Liao, University of Kentucky

The above committee determined that the thesis is acceptable in form and content and that a satisfactory knowledge of the field covered by the thesis was demonstrated by the candidate during an oral examination. A signed copy of the Certificate of Approval is available from the School of Graduate and Postdoctoral Studies.

ABSTRACT

The real-time state of current is essential to precisely monitor and control the AC power systems. It is also crucial for detecting various types of faults that may lead to long duration and wide area outages and affect the reliability and dependability. Traditional core wound window type current transformers (CTs) are widely used for current measurement at present. Increasing number of distribution energy resources integrated to the power systems network require a greater number of such instrument transformers for efficient monitoring and control of the grid. However, these CTs require complex and time-consuming operational procedure for installation and maintenance. In addition, they have a major drawback of saturation. To overcome this drawback, they need a higher accuracy leading to bigger size and higher costs and, therefore, beget the need for alternative current measurement techniques. They also pose a serious hazard of explosion if their secondary windings are left open circuited.

In this thesis a technique of non-invasive contactless current measurement using Tunneling magnetoresistive (TMR) sensors is proposed and implemented for AC power systems. The proposed sensors overcome the aforementioned drawbacks of the CTs and provide more accurate outputs for asymmetrical currents during fault conditions. A thorough investigation is carried out to study the effect of distance, conductor insulation, and frequency of source current on their performance while applied for single-phase and three-phase current measurements.

The sensors were calibrated to overcome the inequality in the sensed magnetic field due to the various aspects such as the distance from the source, minute structural variations, the magnitude of the source current, and harmonics.

This thesis introduces a new technique to determine the phase angle error in absence of time-synchronized data. The weighted fusion technique is applied to six pair combinations from an array of four sensors in a three-phase triangular and horizontal structure for accuracy improvement. The measurement accuracy based on the sets of weighting factors corresponding to a minimum TVE showed promising and successful validation of the magnetic sensors for a possible replacement of CTs in the ac current measurement.

Keywords: non-invasive; magnetic field sensors; three-phase current phasors; total vector error; tunneling magnetoresistance; Discrete Fourier Transform

AUTHOR'S DECLARATION

I hereby declare that this thesis consists of original work of which I have authored. This is a true copy of the thesis, including any required final revisions, as accepted by my examiners.

I authorize the University of Ontario Institute of Technology (Ontario Tech University) to lend this thesis to other institutions or individuals for the purpose of scholarly research. I further authorize University of Ontario Institute of Technology (Ontario Tech University) to reproduce this thesis by photocopying or by other means, in total or in part, at the request of other institutions or individuals for the purpose of scholarly research. I understand that my thesis will be made electronically available to the public.

PRASAD SHRAWANE

STATEMENT OF CONTRIBUTIONS

Part of the work described in Chapter 1 and 2 has been published as:

[1] **P. Shrawane,** T. S. Sidhu, "Estimation of Three-Phase Currents in Overhead Power Line Conductors Using the Numerical Model of Magnetic Fields," Journal of Progress in Electromagnetics Research C, Vol. 97, pp. 123-137, 2019. ISSN: 1070-4698, E-ISSN: 1559-8985.

[2] **P. Shrawane,** T. S. Sidhu, "Current Measurement using Noninvasive Sensors in Mobile Medium Voltage Substations", Proceedings of IEEE Autotestcon 2019 conference, Maryland, USA.

Part of the work described in Chapter 3, 4, 5, and 6 has been published as:

[1] **P. Shrawane**, T. S. Sidhu, "Performance Evaluation of GMR and TMR Sensors to Estimate Current Phasors in Power Systems", IEEE Sensors 2020 Conference.

[2] **P. Shrawane,** T. S. Sidhu, "Comparison of TMR Sensors with Hall Effect Sensors for Applications in Smart Grid Monitoring and Protection", published in the IEEE proceedings of EPEC 2020 (IEEE Electric Power and Energy Conference 2020), Edmonton, Alberta, Canada.

[3] **P. Shrawane, T. S. Sidhu, "**Performance of a Noninvasive Magnetic Sensor-Based Current Measurement System in Power Systems', MDPI Journal of Electronics 2021, 10, 2869. https://doi.org/10.3390/ electronics10222869, pp 1-21.

[4] **P. Shrawane**, T. S. Sidhu, "Non-invasive Magnetic Sensors for Measurement of Current Phasors in Power Systems: Calibration and Validation" 2021 IEEE 11th International Workshop on Applied Measurements for Power Systems (AMPS), October 2021, Cagliari, Italy.

[5] **P. Shrawane**, T. S. Sidhu, “Application of Magnetic Sensors for Measurement of Current Phasors in Power Systems”, IEEE 2021 IEEE Electric Power and Energy Conference 2021, Edmonton, Alberta, Canada.

[6] **P. Shrawane**, T. S. Sidhu, “Factors Affecting Performance of Noninvasive Magnetic Sensors for Current Measurement in Power Systems”, IEEE International Instrumentation Measurement Technology Conference (IEEE I2MTC 2022), Ottawa, Canada.

Part of the work described in Chapter 7 has been published as:

[1] **P. Shrawane**, T. S. Sidhu, “Detection of Phase and Neutral Fault Currents by Using Noninvasive Sensing and Electromagnetic Field Modelling”, proceedings of IEEE Photonics and Electromagnetics Research Symposium (PIERS) 2021 Conference Hangzhou, China.

I performed most of the research study, experimentation, testing, validation, analysis, and writing of the manuscript.

ACKNOWLEDGEMENTS

First and foremost, I would like to express my deepest gratitude to my supervisor, Dr. Tarlochan Sidhu, for his invaluable supervision, time, and continuous support during the course of my Ph.D. degree. His patience and thorough approach towards solving problems helped me grow and become a good researcher. I am very grateful to him for his moral and financial support in conducting this research. Without his technical expert advice this research would not have been possible.

My special thanks to Dr. Sheldon Williamson for allowing me to use his laboratory and equipment during the initial stage of the research experiment. I would also like to thank Mr. Rick Szymczyk and Mr. Anthony Van De Watering for their assistance during the experiment conducted at the General Motors Climatic Wind Tunnel facility in Oshawa. My gratitude also goes to Mr. Joel Stewart for his assistance in administrative tasks.

This Ph.D. is successfully complete because of the unconditional love and moral support of my dear wife, Kshama, and my sweet children, Prasuk and Prachi. I am indebted to them for their sacrifices. Many thanks to my sisters, Ms. Smita Shrawane and Dr. Shilpa Shrawane for their continued help in taking care of my family during the pandemic. Additionally, I also express my sincere thanks to Mr. Mark Van de Rydt, Mr. Philip Guido, Mr. Scott Chartrand, and Mr. Landon Duplessis for their great friendship and support. I would also like to thank my friends Mr. Jigyesh Sharma and Mr. Adeeph Konzhigul for their moral support during the final phase of my research.

I dedicate this thesis to my beloved parents. Words cannot express how grateful I am to my parents for the innumerous sacrifices they have made. They are my inspiration and the cause for every success in my life. They always stood with me in all stages of my life. I wish my father could live three more years to witness the completion of this dream and offer his blessings in person. Love you so much Aai and Baba! Miss you Baba!

TABLE OF CONTENTS

LIST OF TABLES

LIST OF FIGURES

LIST OF ABBREVIATIONS AND SYMBOLS

GMR	Giant Magnetoresistance
TMR	Tunneling Magnetoresistance
MF	Multiplying Factor
AC	Alternating Current
DC	Direct Current
RMS	Root Mean Square
CT	Current Transformer
DFT	Discrete Fourier Transform
FEM	Finite Element Method
SAIDI	System Average Interruption Duration Index
CAIDI	Customer Average Interruption Duration Index
SCADA	Supervisory Control and Data Acquisition
GPS	Global Positioning System
RTU	Remote Terminal Unit
PMU	Phasor Measurement Unit
FDTD	Finite Difference Time Domain
WI	With Insulation
NI	No-Insulation
CWT	Climatic Wind Tunnel
EMF	Electromagnetic Field

Chapter 1. Introduction

Electric power systems worldwide are experiencing an unprecedented growth in power energy demand propelled by revolutionary growth in the industrial, domestic, and digital sectors. Vast digitization of banking, finance, sales and information technology sectors has resulted in an added energy demand. The power utility companies are welcoming independent generators on a small and big scale to cater to the ever-increasing demand. Consequently, integration of these distributed energy resources to the electric power transmission and distribution network has increased its complexity. In these circumstances, there is an additional responsibility on the shoulders of grid operators to monitor and operate the grid while maintaining reliability and power quality [1]. In absence of modern protection strategies and equipment, a fault on a solar or wind power generation station may cause an outage on the feeder of the host utility adding up to the operational cost for utilities [2]. Therefore, modernizing the system and monitoring the power network at various crucial nodes with the help of latest information acquisition technologies and develop a robust control network has become a necessity for every power utility company [3, 4]. Transformation of the present power grid to smart grid will modify the whole power industry and its relationship with utilities, shareholders, regulators and consumers [5, 6]. For transmission line network, wide-area-monitoring (WAM) technology can help preventing potential grid fault adaptively [6].

In North America, the power distribution utilities are evaluated based on their performance and reliability indices that are related to their total number of power interruptions and duration of power interruptions per year. These indices are System Average Interruption Duration Index (SAIDI), Customer Average Interruption Duration Index (CAIDI), and System Average Interruption Frequency Index (SAIFI) [7]. The interruptions are caused because of many reasons, such as, power system faults due to extreme weather conditions, equipment failure, planned outages, animals, vehicle accidents and theft or vandalism [8]. The risk of equipment failure in transmission and distribution infrastructure is a major governing factor for the capital expenditures as well as the reliability of the power delivery. As per the national power outage data of Canada for the year 2017, there were 89 out of 399

reported outages because of the faulty equipment, which is 22.31% of total outage time and affected 2.6 million people in Canada [8]. Moreover, equipment outage schedules are an external factor by power generation, transmission and distribution companies which affect their reliability indices [8].

Among substation equipment, current and voltage transducers are the major equipment that help in acquiring the latest status of the power. Current measurements are very helpful in detecting fault currents, system imbalance and avoiding power outages and wide area blackouts. The following sections of this chapter give a brief account of the technologies in practice at present with their drawbacks and the alternative technologies that can be a successful replacement.

1.1 Research Background

The phasor measurement units (PMU) synchronized by the time stamps of global positioning system (GPS) are the most accurate applications in power systems [6]. These PMUs gather real time power parameters and send this information to a remote terminal unit (RTU) which interface with the centralized SCADA system. This information is then used for power transmission regulation and protection. Various sensing techniques based on different sensing mechanism are applied for obtaining the energy parameters for PMUs. Since current in high-voltage transmission system is very high, it cannot be directly applied to PMUs measuring instruments. Therefore high-voltage AC transmission line current is measured by conventional CTs which have major disadvantages such as saturation and heating. To avoid saturation and obtain more accuracy, a higher transformation ratio CT is needed which results in higher cost. They need de-energization of the system for installation and maintenance which leads to temporary outages [6]. In these circumstances, replacement of conventional current measurement equipment with a new non-invasive contactless digital technology-based sensors can help reduce the system outages for installation and maintenance of the smart grids.

In case of medium voltage and low voltage power distribution system, the power distribution feeders are protected with the help of reclosers, fault interrupters, sectionalizers, and fuses. All se protecting devices measure the phase current continuously

and operate when the current during a fault condition exceeds their set value of the pick-up current. These devices limit the extent of momentary outages to specific laterals on feeders. Thus, it decreases the need for truck rolls when outages occur and prevent these monetary outages from affecting customers. Linear and hysteresis-free current sensing devices that are cheaper than CTs for such protection equipment will not only help in operational cost reduction, but also help in current monitoring at the sectionalizer levels and help improve demand management.

Fuses or fused switches are installed on the laterals that run off the feeders and at locations where there is a transition from overhead to underground feed. Generally, fuse-blowing or fuse-saving scheme are applied to protect these laterals. The time-current characteristics of these fuses, and reclosers are coordinated with the main breaker on the feeder at the substation [9, 10]. There is a mix of the protection schemes for feeders when there is a transition from underground to overhead and vice versa. In such case, the protection of the laterals and the transition sections may not be adequate only by fuses. Identifying the correct side of the fault on the laterals and block reclosing for underground faults but enabling the reclosing for overhead fault clearing will keep the outage to only specific faulty section of the feed [10]. At such locations, having an information of current is very valuable for fine tuning of the pickup value of fault current in the protective equipment as well as transmit the recorded current value to the data control center.

1.2 Traditional Current Measurement Device

Traditionally, current measurement is accomplished by use of conventional magnetic ferrous core CTs. They are installed in transmission and distribution substations at the incoming and outgoing feed locations. A conventional CT isolates the high voltage power source from the measurement equipment by transforming a high value current to a low value current based on its turns' ratio and burden across the secondary terminals. Their size, weight, cost, and installation procedure increase with the increase in the voltage level [9, 10]. Thus, CTs for transmission (high voltage) level are bigger, costlier and take more installation and maintenance time than those for the distribution (medium voltage) level.

The magnetic core of the CT saturates with a sudden high magnitude of starting current and during fault where fault currents contain decaying DC component. The saturation

voltage is the symmetrical voltage across the secondary winding of the CT for which the peak induction just exceeds the saturation flux density. This leads to inaccurate sensing of the primary side current on the secondary side [11-14]. Saturation caused by heavy starting fault current and transient currents is a common problem in protection CTs. It cannot provide accurate estimates of the sensed primary current due to saturation. Moreover, the CT saturation with an inductive burden produces a lower distortion index and causes trip delays in protective relays [11].

The remanent flux in the CT core depends on the flux in the core immediately before primary current interruption. The magnitude of flux is determined by the value of symmetrical primary current, the DC offset and the impedance of the secondary circuit. Maximum remanent flux is obtained when the primary current is interrupted while the current transformer is in a saturated state [12]. Most of the times, the fault current is interrupted in a few cycles. The fault current duration can be much shorter than the time constant of the primary circuit. The result is a remanent flux in the CT core that can only be removed by demagnetization. It will not be affected by normal load current. With the increase in the system voltage, the value of current also increases and therefore, the percentage of remanent flux also increases. It has been observed that 39% of the CTs have 0% to 20% of the remanent flux [12, 13]. This signifies that the CTs are susceptible to saturation if not demagnetized after the fault. IEEE C57.152-2013 describes two methods for demagnetization of the core, the first being application of a diminishing alternating current to the windings [14]. It is impractical and involves safety hazards. The second method is to neutralize the magnetic alignment of the core by applying a DC voltage of alternate polarities to the CT winding for decreasing intervals and continue till the current level reaches zero [14, 15]. There are commercial products available with detailed operating procedures to perform the demagnetization procedure on CTs in the field, one of which is DEM60R [16]. Also, it is an expensive procedure to demagnetize the CT if the fault is non-recurring. This implies, the system needs a complete reset and restart after the fault. It poses a great challenge while employing these CTs for protection and control of the system. This increases the outage time and consequently the cost of operation.

Various protection functions are affected by the saturation effect of the CT. There is a possibility of severe saturation on internal faults, particularly in the presence of DC offset,

which could prevent or delay differential relay operation [18]. If the fault clearing is made faster, then the time taken to clear the fault is less than the time to saturation for a CT. Selection of higher turns ratio CTs is another way to avoid the saturation, which signifies more cost.

The time-current characteristics used in a fault-coordinated system can minimize, but not eliminate, possible fault coordination errors because of CT saturation on protective relay performance. Choice of higher capacity relays can avoid this problem but increase the operation cost.

A typical conventional CT has the circuit as shown in the Figure 1.1 [12]. The CT impedance can be expressed as a resistance (R_{CT}) and an inductance (L_{CT}) in series. The magnetizing reactance of the CT can be expressed as a parallel inductance (L_m) in parallel with the load. Here, the load is considered as a pure resistance (R_L)

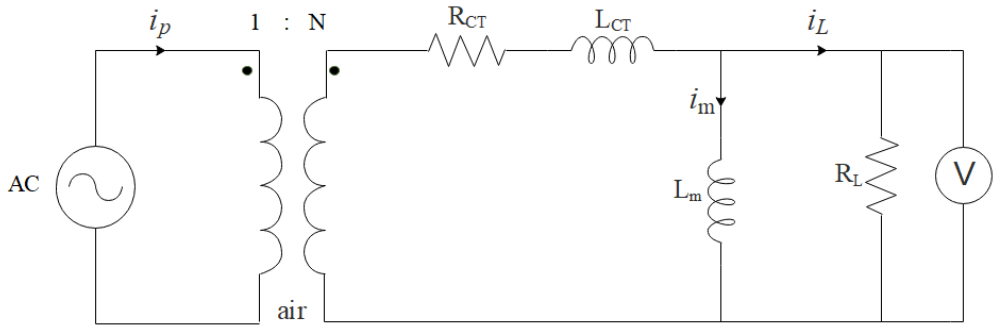

Figure 1.1 Equivalent circuit of a wound-core current transformer

The voltage, V_S across the secondary terminals of the CT is given by the following equation

$$V_s = -N\frac{d\phi}{dt} = -N \times A \times \frac{\mu_0\mu_r}{L_m} \times \frac{d}{dt}\left(i_p - N \times i_L\right) \tag{1.2.1}$$

where, $\mu_0\mu_r$ the permeability constants of free space, and $\mu_0\mu_r$ is the relative permeability of the iron core medium, $d\phi/dt$ is the rate of change of flux with respect to time, N is the number of turns, A is the area of cross-section of core.

$$i_L = \frac{i_p}{N} - \frac{L_m}{N^2 A \mu_0 \mu_r} \int V_s dt \tag{1.2.2}$$

$$i_L = \frac{i_p}{N} - \left(\frac{1}{L_m} \right) \int V_s dt \tag{1.2.3}$$

The second term of magnetizing inductance in the above Equation (1.2.3) shows the inability of the CT to measure DC currents. If the primary current i_p contains a DC component, then the magnetizing current i_m will increase until the full DC component flows through the L_m. Therefore, in this configuration, CT will not be able to measure the DC component of the current.

For a high frequency, L_m will be high, and therefore, the second term in the Equation (1.2.3) will be minimal. This way, i_L will be directly proportional to the primary current i_p, and can be measured by means for a shunt resistor R_L. This resistance is also called as 'Burden' or 'Load' on CT. The losses within R_L can be kept low by using a high number of secondary turns, N.

The magnetizing current through L_m causes a measurement error because this current bypasses the load resistor (burden or sensor resistor) and does not contribute to the voltage across R_L. This phenomenon is called as "Droop" and refers to the decreasing sense voltage when a current pulse with large on-time is applied at the primary side. This droop can be decreased by having a core with high permeability $\mu_0 \mu_r$ and applying a smaller load resistor R_L.

The other parameters such as,

i) Magnetizing reactance, L_m,

ii) Area of cross-section of core, A

iii) Secondary winding capacitance

cannot be changed drastically or are difficult to modify. This becomes a major drawback of the conventional CT. The core permeability can be increased and that depends on the type of material. The higher permeability material comes at a higher cost.

Another drawback of magnetizing reactance, L_m is that it exhibits hysteresis and saturation. The thermal resistance between the transformer core and air is high so that even a small power dissipation in the CT will lead to overheating of the core. Therefore, one must make sure that the peak magnetizing current does not saturate and, consequently, overheat the core [14].

A CT could become open circuited due to wiring error at the time of installation, loose connection, or accidental opening of the test switches in the switchgear control panels that are in the CT secondary circuit. The open circuit condition in CTs can result in extremely high overvoltage across their secondary terminals that may lead to explosion and a serious life-threatening situation. While the primary circuit of the CT is carrying current, an open circuited secondary condition leads to the current flow through its high impedance of magnetizing reactance, L_m, generating overvoltage that drives the CT into saturation. Under saturation, the rapidly changing magnetic flux during each half cycle results into very high excitation current appearing across the open terminals of CT secondary winding increasing the voltage to exceed the limits and result into explosion The overall performance and the drawbacks in the conventional CTs gave inspiration to explore alternative techniques of current measurement. Next section gives a brief account of these techniques.

1.1 Alternative Technologies for Current Measurement

Current measurement can be achieved by applying a few principles such as Faraday's law of induction, Ohm's law, Faraday's effect, and magnetic field sensing [18-24]. Shunt resistors make use of the Ohm's law. A significant drawback of this kind of current sensor is the unavoidable electrical connection between the currents to be measured and the measurement circuit. Isolation amplifiers can be used to overcome this drawback, but they are expensive. They also deteriorate the accuracy, bandwidth, and thermal drift of the original current sensing methods [18, 19]. The voltage drop across the resistor is used as a proportional measure of the current flow. However, the I^2R losses across the shunt resistor

restrict the use for high current application. The shunt resistors are commonly used to measure direct currents up to 100-200 A. For higher currents, they become bulky in size and are not suitable for device integration [20]. They cause voltage drop and consequently, the circuits connected after the shunt resistor are no longer related to ground. This can be a problem in analog circuits.

Magnetic field sensors work on the principle of Faradays' law of induction like the current transformers discussed in the previous section. They can measure both static and time varying magnetic fields. There are three basic configurations with magnetic sensors, open loop, closed loop, and a combination of the magnetic sensor with other sensors such as Hall Effect Sensors and Rogowski coil [20].

Rogowski coil has an advantage over the current transformer because it does not contain any ferromagnetic material. It provides an excellent linearity and large dynamic range. The coil manufacturing needs a great precision with constant winding density and diameter. The precision needs correct detection of the flux linkage proportional to the current change. So, if the coil is not centered around the conductor correctly, then, the measurement error increases [20, 21].

Hall Effect sensors are widely used in various applications for measuring a current from a few milli amperes to 100 A. The Hall voltage is proportional to the vector cross product of the current and the magnetic field [22-24]. It requires signal conditioning to make the output usable for most applications. The signal conditioning consists of amplifier stage and temperature compensation. Also, it needs voltage regulation when operating from an unregulated power supply. To use this effect as a current sensor, additional circuitry is required to compensate for the misalignment voltage and the distinct thermal drift. Misalignment voltage is an offset voltage present at the output at zero magnetic field. The ohmic resistance is responsible for the power loss occurring inside the sensor due to the constant current [22, 23].

Fluxgate sensors consist of ferromagnetic material wound with two coils, a drive and a sense coil. It exploits magnetic induction together with the fact that all ferromagnetic materials becomes saturated at high fields. When a sufficiently large sinusoidal excitation current is passed through the excitation coil, it produces field that periodically saturates in both

directions the soft magnetic material of the sensor core. In saturation, the core permeability drops down and the DC flux associated with the measured DC magnetic field is decreased [25, 26]. Standard fluxgate sensors are commercially successful but so far only in high precision application because of the high cost and size requirements. They consist of a complicated electronics and large number of turns thus reducing the measurement bandwidth. The magneto-optical sensors are based on the Faraday Effect, which have the technical benefit of producing real-time analog images of the magnetic field. The primary disadvantage of this technique is the lack of a quantitative measure of the field [25].

1.2.1 Survey of Magnetoresistive Effect based Sensors: GMR, TMR Sensors

A magnetoresistive effect in thin film ferromagnetic films was discovered in 1988 [27]. There are three major types of the magnetoresistance sensors, Anisotropic- [28], Giant- [29-31] and Tunneling- [30,31] magentoresistive effect-based sensors and, are used for a variety of industrial applications. The Giant Magnetoresistive (GMR) effect occurs in a multilayer sandwich of two magnetic layers that are separated by a thin non-magnetic film [29-31]. The large change of magnetoresistance is explained in literature as a scattering of electrons when they pass through the non-magnetic interface. Electron scattering increases the mean free path of the electron flow, effectively altering the resistance of the medium. In short, a magnetoresistor is a resistor that changes its resistance value in the presence of a magnetic field [31]. A Wheatstone bridge type construction of such GMR resistors allows for maximum and minimum resistance and accordingly measures the positive magnetic field. This Wheatstone bridge configuration allows for both cancellation of temperature effects (thermal drifts) and for a level of immunity to stray magnetic fields. Moreover, in the bridge type structure, the differential output across the bridge as a function of variation of resistance when applied to a certain magnitude of magnetic field demonstrated good linearity and accuracy of detection [32-36]. Therefore, it is proved to be very efficient and accurate in AC current sensing [32-36]. Similar efforts were invested in exploring the possibility of TMR sensors for AC current measurement [37, 38] and it was found they are more suitable and have higher range of sensitivity compared to GMR sensors. There are many industrial applications of the magnetoresistive sensors, a few of which are surveyed

[39-43]. There are various research teams across the globe that worked on the possibility of measuring AC and DC currents using magnetoresistive sensors.

Xi et al. [44] developed a bridge type sensor module using four GMR sensors in the laboratory and proved its performance in measuring DC current up to ± 100 A.

Xu et al. [45] designed a GMR sensor-based clamp for three-phase current measurement and tested its performance on a 10 kV distribution transformer. The experiment gave promising outcome with sensing of 60 A alternating current. However, in this research, there was no continuous sinusoidal waveform recorded. The current was recorded intermittently to get only the amplitude of AC current over a fixed time period. Moreover, there was no result produced for three-phase currents at the same instance and no phasors were obtained.

Poon et al. [46] explored a new technique of counteracting magnetic field to extend the current measurement capacity of GMR sensors from 9 A to 45 A, and showed promising results for a single-phase alternating current.

O. Yong et al. [47] successfully tested the application of GMR sensors for measuring AC currents up to 5 A with a linearity of 99.97%. This research included a single-phase experiment for low magnitude alternating currents.

Bi. et al. [48] developed a sensor module based on TMR sensors for detecting accurately the transmission of weak signals at medium frequency of 50 Hz and magnitude of 3 A. It did not address further details, but only gave the account of capability of the module to measure AC and DC low amplitude currents.

Vopalensky et al. [49] developed a Wattmeter based on AMR sensors and presented the results of phase shift dependence, frequency range and feedthrough. However, the voltage and current range selected was up to 45 V and 1 mA rms. There were no results of single-phase watts with higher values.

Xu et al. [50] designed a circuit with GMR sensor and wireless communication module to enable the sensor for measuring the currents in distribution and transmission network.

However, their research did not cover measurement of the current phasors and did mention about the number of phases.

Qi. Huang et al. [51] employed the TMR sensors for estimation of fault location in an overhead high voltage three-phase conductor system by utilizing numerical simulation and suggested a remote monitoring terminal. This research did not explain the fault in any specific phase and moreover it was only a simulation study result. There was a mention about type of fault detection, but no data was provided on the magnitude and phase angle information about the fault currents.

X. Li. et al [52] used AMR sensors for measurement of DC current of amplitude 3 A and obtained a good measurement accuracy with only 0.1% error. However, this research could not be applied to AC because of the limitation of AMR sensors that were designed only for DC measurement.

L. Meng et al. [53] explored the measurement of AC current in multiconductor system in low-voltage applications using Hall Effect sensors. In this study, the sensors were closely placed to each other and stuck to the current carrying conductors using clamps. The ac measurement accuracy achieved was in the range up to 5%.

D'Antonna et al. [54] utilized array of Hall sensors for measurement of AC current in an application to three-phase low voltage bus-bar system with multiconductors. The experimental results showed limitations because of the crosstalk magnetic fields and the noise in the system. Moreover, the system robustness and accuracy were affected by the orientation accuracy of sensor array and the angle of inclination of the sensors.

1.3 Research Motivation

Protection of power systems is the most crucial to maintain high reliability and dependability and reduce the operational cost of the power grid. Current measurement is required for power measurement, control and protection in power systems and is mostly performed using traditional CTs. Installation and maintenance of these instrument transformers in medium and high voltage power systems is expensive in terms of time and labor. Moreover, inability to install them at multiple locations is another drawback because

of their bulky size, cost, and installation procedure. Their technical and operational drawbacks posing many challenges for their application in power system equipment protection and monitoring is already discussed in Section 1.3. In these practical circumstances, non-invasive contactless current measurement techniques can be a good alternative, provided, such a technique is fully studied, explored, and validated through research. If installed at multiple locations, the non-invasive sensors can also help in spotting the power congestion at various nodes and re-routing the power to reduce load on the distribution and transmission lines. The literature survey on the alternative techniques of current sensing and use of magnetic sensors in AC current measurement gave a detail picture of the present state of their application. It is obviously clear that magnetic sensors are a good fit for measuring alternating current, but there are many gaps found in the literature survey pointing toward the fact that there is no research done until now for their practical applicability on AC power systems. There are various open-ended issues that need to be investigated for proving the success of magnetic sensor in non-invasive current measurement application. These all points motivated this research, and the objectives of the study are defined accordingly.

1.4 Objectives of the Research

The research motivation and primary objective of this thesis are to propose a more accurate and cost-effective current measurement technique for fault detection and monitoring in AC power systems. The goals and objectives of this research are:

- Perform a comprehensive review of the non-invasive current sensing techniques that had been explored till present and applied to measurement of current in low, medium, and high voltage power systems.

- Conduct a theoretical study by developing a mathematical model and simulate the system for medium voltage overhead conductor systems for estimation of current from measured magnetic field.

- Conduct preliminary experiments on a single-phase AC circuit with a few types of sensors to finalize the type of the sensor based on its ability to reproduce sinusoidal current of magnitudes up to at least 25 A.

- Develop mathematical techniques and computational algorithms for calibration and validation of sensors.
- Conduct an experiment in high voltage laboratory to test the sensors for measuring single-phase AC current magnitudes up to 200 A, and if possible, extend the field experiment to measure higher current magnitudes up to 1500 A.
- Design and develop a three-phase resistive circuit experiment setup and conduct laboratory experiments for measurement of magnetic fields produced by three phases. Develop and apply computationally efficient technique for estimation of three-phase current phasors.
- Perform a field experiment for testing the performance of sensors in measuring three-phase currents from 50 A to 200 A.
- Study the performance of the calibrated sensors with respect to certain factors such as distance from the source, sensitivity to low and high frequencies, magnetic field intensity sensed in presence and in absence of conductor insulation.
- Investigate the performance of sensors when applied with input currents of low frequency (1 Hz, 2 Hz, 5 Hz, and 10 Hz), and with input currents of higher order of harmonic frequencies such as, 2^{nd}, 3^{rd}, 4^{th} and 5^{th} harmonic of fundamental frequency (60 Hz). Carry out a comparative analysis of each sensor per phase with its corresponding current transformer and extend the comparative analysis of sensors by using multiple sensor combinations per phase.
- Explore the techniques such as sensor data fusion and weighting factors to improve the measurement accuracy of magnetic sensors.

1.5 Thesis Outline

Chapter 1 includes the research background, and an overview of current sensing technologies in the field of power systems. It also elaborates the working principle and practical limitations of window type current transformer that is vastly used in the present power system substations and network. In addition, a literature survey of the alternative

current sensing technologies and the gap in the literature is augmented in this chapter. Main research motivations, objectives and goals are stated in this chapter along with the thesis outline.

Chapter 2 proposes a new theoretical method of calculating currents in three-phase overhead medium and high voltage network by measuring the magnetic fields generated in the close vicinity of the power line conductors. This chapter explains theory, mathematical model, and simulation results of the estimation of individual phase currents in a three-phase triangular structure of overhead AC power systems.

Chapter 3 aims at testing, evaluating, and finalizing a suitable magnetic sensor that is fully capable of meeting the goals and objectives defined for this research. A comparative performance analysis of four different types of magnetic sensors along with the reasons for selection of the final sensor is presented in this chapter.

Chapter 4 describes the experimental procedure and mathematical techniques applied for calibration and performance validation of twelve TMR sensors that are installed in a single-phase resistive circuit. Moreover, it gives a detailed account of the effect of certain factors such as distance from source, sensor quality, insulation of current carrying conductor, and the effect of harmonics on the magnetic field sensing function of each sensor. The analysis is based on the measurements obtained from laboratory experiment for AC currents up to 25 A. Further, the performance results of the sensors for measuring high currents are also illustrated in this chapter. The experiment conducted in a HV laboratory involved high currents up to 1500 A. A detail analysis of the performance of sensors was performed by obtaining magnitude errors, phase errors and % TVE from DFT by comparing them with input currents produced for the experiment.

Chapter 5 demonstrates the extension of analysis performed for single-phase and presented in Chapter 4. It presents the investigation results of further analysis by applying a new technique for estimation of phase angle error and construct the phasor from real and imaginary components of the current calculated in the previous steps. It also presents a technique of sensor data fusion to improve the accuracy in current phasor measurement for various sensor pair combinations in a single-phase circuit platform. The tables of total vector error (TVE) percentage calculated for each sensor pair combination is included in

this chapter. In addition, this chapter provides details of the field experiment and the performance results of sensors for measuring currents from 10 A 1500 A.

Chapter 6 presents the details of the laboratory experiment performed for three-phase current measurement when the conductors are placed in a triangular arrangement and horizontal arrangement. The results of the calculation of individual phase current phasors and percentage TVE are presented with a comparative analysis with the actual input current as well as with that of current transformer. This chapter also presents the performance results of the field experiment performed at the General Motors Climatic Wind Tunnel facility where the per-phase currents were obtained up to 155.6 A. The additional factor of study during this experiment was measuring the fundamental frequency currents consisting of multiple harmonics that were generated by the electronic components in the load circuit. The performance analysis of the sensors for measurement of three-phase currents with harmonics is described in detail in the last section of this chapter.

Chapter 7 contributes the performance of TMR sensors when applied to sense the unbalanced three-phase currents and the resulting neutral current. In this case, two sensors per phase were utilized to sense the phase currents and one TMR sensor was installed on the neutral of the star connected three-phase resistive load circuit. The performance of the neutral sensor was tested by comparing its output with that of a high accuracy CT installed on the neutral.

Chapter 8 states the summary of accomplishments of the research and concludes with a scope for future work.

Chapter 2. Three-phase Current Estimation Technique using Magnetic Field Density: Modeling and Simulation

2.1 Measuring Magnetic Field

When a current is applied through a conductor, magnetic field is produced surrounding it. This magnetic field consists of magnetic lines of force with their plane perpendicular to the conductor and their centers at the center of the conductor. According to Biot-Savart Law, for a differential length of a filamentary conductor with radius of the circular cross-section limiting to zero, when passed with a current, I, the magnitude of the magnetic field intensity, H, produced around it is directly proportional to the magnitude of current, and differential length, and inversely proportional to the square of the distance, d, between the center of the conductor and the point of measurement of the magnetic field intensity. The Biot-Savart Law can be adopted to determine magnetic field density by assuming the conductor to have an infinite length and the current with a very low frequency such as, power frequency of 60Hz. In that case, the mathematical expression [55, 56] is given as:

$$H = \frac{I}{2\pi d} A/m \tag{2.1.1}$$

In above Equation (2.1.1), $1/2\pi$ is the constant of proportionality. The magnetic flux density, B is given by multiplication of the magnetic field intensity, H with the permeability of the medium. Therefore, Equation (2.1.1) can be expressed as:

$$B = \mu H = \frac{\mu I}{2\pi d} wb/m^2 \tag{2.1.2}$$

For air as a medium, the permeability is represented as μ_0 to finalize the above equation as:

$$B = \frac{\mu_0 I}{2\pi d} wb/m^2 \tag{2.1.3}$$

The unit of the flux density is also expressed as Tesla. From the above equations, it is evident that the magnetic flux density is directly proportional to the current and by measuring flux density the value of current can be obtained. Time-varying magnetic field can be considered as a quasi-static magnetic field because the frequency of the current is extremely low (60 Hz). This also helps in neglecting the effects of resistivity of the conductor. Moreover, the low frequency results into minimal shielding effect caused by the eddy currents [57]. The formula shown in Equation (2.1.3) can be used to calculate the current in a particular conductor if the magnetic field is measured with the help of sensors and placing them at a certain known distance.

The study of magnetic fields generated by multiple sources can be performed in detail for three-phase overhead lines with balanced three-phase voltages. Two types of arrangement for a three-phase overhead medium voltage power distribution system are chosen for the research in this thesis: triangular arrangement and straight-line (horizontal) arrangement [58, 59] as shown in the Figure 2.1. These two types of three-phase overhead conductor arrangements are mostly opted by the North American power distribution systems. However, there are various places where multiple three-phase circuits are present on one pole.

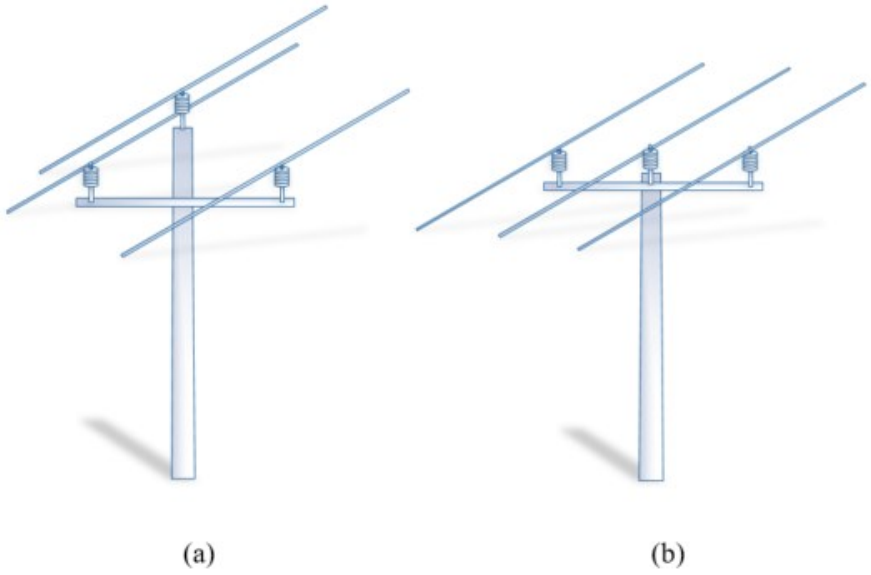

Figure 2.1 Types of three-phase overhead conductor arrangements (a) Triangular and (b) Horizontal

For example, two circuits with vertical arrangement of equidistant three-phase conductors on either side of the pole and a third three-phase circuit with triangular arrangement at the top of the same pole. For the ease of simulation and experiment, only triangular and horizontal structures for three-phase overhead conductors are selected in this research. In both types of structures, three-phase conductors are installed on appropriately sized insulators for safety [58]. The distance between the conductors is as per the standards [59]. In case of the triangular structure as shown in Figure 2.1(a), the horizontal spacing between the two conductors (at the bottom) is 113 cm and the distance of the conductor at the top is 98 cm and is equidistant from the other two conductors. In case of the horizontal structure as shown in Figure 2.1(b), all three conductors are placed in the same horizontal plane and the conductor is the middle is placed at 56.5 cm from the neighboring two conductors [58, 59]. The conductor spacing for triangular arrangement is elaborated in Figure 2.2.

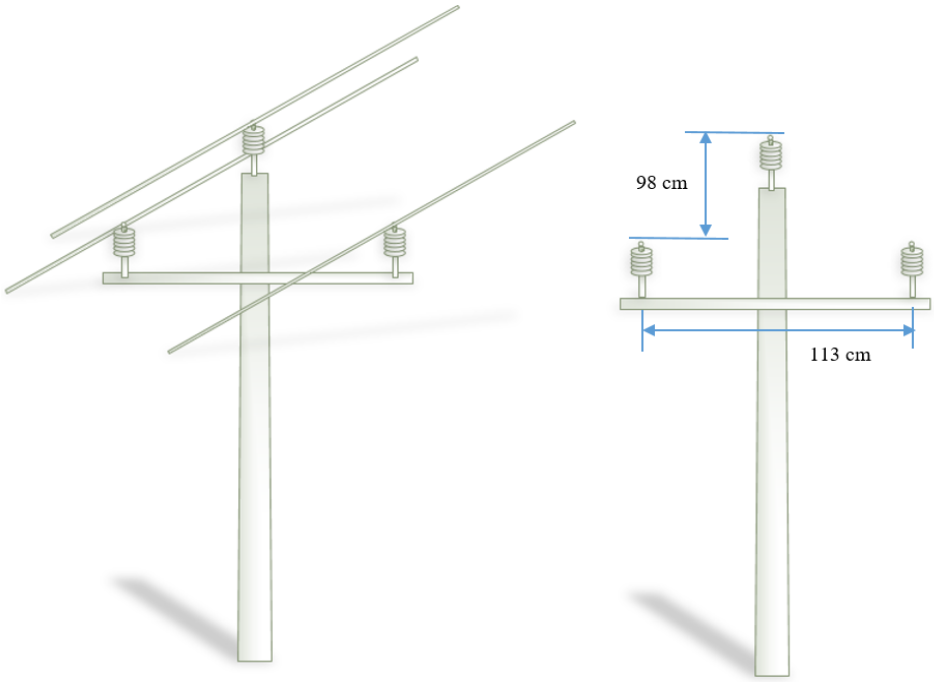

Figure 2.2 Standard spacing between the conductors for a triangular overhead arrangement

The first objective of this research is to investigate the behavior of magnetic fields generated by multiple alternating currents in a three-phase circuit. Therefore, for preliminary assessment a software tool named FEMM was utilized to find the B and H

values in a three-phase single conductor system. A three-phase circuit model with horizontal structure was developed in this software by choosing 350 mcm Aluminum Core Steel Reinforced (ACSR) conductors for each phase. A set of alternating currents of the magnitude 10 A to 100 A at 60 Hz with a phase difference of 120^0 between each other were chosen for the modeled circuit. Figure 2.3 shows the resulting magnetic fields generated by balanced three-phase currents surrounding the conductors for 100 A current. The magnetic field intensity lines are plotted in different colors based on their strength. From this figure it can be observed that each conductor has multiple magnetic field lines surrounding it for distances very close from their centers. With the increase in the distance, these lines of magnetic field interact with each other to form elliptical shape showing a resultant magnetic field surrounding three conductors. The individual conductor's magnetic field interact with the neighboring conductor to form elliptical shape for a distance relatively closer to all conductors and finally becomes one circle surrounding three conductors. This indicates that the magnetic field intensity for individual conductor can be measured accurately for distances closer to each conductor and can become difficult with the larger distances from the center of each conductor.

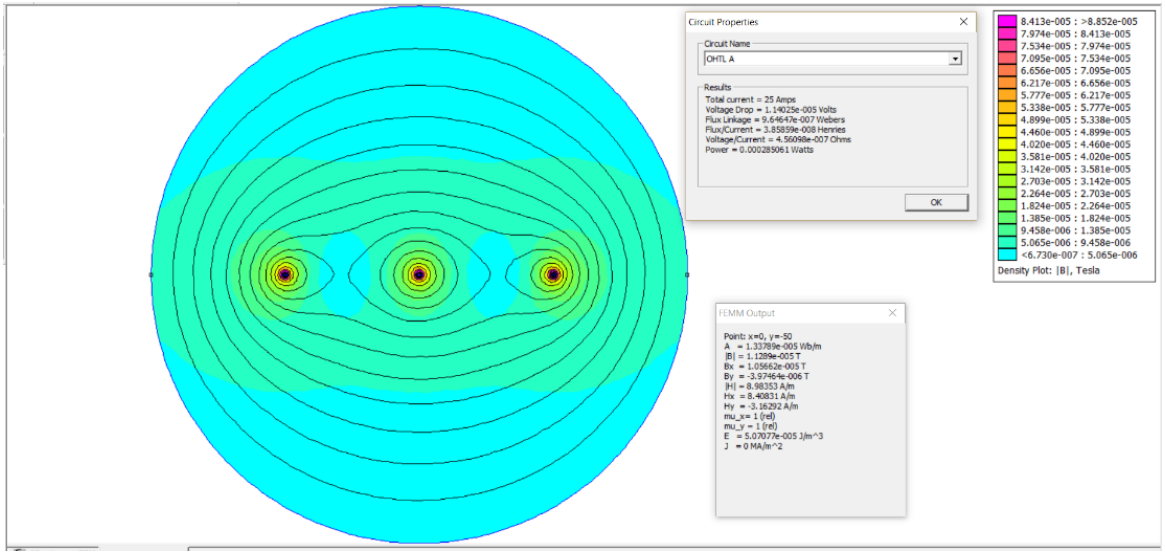

Figure 2.3 Magnetic field when applied with 25 A in three conductors

After viewing the magnetic fields shown in the above Figure 2.3 and the theory explained in this section, it is evident that the magnetic fields interact with each other at points of intersection when three-phase currents flow simultaneously. Therefore, the magnetic field

at any point near any phase conductor will be a resultant magnetic field caused because of the interaction of the magnetic fields by individual phase currents. This will influence the measurement of the current based on the Equation (2.1.3). Therefore, there is a need to apply a mathematical estimation technique which can give the accurate values of currents generated by multiple magnetic fields. The following section explains the mathematical model and technique designed for a three-phase symmetrical system.

2.2 Mathematical Model for Magnetic Field of Three-Phase, Three-Conductor System

Three-phase overhead pole mounted structures for 15 kV distribution system is chosen from the USF standard which gives the clearances between three-phase conductors as shown in Figure 2.1. Each phase generates a magnetic field surrounding it because of time-varying low frequency sinusoidal voltage source. In this scenario, the resultant magnetic field at any point, P1 is a function of the distance from each conductor, time and magnitude of the time-varying current as shown in the Figure 2.4 (a) and (b).

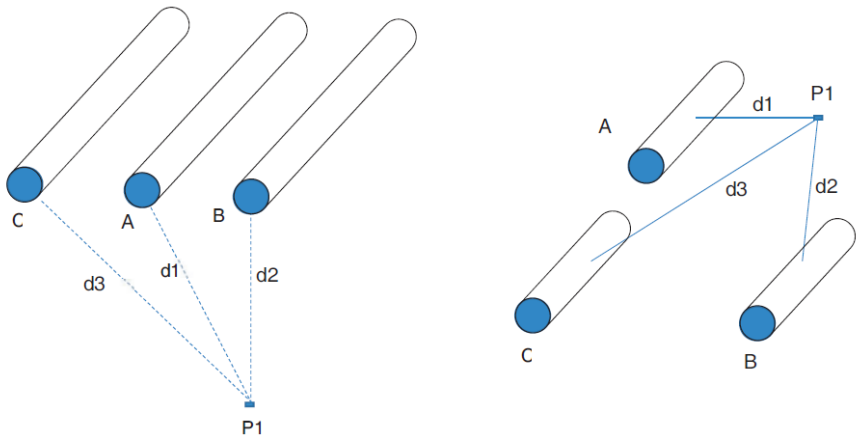

(a) (b)

Figure 2.4 Resultant field at point P1 in case of (a) Horizontal (b) Triangular arrangement

When all three phases have alternating currents $I_A(t)$, $I_B(t)$ and $I_C(t)$, then the magnetic field B_T at point P1 is a function of combined fields due to all three phases and can be given as:

$$B_T\left(I,\theta,t\right)=f\left\{B_A\left(I_A,\theta_A,t\right),B_B\left(I_B,\theta_B,t\right),B_C\left(I_C,\theta_C,t\right)\right\} \tag{2.2.1}$$

In the above equation, Ba, Bb, and BC are the magnetic field densities for phase A, B, and C. Theta A, Theta B and Theta C are the phase angles of the vectors for each current IA, IB and IC, and t is the time instance. Assuming that all three phases are balanced with a phase difference of 120^0 with each other, and at a fixed power frequency of 60 Hz, the resultant magnetic field at point P1, will be a vector addition of individual fields produced by three phase currents varying with time and phase angle, θ and is expressed as:

$$B_{P1}\left(I,\theta,t\right)=\sum_{t=1}^{t=n}\sum_{j=1}^{j=q}\left\{B_A\left(I_{Aj_\theta},t\right)+B_B\left(I_{Bj_{\theta-120}},t\right)+B_C\left(I_{Cj_{\theta+120}},t\right)\right\} \tag{2.2.2}$$

where the variable t in the above equation represents the instances for which currents are circulated through the circuit and the variable j represents the instantaneous value of currents at that time instance. The variable, n denotes total number of time instances and the variable, q indicates the magnitude of current. By placing the equation of calculation for magnetic field as given in Equation (2.1.3) into the above equation to get:

$$B_{P1}\left(I,\theta,t\right)=\sum_{t=1}^{t=n}\sum_{j=1}^{j=q}\left\{\frac{\mu_0 I}{2\pi d_1}\left(I_{Aj_\theta},t\right)+\frac{\mu_0 I}{2\pi d_2}\left(I_{Bj_{\theta-120}},t\right)+\frac{\mu_0 I}{2\pi d_3}\left(I_{Cj_{\theta+120}},t\right)\right\} \tag{2.2.3}$$

In the above equation, d1, d2 and d3 are the distances of measurement point from each phase conductor as shown in the Figure 2.4(a) and (b) The resultant magnetic field obtained by Equation (2.2.3) is a function of the distance of point P1 from each phase, and the current passing through each phase, A, B and C. It is composed of three vectors in three dimensions, X, Y and Z. In this case, the conductors A, B and C are assumed to be in the X-Y plane with the third dimension, Z = 0. Therefore, the magnetic field in the direction of Z-axis will not be required and only two-dimensional magnetic field components, B_X and B_Y are selected. The X-axis being the horizontal axis and the Y-axis being the vertical axis with the origin at point P1, the above Equation (2.2.3) can be utilized to express B_X and B_Y components as:

$$B_{X-P1}(I,\theta,t)=\sum_{t=1}^{t=n}\sum_{j=1}^{j=q}\left\{\frac{\mu_0 I}{2\pi d_1}\left(I_{AXj_\theta},t\right)+\frac{\mu_0 I}{2\pi d_2}\left(I_{BXj_{\theta-120}},t\right)+\frac{\mu_0 I}{2\pi d_3}\left(I_{CXj_{\theta+120}},t\right)\right\} \quad (2.2.4)$$

$$B_{Y-P1}(I,\theta,t)=\sum_{t=1}^{t=n}\sum_{j=1}^{j=q}\left\{\frac{\mu_0 I}{2\pi d_1}\left(I_{AYj_\theta},t\right)+\frac{\mu_0 I}{2\pi d_2}\left(I_{BYj_{\theta-120}},t\right)+\frac{\mu_0 I}{2\pi d_3}\left(I_{CYj_{\theta+120}},t\right)\right\} \quad (2.2.5)$$

The value of the field for X and Y component depends on the magnetic lines of force perpendicular or tangent to the point. With the X-component tangent to the point, the value of the field will be zero, and will be maximum with the vertical case and angle 90^0, considering that the point P1 is vertically below the conductor-B. It is obvious from the Equation (2.2.3) that the magnetic field generated by current $I_B(t)$ will be highest in magnitude compared to those generated by $I_A(t)$ and $I_C(t)$.

This value can be even more accurate if we increase the number of points around the current carrying conductor. Then, the resulting magnetic field will be an addition of the fields produced by three currents at multiple points situated together and will depend on the distance of these points from the conductor. This difference in the distance can be considered either in one dimension or two-dimensions. One of such two-dimensional arrangements is shown in the Figure 2.5.

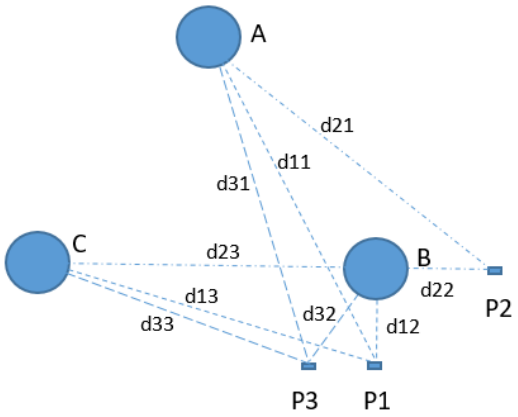

Figure 2.5 Magnetic field at three points from the current source

The equations for resultant magnetic fields produced by each phase current B_A, B_B and B_C measured from multiple points from $P1,.....Pn$, are given as:

$$
\begin{aligned}
B_A(I,\theta,t) &= f\left\{B_A(I_A,\theta_A,t)_{P1} + B_A(I_A,\theta_A,t)_{P2} + ... + B_A(I_A,\theta_A,t)_{Pn}\right\} \\
B_B(I,\theta,t) &= f\left\{B_B(I_B,\theta_B,t)_{P1} + B_B(I_B,\theta_B,t)_{P2} + ... + B_B(I_B,\theta_B,t)_{Pn}\right\} \\
B_C(I,\theta,t) &= f\left\{B_C(I_C,\theta_C,t)_{P1} + B_C(I_C,\theta_C,t)_{P2} + ... + B_C(I_C,\theta_C,t)_{Pn}\right\}
\end{aligned}
\tag{2.2.6}
$$

The total magnetic field, $B_T(I,\theta,t)$ will be the vector addition of all three fields B_A, B_B and B_C show in above Equation (2.2.6) and by following the Equation (2.2.2).

The field intensity measured at more locations helps in gaining more accurate value of the dynamically changing magnetic field that varies with change in time and the phase angle of the source current. As an illustration, consider 36 measurement points, P1, P2 and P3, up to P36 that are situated at certain distances with equal spacing between each other in four directions perpendicular to each other around each phase conductor as shown in the Figure 2.6.

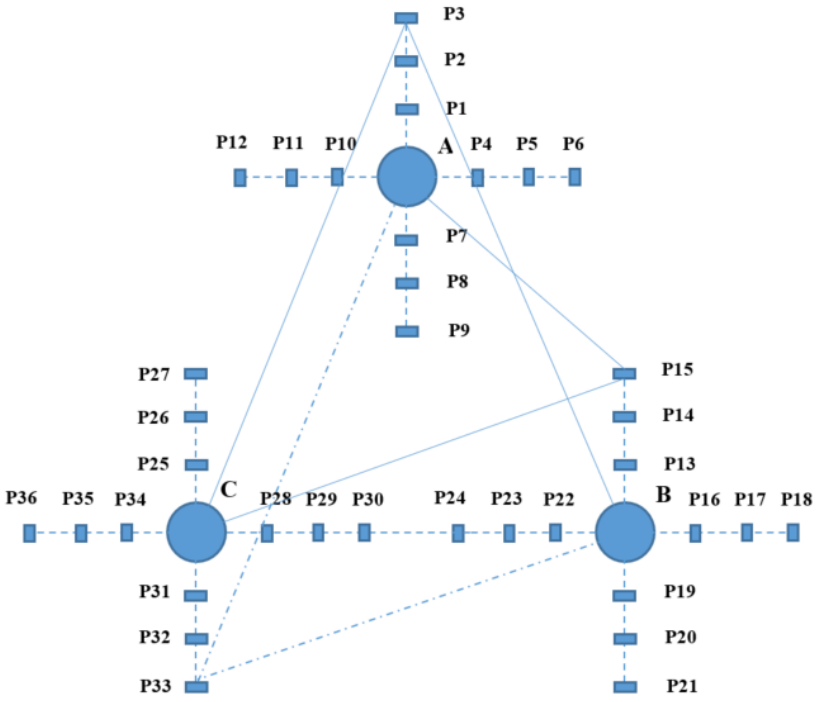

Figure 2.6 Magnetic field at various points from the current sources

For this arrangement, the magnetic fields can be calculated at all points for each phase conductor. The equations of the magnetic flux density for the chosen points by using

Equation (2.2.3) considering the balanced three-phase system where the phase difference between the phases remains the same can be expressed as:

$$
\begin{aligned}
B_{P1}(\mathrm{I},t) &= \sum_{t=1}^{t=n}\sum_{\theta=1}^{360}\left\{\frac{\mu_0}{2\pi d_{11}}\left(I_{A_\theta},t\right)+\frac{\mu_0}{2\pi d_{12}}\left(I_{B_{\theta-120}},t\right)+\frac{\mu_0}{2\pi d_{13}}\left(I_{C_{\theta+120}},t\right)\right\}\\
B_{P2}(\mathrm{I},t) &= \sum_{t=1}^{t=n}\sum_{\theta=1}^{360}\left\{\frac{\mu_0}{2\pi d_{21}}\left(I_{A_\theta},t\right)+\frac{\mu_0}{2\pi d_{22}}\left(I_{B_{\theta-120}},t\right)+\frac{\mu_0}{2\pi d_{23}}\left(I_{C_{\theta+120}},t\right)\right\}\\
B_{P3}(\mathrm{I},t) &= \sum_{t=1}^{t=n}\sum_{\theta=1}^{360}\left\{\frac{\mu_0}{2\pi d_{31}}\left(I_{A_\theta},t\right)+\frac{\mu_0}{2\pi d_{32}}\left(I_{B_{\theta-120}},t\right)+\frac{\mu_0}{2\pi d_{33}}\left(I_{C_{\theta+120}},t\right)\right\}\\
B_{P4}(\mathrm{I},t) &= \sum_{t=1}^{t=n}\sum_{\theta=1}^{360}\left\{\frac{\mu_0}{2\pi d_{41}}\left(I_{A_\theta},t\right)+\frac{\mu_0}{2\pi d_{42}}\left(I_{B_{\theta-120}},t\right)+\frac{\mu_0}{2\pi d_{43}}\left(I_{C_{\theta+120}},t\right)\right\} \qquad (2.2.7)\\
&\vdots\\
&\vdots\\
B_{P36}(\mathrm{I},t) &= \sum_{t=1}^{t=n}\sum_{\theta=1}^{360}\left\{\frac{\mu_0}{2\pi d_{361}}\left(I_{A_\theta},t\right)+\frac{\mu_0}{2\pi d_{362}}\left(I_{B_{\theta-120}},t\right)+\frac{\mu_0}{2\pi d_{363}}\left(I_{C_{\theta+120}},t\right)\right\}
\end{aligned}
$$

These points of measuring the magnetic field from the center of each conductor have a purpose of capturing magnetic field which is decreasing with increasing distance. This information is then used to estimate current in each phase.

2.3 Calculation of Magnetic Field for Three-Phase Circuit

It is difficult to find the exact solution to the magnetic field from the equations derived in the previous section. There are a few numerical methods used by researchers to reach the near accurate approximation of the actual magnetic field. These methods include [60, 61] Finite Difference Time Domain method (FDTD), Method of Moments (MoM), Variational Iteration Method (VIM) and Finite Element Method (FEM). There are research teams that have researched a few mathematical techniques to calculate the magnetic field generated by power line conductors and used it for various applications. They used numerical and semi-numerical techniques to approximate the magnetic fields and validated their methods with the actual measured values. K. Hameyer et al. [62] applied a combination of semi-numerical method and FEM to calculate the magnetic field in 150 kV overhead

transmission lines in Belgium. The mathematical model was developed for Aluminum Core Steel Reinforced (ACSR) conductors in both two- and three-dimensions using Cartesian coordinates system. The values calculated by using the FEM model were compared with the actual measured values with the help of a magnetometer by Holaday Industries, model HI-3604. The meter used for field measurement consists of a circular coil and a fiber-optic receiver with a non-conductive tripod stand. The team found that the results of the FEM model matched with measured values by the meter for a two-dimensional model. In another research, Farah et al. [63] performed a comparative study to find the accurate estimation of magnetic field at the surface of overhead transmission line conductors. This team applied three methods for the computation of magnetic field, namely, method of successive images, FEM using a spatial transformation, also known as Kelvin Transformation, and the traditional FEM. The focus of their study was a 525 kV transmission line with ACSR conductors in Brazil. Their work proposed imposing virtual circular boundaries close to the conductors and assuming the ground to be entirely in external transformed domain. This reduced the study domain of the FEM model and increased the computational accuracy. Since the voltage level considered for the research was high, the model gave a good accuracy. Pao-La-Or et. al [64] presented a two-dimensional time varying finite element model for electromagnetic field approximation in the induction motor. It is found that the mathematical model is very identical to that of transmission lines except this work used the Newton-Raphson method combined with bi-conjugate gradient (BCG) method to reduce the computational time and achieve better convergence. They applied the Galerkin weighted residual method to derive the covariance matrix for the second order partial differential equation of magnetic field in a two-dimensional plane.

The numerical simulation for Maxwell's equations which is performed almost by every research team mentioned used FEM. But this was also explored using the FDTD method using Yee algorithm by M. Mismar [65] in which the author showed the application of this method for a square region with dimension of 5cm. This method had limitations of accuracy and computational time because of restricted mesh size and smaller size of the matrix. Thus, successful efforts towards magnetic field modeling by various researchers

motivated this research to use the FEM based modeling of magnetic fields and obtain the magnetic fields per phase in overhead distribution and transmission system.

A 12.47 kV three-phase triangular structure as explained and shown previously in Figure 2.1 is chosen for the magnetic field calculation at the points as described in Figure 2.6. To obtain the magnetic fields for this case, the model is developed with the help of QuickField. For theoretical study and analysis both, triangular and horizontal arrangements are considered in this thesis. In practical conditions, the spacing between the conductors change because of sag and shaking of the conductor due to wind. In this thesis, these two factors are assumed to be ideally zero giving a constant spacing between each phase conductor for both configurations. Moreover, the length of conductors is assumed to be 10km. The medium voltage for simulation is assumed to be12.47 kV.

The first step towards developing the three-phase model is to design a three-phase medium voltage circuit. The specifications of conductors of size 350 mcm and ACSR type are assigned to the model. The impedance of the ACSR conductors is set to 3.386 Ω considering a length of 10 km. The actual equations for all three-phase voltages in the design are based on time and angle with a frequency of 60Hz and are given as: $V_A = 12470\sqrt{2/3}\sin\left(360\times 60\times t\right)$, $V_B = 12470\sqrt{2/3}\sin\left(360\times 60\times t - 120^0\right)$, and $V_C = 12470\sqrt{2/3}\sin\left(360\times 60\times t + 120^0\right)$. The currents generated by this model are also recorded for reference. Figure 2.7(a) shows the circuit diagram based on the selected parameters. The model design is based on Finite Element Method and therefore, needs definition of the resolution by number of cells and the boundary conditions. For this model, Dirichlet boundary conditions [66] are applied at the outer circumference and at the surface of conductor for each phase. The number of the nodes are chosen to 40,000. The sampling rate is model was set at 0.001 second per set of iterations. This gives a total populated magnetic field surrounding the structure within a radius of 200 cm and is shown in the Figure 2.7(b). These measured values of magnetic fields are then used in the second part of the algorithm to estimate the currents using the Least Squares method explained in the next section.

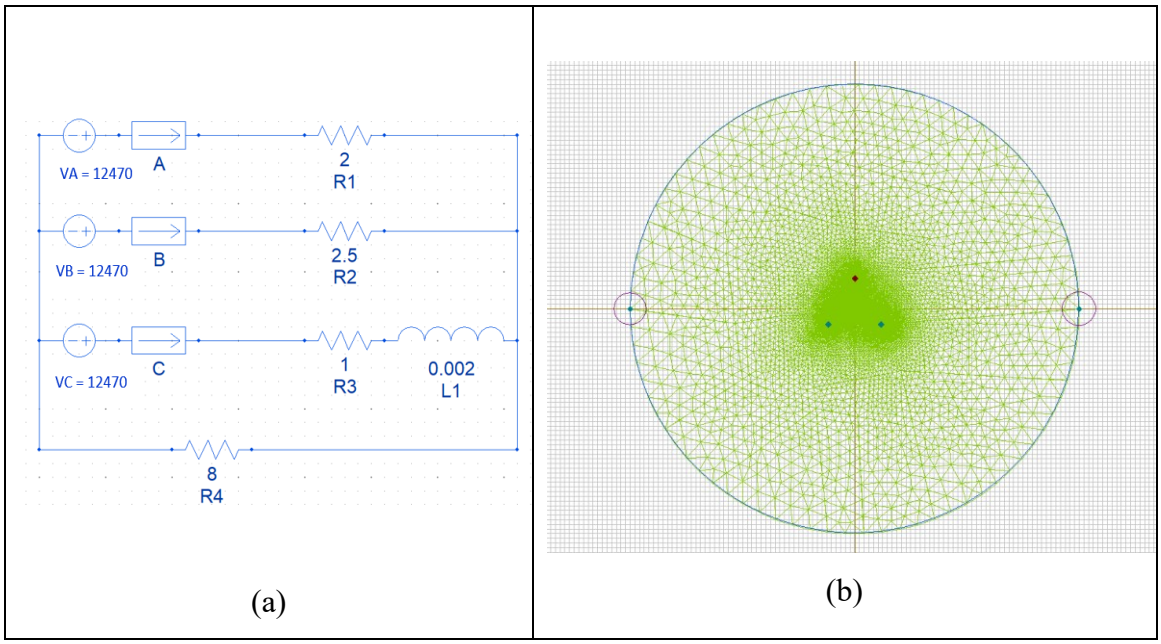

Figure 2.7 Model and circuit for three-phase magnetic field simulation

2.4 Linear Regression Analysis to Estimate Three-Phase Currents

For all points of measurement, the magnetic field equation shows a linear relation between the known and unknown variables. Therefore, the estimation of instantaneous values of current from measured field values can be achieved by applying linear regression technique which becomes the second part of the algorithm. In this method, the magnetic field and distances are assigned to be the known co-variables and currents as response variables. Suppose f is the linear regression function to be estimated from n co-variables and their responses $(x_1, B_1).....(x_n, B_n)$, then it is represented as

$$B = f(X_i) + \xi \tag{2.4.1}$$

where, ξ the noise and considered as negligible for three-phase simulation considering an ideal source of three-phase voltages and knowing the impedance and line length of the circuit. Suppose the regression function, f is chosen for a certain number, $p \le n$ of parameters, $\beta = (\beta_1, \beta_2, ...\beta_p)^T$. The aim is to find the estimates of β represented by $\hat{\beta}$ that minimize the residual sum of squares and given as:

$$f\left(\beta_1,.....\beta_p\right)=\sum_{i=1}^{n}\left(B_i-\sum_{j=1}^{p}x_{ij}\beta_j\right) \tag{2.4.2}$$

Where, $x_{ij}=\left(x_{i1},x_{i2},.....x_{ip}\right)^T$, for $j=1,.....p$ is a vector of feature measurements for ith sensor. The estimated values of β that are represented by $\hat{\beta}$ and are given as $\hat{\beta}=\left(\hat{\beta}_1,\hat{\beta}_2,....\hat{\beta}_p\right)$.

To minimize the Equation (2.4.2), we take its partial derivative with respect to each $\hat{\beta}_j$ and equate to 0. The solution satisfies:

$$\frac{\partial}{\partial\beta_j}f\left(\beta_1,....\beta_p\right)=-2\sum_{i=1}^{n}\left(B_i-\sum_{j=1}^{p}x_{ij}\beta_j\right)x_{ij}=0,\quad j=1,.....p \tag{2.4.3}$$

In order to find the estimator for the linear regression model of currents, it is easier to solve by transforming the equations from (2.2.7), (2.4.2) and (2.4.3) into matrix and develop the MATLAB computational program accordingly. Then, the magnetic field response values will be converted into matrix, B and feature values will be converted into a matrix, X as follows:

$$B=\begin{bmatrix}B_{P1}\\B_{P2}\\B_{P3}\\\vdots\\B_{Pn}\end{bmatrix},\text{ and }\quad X=\begin{bmatrix}x_{11} & x_2 & \cdots\\x_{21} & x_{xx} & \cdots\\x_{31} & x_{32} & \cdots\\\vdots & \vdots & \ddots\\x_{n1} & x_{n2} & \cdots\end{bmatrix}\quad\vdots \tag{2.4.4}$$

The matrix X in this case forms the feature measurement matrix consisting of distances of selected measurement points from each phase conductor. The Equation (2.4.2) will be then expressed as:

$$f\left(\beta\right)=\left(B-X\beta\right)^T\left(B-X\beta\right) \tag{2.4.5}$$

The derivative of the above equation also given in Equation (2.4.3) when divided by -2 becomes

$$B^T X = \hat{\beta}^T X^T X \tag{2.4.6}$$

Taking transpose on both sides of above equation and re-arranging, we get

$$\left(X^T X\right)^T \hat{\beta} = X^T B \tag{2.4.7}$$

It is observed that all the columns in X matrix are linearly independent and therefore, this matrix has full rank. Moreover, the term, $X^T X$ is non-singular and therefore, above equation can be written as follows:

$$\hat{\beta} = \left(X^T X\right)^{-1} X^T B \tag{2.4.8}$$

The above Equation (2.4.8) gives the estimates of three-phase currents. This least square estimation technique gives the estimated values after minimizing the error function based on the covariance matrix and the observed response values of the magnetic fields.

2.5 Computer Simulation and Analysis for Three-Phase Triangular Arrangement Overhead Line

The fields generated by the model are to be measured at points located at specific distance from every phase. To utilize the theoretical analysis performed in this chapter, these points of measurement can also be considered as the location of sensors for the further stage of experiment and, consequently, they can be considered as sensors.

The study of magnetic field and current estimation is organized into three groups. Group I consist of all combinations of the measurement points for three conductors with only one point per phase. Group II has two measurement points per phase and the Group III has three points per phase to utilize all 36 points shown in Figure 2.6. As explained in the previous section, each point has three distances from phase A, B and C. For example, for point P1, the distances d_{11}, d_{12} and d_{13} are calculated from the triangular geometry with reference to the point P1's location at 2.5 cm in the North. Similarly, the distances for points in other three directions are calculated accordingly. Selected points are at the distances of 2.5 cm, 5 cm, and 7.5 cm form each phase and are tagged based on their direction East (E), West (W), North (N) and South (S) as shown in the Table 2.1. This signifies the angles of location

of the points in these directions are 0^0, 180^0, 90^0 and 270^0 respectively. These distances for each point are inserted in Equation (2.2.7) to calculate the magnetic field for each individual point for selected combinations which becomes the first part of the algorithm and computational program developed in MATLAB. The names and numbers of the points aid the algorithm select and assign the data for each point into a particular vector which is grouped into a structure to calculate the residual error function and thus, determine the currents for each phase using the algorithm. Once the magnetic field for all combinations is obtained, the algorithm switches to the next step of estimation of currents for each phase based on the least squared error method explained in the previous section.

Table 2.1 Allocation of twelve points per phase and numbering for algorithm

Phase A				Phase B				Phase C			
	2.5 cm	5 cm	7.5 cm		2.5 cm	5 cm	7.5 cm		2.5 cm	5 cm	7.5 cm
N	1	2	3	N	13	14	15	N	25	26	27
E	4	5	6	E	16	17	18	E	28	29	30
S	7	8	9	S	19	20	21	S	31	32	33
W	10	11	12	W	22	23	24	W	34	35	36

Magnetic fields generated from the source currents for each phase are shown in Figure 2.8. The instantaneous values of currents are in amperes, and magnetic fields for each phase have the unit of Tesla. The currents generated by the model designed for 12.47kV balanced three-phase system are shown in the Figure 2.9. These currents will be used as a reference for comparing with the estimated currents from the algorithm.

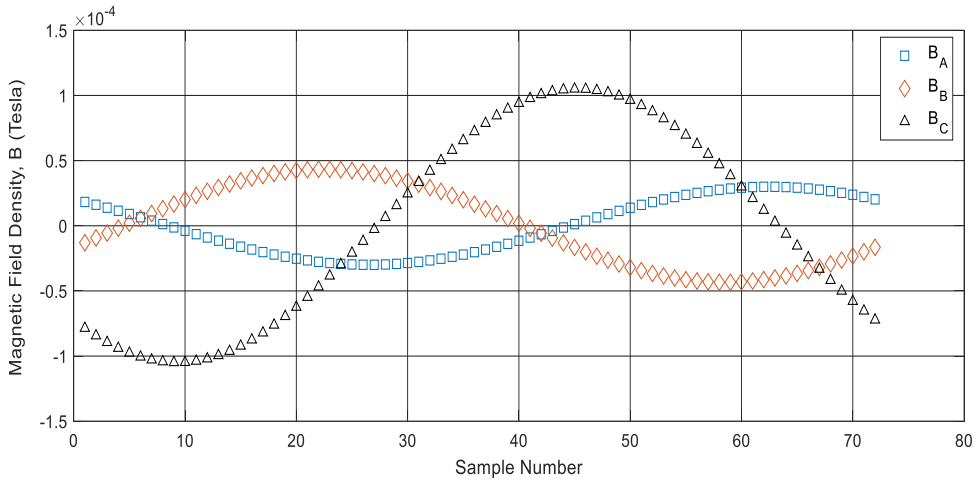

Figure 2.8 Magnetic field density generated by the model for assigned source currents

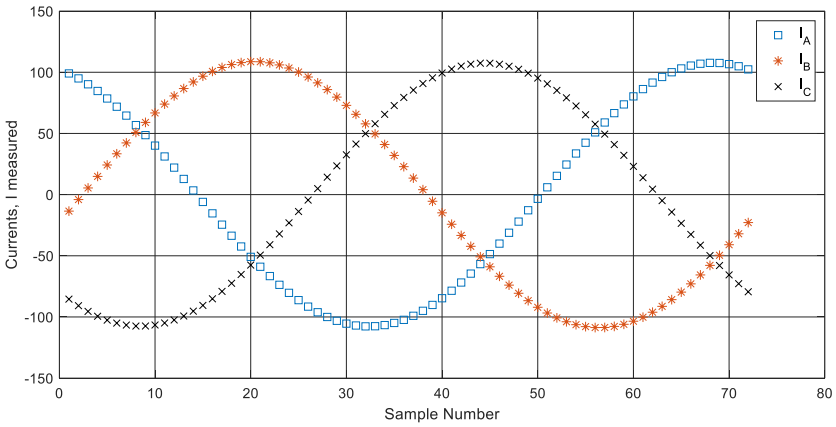

Figure 2.9 Source currents simulated for three-phase system

The following sections demonstrate the results of the simulation performed for three groups where one, two and three measurement point combinations are used.

2.5.1 Simulation Results for Group I: One Measurement Point per Phase

There are 24 cases designed based on various combinations of locations of measurement points and their distances of 2.5 cm, 5 cm and 7.5 cm from each phase conductor. The results for all cases are shown in the Table 2.2. First column gives the case number and a particular combination based on a labeling convention for based on the measurement point's location selected for each phase. For 24 combinations of the points based on their locations gave magnetic field at specific point and it is used in the algorithm for estimation

of per-phase current. For example, Case#a1 in the Table 2.2 consists of one point per phase selected in the North direction and each point is at the same distance from each phase. By referring the label of each point from Figure 2.6 and Table 2.1 it can be inferred that these points of Case#a1 are closest to three-phase conductors and are points P1, P13 and P25. From Figure 2.6, it is evident that they are all in the North direction. Thus, their labeling is N1, N13 and N25. This implies each point per phase is at 2.5 cm at an angle of 90^0 from the center of phase conductor. Their angle from the respective phase conductor is 90^0, consequently, the Case#a1 gets the combination label as 90N_90N_90N. Similarly, the magnetic field measurement points for all three-phases at 5 cm are defined as N2, N14, N26, and have the same orientation label as 90N_90N_90N, but their number indicates their distance from each phase by following the Figure 2.6. The table also shows some cases with labels "ZW" and "ZE" which indicate that the points are either in the West or East direction at 0^0. For example, the Case#a14 label shows the configuration, 90N_ZE_ZW and the points for Phase A, B and C are N2, E17 and W35, which indicates measurement point for phase-A is at 5 cm at an angle of 90^0, point for phase-B is at 5 cm in the East at 0^0 and the point for phase-C is at 5 cm in the West at 0^0. Thus, columns 2, 3 and 4 of Table 2.2 indicate the measurement point for each phase and indicate its direction as well as distance from the phase. The last three columns of this table give the maximum errors in amperes after comparing the estimated per-phase currents with their actual currents. The algorithm also gave the results of the minimum errors for each current and for each case. These results are given in the Table A.1 of Appendix A.

Figure 2.10 (a), (b) and (c) show the difference between the estimated and actual current for Phases A, B and C respectively obtained for Case#a11.

Table 2.2 Estimation errors in Amperes for group I: One measurement point per phase for triangular arrangement of three-phase system

Case	Ph-A	Ph-B	Ph-C	I_A_error (A)	I_B_error (A)	I_C_error (A)
a1: 90N_90N_90N	N1	N13	N25	1.29	3.43	3.20
a2: 90N_90N_90N	N2	N14	N26	2.03	7.52	7.74
a3: 90N_90N_90N	N3	N15	N27	2.93	11.43	11.92
a4: ZE_ZE_ZE	E4	E16	E28	2.51	3.25	3.15
a5: ZE_ZE_ZE	E5	E17	E29	5.83	2.34	9.31
a6: ZE_ZE_ZE	E6	E18	E30	8.91	3.87	14.00
a7: 90S_90S_90S	S7	S19	S31	5.05	1.10	2.18
a8: 90S_90S_90S	S8	S20	S32	9.95	3.53	4.71
a9: 90S_90S_90S	S9	S21	S33	15.42	5.56	6.82
a10: ZW_ZW_ZW	W10	W22	W34	4.26	2.80	0.87
a11: ZW_ZW_ZW	W11	W23	W35	6.71	7.79	2.26
a12: ZW_ZW_ZW	W12	W24	W36	10.26	12.55	4.06
a13:90N_ZE_ZW	N1	E16	W34	1.28	3.37	0.93
a14:90N_ZE_ZW	N2	E17	W35	1.73	2.36	2.04
a15:90N_ZE_ZW	N3	E18	W36	2.19	3.50	3.31
a16: 90N_90S_90S	N1	S19	S31	**1.23**	**1.15**	**2.21**
a17: 90N_90S_90S	N2	S20	S32	1.54	3.62	4.79
a18: 90N_90S_90S	N3	S21	S33	3.56	5.78	6.96
a19: 90N_90S_ZW	N1	S19	W34	**1.19**	**1.13**	**0.89**
a20: 90N_90S_ZW	N2	S20	W35	1.51	3.49	2.19
a21: 90N_90S_ZW	N3	S21	W36	1.74	5.52	3.70
a22: ZE_90S_ZW	E4	S19	W34	2.56	1.14	0.95
a23: ZE_90S_ZW	E5	S20	W35	5.95	3.60	2.34
a24: ZE_90S_ZW	E6	S21	W36	9.22	5.75	3.95

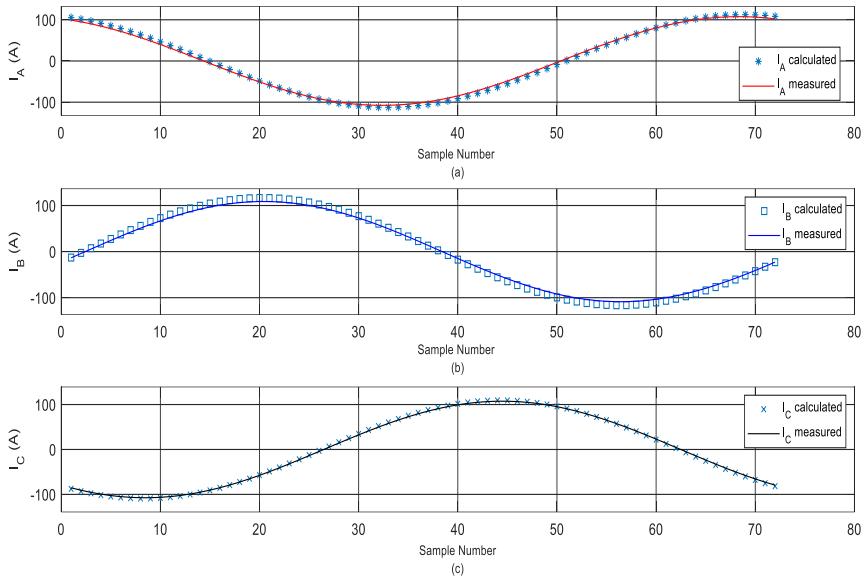

Figure 2.10 Case#a11: estimated and actual currents for (a) Phase-A, (b) Phase-B, (c) Phase-C

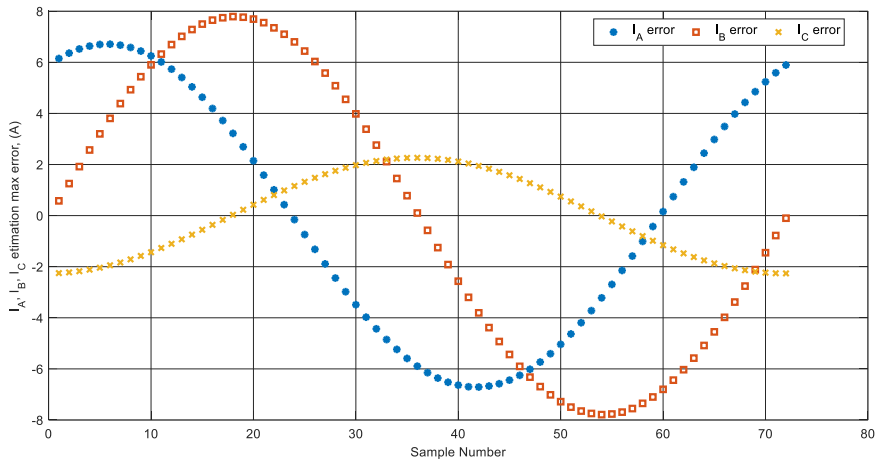

Figure 2.11 Estimation errors (maximum) in amperes for phase-A, phase-B and phase-C, Case#a11

The estimated currents were observed to be very close to the actual currents as shown in the Figure 2.10 (a), (b) and (c). This proved the advantage of applying least squared error algorithm in the estimation of the currents form the measured magnetic fields. Moreover, the maximum and minimum errors were calculated for each phase by comparing them with

the actual phase currents. For phase-A the maximum error was 6.71 A, for phase-B 7.79 A and for phase-C it was 2.26 A as shown in Figure 2.11.

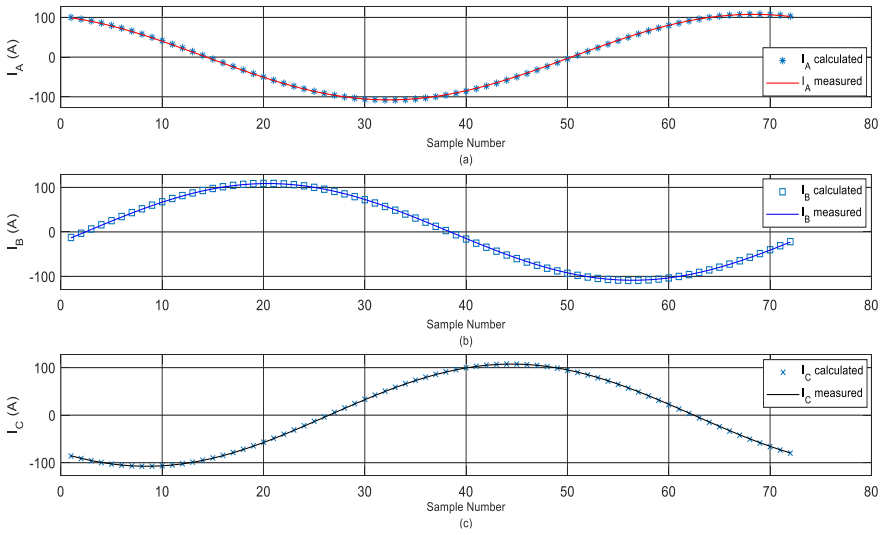

Figure 2.12 Case#a19: estimated and actual currents for (a) Phase-A, (b) Phase-B, (c) Phase-C

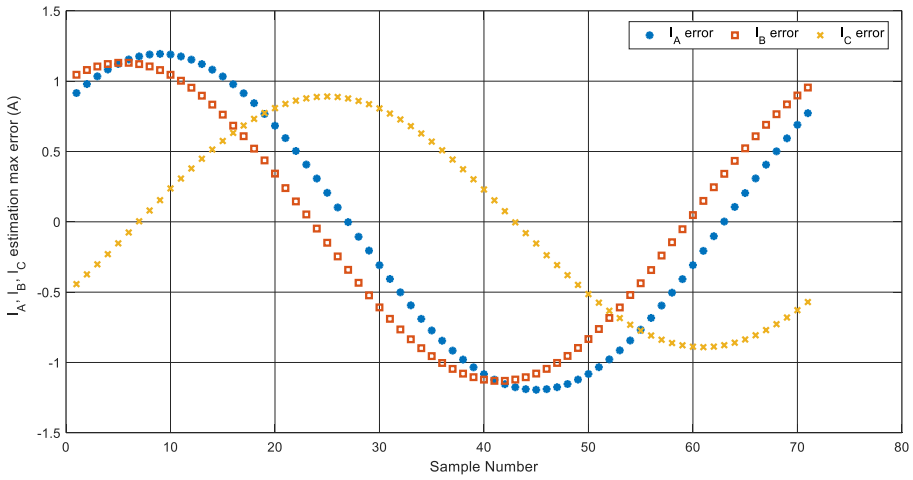

Figure 2.13 Estimation errors (maximum) in amperes for phase-A, phase-B and phase-C, Case#a19

The errors for Case#a11 were found maximum as compared to other combinations because all measurement points were in the West direction for all three-phases. The maximum estimation error in amperes was observed to be far less for Case#a19 when the

measurement points were 90U for phase-A, 90D for phase-B and ZW for phase-C at 2.5cm and the calculated values of maximum errors were 1.19 A, 1.13 A, and 0.89 A for phase-A, B and C respectively. For the same group when the distance increased from 2.5 cm to 7.5 cm, the maximum error did not change drastically for phase-A, but there was a significant increase in the errors for phase-B and phase-C. This is evident from the Table 2.2 where the Case#a21 gave the maximum errors of 1.74 A, 5.52 A and 3.72 A. This indicates that the magnetic field weakened with the increase in the distance from 2.5 cm to 7.5 cm even when the measurement points were far from each other.

Table 2.2 shows major eight combinations of the locations for points per phase, and then each combination repeated for three distances. Therefore, for each combination it was observed that the errors were less for the distance 2.5 cm from each phase. These errors were high for symmetrical combinations where all measurement points were in the same direction and shown in the Table 2.2. The cases from Case#a1 to Case#a12 showed higher values of errors per phase as compared to the combinations chosen for Case#13 to Case#24. The highest value of the error of 9.22 A was observed for Case#9 where all measurement points were in the South direction at 7.5 cm for the first group of 12 cases whereas for the remaining 12 cases. In this configuration, the sources of errors are because of the distance from each phase conductor, the interference, and the angle of incidence. In addition, the number of nodes selected in the FEM based simulation of magnetic field introduces a slight error. Greater the number of nodes, higher is the accuracy in capturing the magnetic field at the chosen point of measurement, but simultaneously increases the computation time and therefore becomes a practical limitation in the simulation study.

2.5.2 Simulation Results for Group II: Two Measurement Points per Phase

As in the previous section, a set of 24 combinations were also defined by considering two points of measurement per phase. The choice of directions remaining the same as that of single sensor, total six sensors were considered per case of simulation. The fields were chosen for the same configuration of three phase voltage and circuit. The main motive for selecting two points per phase is to improve the measurement accuracy by overcoming the effect of magnetic field interference between phases. The advantage of using the points designed in this group is the freedom of selection of any two points out of three for each

phase and study the dynamical behavior of magnetic field interaction between phases. The combinations based on direction are same as those of the Group I point, except there are a few more variations defined in this group to obtain a better accuracy.

For first eight cases, consecutive two points per phase are selected in the same direction for all three sets. Case#b1 can be taken to clarify the selection criteria. In this case, all six sensors are in the N direction, and they are consecutive for each phase, i.e., for phase A, the points chosen are N1 and N2 which are at 2.5 cm and 5 cm respectively from the center of the phase-A conductor (refer Figure 2.6). Similarly, the points N13, N13 and N25, N26 are in N direction for phase-B and phase-C respectively at the locations 2.5 cm and 5 cm. This method of selecting set of six points for each phase in the same direction continued till Case#b12. Variation is deliberately introduced in selecting two non-consecutively located points per phase. For example, in Case#b8 the points are at 5 cm and 7.5 cm, that means, the points are consecutively located from the center of conductor for all three phases, but this style is changed for Case#b9. In this case, the points are selected in the S-direction, but first point location is at 2.5 cm and the second point location is 7.5 cm and this can be confirmed from Figure 2.6. Similar change can be observed for cases, Case#b3, Case#b6 and Case#b12.

Mixed combinations were chosen for points' direction per phase from Case#b13 onwards, but two points for each phase were kept in the same direction. For example, Case#b13 shows that there are two points for phase-A in N direction with sensor locations of 2.5 cm and 5 cm, whereas for phase-B these points are in E direction and for phase-C they are in W direction with location distances remaining the same as that of phase-A. This style is followed for all cases from Case#b13 to Case#b24 except for Case#b20, in which all six points chosen are in S direction. The combinations and results are given in Table 2.3.

The estimated currents for each phase for Case#b1 are shown in Figure 2.14. The combinations of locations for this case include all points in N direction at 2.5 cm and 5 cm for each phase. The estimation errors in amperes are shown in the Figure 2.15 with a minimum error of 1.37 A for phase-A, and errors of 4% for phase-B and phase-C. These errors are maximum for this direction when the location points are at 5 cm and 7.5 cm for each phase. The errors for phase-B and phase-C are maximum (8.73 A for phase-B and

9.03 A for phase-C) in Case#b2, but for phase-A, the maximum estimation error is only 2.24 A. This is because phase-A conductor is placed 92 cm above the horizontal plane of phase-B and C, and these two phases have the influence of magnetic field produced by phase-A at 7.5 cm, which is affecting the actual magnetic field produced by each-phase at these points and, therefore, resulting in weaker magnetic field. Consequently, the algorithm shows this impact of the interference on phase-B and phase-C and, as a result, the errors are higher compared to that of phase-A. This is also applicable for Case#b5, Case#b8, and Case#b11.

The supporting evidence of higher estimation errors is shown for Case#b8 in Figure 2.16. The maximum errors in Case#b8 are 11.14 A, 4.14 A, and 5.35A for phase-A, B and C respectively. This is because the combination has measurement points at 7.5 cm. The error for phase A is 11.14 A, because the field generated by phase A has interference with those generated by phases B and C. As a result, the magnetic field value itself is less and not the true representation of the actual current flowing in phase-A conductor.

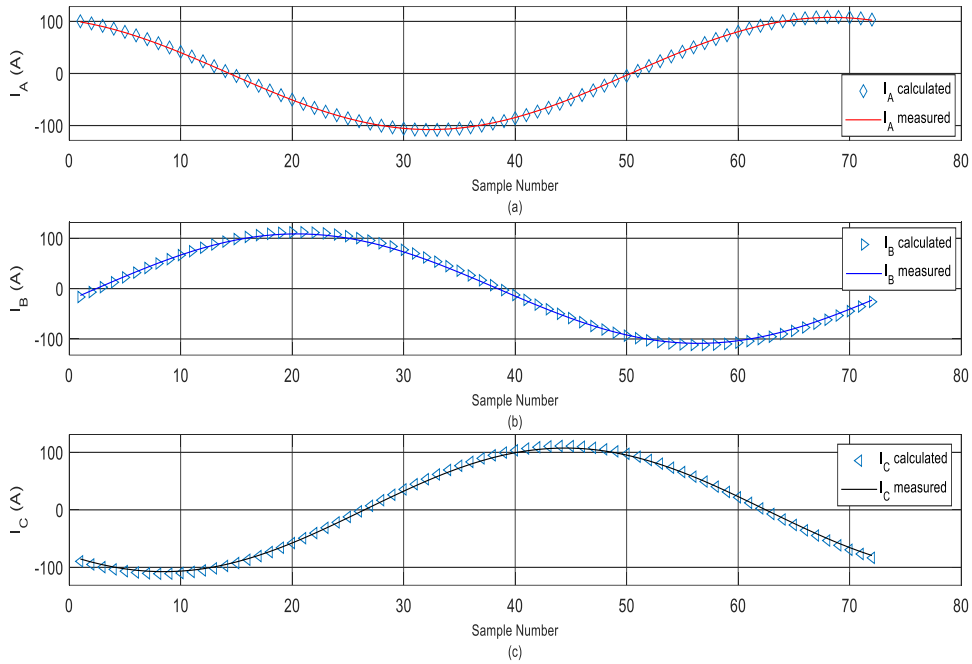

Figure 2.14 Case#b1: estimated and actual currents for (a) Phase-A (b) Phase-B, and (c) Phase-C

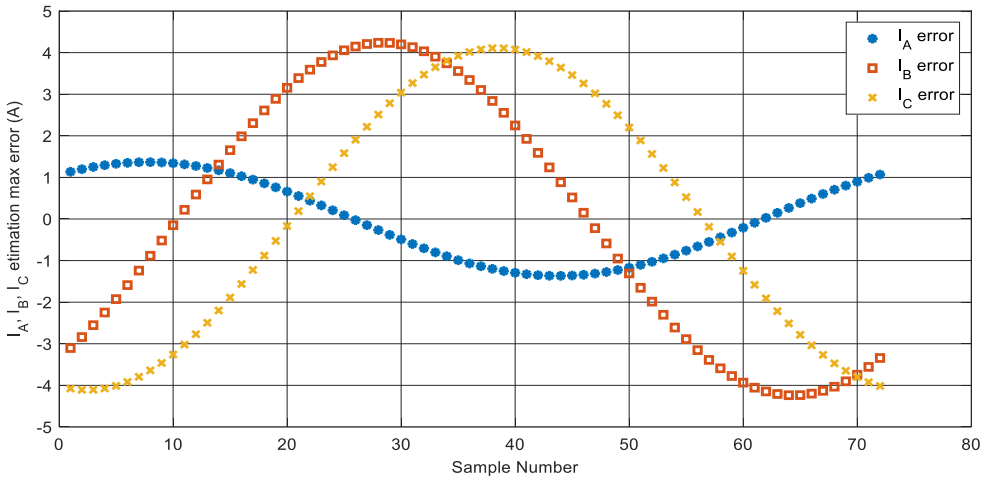

Figure 2.15 Estimation errors (maximum) in amperes for phase-A, phase-B and phase-C, Case#b1

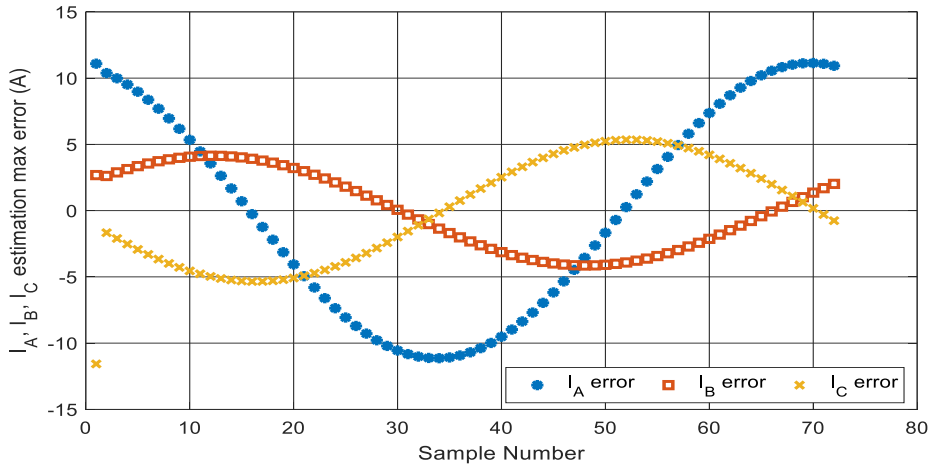

Figure 2.16 Estimation errors (maximum) in amperes for phase-A, phase-B and phase-C, Case#b8

The estimation errors for the rest of two phases are higher, because the measurement points are in South direction of the phases and sufficiently away from each other not to have any interference of neighboring magnetic fields. The results of cases where all measurement points per phase are not in the same direction show that the magnetic field sensing and current estimation accuracy of the algorithm is improved. It is evident from the outcome of combinations from Case#b13 to Case#b24. The directions of the measurement points are different for three phases and there are two measurement points per phase, which

increases the possibility of overcoming the interference of the magnetic field caused by the neighboring phase's field on each other.

In Case#b13, the measurement points for each phase are in North, East, and West direction for phase-A, -B and -C respectively. The distances from the phase for two measurement points are 2.5 cm and 5 cm for first and second point respectively and apply for each phase. In this case, the measurement points of phase-A are in the North from all phases are far from phase-B and phase-C. Similarly, the measurement points of phase-B are in the East direction and for phase-C in the West direction and thus, far from the other two phases. Therefore, the results are better as compared to the first 12 cases with maximum errors of 1.34 A, 2.91 A and 1.10A as shown in the Figure 2.17.

The results of the estimation errors for Case#b17 are shown in the Figure 2.18. In this case, the phase-A measurement points are in the North direction at 90^0, phase-B measurement points are at the similar distances but in South direction at 270^0, and the measurement points for phase-C are in the West direction in 180^0. For all phases, the distances of first and second measurement point per phase are 2.5 cm and 5cm. The angles of orientation in this case give the maximum magnetic field and the directions chosen to give minimum interference of the neighboring phases. Therefore, in this case, the maximum estimation errors are 1.24 A, 1.57 A and 1.08 A, for phase-A, -B and - C respectively.

Case#b19 has the same orientation per phase for measurement points as that of Case#b17, except the distances of measurement points per phase. In this case, the measurement points of phase-A are located at 2.5 cm and 5 cm in the North direction, for phase-B they are located at 2.5 cm and 7.5 cm in the South direction, and for phase-C the measurement points are located at 2.5 cm and 7.5 cm in the West direction. The results are almost similar as of the Case#b17 with a minor variation. The maximum errors are 1.24 A for phase-A, 1.53 A for phase-B and 1.07 A for phase-C as shown in the Figure 2.19. The results for the remaining cases up to Case#b24 show that the errors for each phase are relatively lower than those for the cases from Case#b1 to Case#b12. Moreover, it is observed that the distance from the center of each phase's conductor does not impact much as compared to the location closer to the neighboring phase.

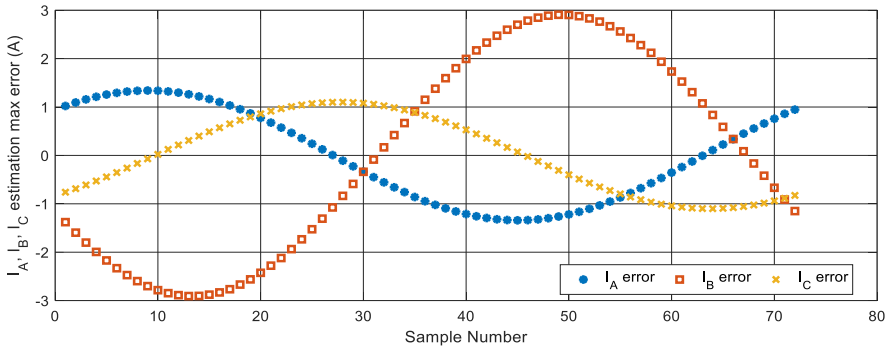

Figure 2.17 Estimation errors (maximum) in amperes for phase-A, phase-B and phase-C, Case#b13

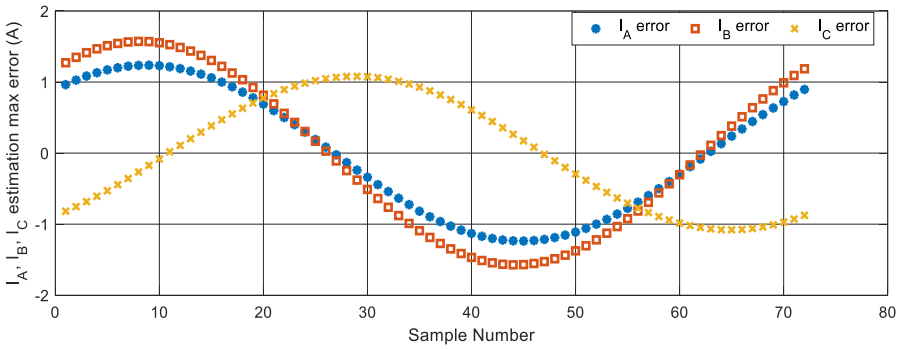

Figure 2.18 Estimation errors (maximum) in amperes for phase-A, phase-B and phase-C, Case#b17

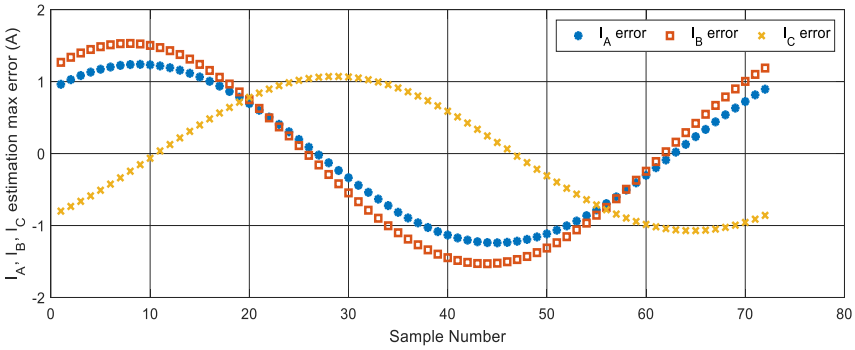

Figure 2.19 Estimation errors (maximum) in amperes for phase-A, phase-B and phase-C, Case#b19

2.5.3 Simulation Results for Group III: Three Measurement Points per Phase

After developing the computer simulations for one and two measurement points per phase, it was expanded to accommodate the simulations for three measurement points per phase. In this experiment, all three measurement points per phase were placed in the same direction with a spacing of 2.5 cm, 5 cm, and 7.5 cm. It was observed that the combinations of directions were giving repetitive results and therefore, the experiment was limited to only six cases. These combinations and the maximum estimation errors obtained for each current are given in Table 2.4. For the first three cases, the directions and locations of measurement points were the same for all three phases. First case had all three measurement points in the North direction, second case in the East direction and the third case in the South direction. Figure 2.20 shows the estimated currents per phase and their comparison with the actual currents and, Figure 2.21 shows the maximum errors in the estimated currents for all phases for Case#c1 where all sensors are in the North direction.

The errors are found to be maximum for the combination where all sensors are in the South direction and the maximum error in the estimation is for the Case#c3 with errors of 6.65A for phase-A, 1.87 A for phase-B and 2.99 A for phase-C as shown in the Table 2.4. The reasons for higher estimation errors are similar to those explained in the previous section for two measurement points. The errors may get higher in this configuration because of the measurement points being farther as compared to the first two configurations of single and two measurement points.

Table 2.3 Estimation errors for group II: Two measurement points per phase for triangular arrangement of three phase system

Case	Ph-A	Ph-B	Ph-C	$I_{A\_}$ error (A)	$I_{B\_}$ error (A)	$I_{C\_}$ error (A)
b1:90N_90N_90N	N1, N2	N13, N14	N25, N26	1.37	4.24	4.11
b2:90N_90N_90N	N2, N3	N14, N15	N26, N27	2.24	8.73	9.03
b3:90N_90N_90N	N1, N3	N13, N15	N25, N27	1.33	4.23	4.08
b4: ZE_ZE_ZE	E4, E5	E16, E17	E28, E29	3.14	2.76	4.37
b5: ZE_ZE_ZE	E5, E6	E17, E18	E29, E30	6.77	2.76	10.75
b6: ZE_ZE_ZE	E4, E6	E16, E18	E28, E30	3.10	2.98	4.23
b7: 90S_90S_90S	S7, S8	S19, S20	S31, S32	6.02	1.56	2.67
b8: 90S_90S_90S	S8, S9	S20, S21	S32, S33	11.14	4.14	5.35
b9: 90S_90S_90S	S7, S9	S19, S21	S31, S33	5.92	1.52	2.62
b10: ZW_ZW_ZW	W10, W11	W22, W23	W34, W35	4.76	3.80	1.07
b11: ZW_ZW_ZW	W11, W12	W23, S24	W35, W36	7.79	9.25	2.76
b12: ZW_ZW_ZW	W10, W12	W22, W24	W34, W36	4.87	3.78	1.07
b13:90N_ZE_ZW	N1, N2	E16, E17	W34, W45	1.34	2.91	1.10
b14:90N_ZE_ZW	N2, N3	E17, E18	W35, W36	1.85	2.70	2.42
b15:90N_90S_90S	N1, N2	S19, S20	S31, S32	1.28	1.61	2.70
b16:90N_90S_90S	N2, N3	S20, S21	S32, S33	1.81	4.26	5.44
b17:90N_90S_ZW	N1, N2	S19, S20	W34, W35	**1.24**	**1.57**	**1.08**
b18:90N_90S_ZW	N2, N3	S20, S21	W35, W36	1.58	4.10	2.64
b19:90U_90S_ZW	N1, N2	S19, S21	W34, W36	**1.24**	**1.53**	**1.07**
b20:90N_90S_90S	N2, N3	S19, S20	S31, S32	1.62	1.60	2.70
b21: ZE_90S_ZW	E4, E5	S19, S20	W34, W35	3.21	1.59	1.15
b22: ZE_90S_ZW	E5, E6	S20, S21	W35, W36	6.94	4.24	2.80
b23: ZE_90S_ZW	E4, E6	S19, S21	W34, W36	3.17	1.55	1.13
b24: ZE_90S_90D	E4, E5	S19, S20	S31, S32	3.15	1.63	2.64

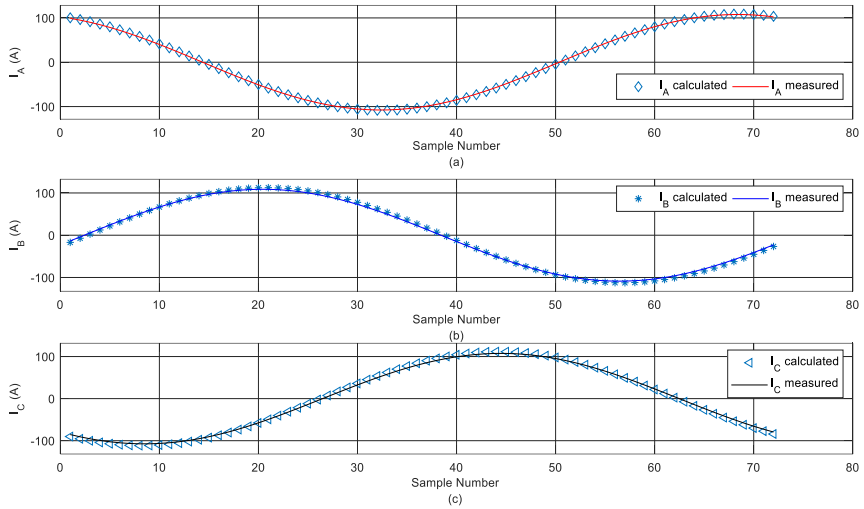

Figure 2.20 Case#c1: estimated and actual currents for (a) Phase-A, (b) Phase-B, and (c) Phase-C

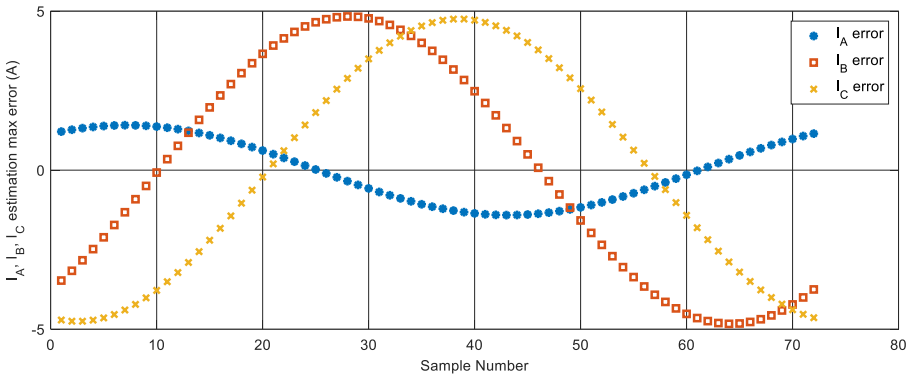

Figure 2.21 Estimation errors (maximum) in amperes for phase-A, phase-B and phase-C, Case#c1

The errors go on diminishing with the change in the combination of directions similar to the pattern observed in the previous two groups of measurement points. For example, for cases Case#c4, #c5 and #c6 these errors are less compared to those for the first three cases. Figure 2.22 shows the performance for the Case#c5 where the maximum error is 2.77 A for phase-B. Similarly, the errors obtained for Case#c6 are the lowest compared to all cases in this group and are shown in the Figure 2.23.

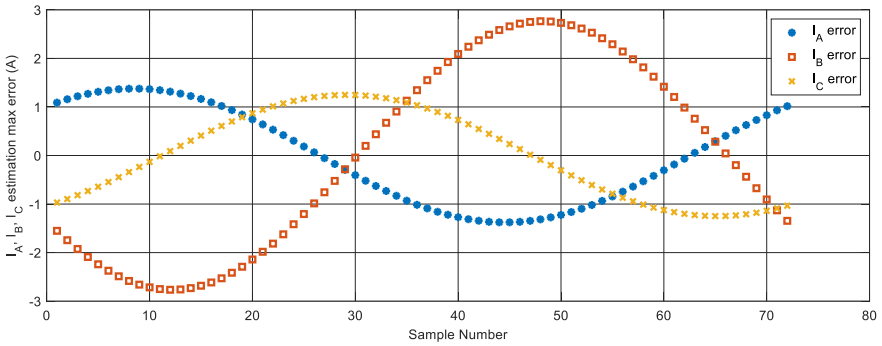

Figure 2.22 Estimation errors (maximum) in amperes for phase-A, phase-B and phase-C, Case#c5

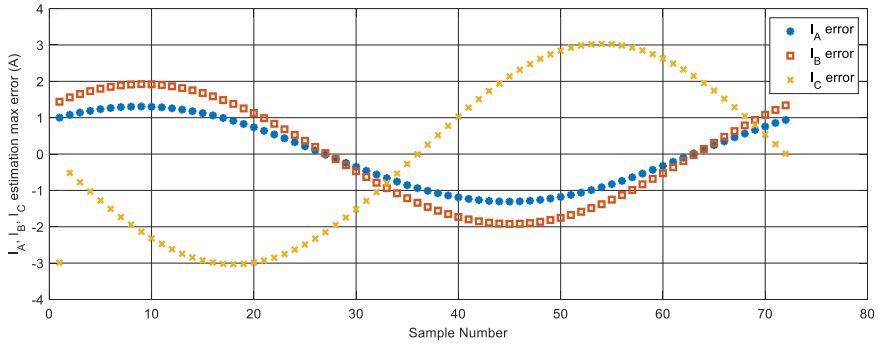

Figure 2.23 Estimation errors (maximum) in amperes for phase-A, phase-B and phase-C, Case#c6

For Case#c6, first set of measurement points for phase A are in the North direction, measurement points of phase-B and phase-C are in the South direction. This arrangement offers the best scenario for all three measurement points per phase with minimum interference of the neighboring phase magnetic fields and, therefore, the magnetic fields' values give the true representation of the field generated by respective phase. Overall, the results obtained for this group for all cases show that by increasing number of measurement points per phase increases the accuracy of the algorithm and, consequently, the estimated currents.

Table 2.4 Estimation errors for three measurement points per phase for triangular arrangement of three phase

Case	Ph-A	Ph-B	Ph-C	$I_{A\_}$ error (A)	$I_{B\_}$ error (A)	$I_{C\_}$ error (A)
c1	N1, N2, N3	N13, N14, N15	N25, N26, N27	1.41	4.83	4.75
c2	E4, E5, E6	E16, E17, E18	E28, E29, E30	3.59	2.62	5.15
c3	S7, S8, S9	S19, S20, S21	S31, S32, S33	6.65	1.87	2.99
c4	W10, W11, W12	W22, W23, W25	W34, W35, W36	5.21	4.51	1.25
c5	N1, N2, N3	E16, E17, E18	W34, W35, W36	1.38	2.77	1.25
c6	N1, N2, N3	S19, S20, S21	S31, S32, S33	1.31	1.92	3.03

2.6 Computer Simulation and Analysis for Three-Phase Horizontal Arrangement

The simulation and analysis of the effect of magnetic fields produced by three-phase overhead system when the structural arrangement of phases is in a horizontal plane is explained in this section. The structural arrangement and distance between each phase are referred from the USF standard [58, 59]. The model is developed in the same fashion as that of previous type of structure and the three-phase circuit of the model is designed for 12.47 kV system. The arrangement of measurement points in all four directions perpendicular to each phase conductor are as shown in the Figure 2.24. The measurement point distances and locations are same as that of the previous type and shown in Table 2.1. The computational program remains the same for both parts, the calculation of the magnetic field per phase and the estimation of three-phase currents based on the distance matrix, X. This matrix is changed because of the distances of each phase and the measurement points from each phase when considering the effect of neighboring magnetic field.

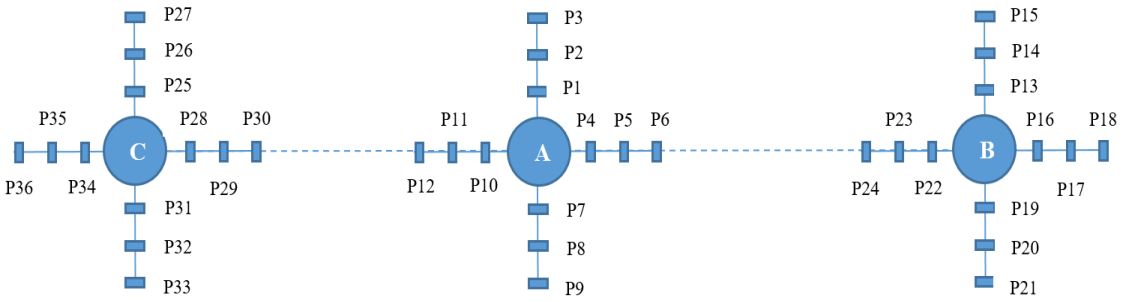

Figure 2.24 Measurement points location per phase for three-phase horizontal arrangement

The simulation is performed for three groups, same as that of the previous section in which there are single, two and three measurement points per phase. There are 24 combinations of the measurement points designed in the Group I and Group II, and six cases designed for the Group III. The results are explained and discussed in the following sub-sections.

2.6.1 Simulation Results of Group I: One Measurement Point per Phase

The results of the Case#a1 with comparison between estimated current and the actual currents for all phases are shown in the Figure 2.25. In this case, the measurement points for all phases are in the North direction and, therefore, faced minimum interaction with the neighboring phase's magnetic field. The maximum errors in estimation are 3.36 A, 2.24 A, and 2.53 A for phases A, B and C respectively and are shown in the Figure 2.26.

In this phase arrangement, the maximum errors are observed for the cases when the measurement points are in the same plane as that of the conductors and when all points are either in the East direction or West direction. For example, Case#a7 and Case#12 show the maximum errors because the measurement points are closer to the neighboring phase. Consequently, there is maximum interference of the magnetic fields resulting in weaker magnetic fields and, therefore, final results of estimation of currents show higher errors.

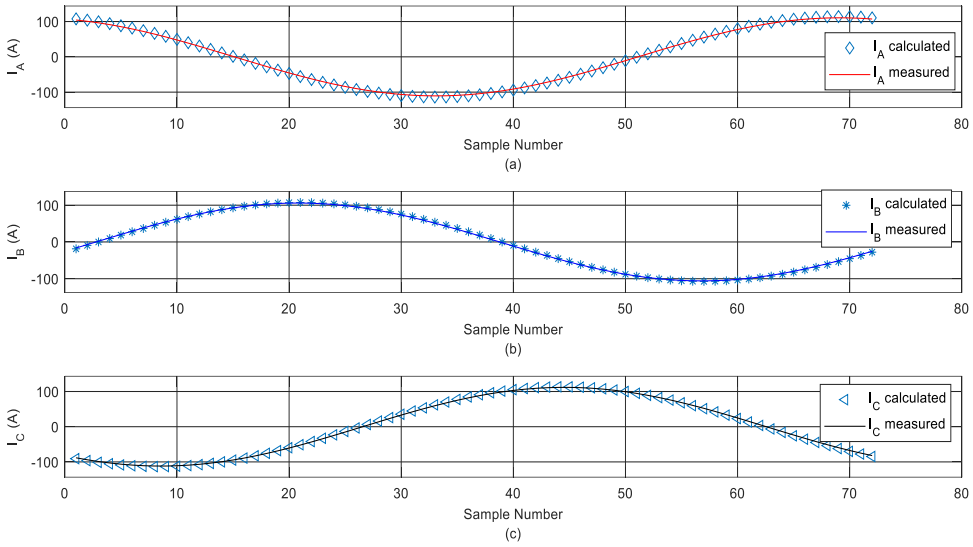

Figure 2.25 Case#a1: estimated and actual currents for (a) Phase-A, (b) Phase-B, and (c) Phase-C

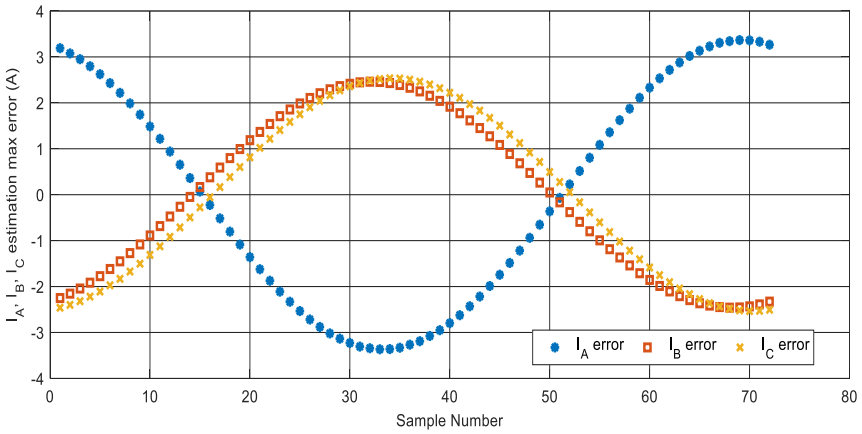

Figure 2.26 Estimation errors (maximum) in amperes for phase-A, phase-B and phase-C, Case#a1

The values of the magnetic fields per phase become more accurate when the measurement points are chosen in the direction and distance in such a manner that they have minimum interaction of the neighboring magnetic fields. This results in getting better estimation of the currents. The combinations of the measurement points per phase from Case#a13 to

Case#24 shown in the Table 2.5 indicate this difference as compared to the first twelve cases.

The minimum errors are observed in Case#a16 and Case#a19. In the first case, the measurement points are in North, South and South direction for phase A, B and C respectively, and, at the same distance of 2.5 cm from the respective phase. At these points, the respective phase's magnetic field is present with less impact of the field generated by the adjacent phases. Similarly, for Case#a19, the measurement points are located at North, South and West direction at the closest distance from each phase. Moreover, the geometry shown in Figure 2.24 indicates that the combination of measurement points chosen in this case have minimum interaction of the fields by phases on each other and, therefore, provides best results. The maximum errors in the estimation of phase-A, -B, and -C currents is 3.21 A, 2.84 A, and 2.43 A respectively.

Table 2.5 Estimation errors in Amperes for group I: One measurement point per phase for horizontal arrangement of three-phase system

Case	Ph-A	Ph-B	Ph-C	I_A_error (A)	I_B_error (A)	I_C_error (A)
a1: 90N_90N_90N	N1	N13	N25	3.36	2.45	2.53
a2: 90N_90N_90N	N2	N14	N26	9.66	7.39	7.91
a3: 90N_90N_90N	N3	N15	N27	4.30	3.15	3.32
a4: ZE_ZE_ZE	E4	E16	E28	8.76	1.82	8.16
a5: ZE_ZE_ZE	E5	E17	E29	20.69	5.52	20.37
a6: ZE_ZE_ZE	E6	E18	E30	9.67	9.43	11.34
a7: 90S_90S_90S	S7	S19	S31	3.04	2.75	2.91
a8: 90S_90S_90S	S8	S20	S32	10.22	8.07	7.89
a9: 90S_90S_90S	S9	S21	S33	15.54	11.43	12.44
a10: ZW_ZW_ZW	W10	W22	W34	9.58	7.16	2.13
a11: ZW_ZW_ZW	W11	W23	W35	21.44	16.68	1.06
a12: ZW_ZW_ZW	W12	W24	W36	34.90	25.76	3.66
a13:90N_ZE_ZW	N1	E16	W34	3.05	2.18	2.44
a14:90N_ZE_ZW	N2	E17	W35	8.87	6.41	0.80
a15:90N_ZE_ZW	N3	E18	W36	11.31	17.48	4.03
a16: 90N_90S_90S	N1	S19	S31	**3.39**	**2.77**	**2.92**
a17: 90N_90S_90S	N2	S20	S32	9.69	8.03	7.86
a18: 90N_90S_90S	N3	S21	S33	15.22	11.39	12.41
a19: 90N_90S_ZW	N1	S19	W34	**3.21**	**2.84**	**2.43**
a20: 90N_90S_ZW	N2	S20	W35	9.09	8.18	0.51
a21: 90N_90S_ZW	N3	S21	W36	13.96	11.68	0.66
a22: ZE_90S_ZW	E4	S19	W34	24.92	10.34	2.14
a23: ZE_90S_ZW	E5	S20	W35	11.27	3.61	2.56
a24: ZE_90S_ZW	E6	S21	W36	34.27	14.02	3.26

2.6.2 Simulation Results of Group II: Two Measurement Points per Phase

In this case, there are two measurement points per phase and, therefore, show better results for the same combinations of directions as that of Group I. The results are shown in the Table 2.6.

From results of all cases in this Group, it is observed that increasing the number of points does not help in improving the estimation accuracy of the currents. The reason being the phases lying in the same plane, they have maximum interaction of the magnetic fields. This is also evident form Figure 2.1. The maximum errors in this group of combinations were found for Case#b22: ZE_90S_ZW with maximum estimation errors of 24.92 A for phase-A. The minimum error for all phases among 24 cases was observed for Case# b13:90N_ZE_ZW with errors values of 4.12A, 2.56 A and 2.13 A for phase-A, -B and -C respectively as shown in Figure 2.27.

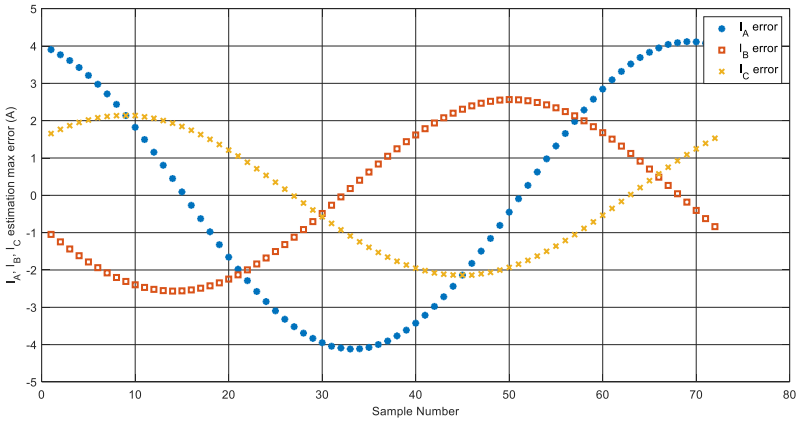

Figure 2.27 Estimation errors in amperes for phase-A, phase-B and phase-C, Case#b13

2.6.3 Simulation Results of Group III: Three Measurement Points per Phase

The simulation study for combinations of three measurement points per phase was also performed for this horizontal structure and the results of maximum error per phase are given in the Table 2.8. It is observed that the worst combination was Case#c2 with all measurement points in the East direction with a maximum error of 12.57 A, and the best combination was Case#c5 with errors less than 5 A for all three phases.

Table 2.6 Estimation errors in Amperes for group II: Two measurement points per-phase for horizontal arrangement of three-phase system

Case	Ph-A	Ph-B	Ph-C	$I_{A\_}$ error (A)	$I_{B\_}$ error (A)	$I_{C\_}$ error (A)
b1:90N_90N_90N	N1, N2	N13, N14	N25, N26	4.50	3.31	3.47
b2:90N_90N_90N	N2, N3	N14, N15	N26, N27	11.22	8.56	9.24
b3:90N_90N_90N	N1, N3	N13, N15	N25, N27	4.30	3.15	3.32
b4: ZE_ZE_ZE	E4, E5	E16, E17	E28, E29	10.96	1.97	10.40
b5: ZE_ZE_ZE	E5, E6	E17, E18	E29, E30	23.21	12.00	13.34
b6: ZE_ZE_ZE	E4, E6	E16, E18	E28, E30	10.96	5.03	6.98
b7: 90S_90S_90S	S7, S8	S19, S20	S31, S32	4.35	3.70	3.81
b8: 90S_90S_90S	S8, S9	S20, S21	S32, S33	11.72	9.03	9.22
b9: 90S_90S_90S	S7, S9	S19, S21	S31, S33	4.05	3.45	3.69
b10: ZW_ZW_ZW	W10, W11	W22, W23	W34, W35	11.87	9.01	1.73
b11: ZW_ZW_ZW	W11, W12	W23, S24	W35, W36	25.44	19.39	1.61
b12: ZW_ZW_ZW	W10, W12	W22, W24	W34, W36	11.93	8.90	1.97
b13:90N_ZE_ZW	N1, N2	E16, E17	W34, W45	**4.12**	**2.56**	**2.13**
b14:90N_ZE_ZW	N2, N3	E17, E18	W35, W36	8.83	14.72	10.23
b15:90N_90S_90S	N1, N2	S19, S20	S31, S32	4.52	3.71	3.82
b16:90N_90S_90S	N2, N3	S20, S21	S32, S33	11.25	8.99	9.17
b17:90N_90S_ZW	N1, N2	S19, S20	W34, W35	9.69	8.03	7.86
b18:90N_90S_ZW	N2, N3	S20, S21	W35, W36	10.51	9.17	0.34
b19:90U_90S_ZW	N1, N2	S19, S21	W34, W36	4.27	3.58	2.20
b20:90N_90S_90S	N2, N3	S19, S20	S31, S32	10.29	4.01	4.12
b21: ZE_90S_ZW	E4, E5	S19, S20	W34, W35	11.26	3.94	2.48
b22: ZE_90S_ZW	E5, E6	S20, S21	W35, W36	**24.92**	**10.34**	**2.14**
b23: ZE_90S_ZW	E4, E6	S19, S21	W34, W36	11.27	3.61	2.56
b24: ZE_90S_90D	E4, E5	S19, S20	S31, S32	11.21	3.87	3.67

Table 2.7 Estimation errors in Ampere for group III: Three measurement points per phase for horizontal arrangement of three-phase system

Case	Ph-A	Ph-B	Ph-C	$I_{A\_}$ error (A)	$I_{B\_}$ error (A)	$I_{C\_}$ error (A)
c1	N1, N2, N3	N13, N14, N15	N25, N26, N27	5.21	3.86	4.09
c2	E4, E5, E6	E16, E17, E18	E28, E29, E30	12.57	3.75	8.51
c3	S7, S8, S9	S19, S20, S21	S31, S32, S33	5.10	4.22	4.40
c4	W10, W11, W12	W22, W23, W25	W34, W35, W36	13.61	10.30	1.59
c5	N1, N2, N3	E16, E17, E18	W34, W35, W36	4.67	3.26	5.37
c6	N1, N2, N3	S19, S20, S21	S31, S32, S33	5.24	4.24	4.41

2.7 Summary

In this chapter, a new current measurement technique is mathematically derived and analyzed. The performance of the technique is successfully validated using simulations. The simulation and modeling of the magnetic field to estimate the currents in each individual phase is successfully performed using least squares algorithm in MATLAB. The basis of this research is the Maxwell's second order differential equations.

The best-case results show that there is a specific combination of the locations from each phase which helps in minimum overlapping of the neighboring magnetic fields and the currents can be calculated with maximum accuracy. The least squares method with residual error function was proven to be successfully applicable to calculate the individual currents from mixed magnetic fields. The worst-case results show that fields weaken with increased distance and, because of interference of neighboring fields.

This theoretical modeling and simulation study concluded to two major outcomes for future applications regarding sensing of magnetic field for estimation of currents; the first being that there is a specific combination of the directions for each sensing or measuring point

for maximum accuracy. It is North, East, and West for the triangular structure; the North direction is for Phase A, East direction is for Phase B and the West direction is for Phase C conductor. Measuring points are away from the neighboring phases and, therefore, there is minimum interference of the magnetic fields produced by the neighboring phase conductors. The second outcome is that if there are two measuring points, one at 2.5 cm and the other at 5 cm, then they increase the current estimation accuracy. Therefore, the results of this research recommend use of a set of two magnetic field sensing points in North, East and West direction each at 2.5 cm and 5 cm from each phase to achieve maximum accuracy in current estimation. The distance shall not be more than 5 cm in case the contactless sensors are used for measuring the magnetic field of each phase.

The simulation results have provided a solid foundation for the hardware design and experimental setup in the laboratory. By employing pair of sensors or even more sensors at the same distance along the length of conductor around the conductor, the error in measurement can be reduced. The analysis shows that the accuracy depends on the number of sensors and the distance of the sensor from the conductor.

Chapter 3. Selection of Magnetic Sensors: Testing and Validation

In the recent past, new sensors based on digital technology are deployed in the power systems to compete with the conventional instrument transformers. A common objective of exploring such technologies is to save time and cost in the installation, maintenance and operation of the substations and power network. Pursuing this objective, world-class manufacturing companies such as Siemens and ABB have introduced the concept of digital switchgear and introduced fiber optic based CTs [67, 68].

The primary objective of estimating currents by measuring the magnetic field needs a suitable sensor that has the capabilities of sensing magnetic field generated by alternating current of medium voltage level. This can be achieved by performing a survey of the magnetic sensors available in the market, investigate their application eligibility by studying their specifications. In addition, designing and conducting a set of preliminary experiments to apply certain tests to study their performance is also necessary. The main aim of this research is to find the replacement option, which is non-invasive in application for current measurement, and therefore, contactless magnetic sensors were focus while selecting the sensors.

This chapter provides a detail account of sensor selection strategy, development of an experimental set up in the laboratory, experiments, and results of the performance evaluation of four types of sensors.

3.1 Contactless Sensors for Application in Current Measurement

Contactless sensors have a wide variety of sensors available from various manufacturers. The method of working of these sensors is either based on Hall Effect or Magnetoresistive (MR) Effect. The advantage in both types of sensors is that they are noninvasive and can sense the magnetic field when kept in the vicinity of the current carrying conductor. For this research, three manufacturers' sensors were investigated. The first type was the Hall Effect based sensors manufactured by Allegro Microsystems [–69 - 71]. These current sensor ICs

have the option of sensing both AC and DC currents and are ideal for load detection and management. The sensor ICs are very accurate and have a temperature compensation function programmed based on the temperature sensors built on the same circuit board. A similar type of sensor available in the market was MLX90215, manufactured by Melexis [72]. The biggest disadvantage of these sensors is that they are not truly non-invasive. The leads of the copper circuit need to be connected to the current source and the Hall transducers which are in the vicinity of this conductor then function to produce the voltage output. Therefore, these sensors cannot be called truly non-invasive. Moreover, the sensors have inbuilt microcontrollers which need programming or calibration based on the application. This feature is not of any help for this research, because it gives the prefabricated, pre-programmed sensor IC.

The second type of sensors investigated are HMR2003 [73] manufactured by Honeywell and work on Giant MagnetoResistance (GMR) Effect. These are three-axis sensors and used mostly as a magnetometer for sensing the magnetic field in various applications such as performance investigation of photomultiplier tubes [74], attitude determination in satellite simulator [75], and for nanosatellite space applications [76]. There are three types of magnetoresistance effects, anisotropic, giant and tunneling as explained in the Chapter 1. The sensor HMR2300 is a complete device with actual GMR sensors (HMC2003) integrated in a circuit along with a microcontroller that processes the sensed magnetic field in three directions and provides the output in terms of magnetic field measured in Gauss. The output is not voltage or magnetic field density, but it is a binary number in ASCII format. The user must convert the ASCII number into Gauss or Tesla by using the conversion chart provided in the datasheet of the sensor [73]. Further details are mentioned in the experiment setup section and the performance analysis section where the actual use of the output to gain the information of current is required.

The third type of sensors investigated for this research are the GMR and TMR type sensors manufactured by NVE Corporation [77, 78]. Three types of spintronic GMR and TMR sensors were chosen to perform the experiment with only single-phase current sensing for a range of 1 A to 20 A AC, 60 Hz. Three of these sensors are GMR effect based (Sensor #1, #2 and #3 respectively) and one is TMR Effect based (Sensor#4). Sensor#3 is Honeywell's HMR2300 sensor. Their details are shown in Table 3.1.

Table 3.1 Sensor specifications

Factors	**Sensor#1**	**Sensor#2**	**Sensor#3**	**Sensor#4**
Manufacturer	**NVE**	**NVE**	**Honeywell**	**NVE**
Sensitivity	36 mV/V/mT	36 mV/V/mT	47.5 mA/0.1mT	20 mV/V/mT
Hysteresis	2%max	2%max	0.2%	1%max
DC Supply Voltage	12VDC	12VDC	15VDC	5.5VDC
Analog Ouput	mV to mT	mV to mT	ASCII	mV to mT
Sensing Limits	5A AC/DC	30A AC/DC	2Tesla	200A AC/DC
Linear Range	0-3.5A	0-30A	0.2mT	+/-10mT

Sensor#1, #2, and #3 have negligible insertion resistance. The sensor#3 is the Honeywell sensor and has three axis measurement capacity by which the field in X-, Y- and Z- direction can be measured. Sensor#1 and #2 have inherent electrical isolation and can work for both AC and DC current measurement. The Sensor#4 has capacity up to 200 A, and is based on the Tunneling Magnetoresistance (TMR) effect. In this sensor, the current through the traces generates a magnetic that is read by the sensor. The magnetic field is represented by the formula as

$$H = \left(\frac{0.4I}{w} \times \tan^{-1}\left(\frac{w}{2d} \right) \right) \tag{3.1.1}$$

Where, the magnetic field H is in milliTesla, the width of the trace w in mm and the distance, d in mm. All selected sensors are designed to have a Wheatstone bridge configuration as shown in Figure 3.1 that helps in reducing the hysteresis problem and maintain the linearity in the output. When current passes through the sensor, it produces a magnetic field proportional to the current, in a direction perpendicular to the trace. This bridge has a cross-sensitivity to detect this field orientation and produces a differential output proportional to the field and the power supply. The major advantage of all these four sensors is that they are noninvasive type. Therefore, unlike conventional current transformers, these sensors do

not need to be installed surrounding the current carrying conductor to measure the magnetic field. Following this advantage, further experimental setup is developed for measuring the magnetic field for all four sensors and is explained in the next section.

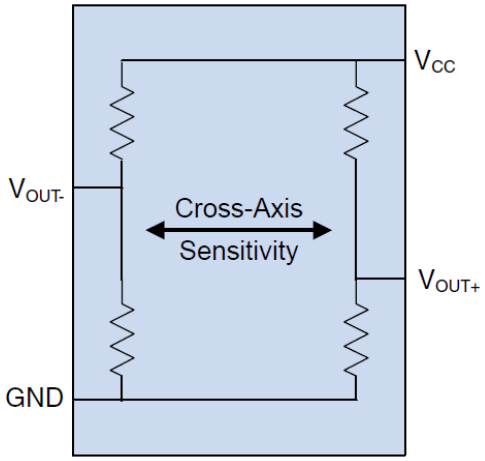

Figure 3.1 Wheatstone bridge structure of sensors

The evaluation of the sensors is based on three major criteria:

a) Efficacy of sensing magnetic field at various distances from the source

b) Sensitivity to pick up the magnetic field generated by various magnitudes of an alternating current.

c) Range of linearity in sensing without saturation.

The other criteria selected for finalization are:

- Ease of measurement and recording the output of sensor
- Programming of the sensor in case it comes with a microcontroller inbuilt on the integrated circuit.
- Troubleshooting, maintenance, and repair of the sensor
- Complexity of techniques and time required to process the recorded data and apply algorithms to estimate the current.
- Cost of the senor

- Operating DC voltage
- Size
- Availability in the market

3.2 Measurement of Magnetic Field using Magnetic Sensors

The magnetic field generated by the current carrying overhead conductors depends on the type of the current that generates the field. In case of the low frequency alternating current in distribution and transmission line networks, the Biot-Savart Law can be applied to determine the magnetic field intensity, H, by assuming the conductor of an infinite length carrying a current of low frequency, such as power frequency of 60 Hz. In that case, the magnetic field density, B will be represented as:

$$B = \mu_0 H = \frac{\mu_0 I}{2\pi d} wb/m^2 \tag{3.2.1}$$

Where, μ_0 is the permeability of air as a medium. Since, the frequency is low (60 Hz), the time-varying magnetic field can be considered as a quasi-static magnetic field and therefore, the effect of the resistivity of conductors and the shielding effects caused by eddy currents can be assumed to be negligible.

The measurement of magnetic field can be considered using Cartesian coordinate system with the magnetic field components in x, y and z direction. Figure 3.2 illustrates a single-phase conductor with the magnetic field in clockwise direction and a sensor, S_1. This sensor is placed at a distance, d from the center of the conductor at an angle of incidence β.

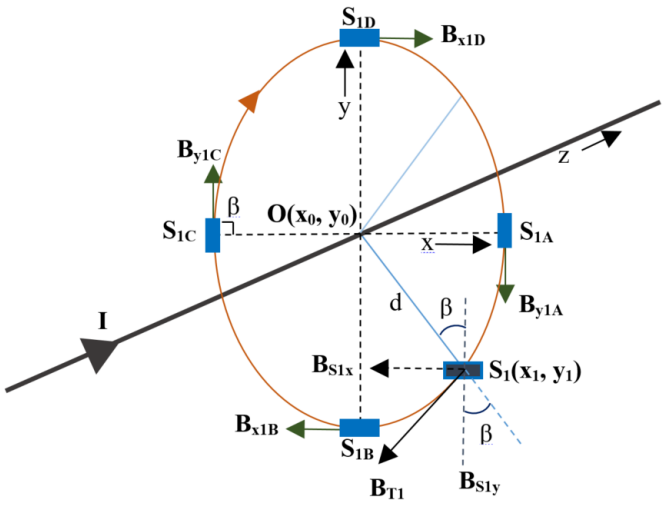

Figure 3.2 Possible locations of contactless sensor around the conductor

The magnetic field in the Z-direction is parallel with the axis of the conductor or the current flow and therefore, is assumed to be negligible. Thus, at any angle of incidence, the magnetic field will have only two components, B_x and B_y. If it is assumed that the coordinates of S_1 are (x_1, y_1) with the center of conductor at $O(x_0, y_0)$, then the magnetic field sensed by the sensor at this location can be written as

$$\vec{B}_{S1y} = \left\{\frac{\mu I}{2\pi d} * \sin(\beta) * \left[\sqrt{(y_1 - y_0)^2 (x_1 - x_0)^2}\right]^{-1}\right\}.\hat{e}_y$$
$$\vec{B}_{S1x} = \left\{\frac{\mu I}{2\pi d} * \cos(\beta) * \left[\sqrt{(y_1 - y_0)^2 (x_1 - x_0)^2}\right]^{-1}\right\}.\hat{e}_x \quad (3.2.2)$$

In the above equation, $\hat{e}_x$ and $\hat{e}_y$ are the unit vectors in X- and Y-direction and β is the angle of incidence. The resultant magnetic field at the sensor location S1 at a distance d will be then given as:

$$B_{T1} = \sqrt{B_{S1x}^2 + B_{S1y}^2} \quad (3.2.3)$$

The magnetic field sensed by the sensor at S_1 depends on the angle of orientation and the location. This field will be maximum if the angle β is 90^0. It has been already demonstrated in Chapter 2 that the maximum magnetic field component will be achieved if the tangential component of the sensor is matched with that of the magnetic field and therefore, bringing

it to zero. By doing so, the $\sin(\beta)$ component will give the tangential component and $\cos(\beta)$ will give the perpendicular component. Thus, only one component will be required when β is 90^0. This will make the field resolve the X and Y components to one single component and furnish the maximum value of the magnetic field and is used for sensors#1, #2 and #4 experiment in this chapter. The possible locations for sensing maximum magnetic field for sensor can be at any angle of incidence with one shown at angle β and other four locations at 90^0 such as S_{1A}, S_{1B}, S_{1C} and S_{1D} as depicted in Figure 3.2. The location S_{1B} is used for all four sensors in the experiment conducted for the selection process of sensors.

3.3 Experimental Setup

The experiment is set up for single-phase resistive circuit. A six-meter-long AWG#4 insulated XLPE cable was installed at a height of 40 cm from the plane of experiment table on two wooden supports. One end of this cable is connected to a wire-wound, silicon coated 1500 W resistance with a value of 10 **Ω**. Omicron CMC356 [80] is used for injecting alternating currents up to 15 A. Taking reference of the location S_{1B} from Figure 3.2, the sensor is placed below the conductor with a variable height adjustment stand to achieve variation in the distance d in the direction as shown in Figure 3.4. This figure represents sensor#1, 2 and 4 which are insensitive to the orientation axis. Provision is made to install two sensors at the same time for measuring the magnetic field. The sensors are provided with power supply using Agilent E3631A regulated power supply. For data acquisition, NI-USB6210 [81] with 16 analog input channels analog to digital converter is employed. The analog inputs are programmed in differential mode to achieve the negative and positive half-cycles of the outputs from sensors. The block diagram of the experiment is as shown in Figure 3.3. This diagram shows the setup common for single-phase as well as three-phase circuits.

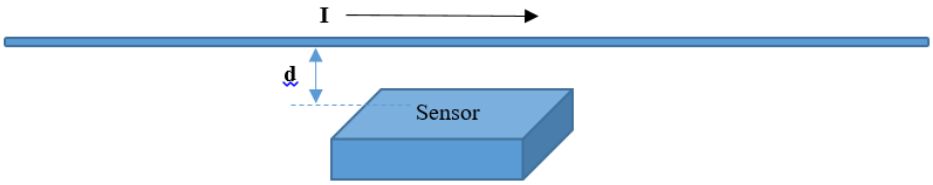

Figure 3.3 Sensor placement under the conductor

There were 33 combinations performed for measuring the magnetic field for each sensor. Input current injection was varied from 1 A to 15 A for three distances, 0.25 cm, 1 cm, and 2.5 cm for each sensor. Total 126 tests were performed and for every test with each value of alternating current, the analog output of the sensor was sampled at the rate of 64000 samples per second. 8000 samples were recorded for each test. The sampling clock of the ADC was used for achieving the desired sampling time. The samples were recorded using differential configuration of the analog to digital conversion. This configuration helped to record the bipolar response of the sensors for an alternating current. The experimental setup with non-invasive sensors is shown in Figure 3.4. From the analog output waveforms of sensors on the ADC software, it was observed that the sensing strength of all sensors was weakening with increase in the distance after 1cm, and at 2.5 cm, there was a significant difference in the amplitude of the measured output waveform compared to that of at 0.25 cm. Therefore, the results were taken for only 0.25 cm distance for all four sensors for alternating currents of 1A, 2A, 3A, 4A, 5A, 6A, 8A, 10A, 12A, 14A and 15A rms.

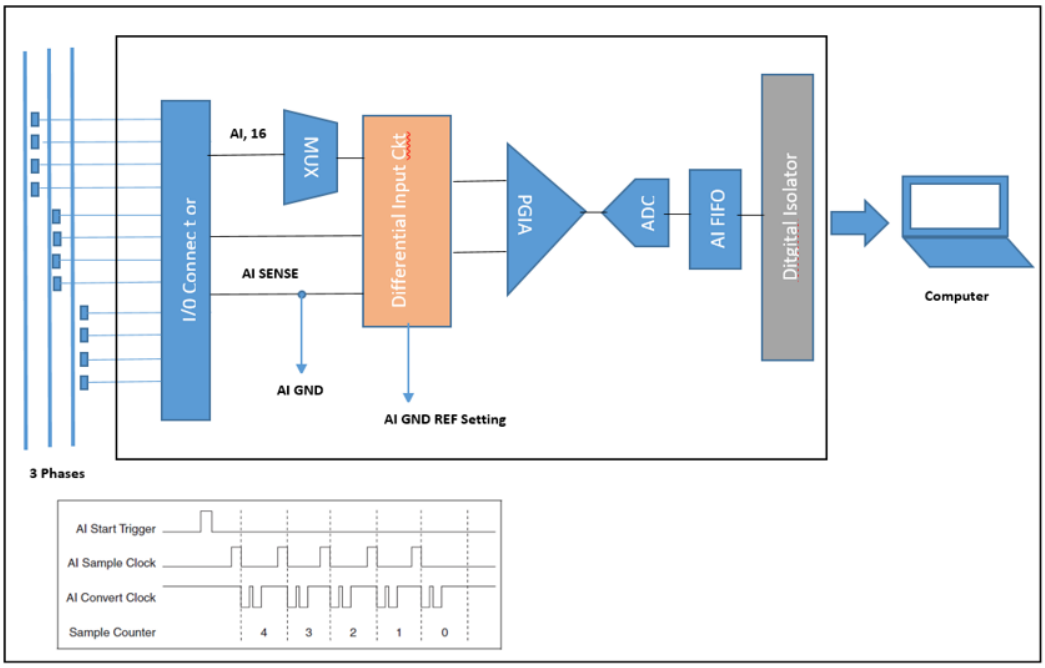

Figure 3.4 Experiment architecture diagram

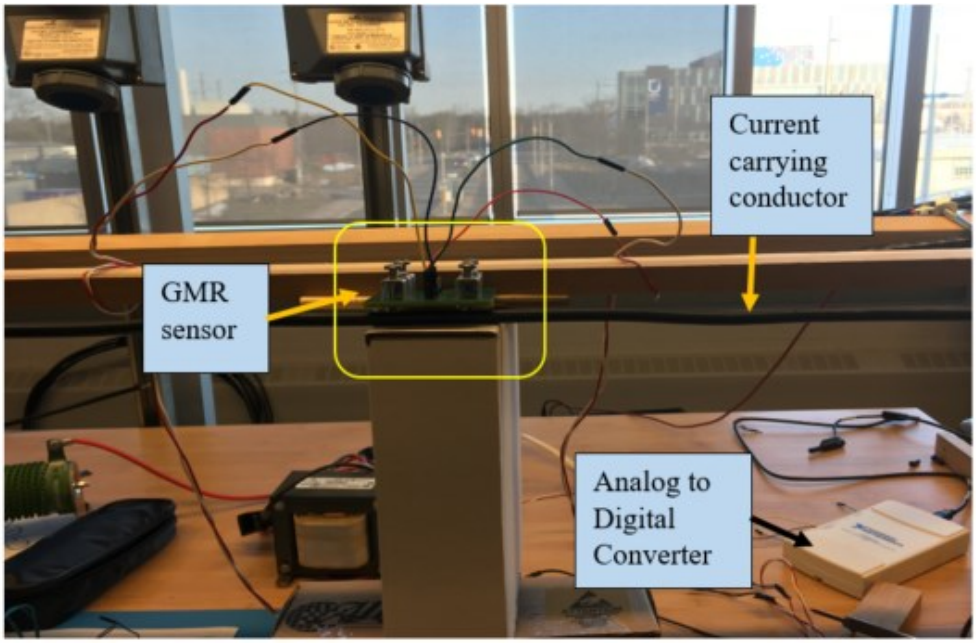

Figure 3.5 Experiment setup for GMR sensor

3.3.1 Experimental Setup for Three-Axis Sensor

Sensor#3 has a capability of sensing magnetic field in X-, Y- and Z-direction. Its orientation affects the magnetic field sensitivity for a particular axis. Therefore, all possible orientation combinations were tried for this sensor to achieve the maximum magnetic field density sensing and are shown in the Figure 3.6.

In case of sensor#3, even though it is a GMR sensor, the output is not in the form of voltage. It is a transformed value to the binary values or ASCII values depending on the selection of the sampling rate. Moreover, isolation was needed for the power supply to sensor#3 to maintain the voltage bias for avoiding the errors in producing the output. The output type selection depends on the sampling rate. For this experiment, the output was in terms of ASCII and, therefore, the recording was achieved using TeraTerm software. Because of the special type of output of Sensor#3, the software by National Instruments analog to digital conversion was incompatible for this sensor but it was used for the other three sensors. The details of experiment procedure and the output of this sensor are shown in the Appendix B.

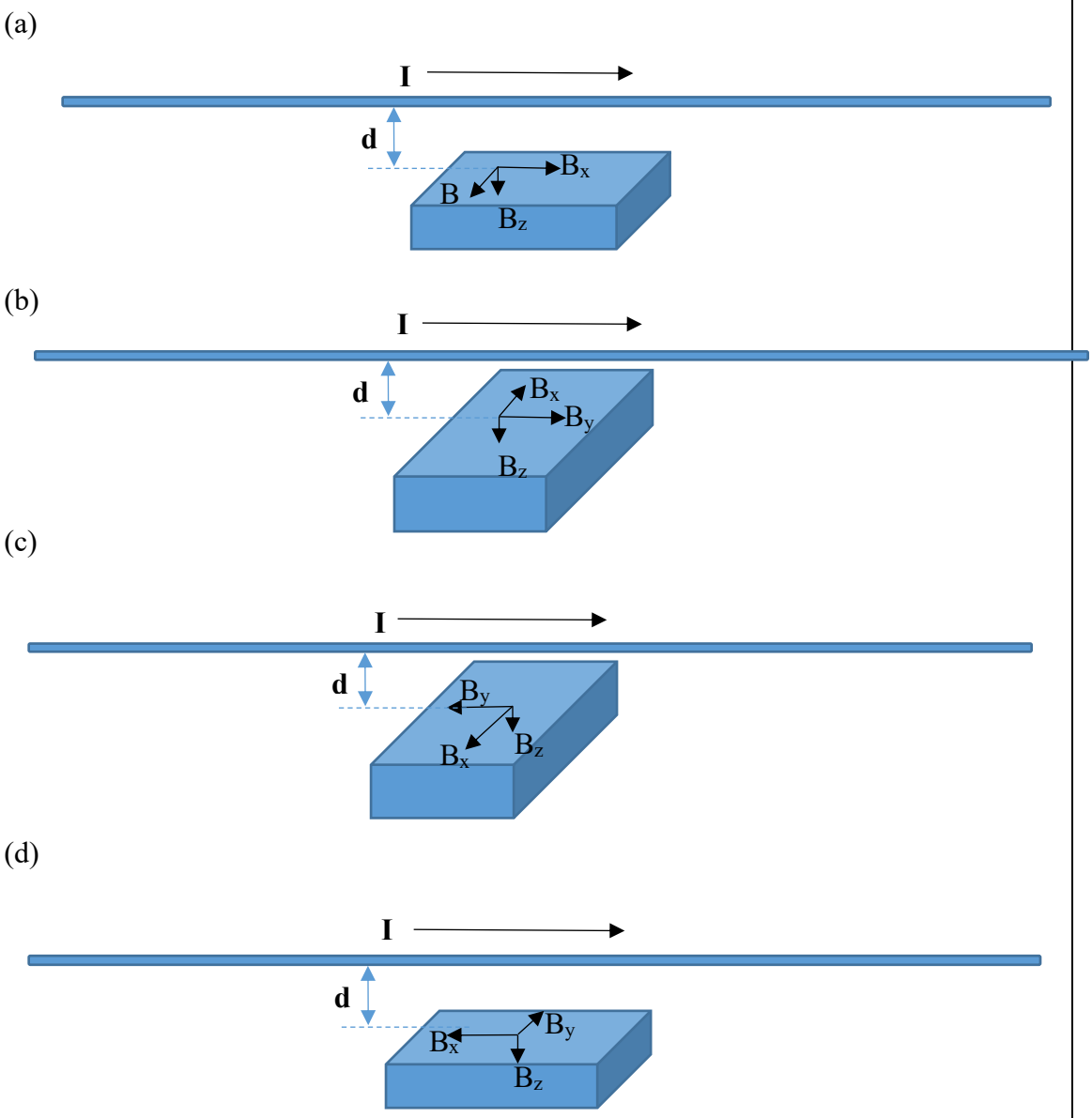

Figure 3.6 Orientation of sensor (a) B_x field in the flow of current (b) B_y field in the flow of current (c) B_y field opposing the flow of current (d) B_x field opposing the flow of current

3.4 Performance Evaluation

The main objective of this experiment is to check the ability of sensors to produce a sinusoidal output waveform that can correlate with the alternating current input. Therefore, for verification, the raw data of recorded outputs were filtered using a low pass filter. In this case, the filter was applied with a cut-off frequency of 4 kHz since the number of samples and the sampling rate was known. In addition, the frequency of alternating input current was fixed at 60Hz, and the number of samples recorded were 8000. The window-type method was chosen for designing a simpler filter with specific preference to Kaiser Window method. The group delay introduced in the filter because of the higher order of the filter and window method was also compensated in the algorithm. There was an offset incorporated in the outputs of all four sensors. This is evident from Figure 3.7.

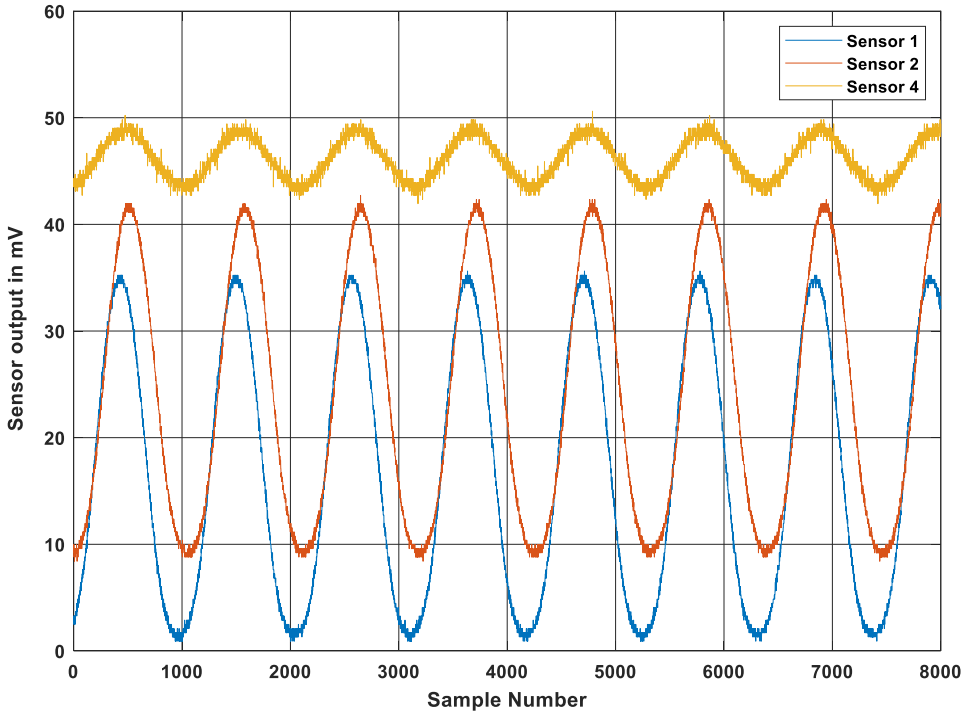

Figure 3.7 Output response for an input current of 2 A by sensors #1, #2 and #4

The waveform with values varying from 35 mV to 45 mV is for sensor#4 and the other two are for sensor#1 and #2. The output in mV is converted to mT by using the sensitivity values as shown in Table 3.1. These values are used to calculate current from the magnetic

field using Equation (3.1.1). The results of the filtered data converted from mV to Tesla are shown for 2 A input in Figure 3.8. The difference in the outputs clearly shows the capability of each type of sensor measuring weak magnetic field generated by an alternating current of 2 A. The quality of the output is dependent on the range of sensing and, also on the type of the sensor. Lower the range, weaker is the sensor and therefore, weaker is the measured output. Sensor # 1 has range only up to 5 A, Sensor#2 has range up to 30 A. Therefore, the fields sensed by these sensors are not so accurate as compared to Sensor # 4. Moreover, these two sensors are GMR type sensors, whereas Sensor# 4 is a TMR sensor and has the range of sensing up to 200 A. Therefore, the output of sensor # 4 is the most accurate as compared to the other two sensors.

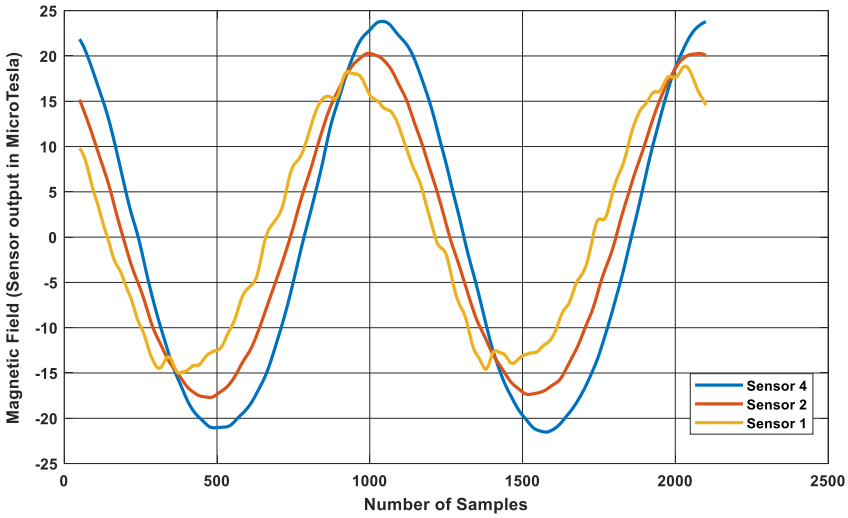

Figure 3.8 Filtered outputs of sensors #1, #2, and #4

The filter performance was tested for all measured outputs of the sensor#4 for input currents of higher range such as 10 A, 15 A, 20 A and 25 A and is shown in the Figure 3.9. The output shown in the Figures 3.9(a) and 3.9(b) are for the magnetic field measured from a distance of 0.25 cm and 1 cm respectively, whereas the outputs shown in Figure 3.9(c) and Figure 3.9(d) are for the case when the sensor#4 was kept at distances of 2.5 cm. The results show that sensor#4 is capable of sensing magnetic field with equal accuracy for the distance ranging from 0.25 cm to 2.5 cm. Moreover, it was observed that the group delay chosen for the filter resulted in maintaining the correlation with the actual raw output and showed good performance in all cases.

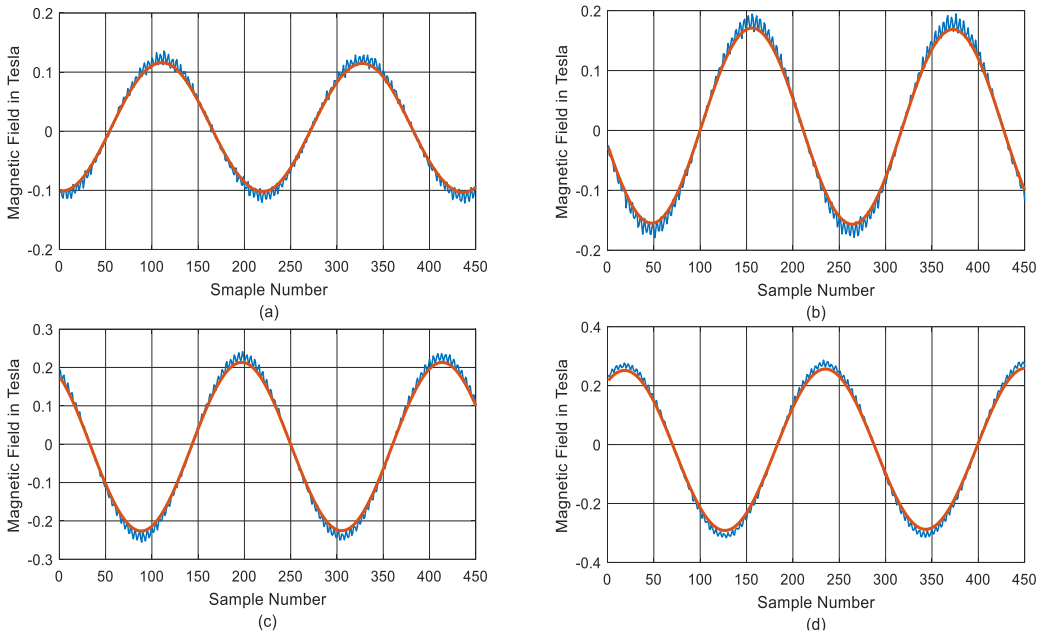

Figure 3.9 Filtered magnetic field for (a) 10 A, (b) 15 A, (c) 20 A, (d) 25 A for sensor#4

The ability of the magnetic sensor to produce a sinusoidal analog output is based on the bipolar function of the sensors and decided by the structure of layers while manufacturing the sensors.

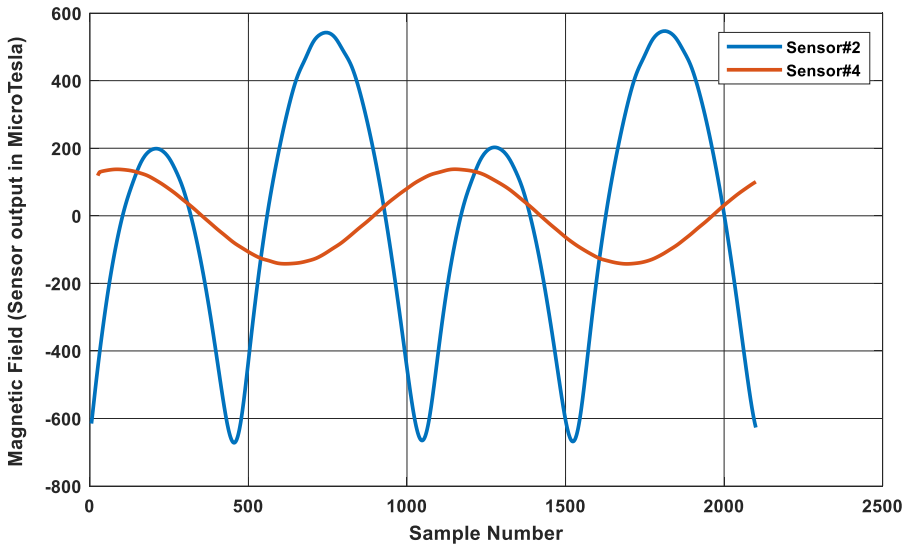

Figure 3.10 Output response to 1 A by sensor#2 and sensor#4

However, it was observed for sensor#2 that even though it had this capability mentioned in the specifications, it produced rectified outputs for both positive and negative cycles of the alternating current. For 1A input, only sensor#4 showed a sinusoidal output as shown in Figure 3.10. This is because of the 20 kΩ resistance in the Wheatstone bridge of this sensor. The other sensors (1&2) have only 2.2 kΩ resistance which resulted into less sensitive to produce the differential output. Sensors of 5 A and 30 A range could not follow the bipolar function to produce a negative waveform for the negative cycle of the current. Sensor#4 of 200A could function as bipolar and produced sinusoidal analog outputs. All sensors picked up noise in addition to the magnetic field. The amount of noise inclusion varied with the sensors and, with their magnetic field sensing capacity. This variation is clearly visible in the filtered outputs by three sensors, #1, #2 and #4 and is shown in Figure 3.7 for 1A. It was observed that sensor#1, and #2 were more susceptible to noise. On the other hand, sensor#4 showed less noise addition and is evident from Figure 3.8. Moreover, it was observed that if the distance from the source is increased for sensor#1, and #2, then for currents after 5 A, these GMR sensors started showing saturation and, consequently, their output was not pure sinusoid as shown in the Figure 3.11.

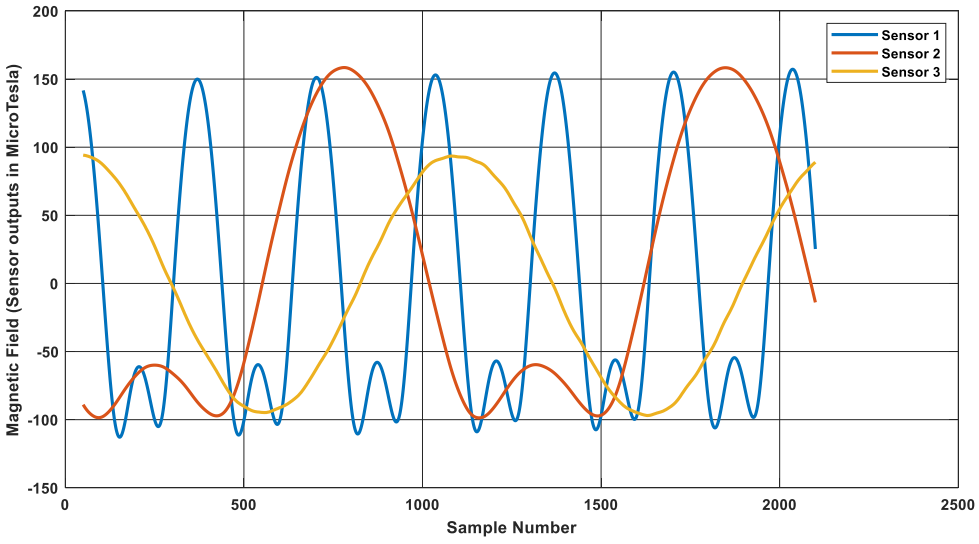

Figure 3.11 Output response to 5A by sensor#1, sensor#2 and sensor#4

3.4.1 Current Estimation from Magnetic Field

The magnetic field output results obtained after using the filter techniques for sensor#4 can be used to calculate current for respective cases measured during the experiment. This can be achieved by rearranging the Equation (3.2.1) as:

$$\hat{I} = B \times \frac{2\pi d}{\mu_0} \tag{3.4.1}$$

The values of magnetic field, B obtained for each case of injected input current, I and for respective distance, d are known. Moreover, the value of the constant μ_0 is known. Inserting all known values in the right-hand side of Equation (3.4.1) the current for respective case is estimated. The analysis was carried out by developing a computational program in the MATLAB software for three sensors, Sensor#1, #2 and #4 with the stages including application of filter technique for measured output for all cases, conversion of filtered output to magnetic field and then the estimation of current from the magnetic field using Equation (3.4.1). Figure 3.12 shows the sensor output measured for 1 A input current before and after the application of the filter. With the application of filtered magnetic field the current is estimated. Figure 3.13 depicts the estimated current sensor#4 for case of 15 A.

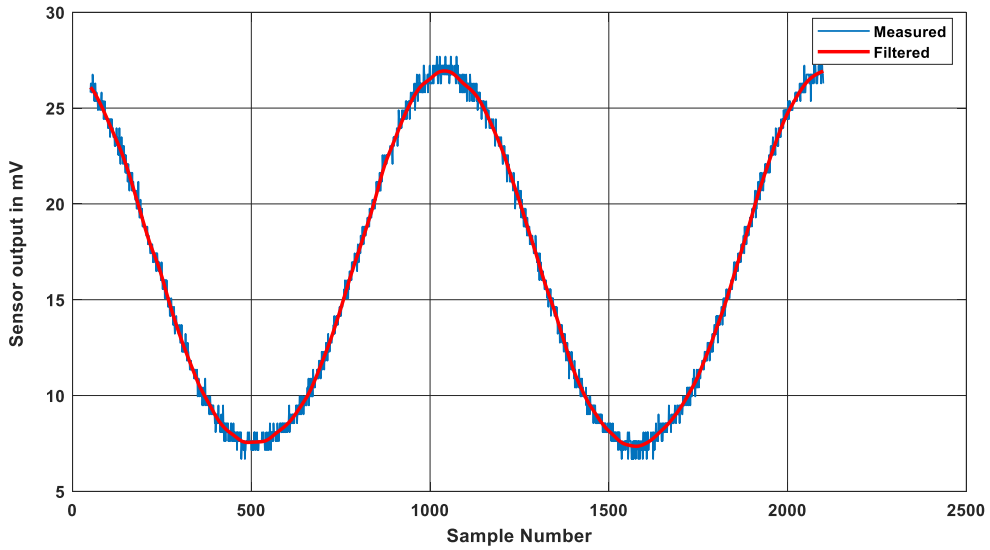

Figure 3.12 Measured and filtered output of sensor# 4 for 1 A input current

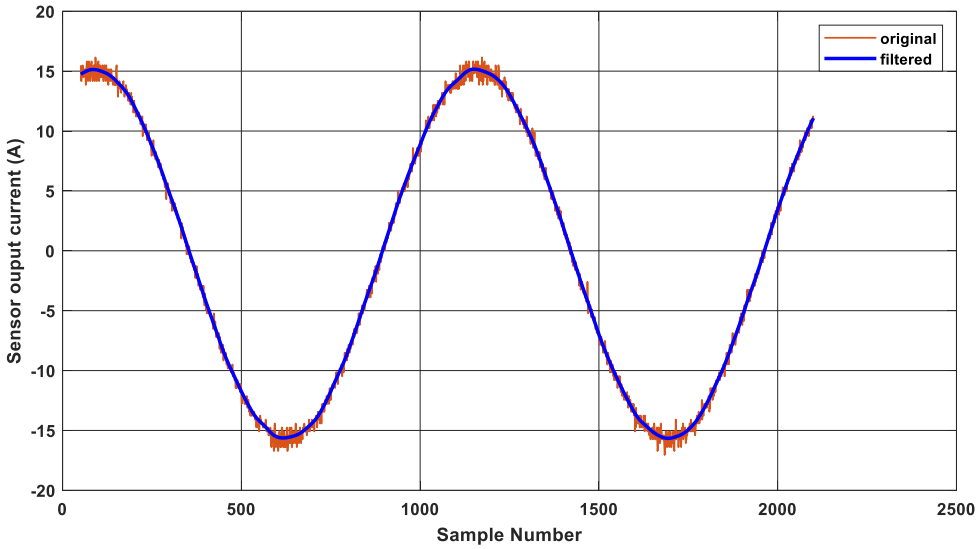

Figure 3.13 Estimated current from the raw and filtered output of sensor#4 for 15 A input current

In the final stage of the analysis, the currents thus obtained for each case were compared with the input current as the source current injected using the Omicron was known for each case of the experiment. Therefore, a reference sinusoidal input current for 60 Hz and number of samples matching to that of the measured data was constructed for each case in the computational code. Using this reference current, the percentage relative error was calculated comparing its samples with those of the currents obtained from the magnetic field for each case for the selected sensors. At the last stage, the percentage error was calculated for each case using the estimated current samples and the reference current samples. The percentage errors between the actual and the estimated current are obtained for sensor#1, #2 and #4 and shown in Table 3.2. All values are shown for the distance of 2.5 cm from the source. Therefore, this table provides the worst possible outcome of the sensors. From this table, it is evident that the sensor#4 did not show good performance for the lower values of current from 1A to 6A, the reason being the higher resistance at the bridge differential output. On the other hand, the sensors #2 being designed for lower values of currents, showed a better response than the sensor #4. The higher values of percentage error for sensor#1 show that it could not perform for lower values of currents and its capacity was limited being for sensing magnetic field generated by currents up to 5 A. Sesnor#2 showed

errors between 12% and 25% for all currents. These errors were less when the sensor was placed at a distance of 0.25 cm and 1.0 cm from the current carrying conductor. The performance of sensor#4 increased in quality with the increase in the source current. This is evident from Table 3.2. The errors were reduced with the increase in the magnitude of source current.

Table 3.2 Errors for sensors#1, #3 and #4

Current AC	**Magnetic Field (mTesla)**	**Sensor#1 %error**	**Sensor#3 %error**	**Sensor#4 %error**
1A	28.28	13.62	23.82	26.67
2A	56.57	18.25	25.37	38.18
3A	84.85	32.11	13.85	24.25
4A	113.14	34.90	14.29	23.19
5A	141.42	39.24	12.59	22.54
6A	169.71	--*	14.70	9.02
8A	226.27	--*	21.57	3.39
10A	282.84	--*	24.89	3.92
12A	339.41	--*	23.21	2.97
14A	395.98	--*	19.57	1.30
15A	424.26	--*	23.74	1.80

--*: over limit.

3.5 Summary

A detailed experimental study for evaluating the performance of the GMR and TMR sensors was conducted. In case of sensor#3, it was observed that the output of this sensor was difficult to measure, record and process for getting the final current output and therefore the analysis was conducted only to the stage of obtaining magnetic fields. This

sensor proved to be non-practical for the experimental application designed for this research. Its size and connection procedure in the measurement circuit did not fall through the standard process of measurement. Moreover, this sensor was very expensive as compared to the NVE sensors. Therefore, it was disqualified for the further stage of research. The GMR sensors did not qualify all points defined for the selection criteria for sensors. The distance from the source and the saturation were the most important factors considered for their evaluation.

After performing detail analysis, it was inferred that the TMR sensor is better than the GMR sensor in sensing magnetic field for current estimation. It showed no saturation for currents up to 15A and the change in distances did not affect its sensitivity. This is evident from the results obtained for the percentage error when the sensor was kept at 2.5 cm. Moreover, the power supply voltage requirement of TMR sensor is only 5.5 VDC which is advantageous for the application of these sensors in current phasors estimation in overhead conductors of power systems. Overall, the TMR sensor successfully passed criteria of distant sensing, sensitivity, and linear range with no saturation. The success of this performance evaluation makes the TMR sensors to be used for current estimation in the next phase of this research.

Chapter 4. Calibration and Validation of Magnetic Sensors

4.1 Adopting Magnetic Sensors in Current Measurement Application

The preliminary experiment carried out for TMR sensors, and the corresponding results presented in the previous chapter proved their suitability for performing the laboratory experiments for higher current setup and achieve the defined objectives of this research. To validate the applicability of TMR sensor for AC current measurements, it is important to begin with the study of its performance and prove its accuracy for single-phase current measurement.

To achieve this objective, the essential steps are to test, calibrate and validate the sensor for various scenarios such as current with a range of magnitudes, harmonics and various distances from the current carrying conductor. In addition, the performance of the sensors needs to be tested for their ability to accurately sense the magnetic field from particular distances in the presence of additional frequencies other than 60 Hz as well as in cases where there are insulated cables and bare conductors. The calibration of the TMR sensor based on these factors will help to achieve the maximum accuracy in terms of current measurement. These objectives can be accomplished by testing these sensors in a laboratory setting. The laboratory experiment did not cover some factors such as the effect of extreme temperature and rain. Moreover, the effect wind causing sag in the conductors and consequently changing their distance from sensors was not considered in the experiment. The calibration was performed with a basic assumption that the distance between the conductors and sensors remained the same throughout the experiment.

A sensor array is observed to deliver more accurate results than a single sensor. Therefore, it is planned to deploy twelve sensors for current measurement, with four sensors per phase to sense three-phase currents for the final stage of this research. Use of multiple sensors per phase render more scope to reduce the measurement error. This can be achieved by applying various possible methods such as combining the magnetic field sensed by sensors, taking weighted average of outputs of sensors, or simply choose the best sensor output when applied for either single or three-phase current measurements.

The experiment and analysis are conducted on twelve sensors to calibrate them and check their performance compared to each other, and verify their behavior in presence of the same magnetic field. The purpose of this study is to explore any manufacturing deficiency or variation in the sensors and, consequently, finalize whether all sensors can be calibrated with same calibration factor, or they would need individual calibration factors based on their quality. This approach will also help to calibrate sensors for achieving maximum accuracy in current measurement. This chapter presents a detailed analysis of calibration and comparative performance of twelve sensors under various factors mentioned above.

4.2 Multiple Sensors Arrangement

The magnetic field that is sensed by the sensors is a function of the distance (d), the angle of incidence (β), and the magnitude of current (I) and can be expressed as $B = f(I, d, \beta)$. By placing the sensors at various locations, the magnetic field can thus be sensed by multiple sensors simultaneously.

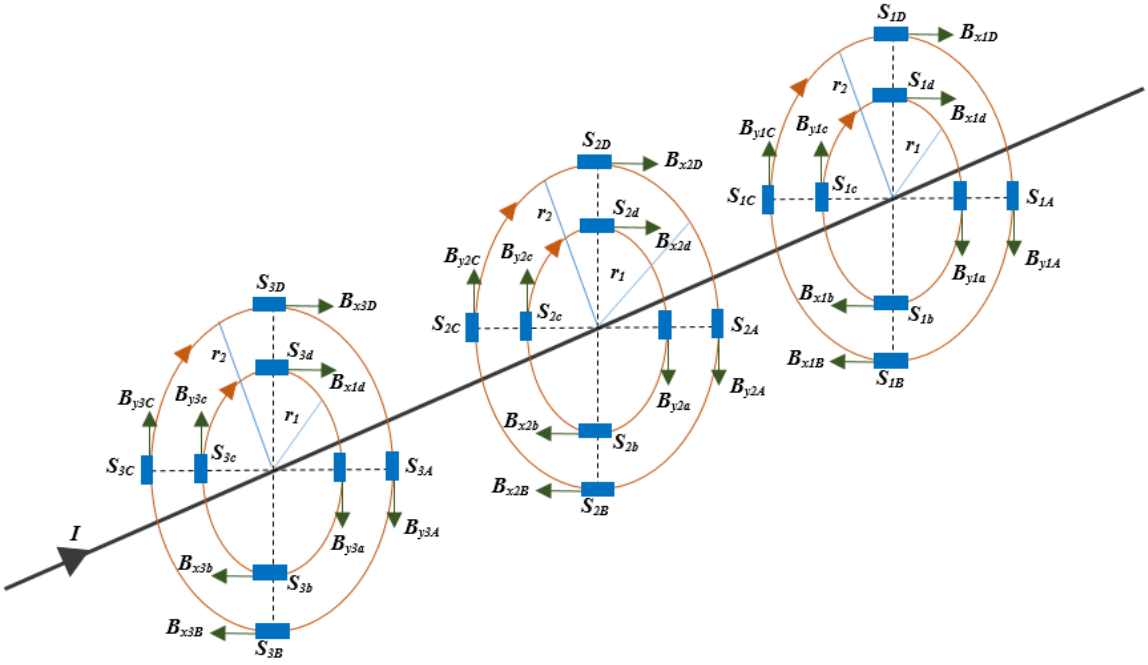

Figure 4.1 Multiple sensors for magnetic field measurement

If we assume the locations of the sensors S_1, S_2,……,S_{12} to be at locations P_1, P_2,…… P_{12} then the resultant magnetic field is expressed as:

$$f\left(I,\beta,t\right)=f\left\{B_{S1}\left(I_A,\beta_A,t\right)_{P1},B_{S2}\left(I_A,\beta_A,t\right)_{P2},.....,B_{S12}\left(I_A,\beta_A,t\right)_{P12}\right\} \qquad (4.2.1)$$

The use of multiple sensors improves the measurement accuracy compared to a single sensor, and this has been researched and demonstrated by various groups in other research studies [46, 47]. Additionally, it has been demonstrated that due to practical issues and manufacturing imperfections, the output of the sensors does not exactly follow the earlier-mentioned theoretical equations. Therefore, it becomes important to calibrate and prepare the sensors to improve the accuracy of the current measurements.

4.3 Experimental Setup for Twelve TMR Sensors

For this experiment, twelve TMR sensors and a multi-stranded XLPE aluminum cable of size AWG#4 were selected. The experiment was performed for a range of magnitudes of alternating currents that ranged from 1 A to 25 A, with sensors at various distances from the conductor. This was achieved by placing the sensors at a right angle from the conductor at the distances of 7 mm, 15 mm, 25 mm, and 35 mm. One of the performance factors was the effect of insulation on the ability of the sensor to detect the magnetic field. Moreover, the application of the measurement of magnetic field is also for the overhead system which usually has conductors with no insulation. To simulate this condition in the laboratory, the insulation of the AWG#4 cable is taken off for a length of 45 cm to accommodate the sensors near the ‘without insulation’ part of the conductor. Six sensors were placed near the bare part, and the remaining six sensors were placed near the insulated part of the conductor during the experiment. The sensors were then interchanged to the record magnetic fields that were sensed for the same current value. Figure 4.2 shows the arrangement of the experimental setup for 12 sensors. A solid-core conventional CT with Class 0.15, 100:100 mA and 19.7 mm diameter is selected to compare its performance with the sensor’s output. This CT is Measurement Canada approved and has exceptionally high

accuracy of 0.15% and mostly used for meter installations. The burden of the CT is designed to meet the IEEE Standard.

TMR sensors are one of the three types of anisotropic magnetoresistance sensors [81]. These sensors have multilayer ferromagnetic electrodes that are separated by a thin insulating barrier that helps the electrons tunnel from one layer to another under the application of a magnetic field. The tunneling effect depends on the orientation of the magnetic field. Under the application of a parallel magnetic field, the magnetoresistance reduces and results in electrons tunneling from one layer to another. When there is an anti-parallel magnetic field, the electrons will have alternating strong and weak scattering effect, resulting in a highly magnetoresistive state [49]. The TMR sensors that were used in this research operate at a voltage of 5.5 VDC. Their sensitivity is 20mV/V/mT typical. This sensitivity is inclusive of the gain because of the sensor, the Wheatstone bridge, and all the electronic components that are a part of the circuit that is embedded onto the sensor chip. This indicates that for various current values, the magnetic field that is produced will be equal to 110 times the voltage output of the sensor. The experiments were conducted in two sets, each with five stages and four parts. These stages and parts were repeated for the No-Insulation (NI) and With-Insulation (WI) cases, as shown in Figure 4.3(a) and (b). The experiment is divided into two parts and four stages as shown in the Table 4.1

In the Part I and for Set 1 of Stage 1, twelve sensors were placed at a distance, d_1= 7 mm from the center of the conductor, with six sensors located near the insulated part, also defined as *WI* part and the remaining six near the non-insulated i.e., *NI* part of the conductor. A current from 5 A to 25 A AC with steps of 0.5 A is passed through the conductor for one minute and for each current, the analog outputs of all 12 sensors are recorded for five seconds using the data acquisition system. An interval of 1 minute is kept between injecting each set of current and, there is a hard stop of 1 minute between each current injection to avoid the saturation or overflow of the A/D channel registers and avoid the recording of null values. The analog values are recorded for five seconds with a sampling rate of 7.2 kHz. This also helped in avoiding any temperature rise of the sensors or the circuit because of higher values of currents for longer durations. Current was injected using an Omicron CMC356 current injection set [79] and the frequency of input current

was selected to 60 Hz for Set 1. The sensor outputs and the CT output were recorded using the NI cDAQ-9174 data acquisition system [81].

Table 4.1 Experiment parts, stages, and sets for array of twelve sensors.

Parts	**Stage 1** **d_1 = 7mm**	**Stage 2** **d_2 = 15mm**	**Stage 3** **d_3 = 25mm**	**Stage 4** **d_4 = 35mm**
Part I: *S_1 to S_6- WI, S_7 to S_{12}- NI*				
S_1, S_2, S_3, S_4, S_5, S_6 With Insulation S_7, S_8, S_9, S_{10}, S_{11}, S_{12} No Insulation Frequency: Set 1 = 60 Hz, Set 2= 120Hz, Set 3 = 180Hz, Set 4 = 240Hz, Set 5 = 300Hz Current: 1A to 25A AC with steps of 0.5A	$B(I_1 = 1.0)$ $B(I_2 = 1.5)$ . . . . . $B(I_{50}= 25)$	$B(I_1 = 1.0)$ $B(I_2 = 1.5)$ . . . . . $B(I_{50}= 25)$	$B(I_1 = 1.0)$ $B(I_2 = 1.5)$ . . . . . $B(I_{50}= 25)$	$B(I_1 = 1.0)$ $B(I_2 = 1.5)$ . . . . . $B(I_{50}= 25)$
Part II: *S_1 to S_6- NI, S_7 to S_{12}- WI*				
S_1, S_2, S_3, S_4, S_5, S_6 No Insulation S_7, S_8, S_9, S_{10}, S_{11}, S_{12} With Insulation Frequency: Set 1 = 60 Hz, Set 2= 120Hz, Set 3 = 180Hz, Set 4 = 240Hz, Set 5 = 300Hz, Currents: 1A to 25A AC with steps of 0.5A	$B(I_1 = 1.0)$ $B(I_2 = 1.5)$ . . . . . $B(I_{50}= 29)$	$B(I_1 = 1.0)$ $B(I_2 = 1.5)$ . . . . . $B(I_{50}= 29)$	$B(I_1 = 1.0)$ $B(I_2 = 1.5)$ . . . . . $B(I_{50}= 29)$	$B(I_1 = 1.0)$ $B(I_2 = 1.5)$ . . . . . $B(I_{50}= 29)$

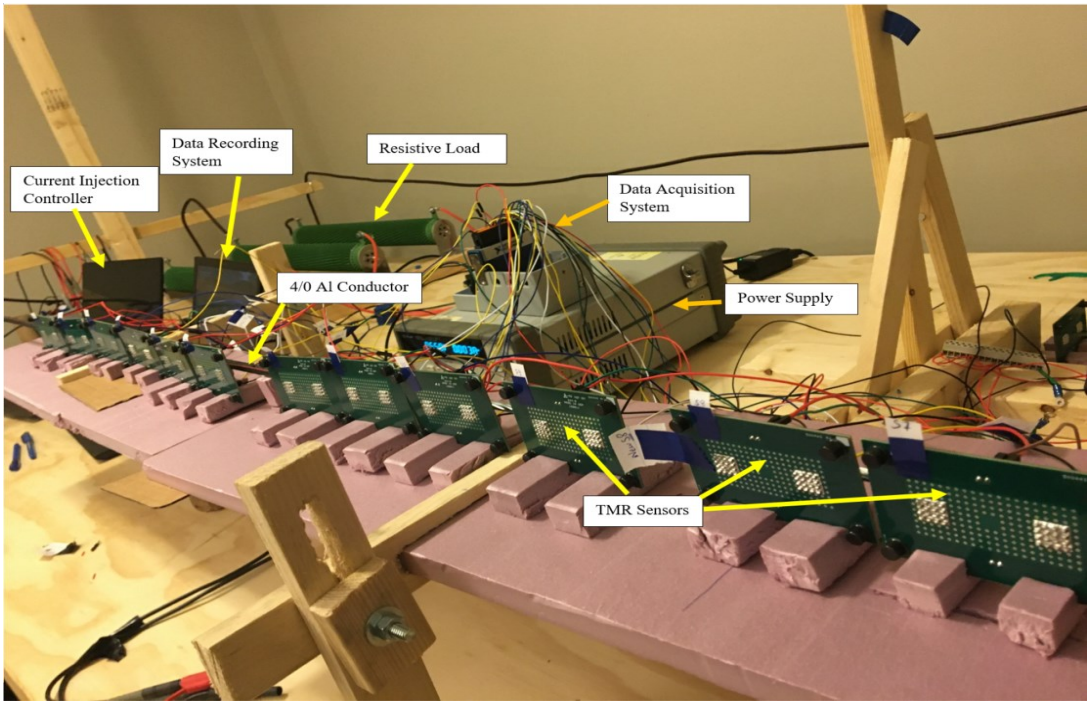

Figure 4.2 Experimental setup with twelve sensors

The sampling rate was kept at 7.2 kHz, and 10,000 samples were recorded for each value of the injected current. Thus, the outputs were recorded for each current value from 1 A to 25 A. For the second set, the current injection setting was changed to inject currents of the second harmonic frequency. Thus, for Set 2, the currents ranging from 1 A to 25 A with 120 Hz were set for circulation in the circuit. The same steps were repeated for Set 2 as of Set 1, and the outputs were recorded. For Set 3, the injected currents were set at the third harmonic frequency (180 Hz), and this pattern continued until Stage 5, where fifth harmonic currents (300 Hz) were injected. The completion of these sets denoted the end of Stage 1 of Part I of the experiment.

For Stage 2 of Part I, the distance of the sensor was changed from 7 mm to 15 mm, and all five sets of currents with five different frequencies were injected from 1 A to 25 A to record the outputs of twelve sensors. This procedure continued for Stage 3, in which all sensors were moved from 15 mm to 25 mm by keeping their placement options near insulation and no insulation part of the cable the same as that of Set 1. For Stage 4, the distance was

changed from 25 mm to 35 mm from the center of the conductor and all sets of various frequency currents were repeated. The completion of Stage 4 denoted the end of Part I.

For Part II, the combination of the sensor and their placement option was changed as shown in the Table 4.1. The first six sensors were moved near the *NI* part of the conductor and the remaining six (from S_7 to S_{12}) were moved near the *WI* part of the conductor. All sets from Set 1 of 60 Hz to set 5 of 300 Hz with current varying from 1 A to 25 A were repeated for each stage from Stage 1 to Stage 4 in the same manner as that of Part I to record the output of twelve sensors.

The experiment with two parts, four stages and five sets of frequencies in each stage resulted in a total of 1160 combinations of the experiment, and therefore, the same number of data files were recorded for the further analysis and calibration of the sensors.

Measurement uncertainty was addressed while performing this experiment. To reduce measurement errors during experimentation, the specifications of all the devices that were involved in the experiment were checked for their performance accuracy. For the current generation test set, Omicron CMC 356 was found to have a resolution of 1 mA, an accuracy of less than 0.05% during magnitude amplification, and a 0.001° resolution for phase amplification. The phase error at 60 Hz was 0.02° for the voltage and 0.05° typical for the current. This test set had 1μs absolute timing accuracy for both voltage and current. The NI-cDAQ-9174 Analog to Digital converter (National Instruments, Austin, Texas, USA) was found to have a timing resolution of 1 ns and a timing accuracy of 50 ppm for the sample rate, with a maximum sampling rate of 500 kHz. To minimize errors from occurring when recording the outputs from the sensors, the sampling rate was selected to be 7.2 kHz/channel, which is well below the limit of 25 kHz/channel. To minimize errors caused by increases in the temperature, the measurements were taken with a time lapse of 1 minute between each current magnitude for every stage in each part as explained above. Thus, the measurement uncertainty was minimized as much as possible.

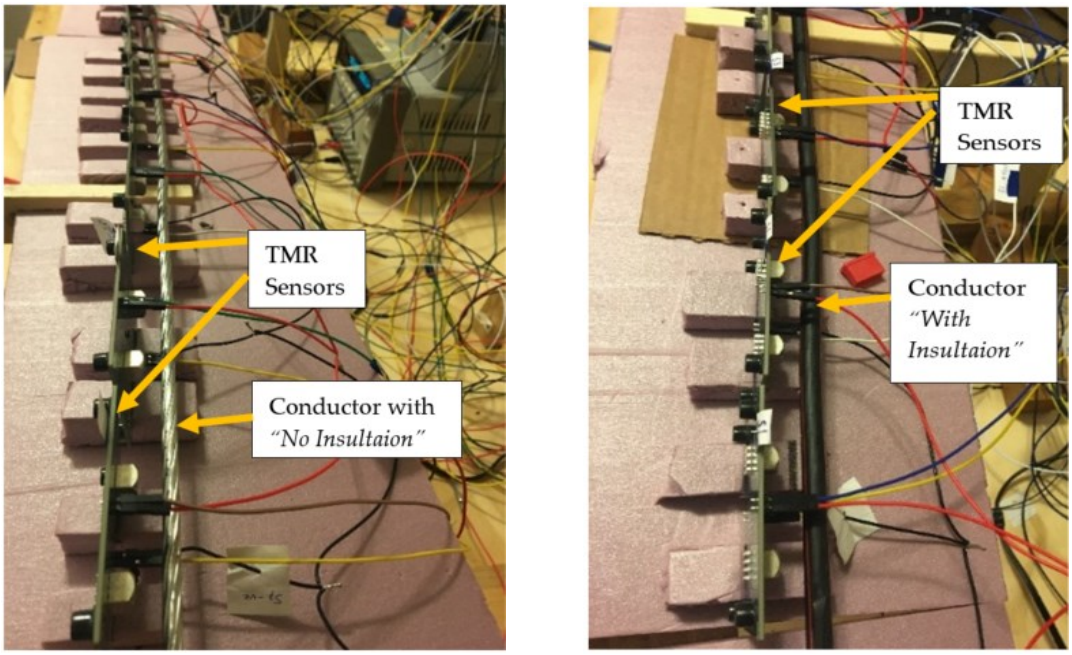

(a) (b)

Figure 4.3 Sensor arrangement near (a) No-insulation and (b) With-insulation part of the conductor

4.4 Calibration of Sensors

The performance of the sensors can be tested appropriately if there is any method by which their capability of sensing magnetic field can be translated to the corresponding current magnitudes. This needs application of suitable methods which can provide that conversion factor which is directly relating the magnetic field sensing capacity to the equivalent current. It was decided to start from a simple method of using the extended form of Faraday's Law and depending on the results of its application, further steps were defined for exploring other accurate and suitable mathematical techniques with characteristics such as computational time and less complex algorithm. The details of such two methods are explained in the following subsections.

4.4.1 Using Direct Method: Biot-Savart Law

The magnetic field has a direct relation with current generated by the source and is also inversely related to the distance from the source, as seen from the Equation (1.1.1). To check the performance of the sensors based on this equation, the measured voltage output

of each sensor for various currents and for various locations of the sensors from the current carrying conductors is converted into magnetic field using the manufacturer's specified conversion factor. Therefore, for each set of measured magnetic fields, the current is calculated by re-arranging the Biot-Savart Law as follows:

$$I = \frac{2\pi dB}{\mu_0} \tag{4.4.1}$$

In this case, the distance "*d*" has four options, d_1, d_2, d_3 and d_4 with actual values of 7 mm, 15 mm, 25 mm and 35 mm. Before using the measured data for each case, the offset was removed from each to make it possible determine the maximum value of the magnitude of currents calculated using the above equation for these distances. The errors are calculated between the maximum value of magnitude of actual currents and the calculated currents. In this first step of using direct relation, the *NI* case data is considered where the sensors are placed near the bare conductor in anticipation that the errors will be less as compared to those of *WI* case. It is observed from these results that the calculated currents are weaker compared to the actual with a variation of the error from 12.48% minimum to 43.76% maximum. The magnetic field weakens with the increase in the distance from the source and, therefore, it was found that the errors for distance d_4 were higher compared to those for distance d_1. The currents calculated from the outputs of sensor S_1 for various input current conditions such as 5 A at 25 mm , 10A at 7 mm, 20 A at 15 mm and 25A at 35 mm distances are shown in the Figure 4.4. The current is calculated from the measured magnetic field by utilizing the unfiltered output and converted to current by applying the Equation (4.4.1). Therefore, it is not a pure sinusoidal output waveform. Moreover, the errors are quite visible in this plot because of the nature of the data, and effect of distance. These observations led to the decision of exploring a better technique to calibrate the sensors accurately and estimate accurate values of currents.

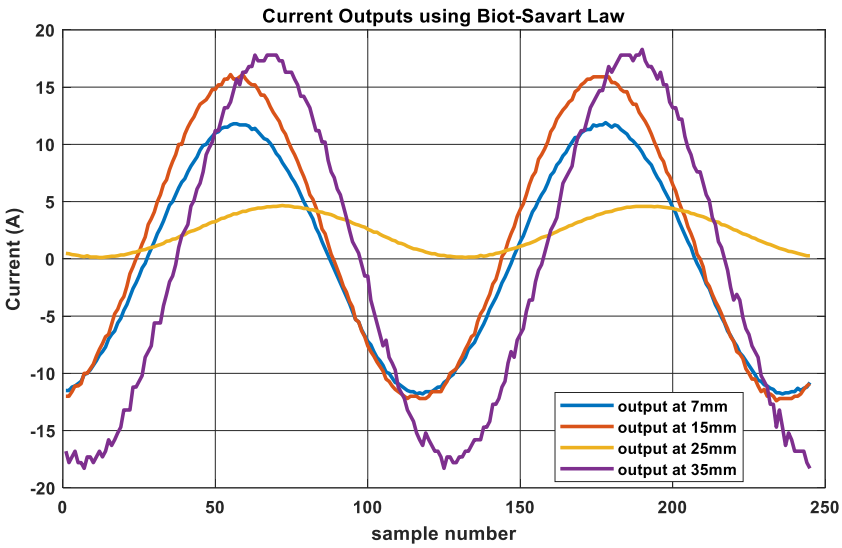

Figure 4.4 Currents calculated using the direct method

4.4.2 Using Discrete Fourier Transform (DFT)

The source of magnetic field is an alternating current and is periodic in nature with a frequency between 0 and 2π and has a definite value of 60 Hz. Therefore, the output of sensors is also periodic and sampled at a sampling rate of 7.2 kHz. During the experimental stage, eight thousand samples were recorded per second for one value of current with the calculation of 120 samples per period. This gave a premise to use the discrete signal for estimating the current phasor using Fourier Transform method. Moreover, this method does not need any filter and offset removal. The measured signal, $B_{d_i}[n]$ for each set of distances, $d_i = d_1, d_2, d_3, d_4$ with a period length, N and $n = 0,1,2,....N\text{-}1$ can be transformed into a sequence, $\mathbf{B}_{d_i}[k]$ using Discrete Fourier Transform as

$$\mathbf{B}_{d_i}[k] = \sum_{n=0}^{N-1} B_{d_i}(n)\, e^{-jk\frac{2\pi}{N}n}\Big|_{i=1,2,3,4} \tag{4.4.2}$$

for $k = 0,1,2,...N\text{-}1$. The waveform represented by N samples can be decomposed using the orthogonality property of the complex sinusoid over the domain $k \in [0, N-1]$ and can also be represented using Euler's complex exponentials for each distance as

$$\mathbf{B}[k]=\sum_{n=0}^{N-1}B(n)\left[\cos\left(n\frac{2\pi}{N}k\right)-j\sin\left(n\frac{2\pi}{N}k\right)\right] \tag{4.4.3}$$

From the transformed waveform obtained above for each measured set of values corresponding to specific currents is then used to calculate the mean value of the multiplication factor (MF). The sampling rate of 7.2 kHz for the measurement of sensor output helped to obtain sufficient samples to apply the orthogonal functions to the DFT algorithm to complete the calculations for one complete cycle of the input current frequency, and then this method was repeated for the remaining data of each case. By following these steps, for each sensor a multiplication factor (MF) for each value of current from 5 A to 25 A, for each distance from 7 mm to 35 mm was obtained.

To verify the performance of the multiplication factor thus obtained using DFT, the current output calculated by applying the MF obtained using DFT for a specific case data was chosen to compare with the output of the conventional CT. Figure 4.5 shows such example where the sensor, S_2 was kept near *WI* part and the injected input current to the circuit was 15 A at 60 Hz.

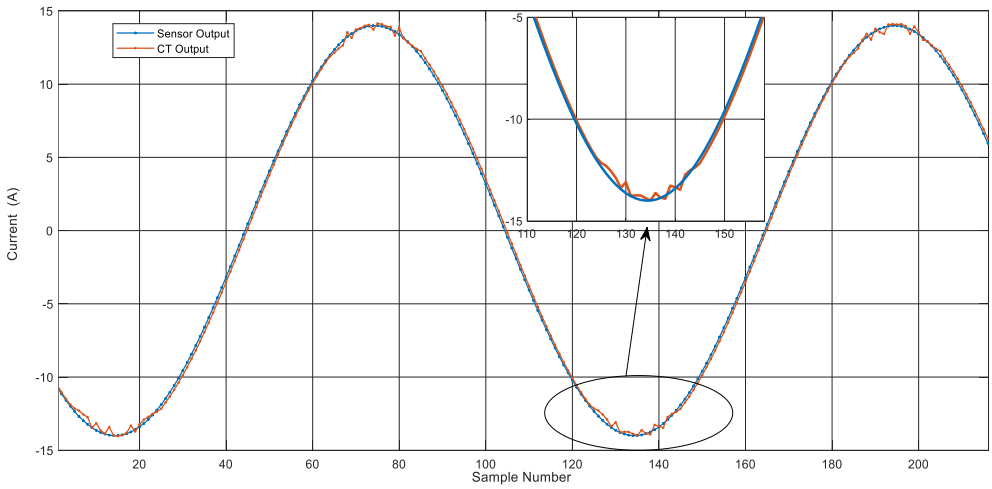

Figure 4.5 Comparison of sensor output with conventional CT output for 15A

This figure shows that the CT output consisting of deformities in the sinusoidal waveform near the positive and negative peaks as compared to smooth sinusoidal obtained using the DFT for sensor, S_5. This proved the accuracy of the DFT method for obtaining the MFs

and thus proceed for further performance verification of all sensors with respect to the factors defined in the objectives.

4.5 Validation of Sensor Performance

The main objectives for calibrating and testing the performance of these TMR sensors were to study and analyze the:

- Effect of variation on the sensor quality that is caused by any slight variation that may occur during manufacturing.
- Effect of distance on sensing the magnetic field that is generated by the current-carrying conductor.
- Effect of insulation and the absence of insulation on magnetic field sensing.
- Effect of harmonics on the current estimation accuracy.

A computational program was developed in MATLAB to implement the DFT algorithm and to perform the steps that were mentioned above for all 1160 cases. The algorithm computed the multiplying factors for the individual currents for each case, and these multiplying factors, along with the resulting calculated current phasors, were stored in separate data files. For analysis, a separate MATLAB program was developed that was able to read these data files for further analysis. The following subsections provide a detailed analysis of the performance of each sensor with respect to the effect of the sensor quality, the effect of distance from the conductor, harmonics, and the state of insulation. The following subsections provide the results of the analysis that are based on each factor.

4.5.1 Sensor Quality

Ideally, all sensors have same specification and sensitivity which makes them respond equally to any specific testing condition and have same MF value for a particular case. The performance uniformity for each sensor is worth investigating because these sensors are manufactured on microscale to arrange the layers of magnetoresistive material and to be integrated with an internal gain with Whetstone bridge configuration. This is an important step to account for because this will provide the capacity of an individual sensor to sense the same magnetic field that is generated by a finite current in the conductor. Moreover,

the results of the algorithm in terms of the multiplying factor for each sensor will depend on its characteristics and measured magnetic field. Consequentially, this analysis will help to define further steps by determining whether the same multiplying factor applies to all sensors or whether each sensor has their individual multiplying factor to calculate the current from the same magnitude of the magnetic field. This section focuses on the analysis and the test results that were obtained from the sensors through various factors, such as variation in the multiplying factors, the amount of magnetic field sensed at the same distance for the same conductor situation, and the current that was able to be estimated with the help of the DFT algorithm. The following subsections discuss the performance details of each sensor accordingly.

4.5.1.a Multiplying Factors for Sensors

To verify the sensor quality, it was determined that measurements would be taken for all sensors that were placed near the without insulation part of the conductor at a distance that was closest from it and for the input current of fundamental frequency. The computation program was developed for all sensors for calculation of the multiplying factors by using the DFT algorithm for each current value of 60 Hz that varied in peak value from 1 A to 25 A in steps of 1 A when the sensors were placed at a distance of 7 mm from the center of the conductor for *NI* case. Since the sensors have the capacity to measure up to 200 A, it was found that their sensitivity for 1 A current is very low. Therefore, the currents from 5 A to 25 A were considered for the performance analysis.

The MFs obtained for twelve sensors are shown in Figure 4.6. It is evident from this figure that each sensor has a different multiplying factor (MF) and that it varies from 565 to 921 for the same amount of source current. Three sensors, S_6, S_8, and S_{11} have MFs that are in the close range from 590 to 616. Similarly, sensors S_1, S_4, and S_{10} show values that are close to each other and in the range from 716 to 738. Sensors S_2 and S_7 have MFs that are almost the same with a variation of 15. Only sensor S_{12} showed a very high value of MFs for all currents and the individual MFs for each current were less consistent compared to those of the other sensors. It is also evident from Figure 4.6 that the MFs become very consistent when there is less variation in the increasing value of current from 10 A onwards.

Therefore, it is anticipated that all sensors will provide consistent performance for all magnetic fields that are generated by currents that are higher than 20 A.

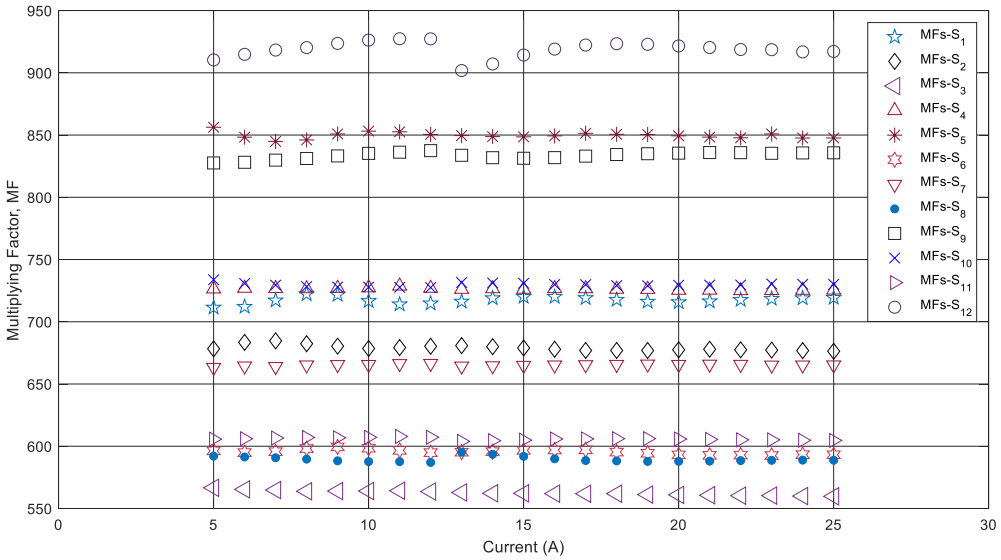

Figure 4.6 Multiplying factors for all sensors when placed at a distance of 7 mm

4.5.1b Sensor Outputs

The current was calculated for each sensor with the help of individual MFs obtained after calibration and for each case of input current, from 5 A to 25 A when the sensors were placed at a distance of 7 mm near the *NI* part of the conductor. Figure 4.7 shows the outputs of all sensors for 5 A, 10 A, 15 A, 20 A, and 25 A as subplots. This figure presents the outputs obtained by using the algorithm in which 4800 samples were selected and the peak magnitude of current calculated for all 120 windows with the application of DFT. The outputs thus obtained for each case closely match with the actual input current with a variation depending on the quality and performance of individual sensor. Figure 4.7(a) shows the maximum variation limits of the output of all sensors from 4.94 A to 5.08 A. For 10 A, this variation is from 9.92 A to 10.07 A as shown in Figure 4.7(b). For 15 A case, the sensors exhibit the variation of current output from 14.93 A to 15.06 A as shown in Figure 4.7(c), for 20 A the variation is shown in Figure 4.7 (d) with limits from 19.94 A to

20.09 A, and for 25 A case, the sensors output variation from 24.92 A to 25.09 A as shown in the Figure 4.7(e)

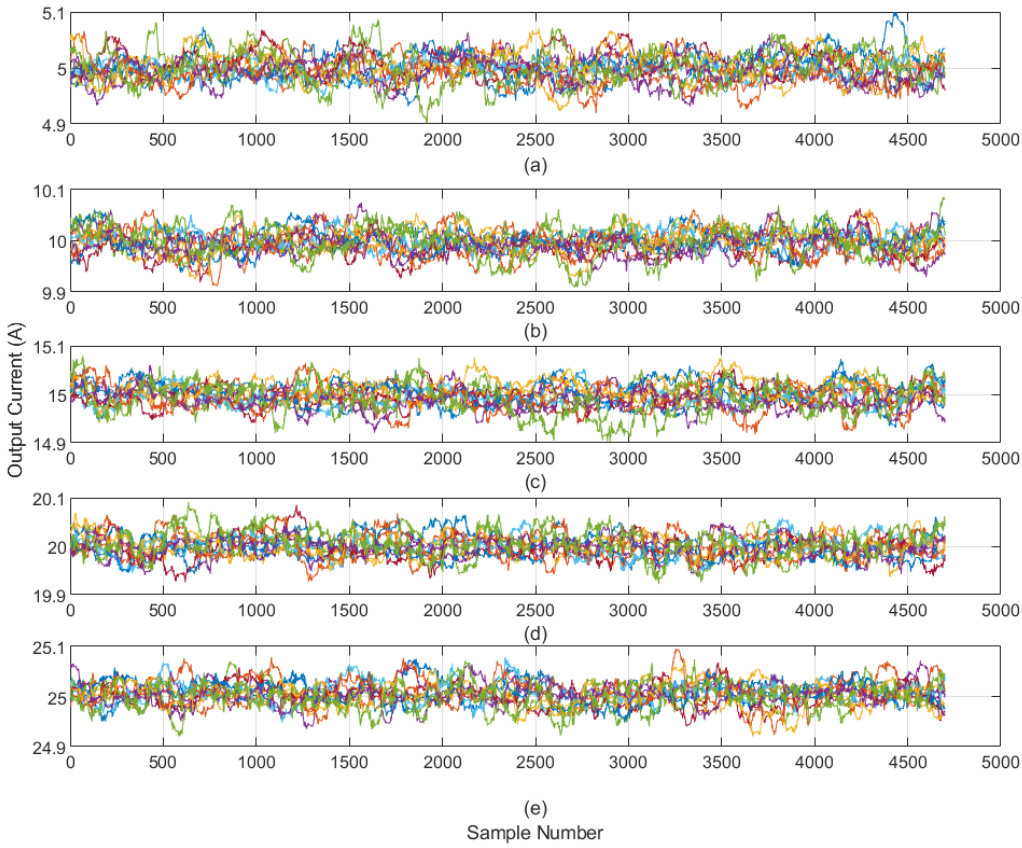

Figure 4.7 Output of all sensors for input current of (a) 5 A, (b) 10 A, (c) 15 A, (d) 20 A and (e) 25 A

Figure 4.8 and Figure 4.9 show the outputs for all sensors for 5 A, and 25 A for 1 cycle of 60 Hz. These figures show an enlarged view of the current outputs of each sensor. Figure 4.8 shows that the outputs are scattered over a range from 4.95 A to 5.06 A, the reason being that the magnetic field is weak when it is generated by a 5 A source. However, it is observed in Figure 4.9 that the outputs are very close to the 25 A value, with a very minor variation that ranges from 24.98 A to 25.04 A for all sensors, except S_1 and S_{12}. The variation for S_1 and S_{12} is also higher compared to other sensors for the case of 5 A current and is evident from Figure 4.8. From these figures, it can be inferred that all sensors except S_1 and S_{12} show good and similar performance for higher values of current. In addition, it is observed that the outputs are well within the limits of ±0.2 A for all sensors except S_1

and S_{12}. This infers that irrespective of the sensor quality, the output of sensors does not vary from the actual value because of the use of the multiplying factors.

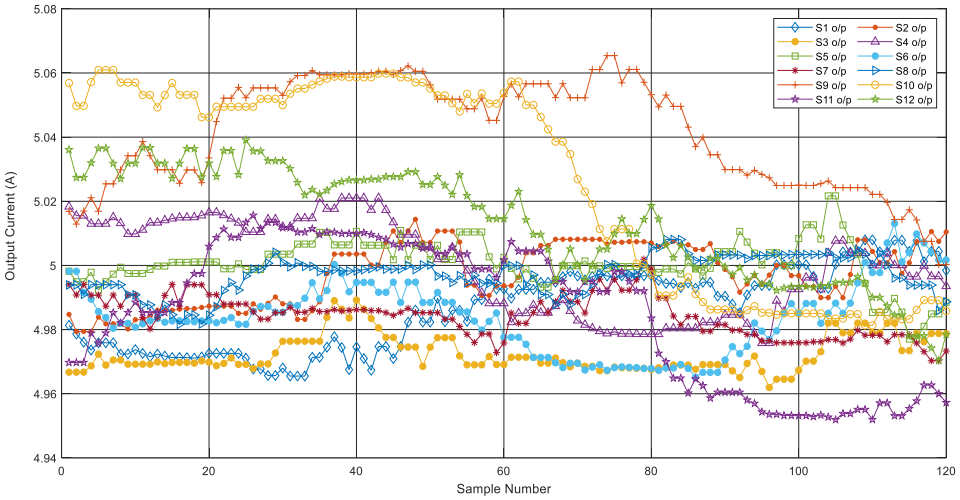

Figure 4.8 Output of all sensors for input current of 5 A

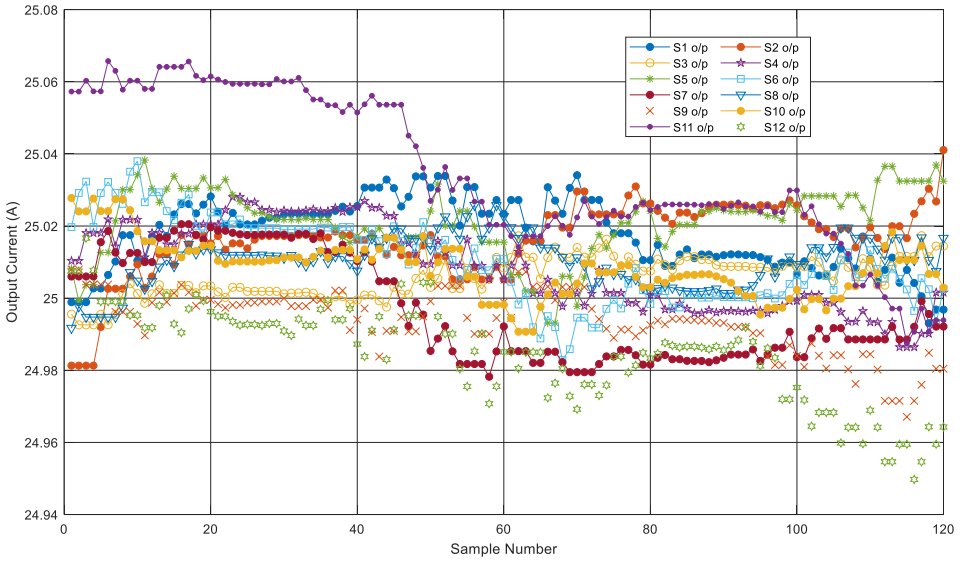

Figure 4.9 Output of all sensors for input current of 25 A

The outputs for each individual sensor were thus observed to vary because of the variation in the sensor quality; therefore, the algorithm calibrates the sensors individually using individual multiplying factors. The sensors with lower MF values show that they are more

sensitive in measuring the magnetic field and need smaller values of multiplying factor to estimate the current phasors from the measured magnetic field. However, for the purpose of analyzing sensors based on the defined objectives, it is concluded that the remaining factors will be studied using the multiplying factors for individual sensors obtained for each current value instead of a mean value for all currents to obtain a more accurate analysis for the effects of distance, harmonics, and saturation.

4.5.2 Distance from Source

According to Equation (4.4.1), the strength of the magnetic field decreases as the distance from the source increases. To determine the relationship between the distance and the multiplying factors for each sensor, the measurements were used for 7 mm, 15 mm, 25 mm, and 35 mm distance from the center of the conductor. The options chosen were the frequency of 60 Hz for currents and the location of sensors was *NI* part of the conductor. Figure 4.10 shows results of the MFs calculated for the sensor S_1. This figure shows that the multiplying factors increase with the distance from the source.

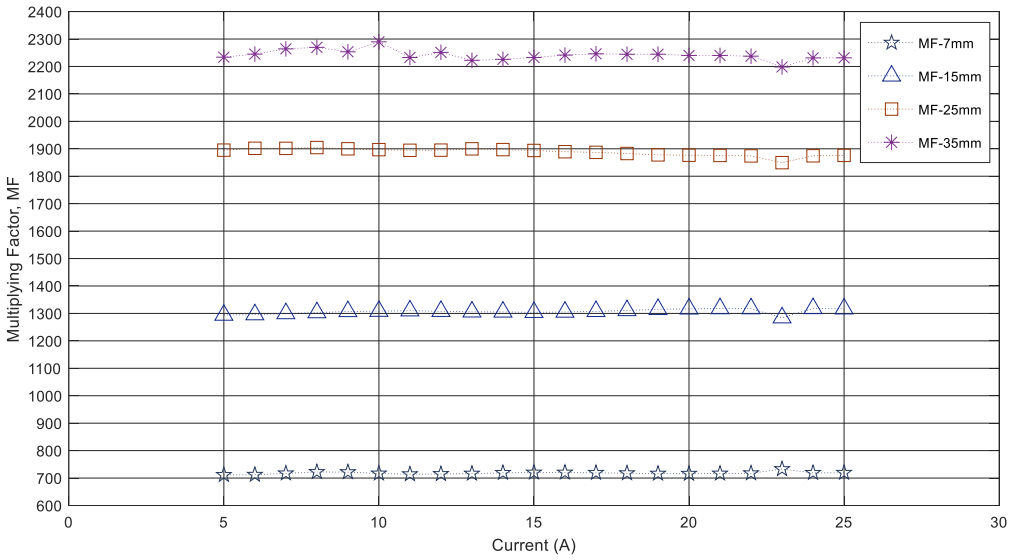

Figure 4.10 Multiplying factors for the sensor S_1 for various distances

For 7 mm, the MFs are in the range of 718 to 730 and for 15 mm. These MFs have range of 1300. The MFs are in the range of 1895 to 1900 for 25 mm, and for 35 mm these values jump between 1900-2250. Figure 4.11 demonstrates the results of multiplying factors obtained for the sensor S_3 like those obtained for S_1. After comparing Figure 4.10 and Figure 4.11, it is prominent that the MFs for S_3 for all distances are smaller in value as compared to those of sensor S_1 for the respective distances. For 7 mm, the range of the MFs is between 550 and 560. For 15 mm, the MFs have almost equal values and are close to 800. For 25 mm, these MFs increase significantly and are in the range of 1360 to 1370, whereas for 35 mm, the values are in the range of 1870 to 1880. This can be attributed to the variation in the manufacturing quality of these two sensors.

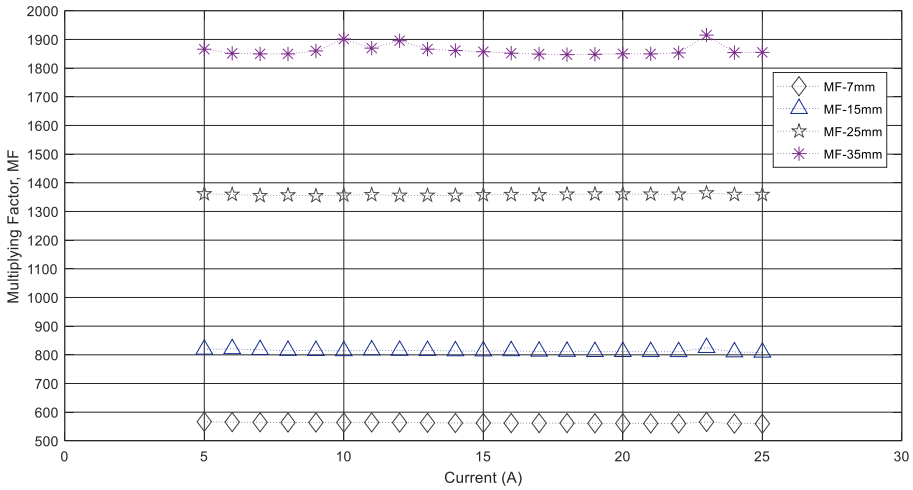

Figure 4.11 Multiplying factors for the sensor S_3 for various distances

Similar to the comparative analysis of S_1 and S_3, to compare all sensors, the MFs were obtained for all sensors for all currents from 5 A to 25 A, and are collectively shown in Figure 4.12 with respect to distance. It is observed from this figure that the MFs show consistency in magnitude for all currents for individual sensor. The magnitudes are varying for one specific distance for all sensors due to the variation in their manufacturing quality. It is evident from the MFs of sensor S_5 and S_{12} for 35 mm distance, which show a large variation in the MFs for initial currents from 5 A to 15 A. The value of the MFs goes on increasing with the increase in the distance from the source. Thus, the MFs are observed to be increasing for each sensor with the increase in their distance from source. The highest

values of MFs are observed in the range of 3200 for 35 mm distance and the lowest values of MFs are observed for 7 mm distance. This proves that the magnetic field is stronger near the conductor. The performance of these sensors become linear and consistent for higher values of current. The variation in the initial values of MFs is attributed to the weaker magnetic fields at lower values of currents and is applicable to all sensors.

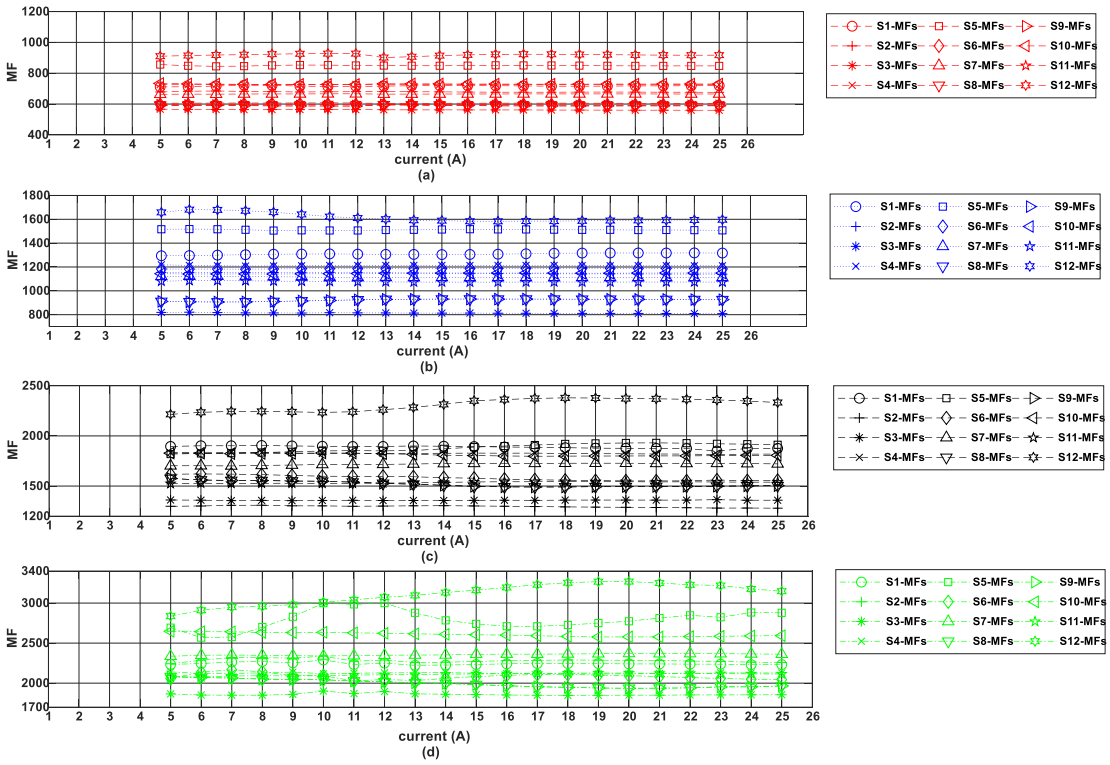

Figure 4.12 Multiplication factors for all sensors and all distances

The MFs obtained from DFT are validated by calculating currents with the help of the independent sets of the measured data for each sensor and for each input current. The performance of these sensors from the calculated individual MFs is assessed by calculating the relative error between the input current and the calculated current. Figure 4.13 shows the Box-and-Whisker plot of the errors for all sensors obtained for all distances and for input current of 5 A, 10 A, 15 A, 20 A and 25 A cases. For 7 mm distance, the relative errors are very small with the average error of 0.267% and the minimum error in the measurement is 0.098%. Average error for 15 mm distance for all currents and all sensors is found to be 0.459%, whereas for 25 mm distance it is 0.637% and 0.976% for 35 mm distance. Figure 4.13 also shows the outliers for case of 15 mm and 25 mm distances.

Taking into consideration the errors of twelve sensors for the complete range of currents, these outlying error values are rare and can be omitted from the general performance analysis. The maximum error for 15 mm distance is 1.063% and for 25 mm it is 1.325%, whereas for 35 mm distance the maximum error found for all sensors is 1.84%.

As explained in Section 4.5.1 the sensors will have varying MFs based on their quality and their distance from the source. It can be concluded from the analysis in this section that when the sensors are closer to the source (conductor), the magnetic field is strong, and therefore, the sensors will provide consistent results, whereas when the distance increases, the magnetic field becomes weaker and, in such case, only higher magnitudes of source currents can produce better results.

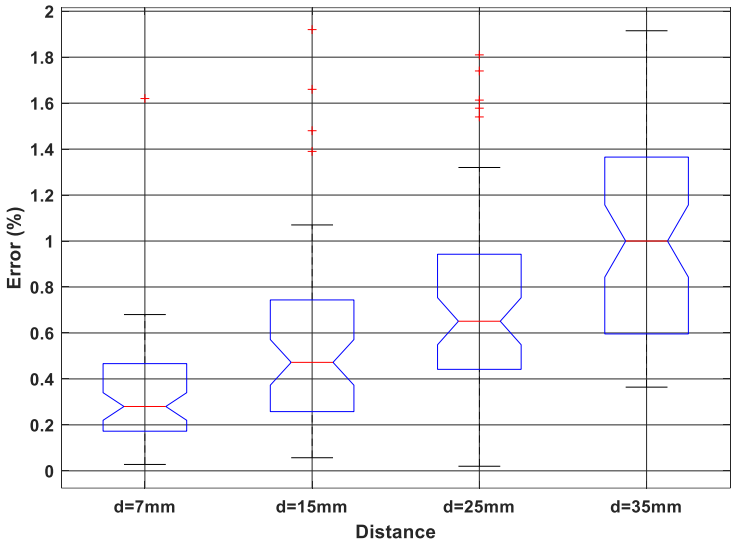

Figure 4.13 Multiplication factors for all sensors and all distances

4.5.3 Insulation

To investigate the ability of the sensors to sense the magnetic fields in presence of a conductor with insulation and without insulation, the measurements for both conditions were taken as mentioned in the Section 4.2 and were used to calibrate the sensors separately followed by the computation of the currents within the range of 5 A to 25 A. The results of the calibration provided multiplying factors for sensor S_1 as shown in the Figure 4.14 for various distances from the center of the conductor and for *NI* and *WI* conditions. From this

figure, it is evident that with the presence of insulation, the multiplying factor value increases even though the distance from the source is same for the sensor and the source current also remained the same in both conditions. This pattern was observed to be similar for all sensors. Figure 4.14 shows that the MFs at 7 mm for *NI* are in the range of 700, and for *WI*, they increase to 900 for all currents. Similarly, for the 15 mm distance, the MFs for the *NI* case are in the range of 1300, and they increase to 1400 in the *WI* case. It is observed that these values are 1900 and 2000, respectively, for the 25 mm distance. For the 35 mm distance, the magnetic field intensity is lower as compared to that at 7 mm resulting in a higher difference between the *NI* and *WI* values of MFs. It can be observed that these values are 2200 and 2600 for the *NI* and *WI* cases respectively for 35 mm.

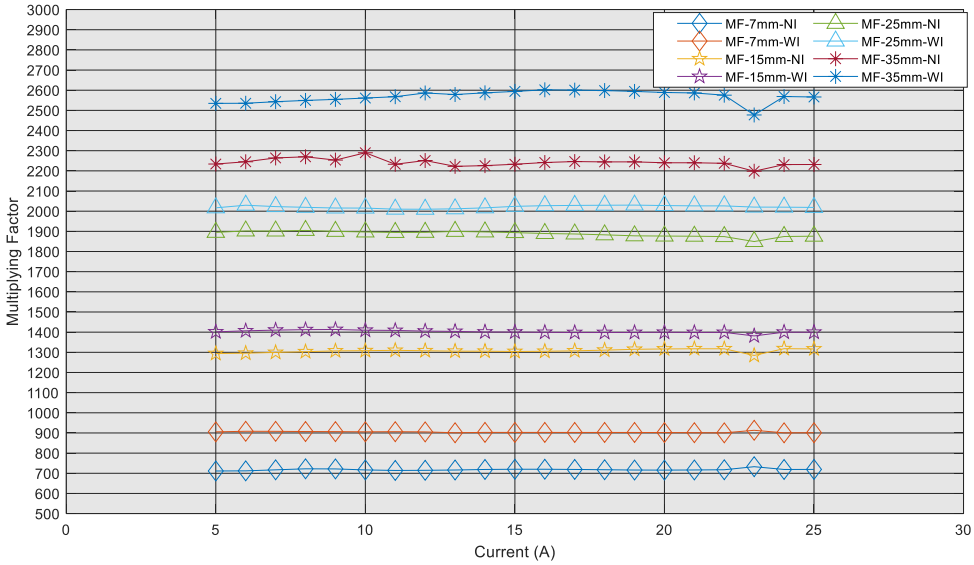

Figure 4.14 Multiplying factors of the sensor S_1 for various distances

To study the performance of a specific sensor under investigation, the output of sensor S_3 for 25 A source current was obtained in the *NI* and *WI* conditions and is plotted together as shown in Figure 4.15. The difference between the output for 25 A source current for *NI* condition is observed to be in the range of 24.99A to 25.023 A, whereas for the *WI* condition this range is from 24.947 A to 24.991 A.

Similarly, the performance of sensors S_4 and S_5 for the input currents of 5 A, 10 A, 15 A, 20 A, and 25 A are shown in Figures 4.15 and 4.16 respectively. From these figures, it is

evident that the output errors do not cross the limit of ± 0.1 A for all selected current cases and in both, *NI* and *WI* conditions. However, more accurate values can be obtained for the *NI* condition compared to the *WI* case when the distance of the sensors from the source is increased. The additional factor that may create a higher difference is the individual sensor quality as described in the previous section.

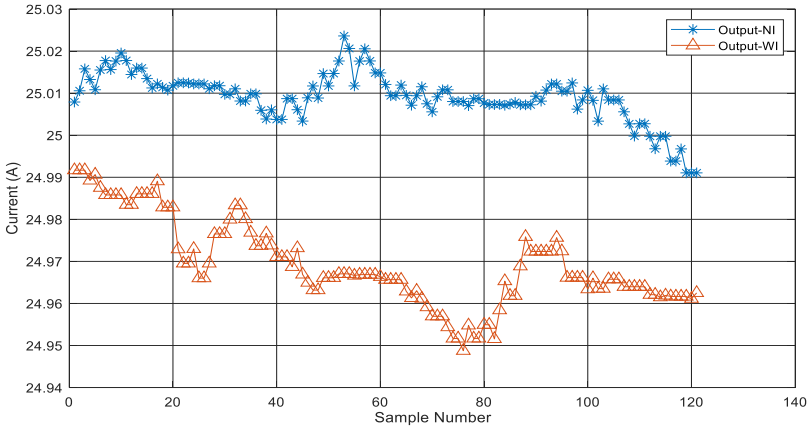

Figure 4.15 Sensor S_3 output input current of 25 A: WI and NI condition

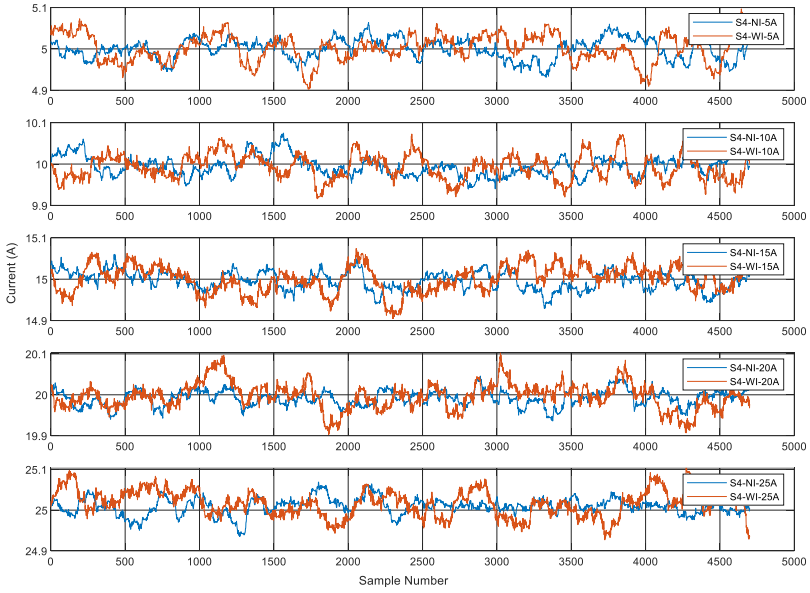

Figure 4.16 Sensor S_4 outputs for input currents of 5 A to 25 A: WI and NI conditions

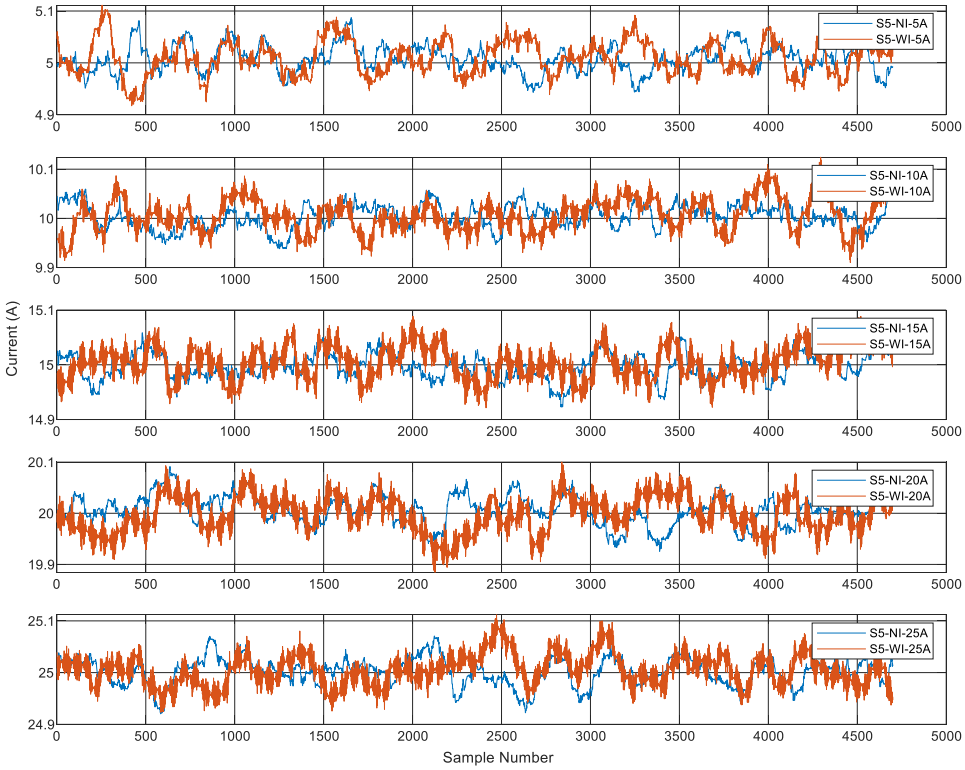

Figure 4.17 Sensor S_5 outputs for input currents of 5 A to 25 A: WI and NI conditions

From these results, it can be concluded that insulation affects the strength of the magnetic field sensing capability of the sensor, and therefore, the multiplying factors may require higher values to obtain the same current magnitude, even when the sensor is kept at the same distance.

To compare the performance of the sensors with the conventional CT, the relative percentage errors between the CT output and the sensor outputs were calculated for both the *WI* and *NI* conditions and for all sensors by considering the distance of 7 mm and input current frequency of 60 Hz. The statistical comparative results are in terms of Box-and-Whisker plots are shown in Figures 4.18 for sensors S_1 to S_6, and in Figure 4.19 for sensors S_7 to S_{12}.

The errors that are presented in Figure 4.18 range from −2.57% to +0.067% for the *NI* condition, whereas the percentage errors vary from −0.38% to +0.18% for the *WI* condition.

The median values for all sensors in the *NI* case in this figure indicate that the errors are between 0.04% and −0.09%, implying that for higher currents, the error is lower. This is also applicable for sensors S_7 to S_{12} and is evident from Figure 4.19. The median value of the errors for the *NI* case was in between 0.05% to −0.05%, whereas these values varied from 0.1–−0.15% for the *WI* cases. Overall, both figures show that the TMR sensors have very low errors in both cases, and that the medians show that their output is very close to the actual current. Therefore, these sensors can be deployed for underground conditions to measure the alternating current carried by underground cables that have insulation as well as for overhead conditions with overhead bare conductors for measuring current.

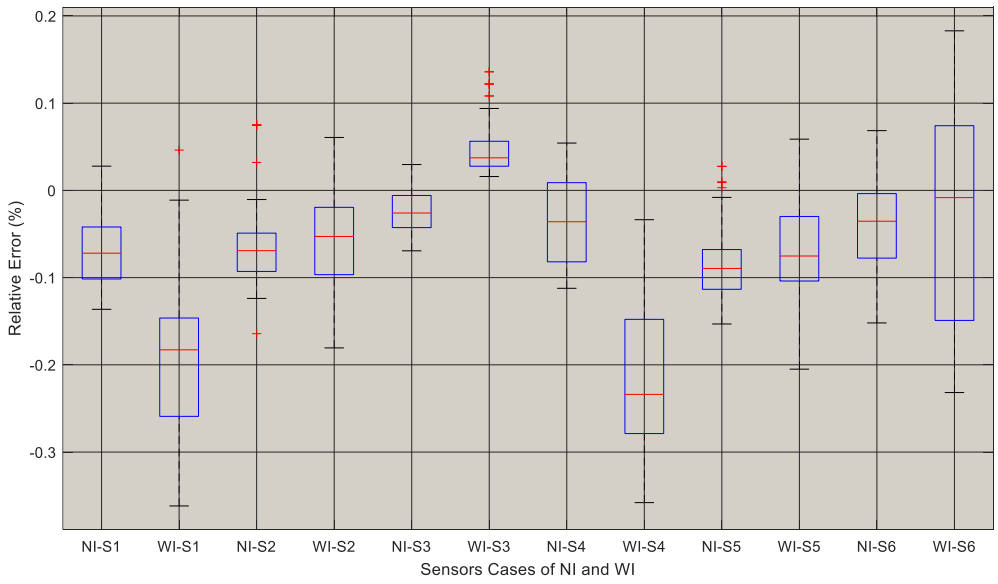

Figure 4.18 Relative errors in outputs of the sensors S_1 to S_6 at 7 mm distance and for WI and NI conditions

To demonstrate the relative errors in case of an individual sensor, the sensor S_4 is considered with relative errors calculated for range of source current values from 5A to 25A applied to *WI* as well as *NI* condition. The results are shown by the Box-and-Whisker plot in Figure 4.20. The median value for all currents for *NI* case is very close to 0%, whereas the median varies with the range from 0.3%to−0.2% for the *WI* case. For *NI* case, the error for 5 A was 0.5% while considering the fact that the sensors are less accurate in sensing lower current values since their rating is up to 200 A. It is evident that for 25 A,

the error rate for all sensors is 0.01% for *NI* condition. Whereas, in case of *WI*, the error value is 0.6% for 10 A and it decreases to −0.001% for 25 A. This indicates that the sensors will be accurate when they are used for higher current applications irrespective of the insulation.

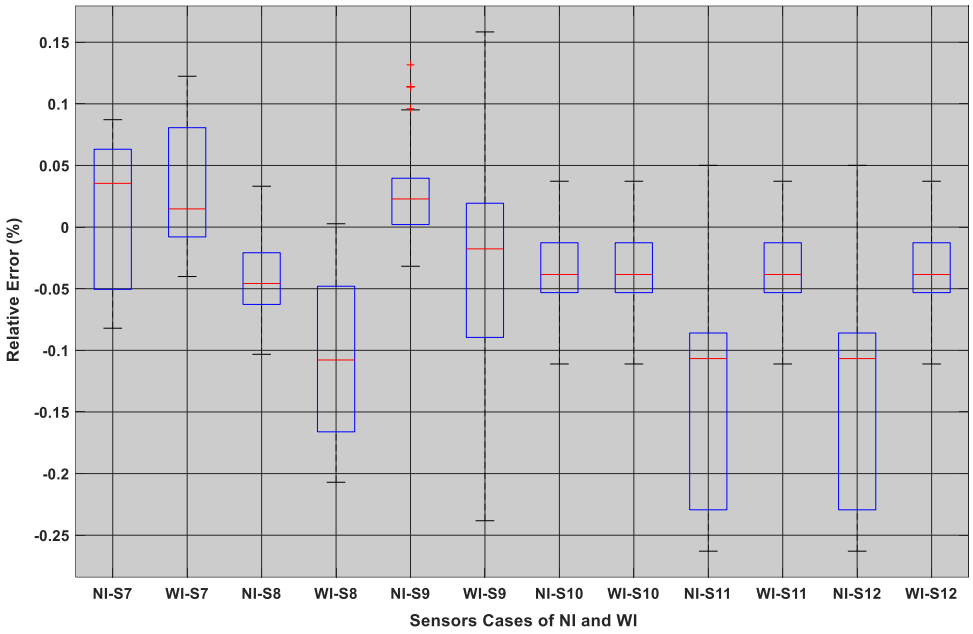

Figure 4.19 Relative errors in outputs of the sensors S_7 to S_{12}: WI and NI case

The performance of all sensors also needs to be confirmed when considering the presence or absence of insulation for higher currents to validate that these sensors will always perform better for higher currents. In this experiment, the maximum value of the source current was limited to 25 A. Therefore, the output of all sensors for 25 A for both the *WI* and *NI* cases was considered for investigation. Figure 4.21 shows these outputs, and it can be observed that all sensors demonstrate more consistent output that is very close to 25 A for the *NI* condition as compared to those for the *WI* condition. The output of sensor S_5 was 25.018 A for *NI* condition, and the minimum value obtained was 24.995 A in the *WI* condition. For *NI* condition, the output for all the sensors was in the range of 25.001 A to 25.01 A. The results of the DFT algorithm for the multiplying factors for both the *WI* and *NI* cases showed a variation of 110 to 120 for each sensor. However, the final output of the

current was very close to the actual current that was injected by the Omicron current injection set, with the errors shown in the figure.

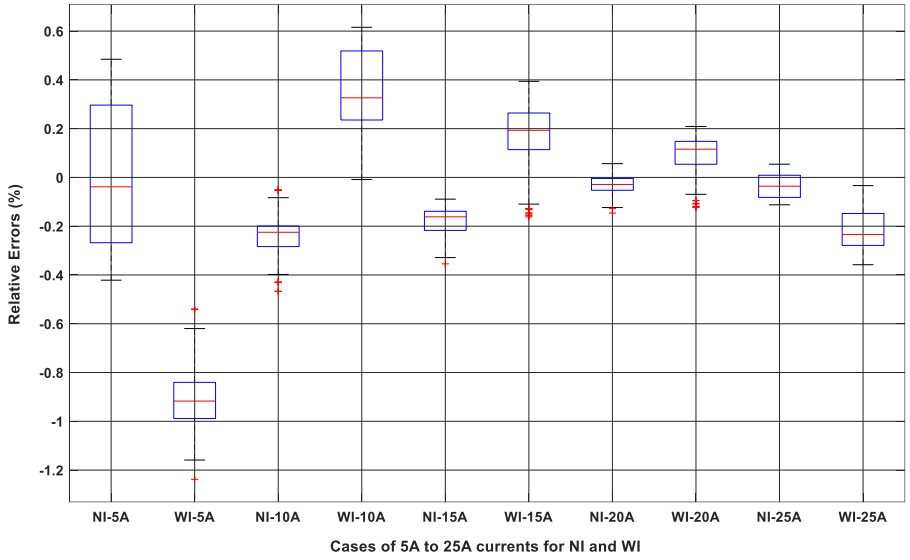

Figure 4.20 Relative Errors in outputs of S_4 at 7 mm distance for input currents of 5A to 25A, and for both, WI, and NI conditions

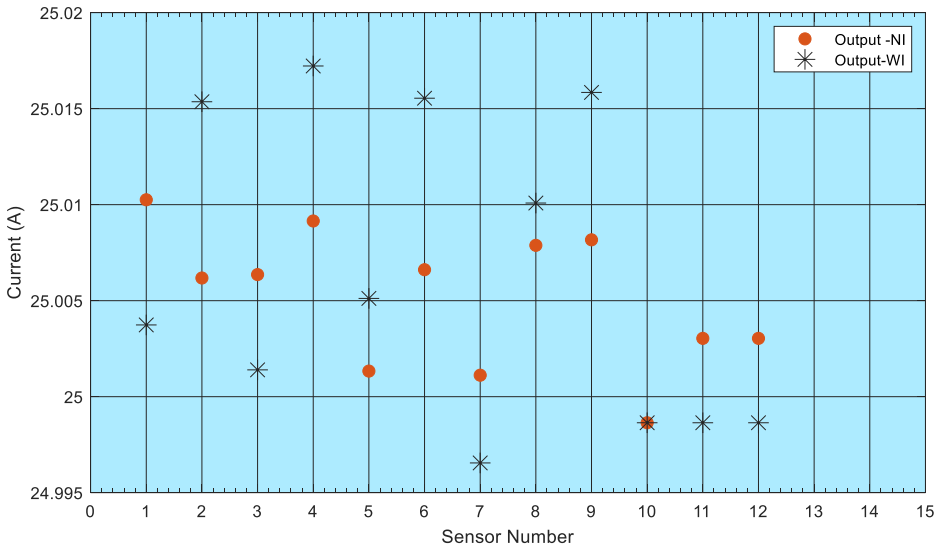

Figure 4.21 Output of all sensors for input current of 25 A and 7 mm distance for WI and NI conditions

The relative error in the output of all sensors for sensing the source current of 25 A is calculated by taking reference of the conventional CT output. The results are illustrated in Figure 4.22 and can be verified that the errors for higher magnitudes are very less in case of bare conductor condition whereas the errors vary a little more in case when the conductor has the insulation. The variation of the errors is observed for NI case to be 0.05% whereas for WI case, the errors are varying up to 0.24%.

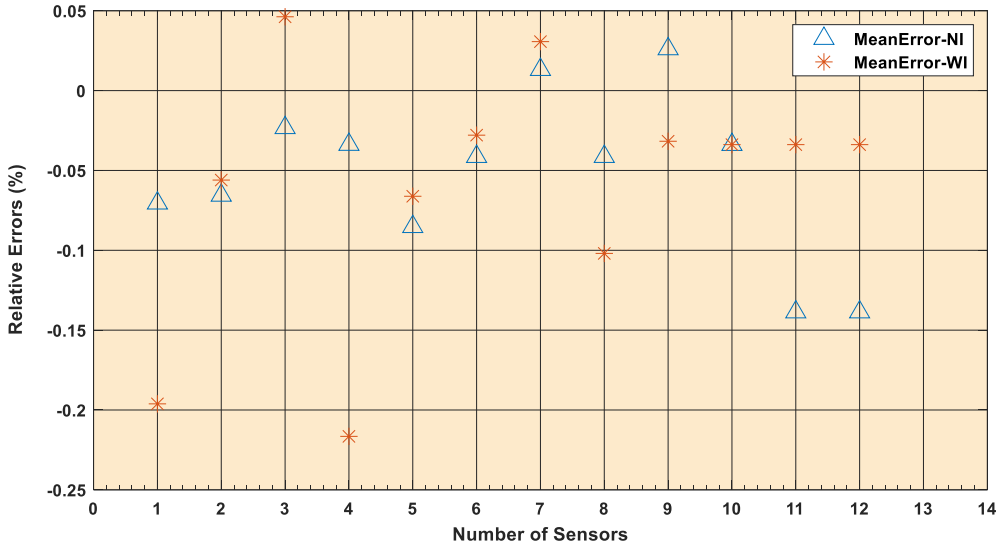

Figure 4.22 Average errors for all sensors for WI and NI cases for 25A

The algorithm developed in this phase of the research demonstrated the accuracy of the chosen method in determining the currents from a magnetic field for a range of currents from 5 A to 25 A. It is anticipated that the accuracy of the sensors at higher currents will be better for both *NI* and *WI* cases due to the stronger magnetic fields. A detailed performance analysis on the insulation infers that the insulation affects the sensing ability of the magnetic field to a certain extent and therefore, the accuracy of the current calculation is affected as well. The path of the magnetic field lines emanating in case of bare conductor is different than those in case of a conductor with insulation. The insulation is damping the magnetic field to a certain degree and therefore, the magnetic field is weaker due to the insulation. Overall, the effect becomes minimal when the source current is higher in magnitude.

4.5.4 Harmonics

The last factor under investigation is the performance of individual sensors in the presence of harmonics. In this case, the application of the sensors is considered for medium-voltage power systems that often have the odd harmonic present in the system. Generally, the protection relays and instrumentation meters eliminate any harmonics that are above the 5^{th} harmonic. Therefore, in this study, the sensors performance was tested for harmonics up to the 5^{th} order. Figures 4.22 and 4.23 show the multiplying factors that were obtained for twelve sensors for currents with the frequencies from 60 Hz to the 5^{th} order harmonic i.e., 300 Hz, and it can be seen that these are almost the same, however, a very small variation in case of 10 A input current was observed. There was less variation for input current of 15 A compared to that for 10 A. The sensors were able to measure the currents with harmonic frequencies as accurately as they were able to measure the fundamental frequency.

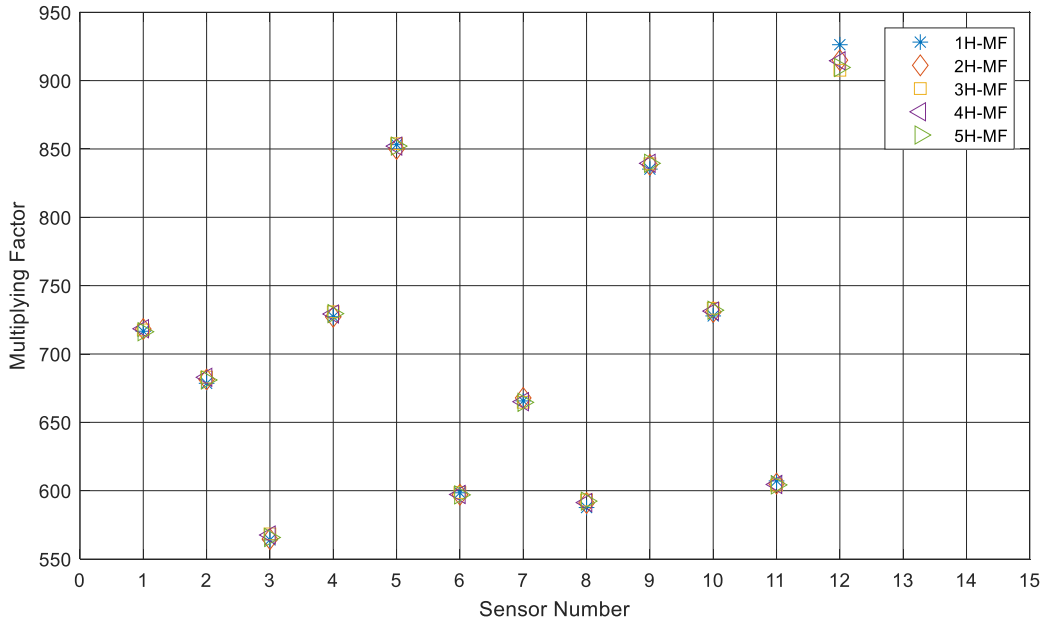

Figure 4.23 Multiplying factors of all sensors for input current of 10 A, 7 mm, 60 Hz and its harmonics: WI and NI cases

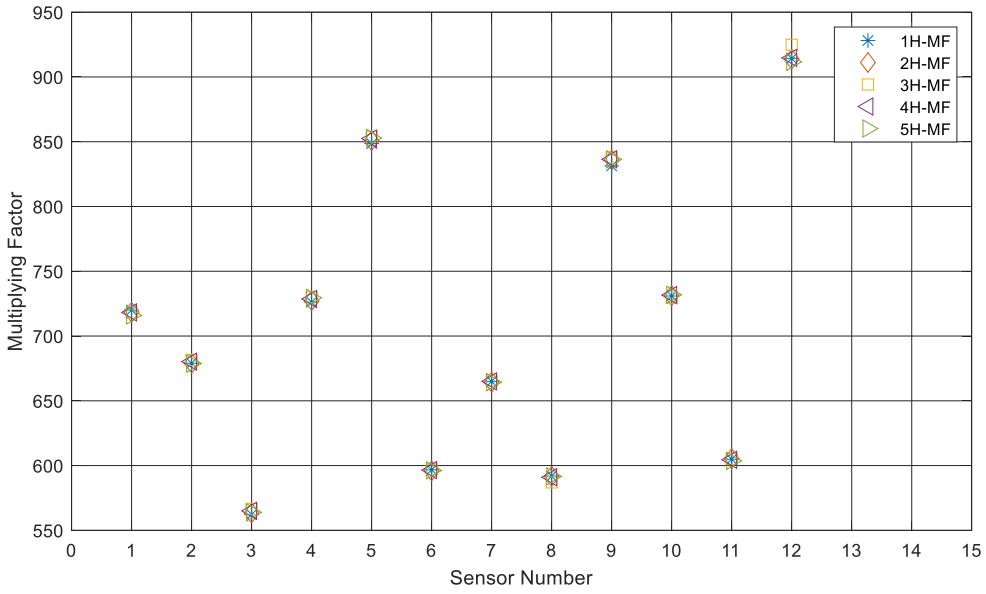

Figure 4.24 Multiplying factors of all sensors for input current of 15 A, 7 mm, 60 Hz and its harmonics: WI and NI cases

To have a clear information about the variation of sensor capacity with respect to change in the frequency of source current, the computational program was developed to calibrate the sensors for various frequencies and obtain the multiplying factors for each frequency and source current under experimental design consideration. From the various sets of results obtained, the MFs obtained for input currents of 5 A and 25 A with respect to the frequencies from 60 Hz to 300 Hz are shown in Tables 4.2 and Table 4.3 respectively.

Table 4.2 shows that sensor S_{12} has a maximum variation in the multiplying factor values ranging from 885 to 919, whereas sensor S_8 shows the second highest variation, ranging from 889 to 604. The remaining sensors have a variation from 4 to 5 units between the multiplying factors for each harmonic. This demonstrates that the harmonics do not affect current measurement when TMR sensors are used.

Table 4.2 Multiplying factors for all sensors with application of 5 A current for various harmonics

Sensors	MFs for a Current of Frequency:				
	60 Hz	**120 Hz**	**180 Hz**	**240 Hz**	**300 Hz**
S_1	711	719	717	719	718
S_2	678	681	679	684	680
S_3	567	567	570	570	567
S_4	726	725	728	728	727
S_5	856	852	858	854	854
S_6	596	598	601	598	599
S_7	663	666	664	665	664
S_8	592	589	604	590	595
S_9	828	838	836	840	837
S_{10}	734	733	740	734	736
S_{11}	606	606	605	605	604
S_{12}	910	919	885	912	903

Table 4.3 shows the multiplying factors that were obtained for all twelve sensors at a source current of 25 A. It can be observed from this table that the MF values are almost the same, with a variation of two units being demonstrated for all sensors except for sensor S_5. There is a variation of the values is from 848 for 60 Hz to 853 to the 5^{th} harmonic current. Sensor S_{12} shows the second highest variation of 4 from 913 to 917, and sensor S_1 shows variation from 715 to 719. The remaining sensors have multiplying factors very close to each other, with a variation of one to two units between all values. The variation is already minimal, and the algorithm applies these to determine the output of the current phasor for each case, with a relative error of 0.005%. The investigation of the sensor performance for the effect of harmonics concluded that the MFs and the current outputs are nearly constant for all sensors, irrespective of the order of harmonic, except for sensors S_8 and S_{12}. The higher MF values for these two sensors are merely because of the sensor quality. Replacing these two sensors with those of a better quality will likely result in a similar performance as that of the remaining ten sensors.

Table 4.3 Multiplying factors for all sensors with application of 25 A current for various harmonics.

Sensors	MFs for a Current of Frequency:				
	60 Hz	120 Hz	180 Hz	240 Hz	300 Hz
S_1	719	718	719	718	715
S_2	676	676	678	678	675
S_3	560	561	564	563	561
S_4	725	727	730	728	729
S_5	848	850	854	852	853
S_6	593	594	595	594	595
S_7	665	664	664	664	664
S_8	589	590	589	590	590
S_9	836	835	836	836	835
S_{10}	730	732	732	732	732
S_{11}	605	605	604	604	603
S_{12}	917	917	917	916	913

4.6 Performance of Sensors at High Currents

After calibration and verifying the performance of the sensor for currents up to 25 A, it was decided to deploy the sensor for measuring high currents up to 1500 A in a HV test laboratory. There are certain errors introduced during the experiment, such as the aging of sensors. To overcome this error, the sensors were tested for their calibration and accuracy one more time before deploying to the high current measurement. It was observed that two sensors were aged over the period of two years and therefore, were replaced with two new sensors with proper testing and calibration. The experimental setup is shown in the Figure 4.25. A high voltage rated insulated cable of size AWG# 4/0 was utilized for this experiment. Sensors were installed inside a custom-made case made from fiberboard for their protection. Three casing contained two-sensors in each and were supplied 5.5 V DC supply through terminal blocks. The outputs of sensors were connected to six channels of NIDAQ-9174 data acquisition system. The high current generating equipment consisted of the voltage controller which was operated by the certified professional to generate pure

sinusoid currents of 60 Hz for circulation in the high voltage insulated cable as shown in the Figure 4.25. The sensors were placed at a distance of 15 cm from the HV cable during these tests. Currents were varied in steps from 50A to 1500A and the outputs of six sensors were recorded for 8 seconds. Simultaneously, currents were also measured with a current probe having an accuracy of 1%. Sensor signals were recorded at a sampling rate of 7.2 kHz/second. The installation of the experimental setup, selection of cables, connection and safety precautions were followed during the experiment by referring the standards [91].

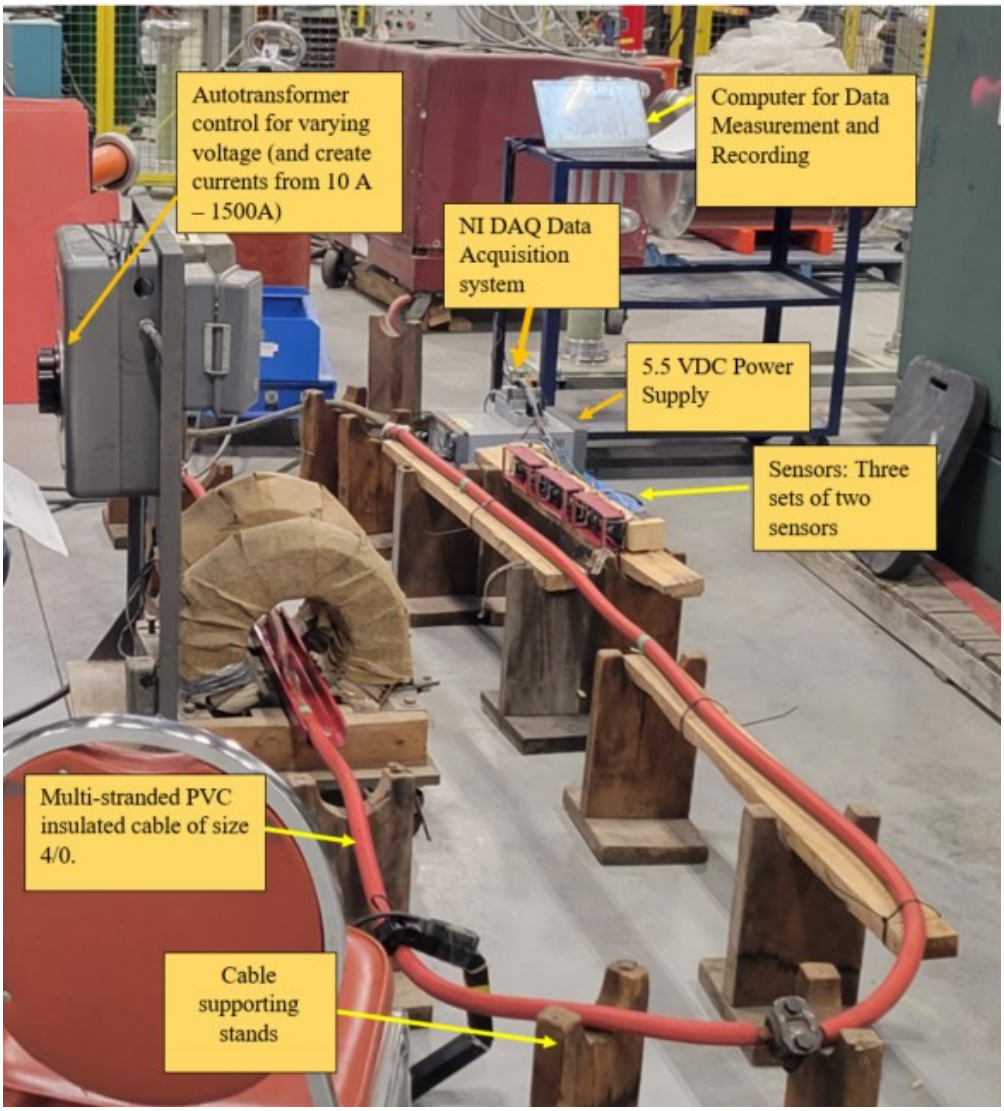

Figure 4.25 Experimental setup at the high voltage test laboratory for measuring high currents

Phasor values for each measurement and for each sensor were calculated using DFT as discussed in earlier chapters. The magnitudes of the currents were compared with those measured by the current probe.

Figure 4.26 shows the magnitude error estimated for the input currents of 500 A, and 1000 A for S_3. The estimation is performed using 4800 samples. It is evident that the estimated output does not vary more than 1.05 A for a 1000 A input current and thus, proving the capability of sensors to measure high currents.

Additionally, the phase errors were estimated for S_3 and are shown in Figure 4.27 for the input currents of 500 A and 1000 A. It is clear from the figure that errors are very small. Similar results were obtained for other values of input currents and are shown in Table 4.4.

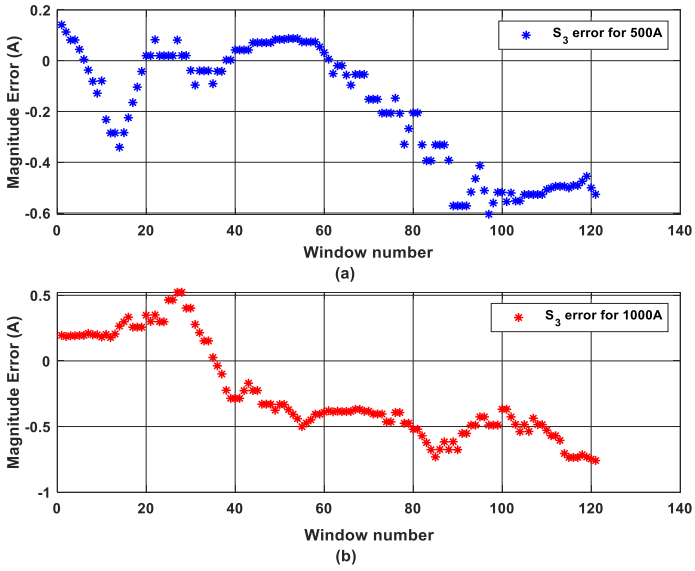

Figure 4.26 Magnitude error of sensor S_3 for input current of (a) 500 A and (b) 1000 A when placed at a distance of 15 cm from the 4/0 cable

The table shows the average magnitude and phase errors, maximum magnitude, and phase errors and maximum and average TVEs for various values of current. The maximum error in the estimation of magnitude is 0.95 A for input current of 100 A. The maximum error in the phase estimation is 0.0118^0. The values of %TVE of S_3 for all currents are shown with their average, maximum and standard deviation in the last three columns of the table. It is

evident that the average value of % TVE is below 0.25% and the maximum value is obtained for estimating input current of 100A.

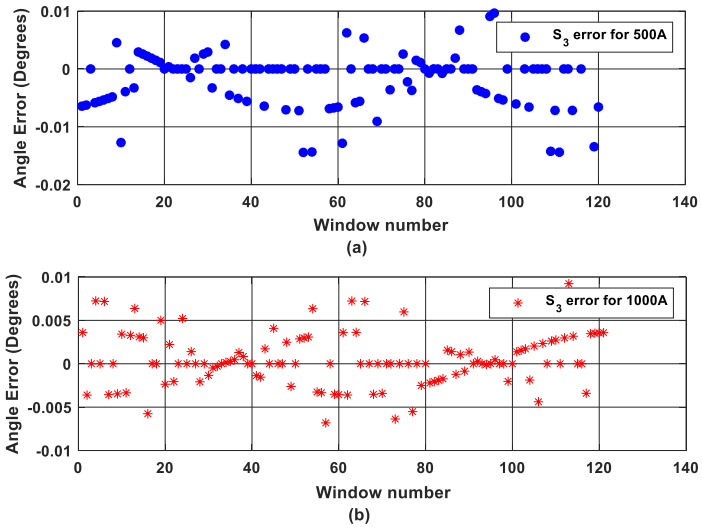

Figure 4.27 Phase error of sensor S_3 for input current of (a) 500A and (b) 1000 A when placed at a distance of 15 cm from the 4/0 cable

Table 4.4 Performance results of sensor S_3 for high currents

Current	Magnitude Error			Phase Error			TVE		
	Avg	Max	S.D.	Avg	Max	S.D.	Avg	Max	S.D.
50A	0.19	0.60	0.30	0.0008	0.0118	0.0047	0.19	0.60	0.30
100A	0.45	0.95	0.27	0.0010	0.0042	0.0023	0.23	0.47	0.13
200A	0.08	0.50	0.35	0.0009	0.0044	0.0017	0.03	0.17	0.12
300A	0.41	0.98	0.20	0.0003	0.0022	0.0010	0.10	0.25	0.05
400A	0.08	0.58	0.28	0.0012	0.0001	0.0007	0.02	0.12	0.06
500A	0.00	0.67	0.30	0.0013	0.0002	0.0005	0.00	0.11	0.05
600A	0.49	0.13	0.29	0.0015	0.0004	0.0004	0.07	0.02	0.04
700A	0.44	0.90	0.29	0.0014	0.0004	0.0005	0.05	0.13	0.04
800A	0.34	0.10	0.26	0.0004	0.0004	0.0003	0.04	0.01	0.03
900A	0.15	0.58	0.23	0.0001	0.0007	0.0004	0.02	0.06	0.02
1000A	0.40	0.92	0.32	0.0011	0.0017	0.0003	0.04	0.09	0.03
1100A	0.12	0.35	0.27	0.0012	0.0016	0.0002	0.01	0.03	0.02
1200A	0.73	0.88	0.23	0.0007	0.0010	0.0002	0.06	0.09	0.02
1300A	0.60	0.76	0.08	0.0003	0.0001	0.0002	0.04	0.05	0.01
1400A	0.25	0.06	0.19	0.0010	0.0007	0.0002	0.02	0.00	0.01
1500A	0.22	0.13	0.15	0.0001	0.0004	0.0002	0.45	0.26	0.29

Standard deviation is also shown in the same table for all input currents, and it indicates the results below 0.30 with most results less than 0.1. These results verify consistent performance of the sensor S_3 in measuring high currents and the errors are within permissible limits of standards [12, 80]. The results of remaining five sensors, S_1, S_2, S_4, S_5 and S_6 with magnitude errors, phase errors and %TVE illustrated in tables similar to Table 4.4 and presented in Appendix C.

All sensors exhibited consistent performance like S_3 and can be verified for their respective tables given in the Appendix C. The estimated current of S_1 for an input of 50 A is shown in the Figure 4.28 which shows a pure sinusoid with an error of 0.21 A (refer results in Appendix C).

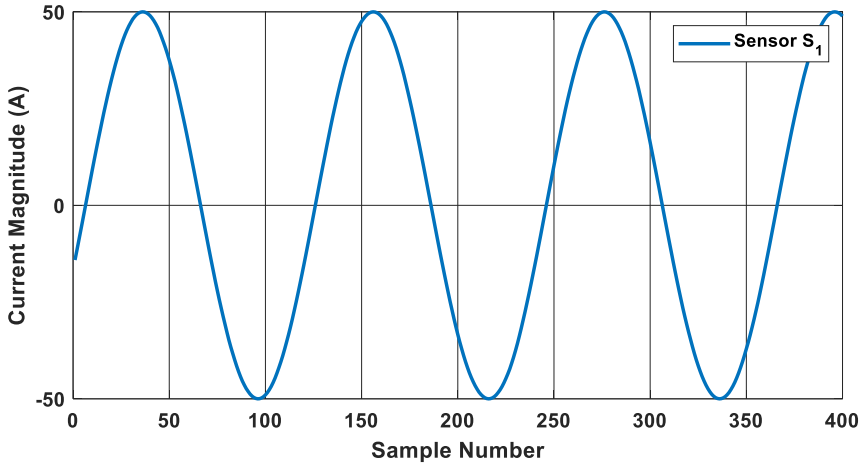

Figure 4.28 Sensor S_1 output for 50 A at 15 cm

Similarly, the estimated output of sensor S_1 for an input current of 1500 A is shown in Figure 4.29. The error in estimation for this case was 0.1A and can be verified from the table of results given in Appendix C. The above two figures of results for 500A and 1500 A verify that the sensor can accurately measure low as well as high currents when placed at 15 cm. The laboratory experiment on single phase was performed for currents up to 25 A only. But the high voltage laboratory experiment verified the sensors performance for high currents.

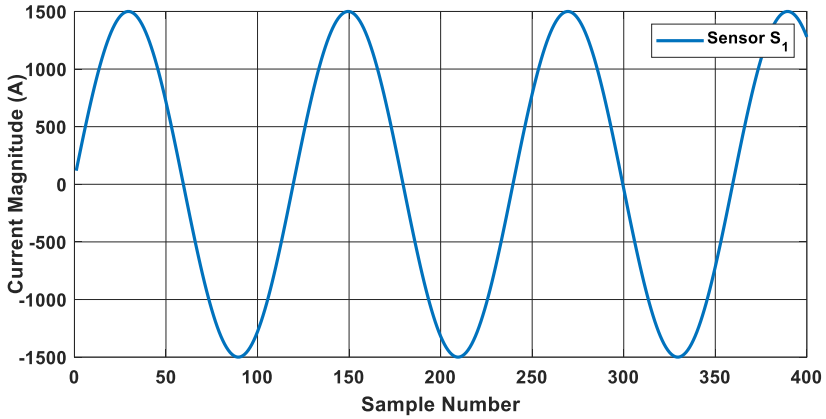

Figure 4.29 Sensor S_1 output for 1500 A at 15 cm

The TVEs estimated for input currents from 30 A to 1500 A for all sensors when placed at 15 cm from the 4/0 cable are shown in Figure 4.30.

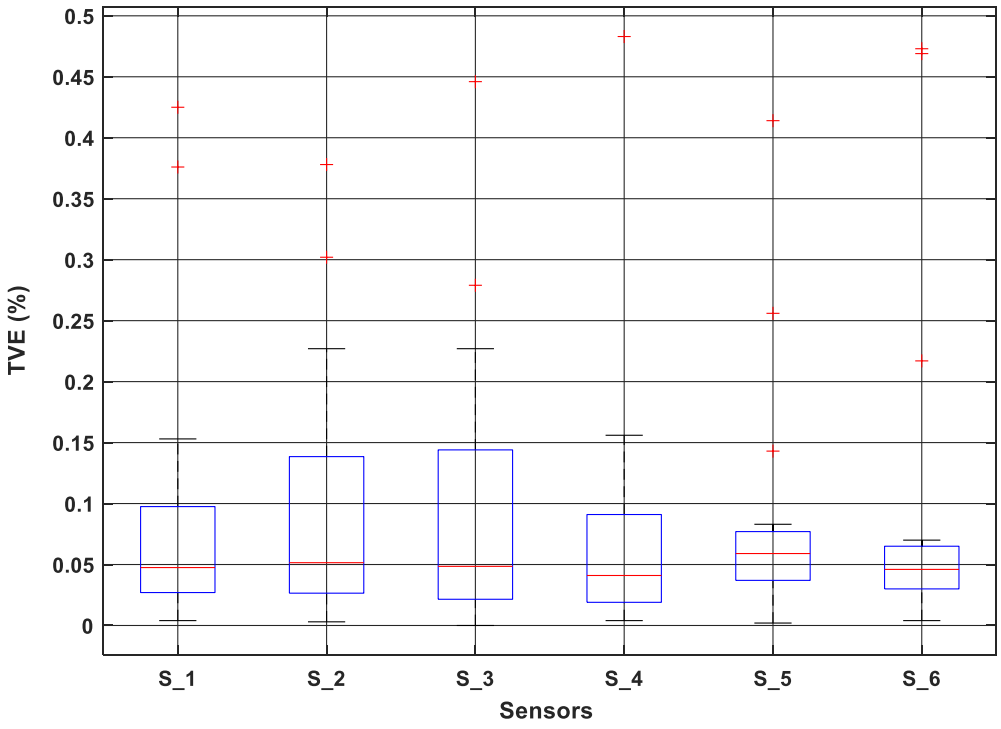

Figure 4.30 Percentage TVE for six sensors estimated for input currents from 30 A to 1500 A

The average TVEs for all sensors are in the range of 0.03 to 0.07% and can be seen from Figure 4.30. The outliers for all sensors which have errors of more than 0.25 % and up to

0.5% are for the lower values of input currents such as 10 A to 40 A. For example, for 30 A the maximum TVE of 0.484% was observed for S_4 and, and 0.46% for S_6 for 30 A input current. Remaining sensors provided errors below 0.5. The %TVE for 10 A, and 20 A were higher than 1% for two sensors, S_2 exhibiting error of 1.624% for 20 A and S_6 showing error of 1.28% for 10 A. This is because the magnetic field intensity at 15 cm produced by 10 A current is weaker than that generated by higher currents.

4.7 Conclusions and Summary

The TMR sensors were calibrated using a single-phase experimental set up and for the highest currents up to 25 A. The performance of calibrated TMR sensors for current measurement was studied for various factors such as, the impact of variation in the sensor quality, distance from current source, insulation, and harmonics. The experiments were conducted by designing various parts and stages to record measurements in detail, and a thorough analysis was performed to study the behavior of the sensors under the four factors mentioned above. With respect to the variation of performance based on the sensor quality, even though the sensor results showed variance in the performance for higher current values, they all exhibited similar behavior except, for sensors S_1 and S_{12}. The variation in the output was not higher than 0.04 A for the input current of 25 A current. The remaining sensors produced satisfactory outputs with an error of 0.0013%. It is expected that the difference of 0.04 A will reduce further when the magnitude in the source current increases. The variation in the distance for each sensor provided their individual multiplying factors, inferring that there is a need to calibrate each sensor separately to achieve a better accuracy in current measurements that is independent of the distance from source or the magnitude of the current. The calibration algorithm produced different values of MFs for the conductors under *NI* and *WI* condition, however, the final calculated outputs of the currents for sensors were very close the injected source current with an error of 0.18% for the conductor *with-insulation*, and in some cases, the final outputs showed an error of −0.38%. For the conductors with *no-insulation*, the results were consistent for all sensors and for all current values from 5 A to 25 A, with errors ranging from 0.4% to −0.24%. The harmonics had no significant effect on the performance of the TMR sensors. They showed very

consistent outputs for all currents ranging from 5 A to 25 A when they were tested for currents with a fundamental frequency up to 5^{th} harmonic. Thus, these sensors can be applied to measure currents containing harmonics. Moreover, after the successful calibration, these non-invasive TMR sensors can be deployed in the current measurement experiments for AC power systems.

The performance of sensors for measuring high currents was tested by conducting an experiment at the high voltage laboratory. The sensors showed satisfactory performance for all currents from 30 A to 1500 A when placed at 15 cm. The errors in estimating total vector error are below 0.5% for all sensors. The standard deviation in calculating the %TVE for all sensors showed a consistently low value indicating that they can be deployed to measure currents in medium and high voltage AC power systems where currents are usually in the range from 300 A to 1500 A.

Chapter 5. Multiple Sensors and Fusion Technique for Improving Current Phasor Estimation Accuracy

5.1 Introduction

The calibration of individual sensors and validating their performance for the estimation of the current magnitudes with the help of measured magnetic field using TMR sensors is successfully achieved. The next phase is construction of a current phasor from the estimated data that will have accuracy close or equal to that of the source current. To achieve this objective, there is a need to check the accuracy of estimation using values of individual MFs or average values of the MFs and explore the need for use of combined data from multiple sensors for current phasor estimation. The aim is to obtain an accurate information of the current phasor that will be a true representation of the known source current flowing through the conductor. The use of multiple sensors can improve the current phasor measurement accuracy.

Therefore, this chapter further investigates the following objectives:

1. Variation in the accuracy of estimated current phasor by utilizing the individual MFs and averaged values of the MFs per sensor in the estimation algorithm.
2. Comparison of the current phasors obtained from individual sensor and by utilizing a sensor-array for known values of the input currents.
3. Effect of lower frequency source currents on the estimation of current phasors an individual TMR sensor and the sensor-array.
4. Effect of higher frequency source currents on the sensor performance

To achieve these objectives, multiple comprehensive laboratory experiments are conducted for low as well as high frequencies to gather the sensor output data by utilizing the single-phase experimental setup that was used for the experiments mentioned in the previous chapters. To study the behavior of sensors at low frequencies, the currents were injected with frequencies of 1 Hz, 2 Hz, 5 Hz, 10 Hz and their magnitudes varying from 5 A to 25 A in the increments of 1 A. For the study of sensor behavior at higher frequencies, the

alternating currents with multiples of fundamental frequencies such as 120 Hz, 180 Hz, 240 Hz, and 300 Hz were injected with their magnitudes varying from 5 A to 25 A in steps of 1 A. Measured data from the ADC was used for estimation of the current phasors. A computational program based on the DFT technique and a current phasor estimation algorithm with stages as shown in the Figure 5.1 was developed in MATLAB software.

Current phasors were estimated for each sensor as well as six combinations of sensor pairs for a set of four sensors. Sensors are calibrated for 60 Hz frequency AC and then are tested for low frequency and high frequency currents. This chapter also introduces the current estimation technique by applying various combination of sensor pairs using four sensors as well as the weighted fusion technique with inverse variance.

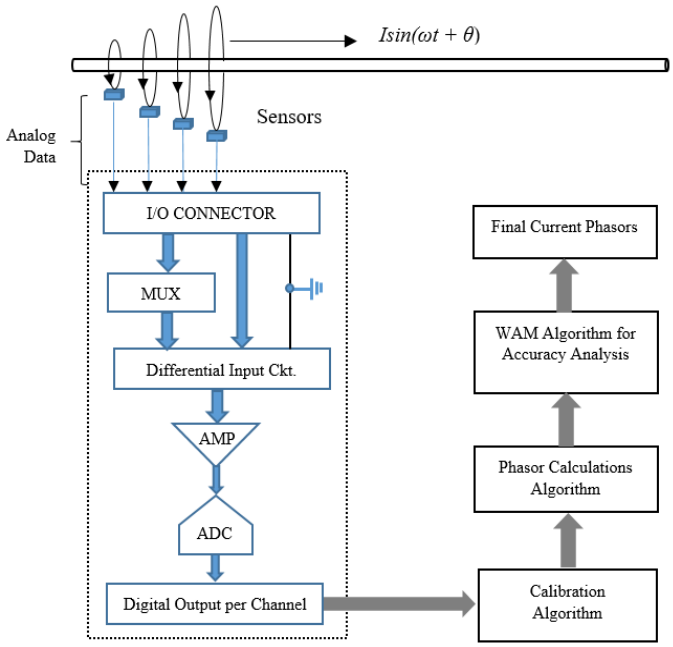

Figure 5.1 Experimental setup for calculation of single-phase current phasor

5.2 Study of Individual MFs and Average MF for Estimation of Current Phasor

The relative errors in the current magnitudes estimated by utilizing the individual MFs for every sensor and for all locations for input currents of 5 A, 10 A, 15 A, 20 A and 25 A are within 0.098% and, are demonstrated in the previous chapter. In the study cases

demonstrated in the previous chapters, the calibration was performed by using the measurements performed for 60 Hz frequency input currents and the MFs were obtained for each current value for all sensors using the DFT algorithm. Keeping the objectives in the previous section in focus, the values of the MFs obtained using 60 Hz data are averaged to get the average MF value for each sensor. In the later phase, these individual and average MFs are used for estimation of the currents from the magnetic field sensed by the sensor for varying frequency source current.

The accuracy of all sensors was investigated for currents of frequency 60 Hz and, of magnitudes ranging from 10 A to 25 A in steps of 1 A, and for all locations using the individual and average MFs. The results of comparison for sensors S_3 and S_4 are shown in the Figure 5.2 and Figure 5.3 respectively. The errors in the outputs for 7 mm distance are found to be in the range from 0.01% to 0.61% for individual MF and ranges from 0.009% to 0.62% but as the current increases from 5 A to 25 A, the errors increase for average MF and decrease for individual MF and are shown in the Figure 5.2(a). The errors for lower values of input currents are higher for both cases when the distance from the source increase. This is evident from the Figures 5.2 (b), (c) and (d) which show the errors in the range of 2.5% and 3.0% for the lower values of current like 5 A and 6 A, and these errors decrease for the higher currents after 15 A. The errors are well below 0.5 % for larger distances including 35 mm for currents higher than 20 A. The difference between the errors obtained using individual MFs and average MFs is within 0.2 % to 0.3 % for all distances and all currents after 10 A. The difference in errors by making use of individual MFs and average MFs is very small. This means the sensor S_3 using average MF can be considered as a good calibration.

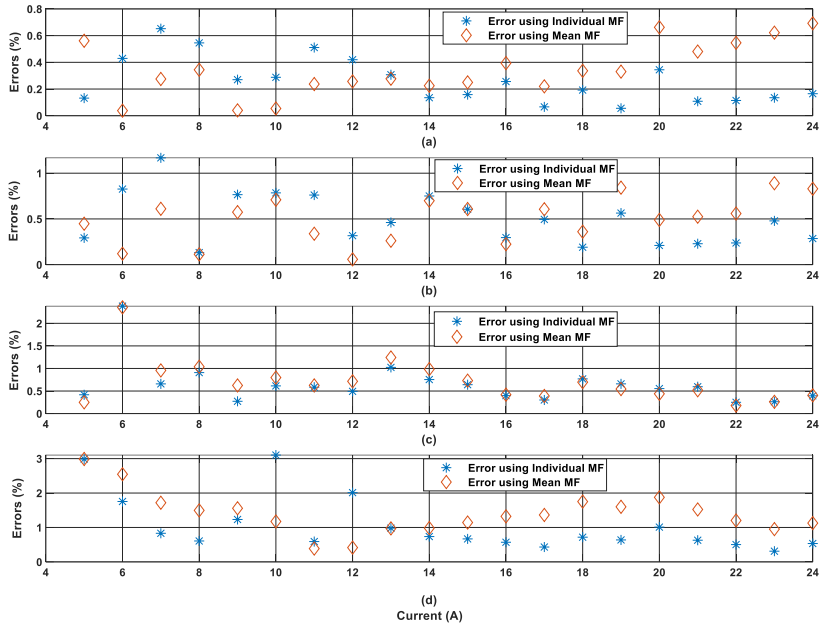

Figure 5.2 Percent errors in the computed magnitudes of current for S_3 using individual and average MFs, (a) at 7 mm, (b) at 15 mm, (c) at 25 mm and (d) at 35 mm

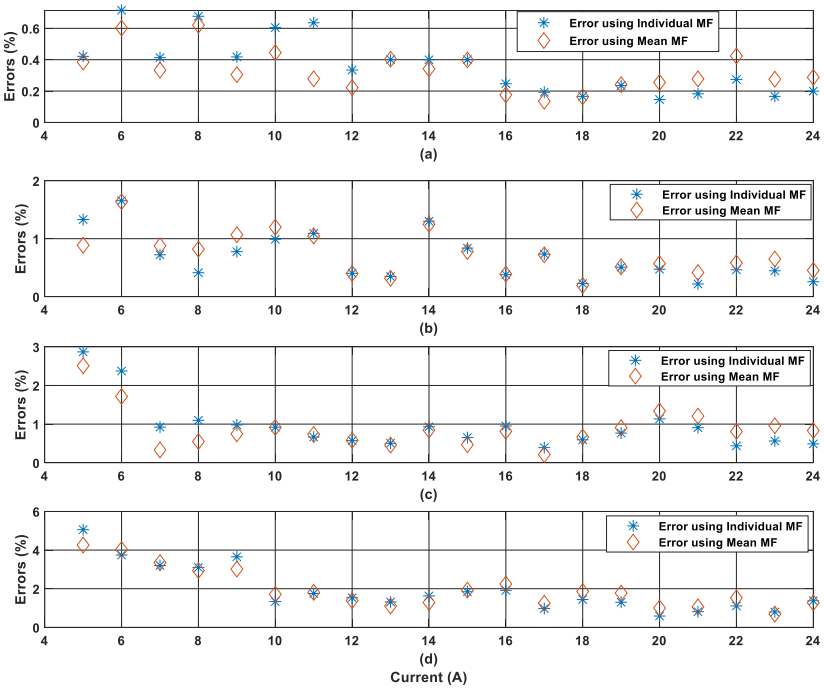

Figure 5.3 Percent errors in the computed magnitudes of current for S_4 using individual and average MFs, (a) at 7 mm, (b) at 15 mm, (c) at 25 mm and (d) at 35 mm

The accuracy of all sensors was investigated for currents from 10 A to 25 A in steps of 5 A and for all distances using the individual and average MFs. Table 5.1 shows the comparative percentage errors for all sensors for input current of 15 A when placed at all specified locations. It is evident from this table that the errors for 15 A using average MF are lower as compared to Individual MF for some sensors. This observation is applicable for sensors, S_1, S_2, S_6, S_7, S_8, S_9 and S_{10}. However, as the distance and current increase, the sensors show better performance using the individual MF as compared to the currents using average MFs and it was confirmed for all sensors except S_5, S_8 and S_9 for input current of 15 A. The performance of S_5 goes on deteriorating with the increase in distance for both individual and average values of MFs. It is evident from the table that the errors using individual MFs increased from 0.37 % for distance, d_1 to 3.12% for distance, d_4, whereas the errors after replacing individual MFs by average MFs were 0.66% for distance, d_1 and 6.0% for distance, d_4. This is the only sensor that resulted in 6.0% error for distance, d_4. Sensor S_9 demonstrated similar performance to that of S_5 and provided second highest error for average MF. However, it was close to that of S_8 for distance, d_4. The sensor S_{11} demonstrated exception by giving less accuracy for larger distances. Its error using average MF for distance, d_4 was almost the same as that for distance, d_1 using individual MF. The percentage error using Average MFs was observed to be less than that using individual MFs for the distance d_3 for sensors, S_1, S_2, S_4, S_5, S_7, and S_{11}. Overall, for the current of 15 A, it was observed that the difference between the errors using individual MFs and average MFs is negligible for all distances except for sensors S_5, S_8 and S_9 and this difference is not too large for S_8 and S_9.

Table 5.1 Sensor errors for 15 A output using individual MF and average MFs

Sensor	% Errors for d_1 = 7 mm		% Errors for d_2 = 15 mm		% Errors for d_3 = 25 mm		% Errors for d_4 = 35 mm	
	Ind.* MF	Avg.* MF	Ind.* MF	Avg.* MF	Ind.* MF	Avg.* MF	Ind.* MF	Avg.* MF
S_1	0.32	0.16	0.55	0.85	1.05	0.73	0.69	1.26
S_2	0.24	0.09	0.72	0.67	0.58	0.01	0.55	0.92
S_3	0.16	0.25	0.61	0.61	0.64	0.73	0.67	1.14
S_4	0.40	0.40	0.84	0.78	0.65	0.47	1.84	1.93
S_5	0.37	0.66	0.82	0.63	1.54	1.07	3.12	6.00
S_6	0.16	0.04	0.57	0.48	0.90	1.05	0.55	0.18
S_7	0.03	0.03	0.45	0.70	0.55	0.11	1.03	0.74
S_8	0.37	0.01	0.13	0.75	0.78	2.59	1.46	2.43
S_9	0.40	0.03	0.26	0.62	0.12	1.92	1.57	2.54
S_{10}	0.33	0.26	0.06	0.16	0.75	1.30	1.59	1.87
S_{11}	0.20	0.32	0.25	0.49	0.68	0.28	0.56	0.84
S_{12}	0.53	0.93	0.41	2.02	0.92	1.21	1.06	1.37

Ind.*: Individual, Avg.*: Average

The variations in the errors become negligible at higher magnitudes of input currents and is evident from the Table 5.2 where the sensors' errors are compared for 25 A. In this table, all sensors demonstrated satisfactory performance for the distance d_1 with errors from individual MFs below 0.25% and using 0.7% using average MFs. For distance d_2, the errors do not have significant variation as compared to those of distance d_1. For distance d_3, the minimum error contribution of 0.02% was by sensor S_8 and maximum error contribution was 0.67% by S_9 using individual MFs. These errors were close to those obtained using the average value of MF for all sensors except, S_2, S_6 and S_9 where, the maximum error was observed to be 2.01%. In addition, sensor S_9 exhibited similar performance of higher error for distance d_4 with percentage error of 2.61% using the average value of MF. The errors calculated for all sensors when placed at the distance d4 were below 1.0% for all sensors except sensor S_4 and S_5, when applied with the individual MFs whereas, these errors were below 1.5% for all sensors except S_2, S_8 and S_9 when utilized average value of MFs. This indicates consistent and good performance by sensors for all distances.

Table 5.2 Sensor errors for 25A output using individual and average MFs

Sensor	% Errors for d_1 = 7 mm		% Errors for d_2 = 15 mm		% Errors for d_3 = 25 mm		% Errors for d_4 = 35 mm	
	Ind.* MF	Avg.* MF	Ind.* MF	Avg.* MF	Ind.* MF	Avg.* MF	Ind.* MF	Avg.* MF
S_1	0.14	0.22	0.11	0.55	0.46	1.08	0.57	1.21
S_2	0.19	0.43	0.23	0.89	0.21	1.35	0.84	1.77
S_3	0.17	0.69	0.29	0.83	0.39	0.40	0.53	1.13
S_4	0.19	0.28	0.25	0.45	0.48	0.83	1.37	1.27
S_5	0.15	0.55	0.41	0.68	0.72	0.96	1.84	0.35
S_6	0.19	0.59	0.44	0.60	0.44	1.98	0.51	1.98
S_7	0.14	0.09	0.06	0.41	0.44	0.28	0.36	0.41
S_8	0.23	0.38	0.20	0.18	0.02	1.35	0.50	2.35
S_9	0.17	0.32	0.24	0.14	0.67	2.01	0.75	2.61
S_{10}	0.16	0.20	0.32	0.09	0.07	0.46	0.64	1.36
S_{11}	0.26	0.42	0.08	0.34	0.31	0.05	0.54	0.08
S_{12}	0.16	0.24	0.31	1.44	0.30	1.08	0.99	1.03

Ind.*: Individual, Avg.*: Average

From the results obtained for all distances and currents for all sensors, it was observed that the error difference between use of individual and average MF is very less. The current injection set in the laboratory has the highest limit of current injection to 25 A. From the tables 5.1 and 5.2 it is inferred that the errors are reducing with the increase in the current magnitude. Therefore, the difference between the use of individual and average MFs will reduce further. The calibration of sensors by utilizing average MF is more practical and less complex for measuring currents of any frequency and magnitude. Therefore, average MFs are used for all further performance analysis studies reported in this chapter.

5.3 Estimation of Phase Angle Error and Total Vector Error

To fully characterize and evaluate the performance of magnetic sensors for estimating current phasors, it is important to determine the phase angle error and the Total Vector Error (TVE). The method for calculation of TVE explained in [83] needs time-synchronization of phasors of input current and the sensor output to determine the

difference in phase angle. The TVE equation as per the IEEE Standard [80] for synchronized vectors stamped at n^{th} time instant is given as:

$$TVE(n) = \sqrt{\frac{\left[(\hat{X}_r(n) - X_r(n)\right]^2 + \left[\hat{X}_i(n) - X_i(n)\right]^2}{\left[X_r(n)\right]^2 + \left[X_i(n)\right]^2}} \tag{5.3.1}$$

where $\hat{X}_r(n)$ and $\hat{X}_i(n)$ are the real and imaginary components of the estimated current phasor from sensor output, and $X_r(n)$ and $X_i(n)$ are the counterparts of the actual input current at time instant, (n). However, in absence of time-synchronization, the above equation needed to be modified by implementing a new technique as discussed below:

The phasor representation of a current signal of single frequency can be presented as:

$$\begin{aligned} X &= \left(X_m\right)e^{j\theta} \\ X &= \left(X_m\right)\cos\left(\theta\right) + j\left(X_m\right)\sin\left(\theta\right) \\ X &= X_r + jX_i \end{aligned} \tag{5.3.2}$$

where, X_m is the peak value of the sinusoidal signal, subscripts r and i indicate the real and imaginary parts of the complex value in rectangular form. The phase angle, θ of the phasor will advance when the phasor is calculated by advancing the data window by one sample and applying a non-recursive algorithm. If the input signal is a perfect sinusoid of frequency, f_s, and there is no error in phasor calculations, the angle will advance by $\Delta\theta$ given by the following equation:

$$\Delta\theta = \frac{360^0}{N} \tag{5.3.3}$$

where N is the number of samples in one cycle expressed using the sampling rate, S as

$$N = \frac{S}{f_s} \tag{5.3.4}$$

For a pure sinusoidal input and, if the sensor output is accurate, the angle difference computed by applying non-recursive DFT between two consecutive data windows will be equal to $\Delta\theta$ as in Equation (5.2.3). However, if the sensor output is not accurate, then angle

difference will not be $\Delta\theta$ and any deviation will be termed as phase angle error. Similarly, the difference between the input current magnitude (X_m) and current phasor magnitude computed by utilizing the sensor output will be termed as magnitude error. For two consecutive data windows, $n-1$ and n, the phase angle error and the magnitude error for the n^{th} data window can be expressed as:

$$\varepsilon\left(X_n\right) = X_m - X_n \tag{5.3.5}$$

$$\varepsilon\left(\theta_n\right) = \Delta\theta - \left(\Delta\theta_{n-1} - \Delta\theta_n\right) \tag{5.3.6}$$

where:

X_n is the computed magnitude at the n^{th} data window.

$\Delta\theta_{n-1}$ and $\Delta\theta_n$ are the computed phase angles for the $(n-1)^{th}$ and n^{th} data windows respectively.

The errors defined by Equation (5.2.5) and Equation (5.2.6) can be transformed into real and imaginary component errors as follows:

$$\varepsilon\left(X_{rn}\right) = \varepsilon\left(X_n\right)\cos\left(\varepsilon\left(\theta_n\right)\right) \tag{5.3.7}$$

$$\varepsilon\left(X_{in}\right) = \varepsilon\left(X_n\right)\sin\left(\varepsilon\left(\theta_n\right)\right) \tag{5.3.8}$$

Where:

$\varepsilon(X_{rn})$ is the error in the real part of the phasor computed at the n^{th} window.

$\varepsilon\left(X_{in}\right)$ is the error in the imaginary part of the phasor computed at the n^{th} window.

Thus, the TVE for the n^{th} data window can be computed using equation given as:

$$TVE(n) = \sqrt{\frac{\left[\varepsilon(X_{rn})\right]^2 + \left[\varepsilon(X_{in})\right]^2}{(X_m)^2}} \tag{5.3.9}$$

The above equation is used to compute the TVEs for the current phasors estimated for all sensors in cases of application of various frequency current and the performance is tested by comparison with the actual current and the CT output current phasors.

5.4 Sensor Performance at Various Low Frequencies

The asymmetrical fault currents in power systems are inclusive of decaying DC offsets that may saturate the conventional iron-core CTs resulting into inaccuracy in measurement. The currents of higher order harmonics generate heat and vibrations in the laminated core of the CTs affecting their performance and operational life. They also result in increased eddy currents adding to the deterioration of CT performance. Moreover, the harmonics affect the phasor measurement accuracy of systems that employ CTs as current transducers. To verify the behavior of TMR sensors in such cases, their performance was tested and compared with that of CT for low and high frequency input currents. Experimental data recorded for both low and high frequencies (1 Hz, 2 Hz, 5 Hz, 10 Hz, 60 Hz, 120 Hz, 180 Hz, 240 Hz and 300 Hz) input currents were used for this analysis. Real and imaginary parts of the current phasors were calculated by making use of the sampled data for both, the magnetic sensors, and CT, by applying the non-recursive DFT algorithm. The magnitude and phase angles were calculated from the estimated real and imaginary parts. The magnitude errors, phase angle errors and TVEs were calculated for both, the sensor output and CT output. The results are discussed in the following sections.

5.4.1 Response to Low Frequencies

The response of the sensor, S_2 and CT for an input current of 25 A of 60 Hz are shown in the Figure 5.4 (a) and (b). S_2 demonstrated lower magnitude error and a slightly higher phase angle error as compared to CT, even though, the error is very low (from -0.02^0 to 0.02^0). However, the average value of the angle error calculated in case of sensor S_2 was 0.0008^0 which is slightly higher as compared to that of the CT.

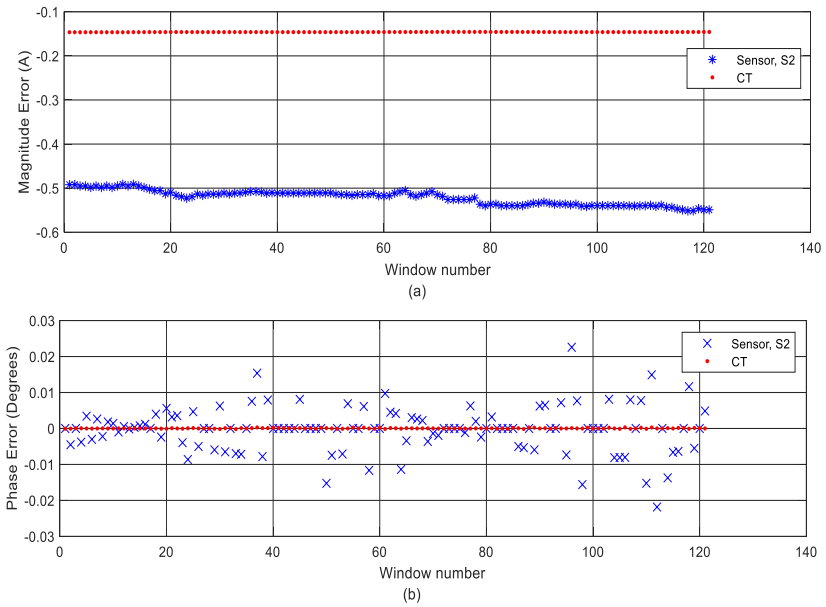

Figure 5.4 (a) Magnitude and (b) Phase angle errors for sensor S_2 and CT for an input current of 25 A at 60 Hz

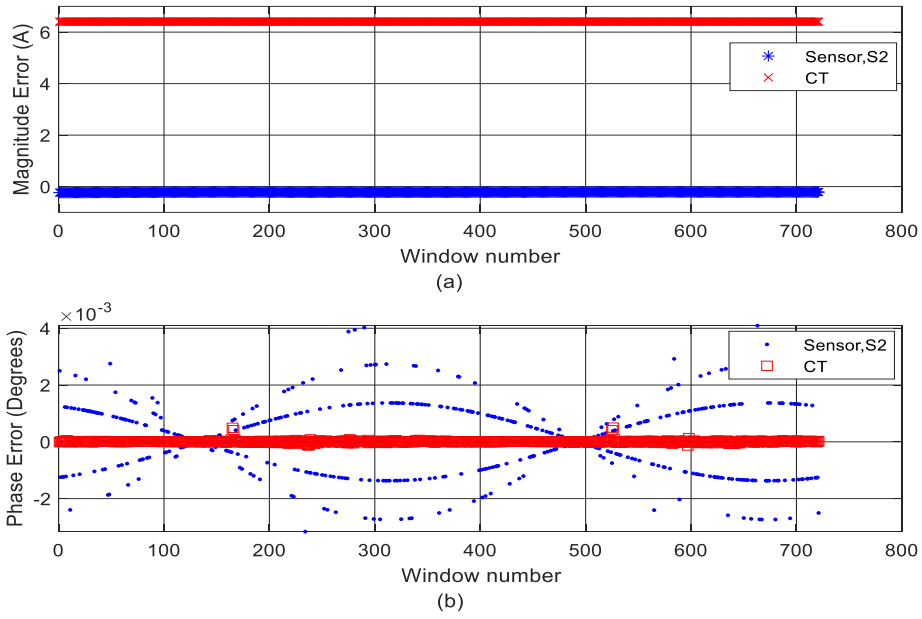

Figure 5.5 (a) Magnitude and (b) Phase angle errors for sensor S_2 and CT for an input current of 25 A at 10 Hz

To examine the effect of a low frequency current, the outputs of CT and sensors were estimated for lower frequencies from 10 Hz to 1 Hz and for currents from 5 A to 25 A. Figure 5.5(a) and Figure 5.5(b) illustrate the magnitude and phase angle errors for an input current of 25 A of 10 Hz respectively. The angle errors being very low for both CT and S_2, there is a significant fall in the performance of CT giving higher magnitude error of 6.4 A as compared to -0.22 A by the sensor S_2. Similar response is demonstrated by the CT for 20 A at the same frequency, 10 Hz and is shown in the Figure 5.6(a) and Figure 5.6(b) for both magnitude and angle respectively. In case of 20 A, the CT error is slightly low as compared to that for 25 A, and it is 2.3 A, whereas, for S_2, the error is varying from 0.012 A to 0.018A. The angle error is a little higher at 20 A for S_2 as compared to that at 25A with an increase of 0.0001^0 which is not a significant difference and can be seen in Figure 5.5(b) and Figure 5.6(b). The magnitude error of CT indicates saturation and is reflected on the magnitude waveform as shown in the Figure 5.7.

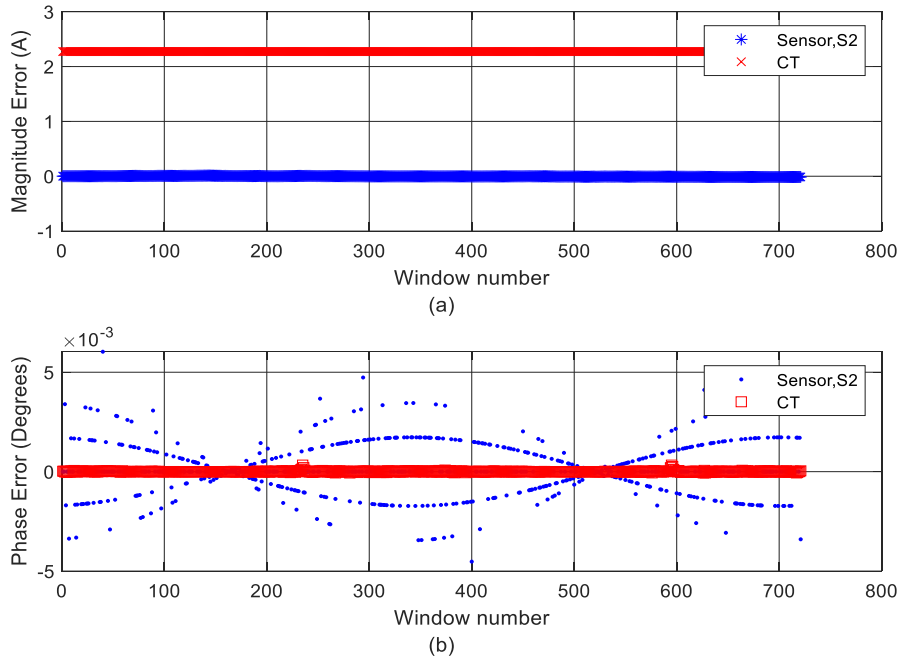

Figure 5.6 (a) Magnitude and (b) Phase angle errors for sensor S_2 and CT for an input current of 20 A at 10 Hz

It is evident that the sensor waveform is a pure sinusoid for an input current of 20 A at 10Hz, whereas, the CT has a distorted waveform showing clear indication of saturation.

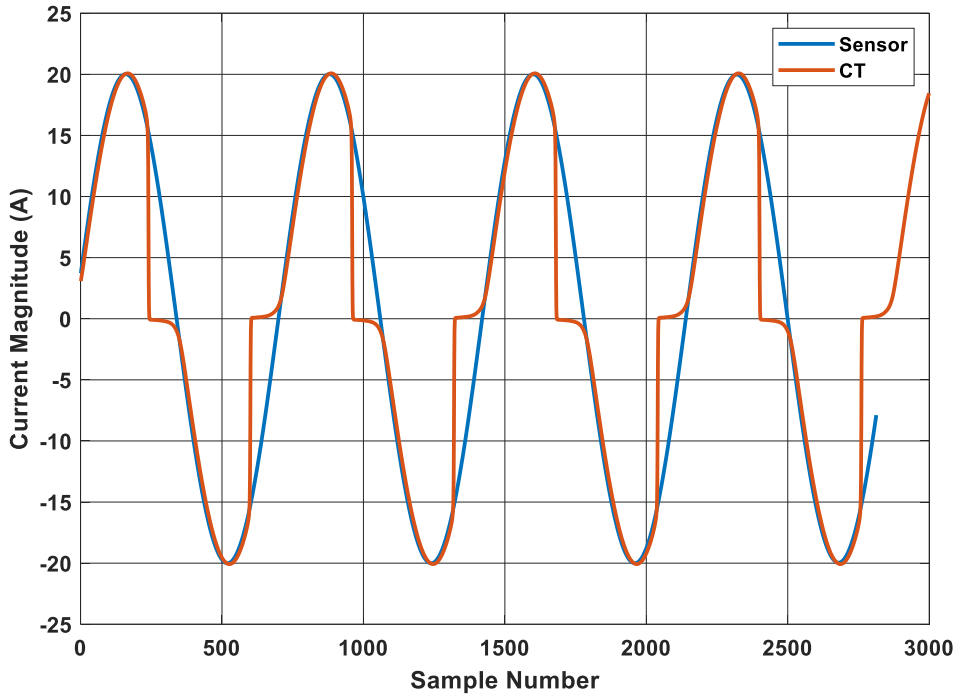

Figure 5.7 Magnitude errors for sensor S_2 and CT for an input current of 20 A at 10 Hz

Further decrease in the frequency and increasing current magnitudes resulted into higher magnitude errors for CT. It is evident from the magnitude errors demonstrated in Figure 5.6(a), distorted waveform of CT as shown in Figure 5.7 for 20 A of 10 Hz and, the magnitude error for 25 A of 5 Hz as demonstrated in Figure 5.8(a). There is an increase in the magnitude error from 0.37 A to 12.19 A for CT, whereas sensor S_2 demonstrated consistent performance with almost negligible error in the magnitude as well as phase angle error. The higher values of magnitude errors of CT imply output with more distortions and impure sinusoidal waveform.

To study the CT and sensor performance at lower magnitudes of currents of lower frequencies, their comparison was performed for 5 A at 5 Hz. Figure 5.8(a) and Figure 5.8(b) show the magnitude and angle errors for 5 A at 5 Hz. The magnitude errors remain

very low, almost close to zero for the CT and 0.31 A for the sensor S_2. Maximum value of the phase angle errors for 5 A at 5 Hz is 0.0073^0 and is shown in Figure 5.8(b).

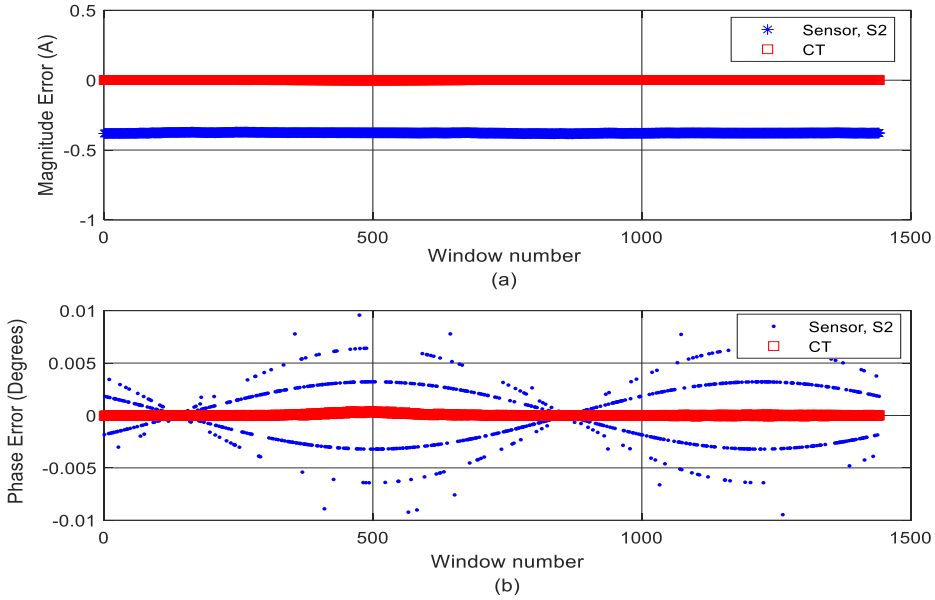

Figure 5.8(a) Magnitude and (b) Phase angle errors for sensor S_2 and CT for an input current of 5 A at 5 Hz

There is a major difference in the magnitude error for CT when the current is increased from 5 A to 25 A for 5 Hz. This is evident after comparison of the response of CT for 5 A and 15 A and by comparing the Figure 5.8 and Figure 5.9. The magnitude error of the CT suddenly increased from 0.01 A to 11.71 A when the current is increased from 5 A to 25 A at 5 Hz. The sensor showed a quite low variation from almost zero to 1.62 A in the magnitude error for the same set of values of input current as shown in Figure 5.9(a). The accuracy in angle calculation increased for S_2 from 0.0073^0 to 0.00014^0 maximum, and the average value of 0.00009^0 as shown in Figure 5.9(b), thus proving that the sensors perform better at lower frequencies as compared to the conventional CT.

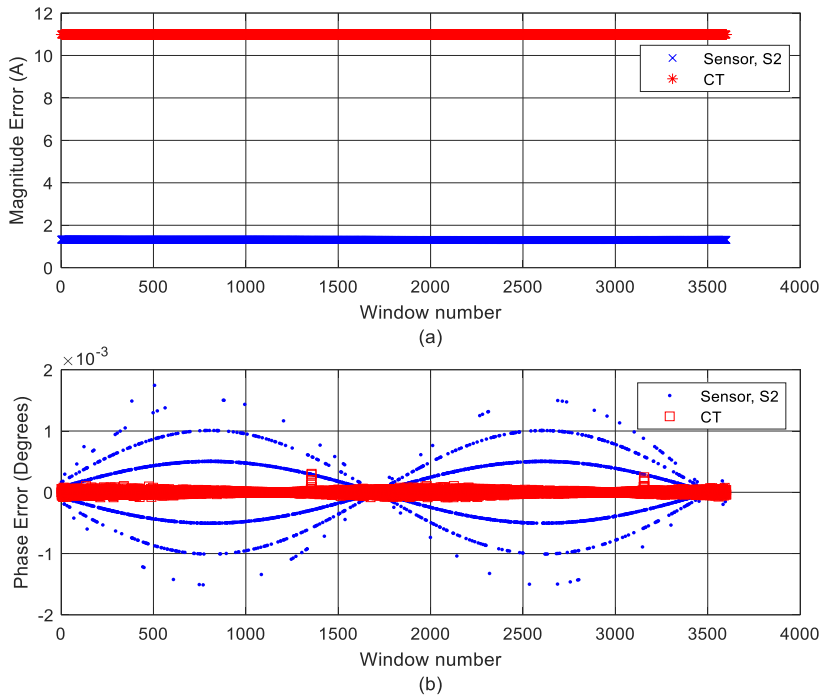

Figure 5.9 (a) Magnitude and (b) Phase angle errors for sensor S_2 and CT for an input current of 25 A, 5 Hz

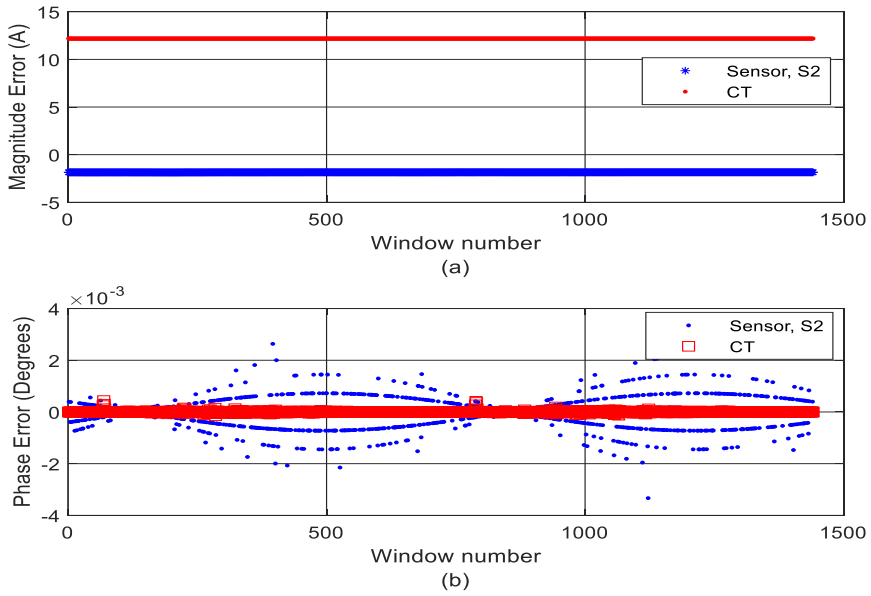

Figure 5.10 (a) Magnitude and (b) Phase angle errors for sensor S_2 and CT for an input current of 15 A, 2 Hz

Lowering the frequency deteriorated the performance of CT and it is evident from the

response of the CT at 2 Hz. The output of CT and S_2 for an input current of 15 A at 2 Hz demonstrated an error of 11.23% in the CT magnitude and 0.12 A for S_2 as shown in the Figure 5.10(a). The angle errors are very consistent for the CT and are in the range of 0.00009^0, whereas, the angle errors as shown in Figure 5.10(b), vary for S_2 and is in the range of 0.0001^0 to 0.0016^0. Considering the IEEE standard [80], these errors are well below the highest acceptable value.

When the current is increased from 15 A to 25 A, and frequency decreased from 5 Hz to 2 Hz respectively, it was observed that the magnitude error for CT increased to 13.7 A, whereas, for S_2 it was 1.16 A, and is shown in the Figure 5.9(a) and Figure 5.10(a).

With the increase in the current and reduction in the frequency from 2 Hz to 1 Hz, it is observed that the performance of the CT further deteriorated. The magnitude error further goes on increasing for CT and is observed to be as high as 19.38 A for 20 A current of frequency 1 Hz as evident from Figure 5.11(a) when compared to a 13.7 A error for 25 A at 2 Hz.

The estimated value of the sensor error is 1.67 A for the input current of 20 A at 1 Hz and shown in Figure 5.11(a) and this is very slight variation from 1.16 A for 25 A at 2 Hz. This verified that the CT response is poor for low frequencies as compared to that of TMR sensors. One more point noted for the CT is the phase angle error with a highest error value of 0.015^0 as compared to 0.00011^0 obtained for the sensor and is shown in Figure 5.11(b).

The TVEs are computed for the CT outputs and are compared with those of the sensor, S_2. The calculated % TVEs are plotted with the help of Box and Whisker plots as shown in the Figure 5.12. After comparing the errors shown in Figure 5.12(a) with those in Figure 5.12(b), it is observed that the sensor S_2 shows consistent performance with very low % TVEs as compared to that of the CT for all frequencies below 60 Hz. The highest average error for S_2 is observed to be 4.55% for currents at 1 Hz whereas for this same frequency the CT exhibit average error of 74.68%. The average error for S_2 at 2 Hz is 2.17% and for CT is 85.72%. At 5 Hz the average errors for 2.55% and 35.8% for S_2 and CT whereas at 10 Hz, these errors are 3.01% and 63.8% respectively proving that the CT has saturated at lower frequencies and is incapable for low frequency applications.

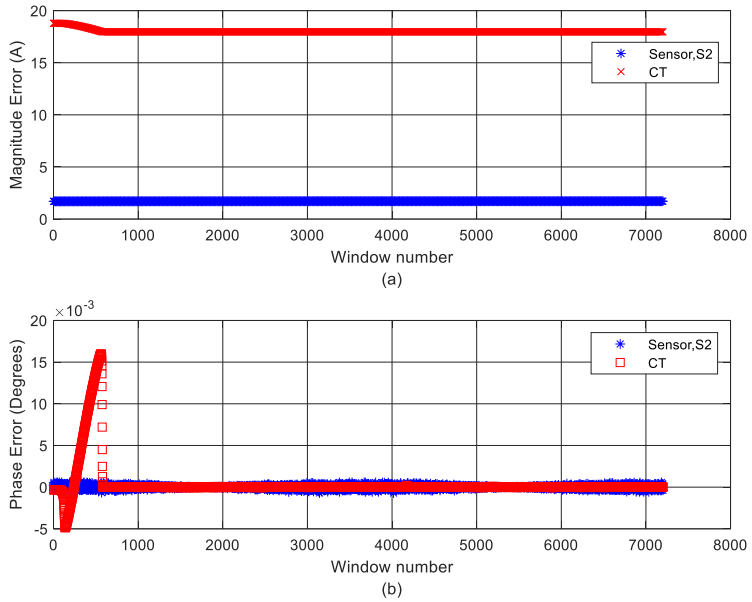

Figure 5.11 (a) Magnitude and (b) Phase angle errors for sensor S_2 and CT for an input current of 20 A at 1Hz

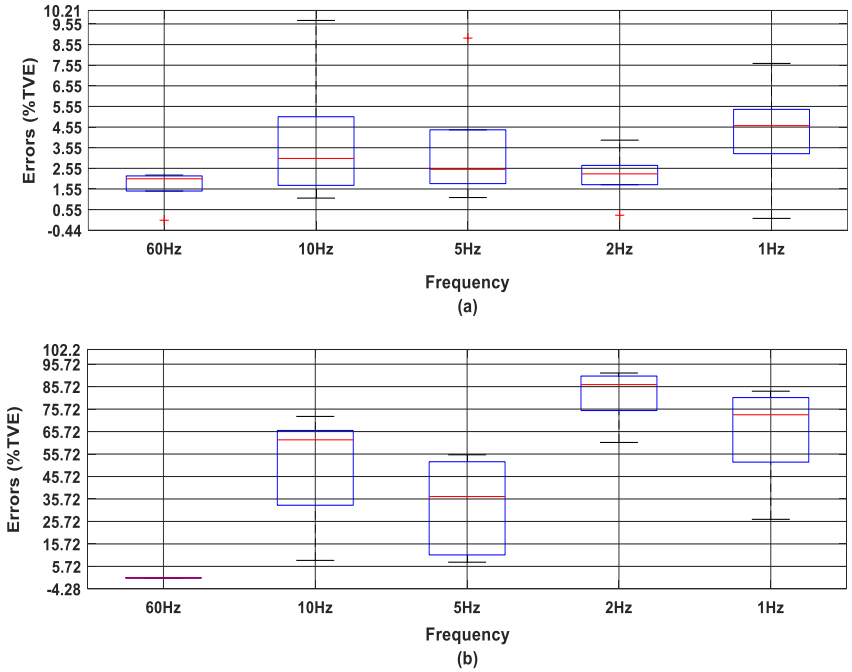

Figure 5.12 TVEs (%) for (a) Sensor S_2 and (b) CT for input currents from 5 A to 25 A of low frequencies

5.4.2 Response to Harmonic Frequencies:

The outputs for various currents at even and odd multiples of the fundamental frequency (up to 5th harmonic) were recorded for four sensors and a CT. TVEs were calculated for sensors output and the CT output. For comparison and analysis purpose, the results of the errors are shown in Figure 5.13 for sensor S_2 and CT. It is observed from Figure 5.13(b) that the TVE increases for the CT with the increase in the harmonic frequency and magnitude of the input current, whereas the errors are consistently below 1% for all harmonics for the sensor S_2 as shown in Figure 5.13(a).

The CTs show good performance at 60 Hz with the average value of total vector errors below 0.05%. However, the average value of the error is gradually increasing with the increase in the harmonic from 1st to 5th and is evident from the Figure 5.12(b), whereas for sensor, there is a consistent performance with average value varying from 0.29% to 0.44% for currents of all harmonics chosen for the experiment.

The increase in harmonics creates eddy currents and, consequently, heats the in the conventional CT, whereas the sensors are immune to such heating because of the lack of any winding and resulting inductance.

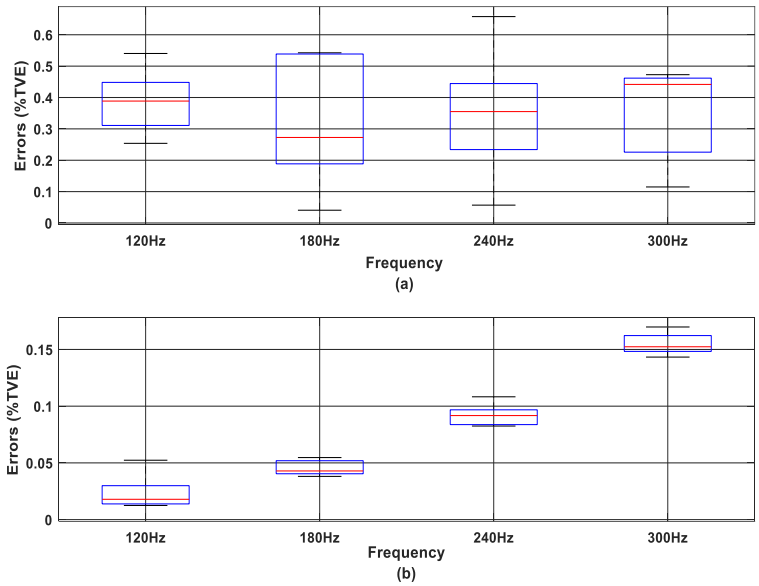

Figure 5.13 TVEs (%) for (a) Sensor S_2 and (b) CT for input currents from 5 A to 25 A of higher orders of frequencies, 120 Hz to 300 Hz

5.5 Duplicate Sensors and Sensor Fusion

As demonstrated earlier, a single magnetic sensor can be sufficient for measurement of currents. However, to achieve the enhanced measurement accuracy and reliability for critical systems, such as protection relays, duplicate current measurement systems may be used. In this section, application of duplicate magnetic sensors and their impact on the performance is examined. The sensor fusion is achieved by combining their outputs by employing sensor data fusion technique. There are various studies reported in the past where, multiple sensors were deployed for measuring a particular parameter [84-86]. Based on the scatter in the estimated parameters and, their dependence on various other supporting conditions during measurement such as, noise etc., multi-variable decision-making criteria or data fusion techniques were applied to improve the measurement accuracy [87, 88]. In this research a variance-based weighting factor calculation technique is utilized for improvement of the accuracy in measurement.

The investigation showed that the estimated polar components obtained by applying DFT technique led to higher accuracy in phase angle estimation compared to that of magnitude. This was consistently evident for all low frequencies under study and, is shown in the Figure 5.5 to Figure 5.11. Therefore, only the estimated magnitudes from the test results with input current of 60 Hz were selected for the application of the variance-based weighted fusion algorithm. The selection of the pair-combinations for four sensors led to six alternatives, $A = \{S_1S_2, S_1S_3, S_1S_4, S_2S_3, S_2S_4, S_3S_4\}$. The variance in the scatter for the computed current magnitudes at 60Hz for all sensors is estimated as

$$\sigma_n = \left[\frac{\sum_{k=1}^{N} I_{pk}^2 - \frac{\left(\sum_{k=1}^{N} I_{pk}\right)^2}{N}}{N} \right]_n \quad \forall n \tag{5.5.1}$$

The variable N represents the total number of the current magnitudes of the estimated values of current, I_{pk} is the estimated peak value of current, and n denotes the sensor

number. Thus, for n sensors, the variances are $\sigma_1, \sigma_2, \sigma_3 ..... \sigma_n$ and n is equal to 4 in this study. Individual weighting factors, (w_{Si} and w_{Sj}) for sensors i and j, respectively are estimated from the variances obtained using Equation (5.5.1) above. The weighting factors for each combination of two sensors are:

$$\begin{bmatrix} \omega_{Si} & \omega_{Sj} \end{bmatrix}_A = \begin{bmatrix} \dfrac{\sigma_j^2}{\left(\sigma_i^2 + \sigma_j^2\right)} & \dfrac{\sigma_k^2}{\left(\sigma_i^2 + \sigma_j^2\right)} \end{bmatrix}_A \quad \forall A \tag{5.5.2}$$

The weighting factors thus estimated are then used to fuse the outputs of two sensors, a and b, to estimate the adjusted real and imaginary parts as:

$$\begin{aligned} \bar{X}_r(n)\big|_A &= \omega_a \hat{X}_{ra}(n) + \omega_b \hat{X}_{rb}(n)\big|_{n=1,2,...N} \\ \bar{X}_i(n)\big|_A &= \omega_a \hat{X}_{ia}(n) + \omega_b \hat{X}_{ib}(n)\big|_{n=1,2,...N} \end{aligned} \tag{5.5.3}$$

where, the subscript r denotes the real part and i denotes the imaginary part of the vector quantity, whereas a and b denote the respective sensor number in the particular combination, A. The set of variables $\varepsilon\left(\hat{X}_{ra}(n)\right), \varepsilon\left(\hat{X}_{ia}(n)\right), \varepsilon\left(\hat{X}_{rb}(n)\right)$, and $\varepsilon\left(\hat{X}_{ib}(n)\right)$ are computed by using Equation (5.2.7) and Equation (5.2.8). To estimate the resultant variables as shown in Equation (5.5.2), similar procedure is followed as that for the individual sensor's TVE calculation, with only exception, that here the real and imaginary parts are combined after multiplying by respective weighting factors. The final equation for computation of TVE in this case is the same as Equation (5.2.8) with a change of replacing the variables by those shown in Equation (5.5.3). TVE is estimated for each of the input currents of different frequencies utilizing the six combinations as:

$$TVE(n)\big|_{A,f} = \sqrt{\frac{\left(\left(\bar{X}_r(n)\big|_{A,f}\right)^2 + \left(\left(\bar{X}_i(n)\big|_{A,f}\right)^2\right.}{\left(X_{m,f}\right)^2}} \tag{5.5.4}$$

where: f represents the input signal frequency, $X_{m,f}$ is the magnitude of the input signal.

The results of TVE obtained for a set of input currents of 1 Hz for two sensor-pair combinations are shown in the Table 5.3. After comparing the performance of all pairs at this frequency, it was observed that the maximum error for 25 A was demonstrated by the pair S_3S_4 and is 1.738% and the minimum error of 1.095% was demonstrated by the pair S_1S_2. It is evident from this table that the sensor pair S_1S_4 demonstrated highest errors as compared to the rest of the combinations for all currents of 1 Hz. Among all combinations, the minimum %TVE is observed to be 0.230% by the pair S_1S_2 for 5A and the maximum error of 1.901% by the pair S_2S_4 for 5 A.

The sensor combination S_1S_4 gave consistently highest errors for all currents at 5 Hz as well as at 10 Hz and can be seen in Table 5.4 and Table 5.5. The exception of this pair for 25 A at 5 Hz is the pair S_3S_4 which yields slightly higher value. The lowest error for 5 A was demonstrated by the pair S_2S_3 with 0.054% and the maximum error of 1.838% was exhibited by sensor pair S_2S_4 for 25 A at 5 Hz. For 10 Hz, the sensor combination S_2S_4 gave maximum value of 1.925% at 25 A, and the sensor combination S_2S_3 gave 0.189% at 5 A.

Table 5.3 Percentage TVE for input current of 1 Hz frequency, all sensor combinations

Current magnitude (A)	**%TVE for S_1S_2**	**%TVE for S_1S_3**	**%TVE for S_1S_4**	**%TVE for S_2S_3**	**%TVE for S_2S_4**	**%TVE for S_3S_4**
5A	0.230	0.814	1.413	0.349	1.901	0.727
10A	0.631	1.298	1.729	0.936	1.663	1.337
15A	0.925	1.370	1.712	1.133	1.649	1.506
20A	1.093	1.461	1.612	1.341	1.617	1.693
25A	1.095	1.482	1.701	1.370	1.643	1.738

The lowest errors overall were observed for the sensor pair S_2S_3 for the test currents of all frequencies.

Following similar procedure, the TVEs were calculated for the CT output and are shown in the Table 5.6. It is clear from the results furnished in Tables 5.3 to 5.5 that the TVEs for two sensor combinations are well within 2% even for input signals of low frequencies. In contrary is the case for CT because it saturates during low frequency input currents and its output is distorted. It can be seen from Table 5.6 that the CT exhibit large %TVEs for 1 Hz, to 5 Hz. The errors at 10 Hz range from 0.271% to a highest TVE of 25.714% for various input currents. The errors increase with the increase in the current and is evident from the Table 5.6.

Table 5.4 Percentage TVE for input current of 5 Hz frequency, all sensor combinations

Current magnitude (A)	**%TVE for S_1S_2**	**%TVE for S_1S_3**	**%TVE for S_1S_4**	**%TVE for S_2S_3**	**%TVE for S_2S_4**	**%TVE for S_3S_4**
5A	0.991	0.704	1.473	0.054	0.944	0.430
10A	1.205	1.083	1.657	0.583	1.165	0.964
15A	1.149	1.098	1.531	0.807	1.698	1.150
20A	1.203	1.255	1.582	1.044	1.759	1.403
25A	1.217	1.277	1.573	1.102	1.838	1.444

Table 5.5 Percentage TVE for input current of 10 Hz frequency, all sensor combinations

Current magnitude (A)	%TVE for S_1S_2	%TVE for S_1S_3	%TVE for S_1S_4	%TVE for S_2S_3	%TVE for S_2S_4	%TVE for S_3S_4
5A	1.883	0.871	1.671	0.189	1.084	0.576
10A	0.839	0.902	1.311	0.571	1.121	0.952
15A	0.924	1.004	1.409	0.685	1.268	1.057
20A	1.761	1.050	1.371	1.022	0.260	1.381
25A	1.109	1.177	1.477	1.029	1.925	1.346

Table 5.6 Percentage TVE for CT Output for Low Frequencies

Current magnitude (A)	%TVE for 1Hz input	%TVE for 2Hz input	%TVE for 5Hz input	%TVE for 10Hz input
5A	60.94	26.78	0.48	0.271
10A	79.85	60.67	11.97	2.163
15A	86.43	73.25	36.79	10.113
20A	89.82	79.94	51.25	11.503
25A	89.76	79.74	60.40	25.714

5.6 Summary

The investigation results reported in this chapter provide satisfactory a firm basis for using TMR sensors for AC current measurement for protection and control of power systems. The sensors showed a better performance as compared to the conventional CTs in estimating the AC current phasors of various frequencies. The sensors were calibrated by

determining the average Multiplying Factors (MFs) which are applicable to estimate current phasors of any frequency. The comparison of the output of TMR sensors with that of the conventional CT for low frequency currents proved that these sensors can be very effective and accurate for measuring the asymmetrical fault currents that have inherent components of low frequency. The CT exhibited high values of TVE for measuring the low frequency current whereas the TMR sensors exhibit very low errors of less than 2%. For the application of protection relaying, A limit of 10 percent is defined in the IEEE Standard [12] for the ratio error for a steady-state, symmetrical secondary current that has no DC-offset equal to 20 times rated secondary current at the standard burden. In contrary, the TMR sensors demonstrated a consistently low %TVE below 2%, and thus qualify for application of current sensing in protective relaying and control in power systems.

The combination of multiple sensors with weighting factors based on the variance of estimated current magnitudes of 60 Hz improved the measurement accuracy of the sensor pairs for all low frequencies. The phasor estimation for currents at 60 Hz as well as for lower and high frequencies can be successfully achieved using individual TMR sensors and, the fusion technique by using multiple sensor combinations. This method is very effective compared to a CT to measure the fault currents, especially when there is a presence of decaying dc component which is made up of low frequencies.

The calibrated sensors can be applied for sensing AC currents. The sensor data fusion technique by choosing the best sensor combinations can yield enhanced performance of the sensors with improved accuracy with %TVE errors well below 2% as compared to those of the CT. This technique is further applied in the study of three-phase current measurement in case of three-phase overhead lines with triangular as well as horizontal structures and, the details of the analysis and results are presented in the proceeding chapters.

Chapter 6. Estimation of Three-phase Current Phasors

6.1 Introduction

The knowledge of three-phase currents with a time stamp can be of great advantage, especially when it is applicable to decision making process such as, real time load flow control, switching, and load transfer among feeders in power systems network. For such applications, the currents are usually measured using the conventional CTs. However, their installation at multiple locations in the distribution or transmission grid and, their maintenance incurs a huge capital cost. Therefore, this method is not exercised by power distribution or transmission utilities. Given an alternative of contactless current sensors, this can be achieved with less hassles and achieve considerable savings, because these sensors have minimal power supply needs and have advantage of easy installation and less maintenance. Therefore, it is important to explore their applicability and performance in measuring currents of three-phase ac power systems.

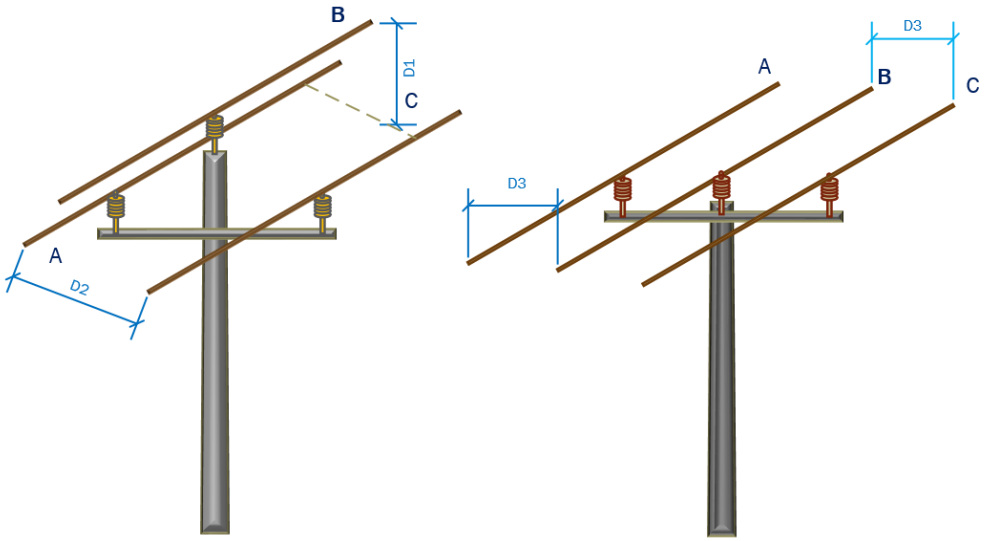

Figure 6.1 Clearances between three-phase overhead conductors for (a) Triangular (b) Horizontal arrangements

In this chapter, the contactless sensors are applied to two types of three-phase structures that are commonly adopted for AC power distribution grids in Canada [59]. These types

are, a) Triangular and b) Horizontal. In type (a), the phase-B is at the vertex of the triangle and the other two phases are in the horizontal plane, equidistant from each other as well as at the height, D_1 = 98 cm from the top conductor and the distance between phase-A and phase-B is D_2 = 113 cm as shown in the Figure 6.1(a). In the horizontal type of structure, all phases are in the horizontal plane with phase-B placed at an equal distance of D_3 = 56.5cm from phase-A and phase-C as shown in the Figure 6.1(b). These distances are also called as clearances and, are followed using the USF standard applicable in the province of Ontario in Canada.

The following sections provide detail information of the experimental setup, the measurements and analysis with individual type of structures and, a comparison of the performance between the two types of overhead conductor arrangements.

6.2 Experimental Setup for Three-Phase Current Measurement using TMR Sensors

A three-phase circuit resistive circuit is designed for this experiment with a provision of three sensors to measuring current of each phase as shown in the Figure 6.2. The equipment utilized for this experiment is from the single-phase experiment with an additional equipment for other two phases. The resistive load is connected in Star-type (Y-type). An insulated aluminum conductor of AWG#4 size with an ampacity of 95 A is deployed for each phase [89]. This type of conductor is commonly deployed in the medium voltage distribution circuit for single-phase power supply in a subdivision [59]. These three conductors are installed on a wood table in the laboratory as shown in the Figure 6.3. The conductors are connected to a resistive load of 1kW for each phase. The other ends of the resistors are connected to one common point, also called neutral point using wires of size, AWG#10. Two-hole Burndy connector lugs and ring type nuts are used to fasten all connection points of wires in the circuit. All connection points are masked with electric tape for safety. Multiple sensors are assigned for each phase. Their number varied from three to four per phase. These sensors are placed on one common side of each phase conductor with the help of wood stands as shown in the Figure 6.3. Three phase conductors are installed at the appropriate height and clearance distances as referred from Figure 6.1(a) and (b) for this experiment. Multi-stranded wires of size AWG#22 with 17 strands are used for connecting the DC power supply to the sensors as well as connect the sensor outputs to

the data acquisition system. NI-9174 DAQ system is used for data acquisition with nine individual channels for TMR sensors outputs and, four channels for four conventional CTs with three CTs for three phases and one for recording the neutral current. The assembly of the sensors per phase is placed on a firm horizontal platform supported by wood stands as shown in the Figure 6.3. Omicron CMC356 current injection test set is used for injecting three-phase currents in the circuit. Three-phases of the circuit are connected to the respective phase output of the test set and the neutral of the circuit is connected to the neutral of the test set with the help of AWG#10 connector wires. For injecting currents of higher magnitude, the test is configured with six current inputs to provide three-phase currents with two leads per phase as per the instructions given in the test set manual.

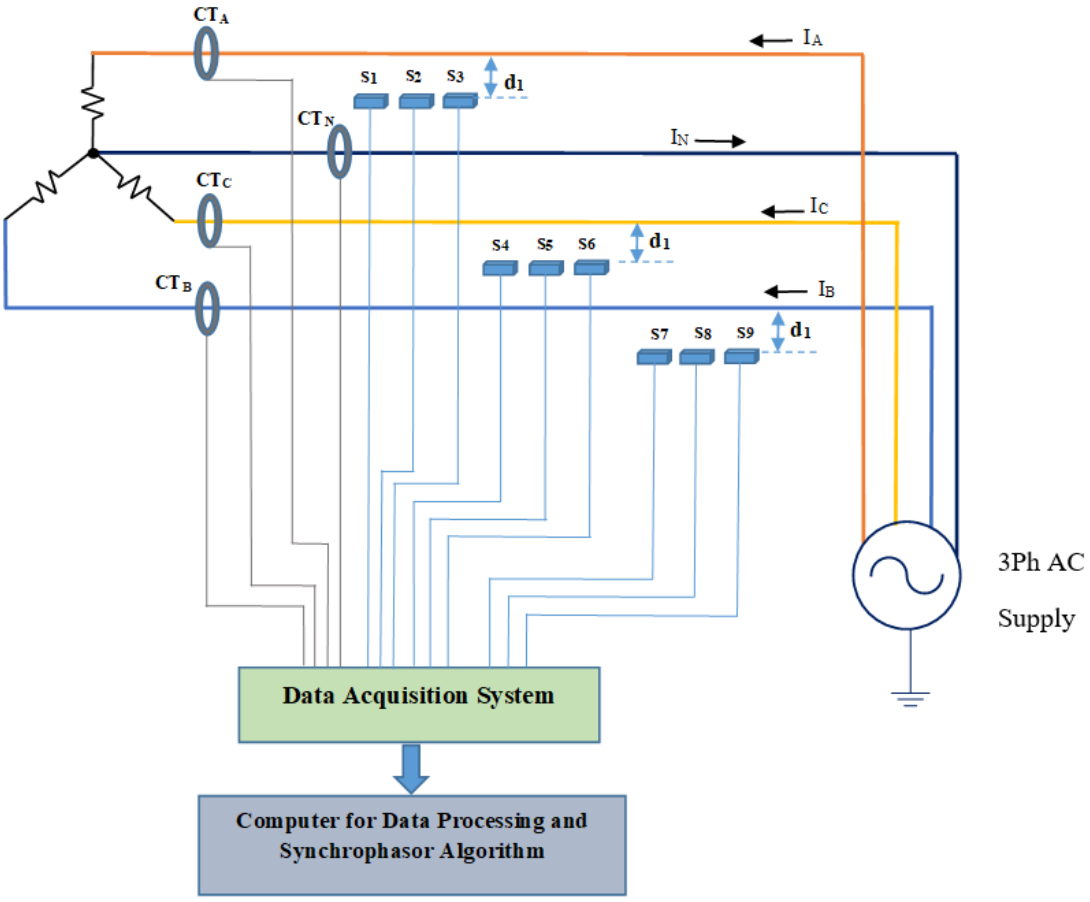

Figure 6.2 Architecture diagram for three-phase current measurement

The three-phase current with varying magnitude injected in the circuit for measurements is referred as “source current” in this and the proceeding sections for ease of description. Standard safety procedures were followed during the installation and connections of the circuit components as well as during injection of three-phase currents and performing the measurements. All connecting points from test set to the circuit were covered with electrical insulation tape to avoid any hazard while injecting currents through the circuit. The test set was grounded to the main circuit using the manufacturer’s standard ampacity leads. Tripping hazards were avoided by strapping the wires to the experiment table and covering them with the wire-covers on the floor. Individual phase conductors were fastened to the wood structures with the help of insulated straps to avoid falling hazard. Customized wood stands with firm supporting bases were prepared for holding the sensor placing plate to avoid the tipping hazard as shown in the Figure 6.3. The set of wires connected to multiple sensors per phase were bunched together and strapped using tie wraps. Each wire was tagged with appropriate labels indicating the sensor names and its purpose at source and destination.

The initial process of the experiment involved steps such as, verification of the connections, safety check, verification of the correct DC power supply of 5.5 VDC to the sensors and, AC power supply to the data acquisition system and to the Omicron test set. A multi-meter is used to check the voltages at each supply point to the set of sensors deployed per phase. Thirteen channels of the data acquisition system were programmed using the DAQ-Exp software to monitor and record output signals from each sensor. The sampling rate of every channel was set to 7.2 kHz to measure 120 samples per cycle for a 60 Hz source current in one second. The voltage range of the data acquisition system was fixed to +/- 10 VDC. The connections and the signal recording function was checked and verified for every channel of data acquisition system. The system thus, was prepared for the measurement for each value of source current.

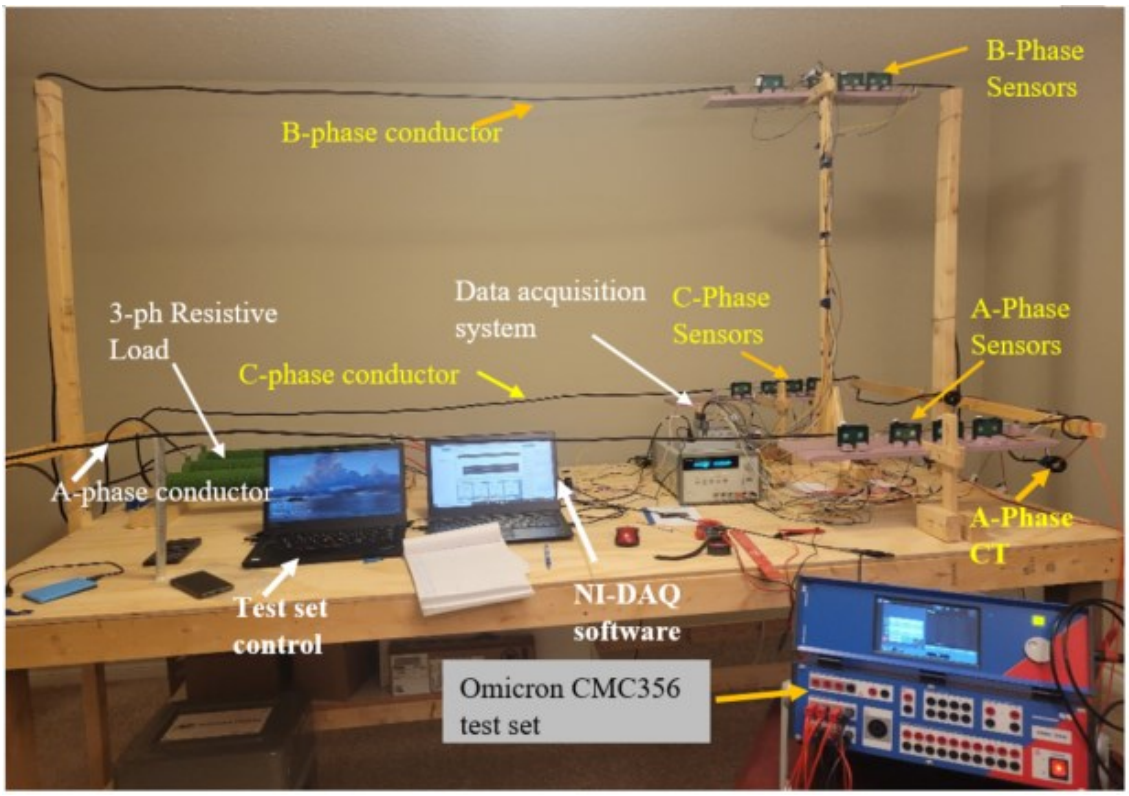

Figure 6.3 Experimental setup for three-phase triangular structure

The main objective of the experiment was to estimate three-phase current phasors by measuring the magnetic field using TMR sensors. The sensors were calibrated from the single-phase experiment and have shown successful performance for low and high frequency source currents. Therefore, their performance with respect to the change in distance and magnitude of source currents needed to be evaluated for a three-phase circuit of two different types of overhead structures. Therefore, the tests and measurement procedure were divided into two parts, first, for the triangular structure setup, and the second, for the horizontal structure setup. The test procedures were designed for each structure with focus on the following objectives:

1) Measurement of magnetic fields when the sensors are placed at various distances from the current carrying conductors of each phase.
2) Measurement of magnetic fields for various magnitudes of balanced three-phase source current of frequency 60 Hz.

3) Measurement of outputs of multiple sensors per phase in stages from one sensor per phase to three sensors per phase.

Tests were carried out with multiple magnitudes of three-phase source currents injected in the circuit when sensors were placed at a particular distance from each phase conductor, and then, repeated for other distances. In this experiment the distances decided were 7 mm, 15 mm, 25 mm, and 35 mm. Therefore, there are four stages of test and measurement for each type of structure. Moreover, these stages were repeated for the arrangement of one sensor, two sensors and three sensors per phase.

Initially, the triangular structure was chosen with one sensor per phase. For the first stage, the sensors were kept at d_1 = 7mm from their respective phase conductor. In this experiment, the insulation on each phase was removed to simulate a bare conductor condition termed as *No Insulation* (*NI*) in previous chapters. Three-phase balanced currents with a constant phase difference of 120^0 were injected in the circuit with a starting current of 1 A for 5 seconds. The outputs of all sensors and CTs were recorded for 4 seconds. The source current was then increased in steps of 1 A up to 15 A and the outputs of each sensor and CT were recorded simultaneously for 4 seconds. Each sample recorded in the data acquisition system had a timestamp and is used to estimate the current phasors. Once the recording was complete for 15 A, the distance of each sensor from respective phase conductor was changed from 7 mm to 15 mm and the steps defined for the first stage were repeated. This procedure was repeated for the distances of sensors at 25 mm and 35 mm from the phase conductors and their output were recorded. Once all four stages are complete, the experiment was repeated for two-sensors per phase and three-sensors per phase and all recorded outputs were stored in Microsoft Excel database.

The structure of three-phase conductors was then changed to horizontal type by maintaining standard distances between each phase and, the tests were carried out with one-sensor, two-sensor, and three-sensors per phase. The procedures for injecting source currents and the distance combinations were followed like that of the triangular structure and the outputs of all sensors were recorded in the same manner for all distances and sensor combinations. After recording the data for all measurements, further process involved development of a computational program consisting of application of DFT method and an

algorithm for estimation of current phasors for each sensor for individual phases. The last stages of this computations program were to estimate the Total Vector Errors (TVE) for each current phasor by comparing them with the source currents. In addition, this algorithm was used for comparing the performance of the measured outputs of CT with sensors in terms of TVE. The steps involved in the computational program are explained in the flowchart shown in Figure 6.4. The following sections present the performance analysis for sensors and CTs.

6.3 Results and Performance Analysis of TMR Sensors for Three-Phase Triangular Structure

The experimental setup for the triangular type of structure and sensors arrangement is shown in the Figure 6.3. It shows an additional fourth sensor for each phase which is kept as a backup but was never used in the experiment while recording the output data. The outputs of sensors recorded for 1 A to 15 A three-phase balanced source currents for one-, two- and three-sensors per phase were stored separately in 45 individual data files for each distance resulting in total 180 measurement data files for the triangular arrangement. The recording was performed at a sampling rate of 120 cycles per cycle for a 60 Hz input current for each phase. Thus, for one cycle, the time per sample per second was 16.66 milliseconds and such 120 samples were recorded for one second. Therefore, the outputs of every sensor were in terms of a sample per 16.6 millisecond and, 9800 samples were used for the DFT and the phasor estimation algorithm. The algorithm also computed the %TVE from the estimated phasors of each sensor as per the steps mentioned in the flowchart and shown in the Figure 6.4.

The algorithm computes the TVE for each cycle of 120 samples by comparing it with the source current. In order to estimate the magnitude error, the algorithm is designed to utilize 600 windows of the output data, with one window of 120 samples and, incrementing it with one sample in each iteration. Similar steps were applied for estimation of the error in phase angle for all sensors by comparing their output with respective source current value of individual balanced phase angles. The results were obtained for all distances and, for increasing order of the number of sensors per phase utilized for each distance from the source current and are presented in the following sections.

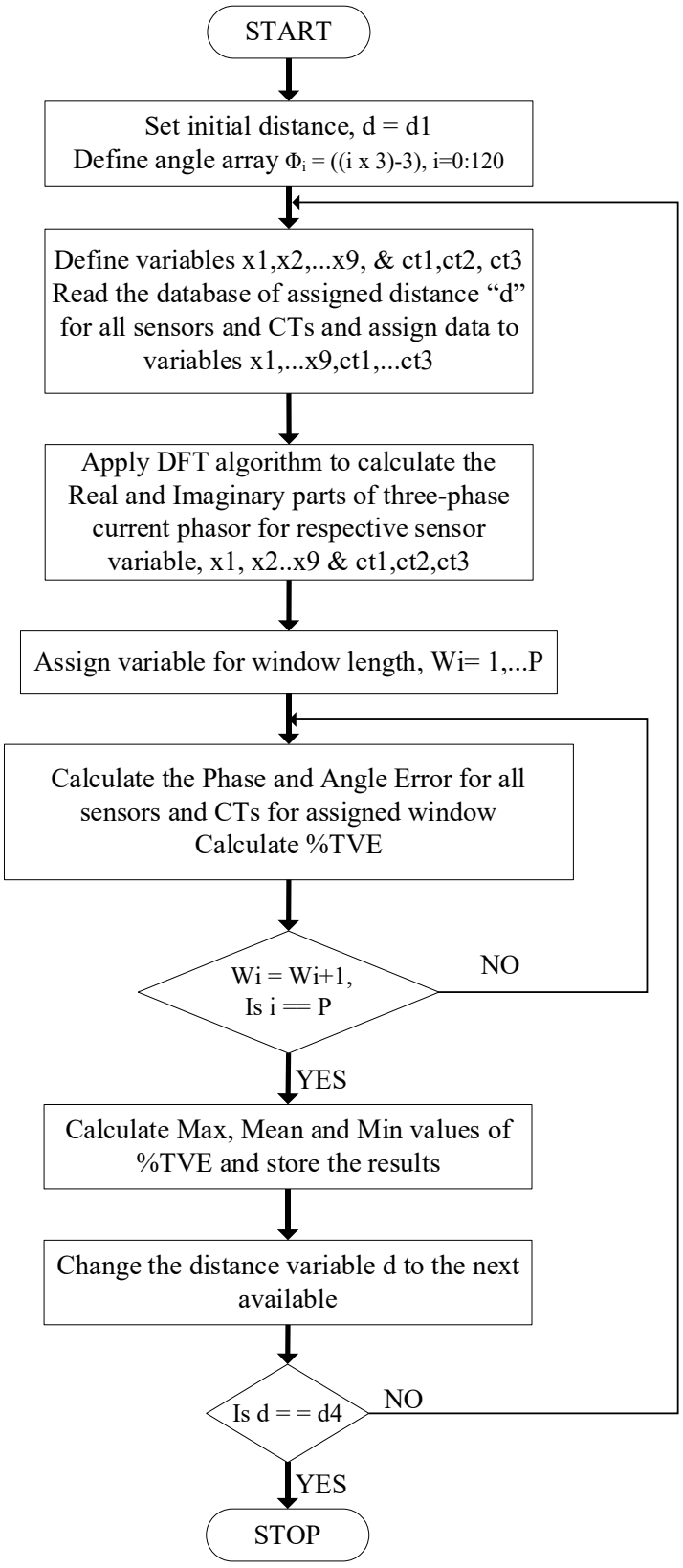

Figure 6.4 Flowchart for three-phase current phasors calculation

6.3.1 Results of One Sensor per Phase at Various Distances

Every sensor deployed in this experiment is tested for its performance using the average MF to obtain the current output with good accuracy and it is verified during the single-phase experiment. Therefore, the algorithm for calculation of three-phase current phasors utilized the average MF. The sensors are numbered as S_1, S_5 and S_9 for A-phase, B-phase and C-phase respectively. The real part and the imaginary part of the output current phasors of 5 A obtained for these three sensors are shown in the Figure 6.5 for the case when the sensors were placed at 7 mm distance from the respective phase conductor. The output of each sensor is shown for one cycle of 120 samples. The error in the magnitude of the estimated phasors for sensor S_1 for A-phase current is observed to vary from -0.023 A to 0.018 A for 600 windows. For sensor S_5 the magnitude error in the estimated current phasor for B-phase is varying from -0.001 A to -0.03 A indicating that the estimated current phasor has higher magnitude than the input current. The sensor for C-phase, i.e., S_9 has the magnitude error in the range of 0.01 A to 0.032 A. The phase angle error in the estimated current phasors of all three sensors were very low ranging from 0.0001^0 to 0.00009^0, thus showing a good performance for 5 A. The errors in magnitude for all three sensors are shown in Figure 6.6 (a) and the errors in angle are shown in Figure 6.7 (a) whereas, the respective errors for three single-phase CTs are shown in Figure 6.6 (b) and Figure 6.7 (b). These figures indicate that CTs provide less variation in their performance for magnitude as well as angle when compared with the input current of each phase.

The output of three sensors when compared with input current of 15 A at 60 Hz show better performance as compared to that of 5 A with average values of TVE of 0.085%, 0.487% and 0.134% for S_1, S_5 and S_9 respectively. The rectangular components of the estimated current phasors for each sensor are shown in the Figure 6.8. Similarly, the errors in estimating the magnitude for each sample for the 15 A current for these three sensors are shown in the Figure 6.9 (a) with average variation of 0.013 A for S_1, 0.022A for S_5 and 0.020 A for S_9 respectively. Similarly, in this case the CTs show -0.045 A for A-phase CT, -0.058 A for B-phase CT, and -0.087A for C-phase CT. The angle errors for the same current were observed to be 0.0001^0, 0.00013^0, and 0.00014^0 for S_1, S_5 and S_9 and are

shown in the Figure 6.10 (a). The angle errors of CTs are shown in the Figure 6.9(b) indicating smaller errors than all sensors.

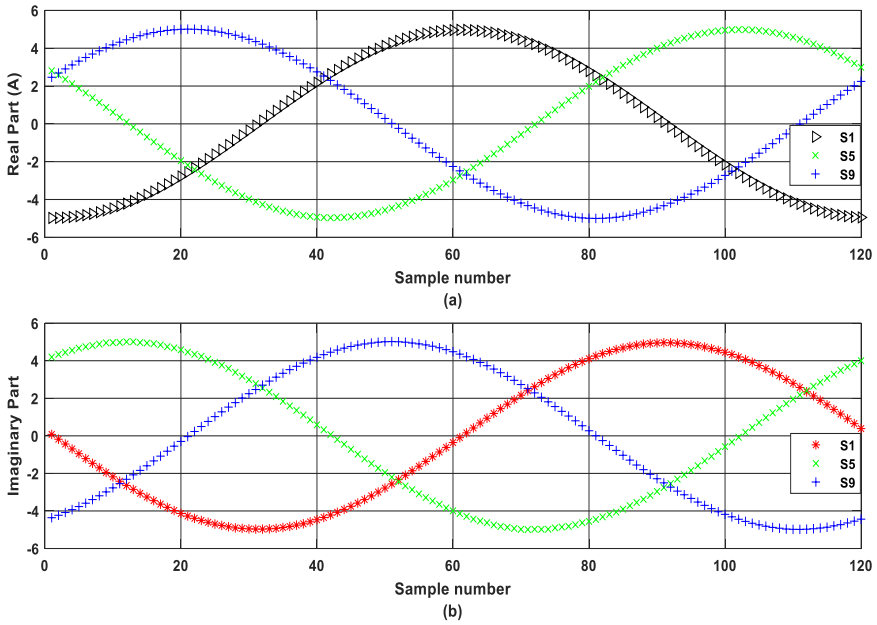

Figure 6.5 Estimated output of sensors S_1, S_5 and S_9 placed at 7 mm distance in triangular structure (a) Real part and (b) Imaginary part for 5 A

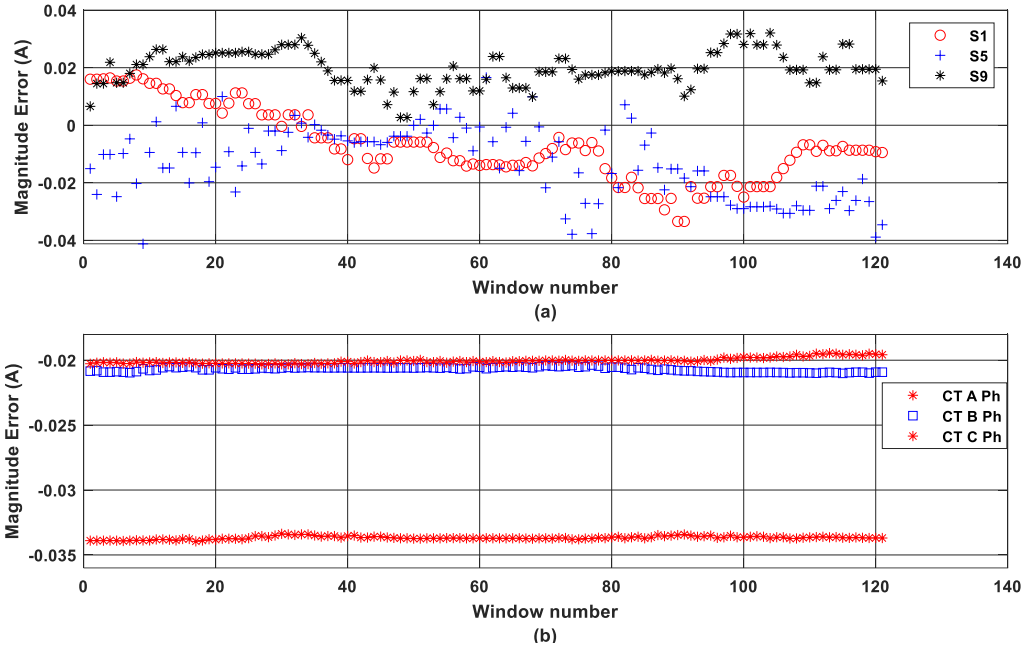

Figure 6.6 Magnitude errors in estimated phasors of 5 A for (a) One sensor per phase at 7 mm and (b) Three phase CTs in triangular structure

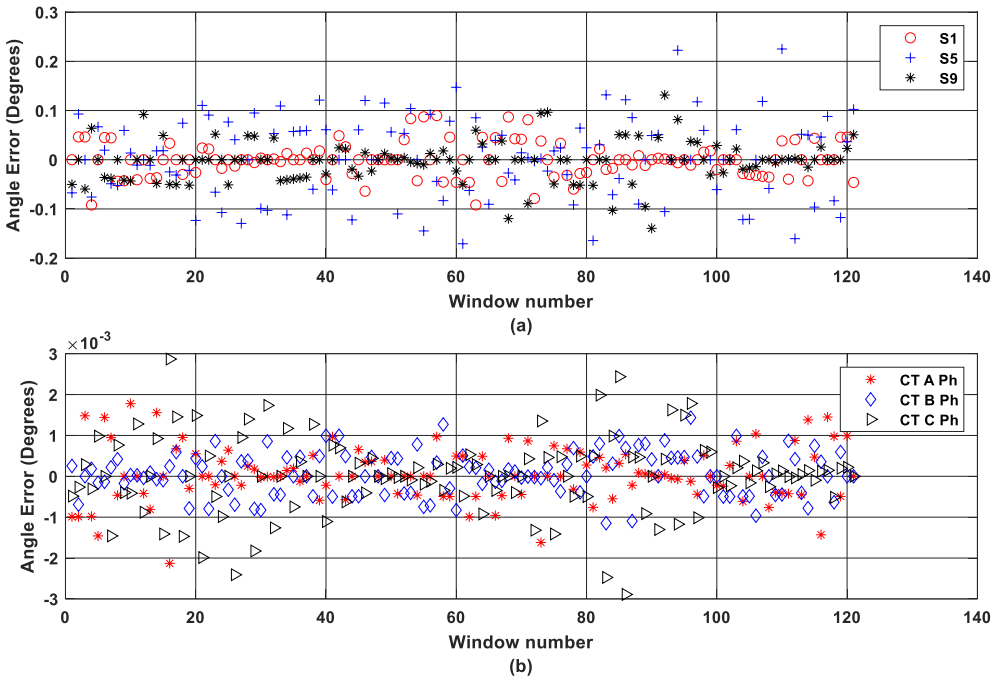

Figure 6.7 Angle errors in estimated phasors of 5 A for (a) One sensor per phase at 7 mm and (b) Three phase CTs in triangular structure

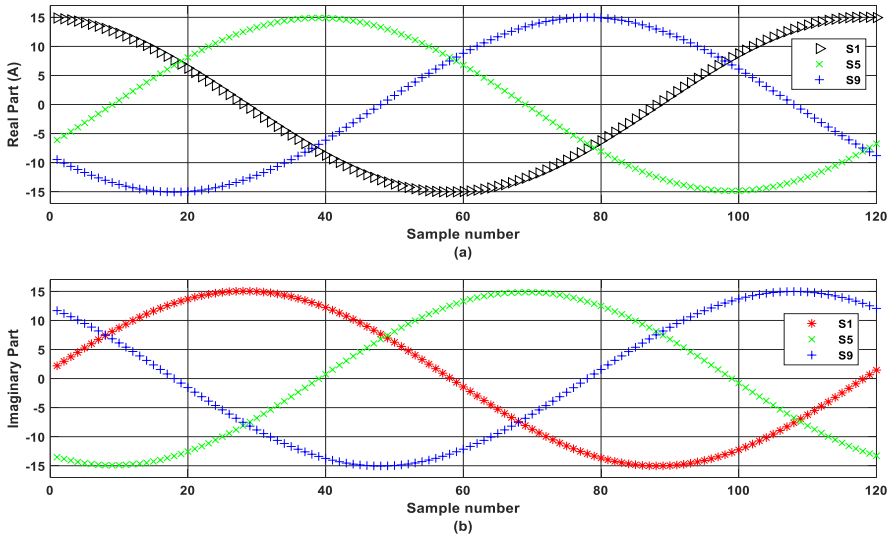

Figure 6.8 Estimated output of sensors S_1, S_5 and S_9 placed at 7 mm distance in triangular structure (a) Real part and (b) Imaginary part for 15 A

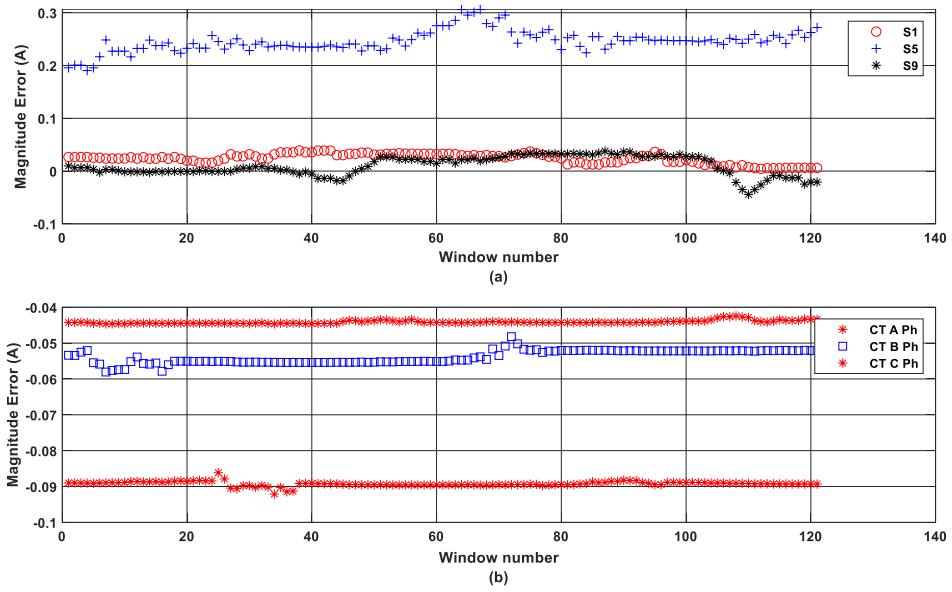

Figure 6.9 Magnitude errors in estimated phasors of 15 A for (a) One sensor per phase at 7 mm and (b) Three phase CTs in triangular structure

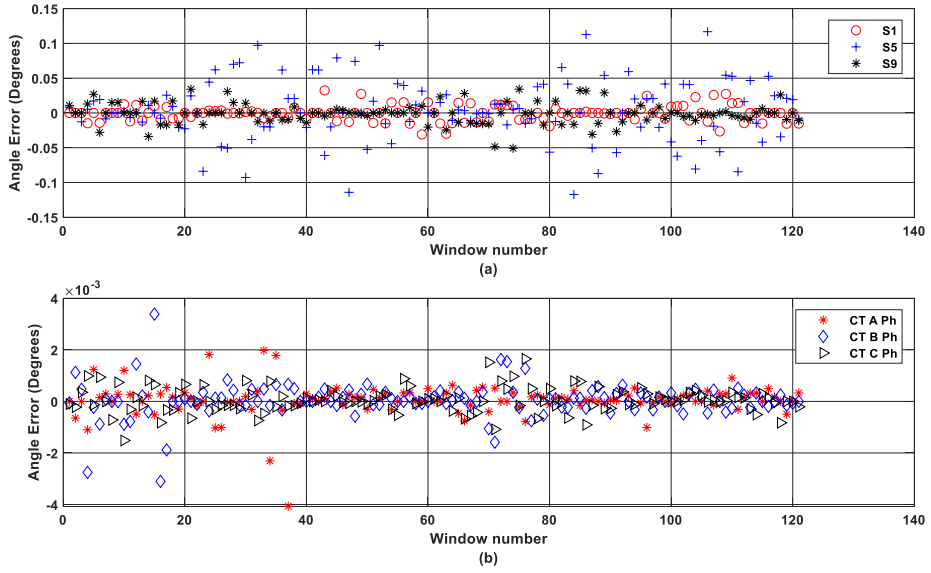

Figure 6.10 Angle errors in estimated phasors of 15 A for (a) One sensor per phase at 7 mm and (b) Three phase CTs in triangular structure

The performance of these sensors is also studied for other distances such as 15 mm, 25 mm and 35 mm. The outputs of the sensors are converted in current phasors, and their rectangular and polar components are applied for comparison with the respective value of the source current. The average values of the magnitude errors of sensor S_1 for each current from 5 A to 15 A estimated from the cases when it was placed at four different distances from each phase conductor are shown in the Figure 6.11 (a). This figure shows a maximum error of 0.1274 A when the sensor was placed at 35 mm from the source conductor. The other distances contributed very low values of the magnitude errors indicating that the sensor is performing well when it was kept closer to the A-phase conductor. The comparison of the angle errors of sensor S_1 shows a consistent performance for all four distances and is shown in the Figure 6.11 (b). It is observed that the angle errors are up to the fourth place after decimal point and are considered almost negligible in all cases for sensor S_1.

Figure 6.12 shows the comparison of TVE for three sensors when placed at 7 mm and their counterpart CT installed on the respective phase. It is evident from this figure that the CTs offer a consistent performance for all values of currents from 5 A to 15 A, whereas the sensors show a variance in their performance. The average values of TVE for each sensor are less than those of respective CT and it is evident from the Figure 6.12.

It is also important to compare the performance of three sensors for all cases of distance and source currents because they are applied to measure a balanced source current with no variability in the phase magnitude and angle. Figure 6.13 shows the Box and Whisker plot for the TVEs obtained for each sensor for four distances. This figure shows that the sensor, S_1 has the highest variation in the performance when placed at 35 mm as compared to S_5 and S_9. The average value of TVE for S_1 is 0.78% when placed at 35 mm whereas, for S_5 it is 0.2% and for S_9 it is 0.41% for the same distance. TVE calculated for each CT deployed on each phase is shown in the Figure 6.14. The CTs also show variation in their performance when applied with the same set of balanced three-phase currents in all cases when the sensors were placed at various distances. For the first case of distance, $d_1 = 7$ mm, all CTs show a larger variation in their performance as compared to the other distances.

This proves that the CTs can also have variation in their output when applied for the same current at different times.

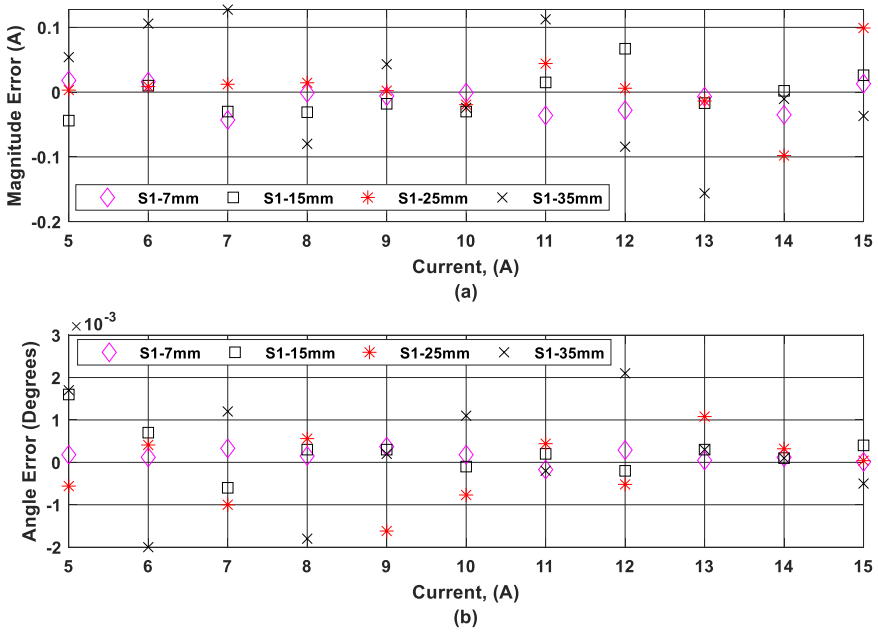

Figure 6.11 Errors of estimated phasors for outputs of A-phase sensor (a) Magnitude error and (b) Angle error

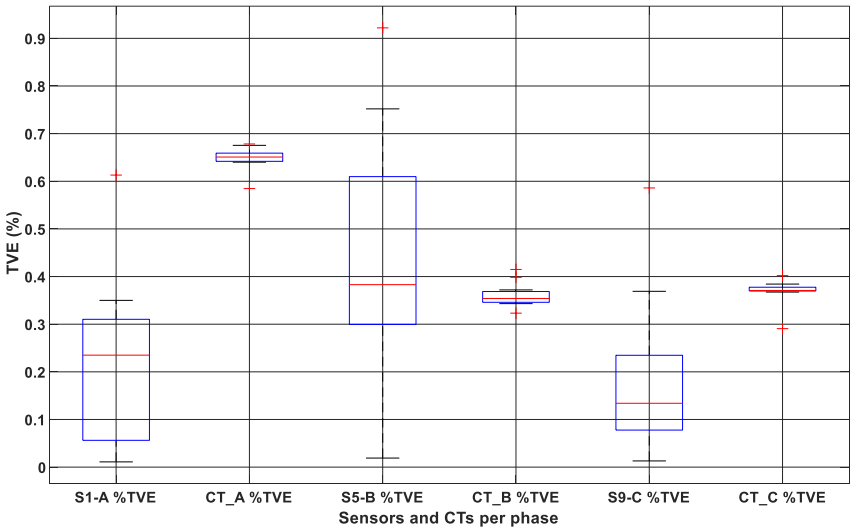

Figure 6.12 TVE of sensors when placed at a distance of 7 mm and TVE of CTs for three-phase currents

The magnitude errors in the estimated phasors for each current for all sensors and for all distances are shown in the Figure 6.15. This figure indicates that only sensor S_1's values are higher for the distance of 35 mm. The performances of all sensors are satisfactory for all remaining cases and currents. These results with their average values are also provided in Table 6.1 for three sensors and in Table 6.2 for three CTs. The outcome of one sensor per phase indicates satisfactory performance for all sensors except S_1 for 35 mm as compared to S_5 and S_9.

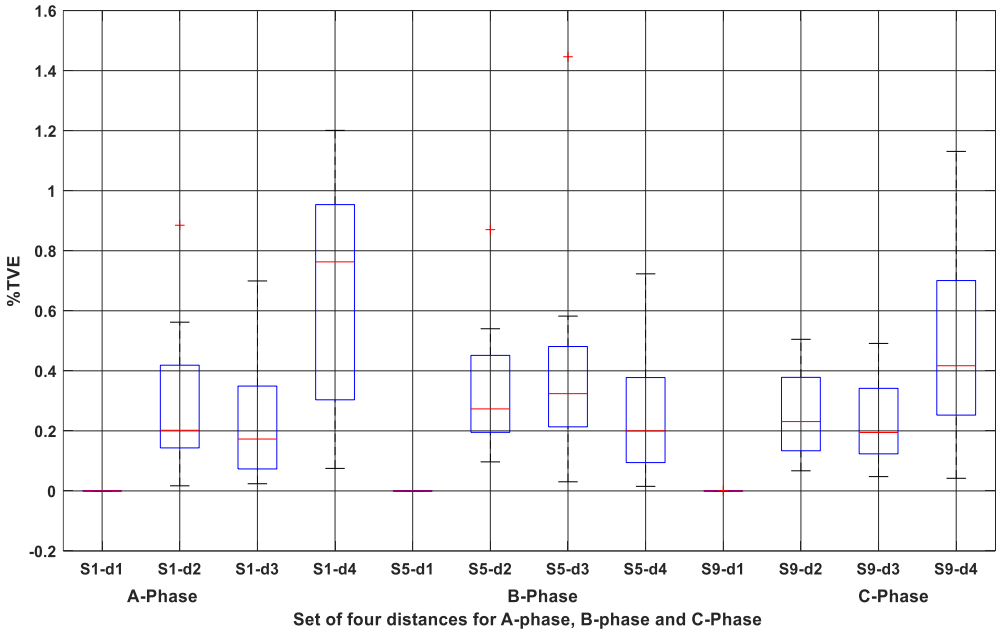

Figure 6.13 TVE for each sensor per phase at all four distances

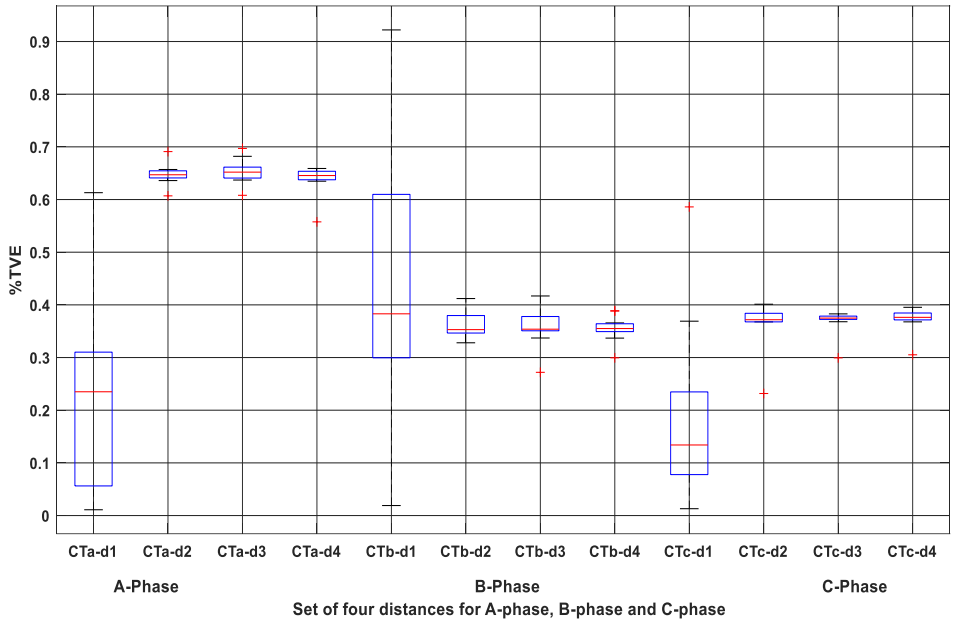

Figure 6.14 TVE for each CT per phase at all four distances

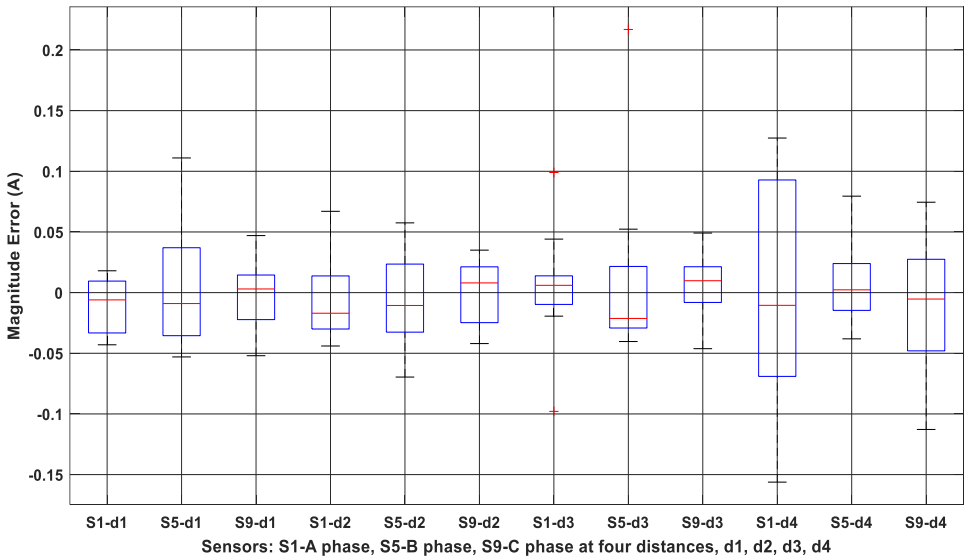

Figure 6.15 Magnitude Error in estimated current phasor for each sensor per-phase at all four distances, phase-A, phase-B and phase-C

Table 6.1 Errors for one sensor per phase at all distances in triangular structure

	Distance of sensors from the conductor of each phase			
	d_1 = 7 mm	**d_2 = 15 mm**	**d_3 = 25 mm**	**d_4 = 35 mm**
% TVE (average)				
S_1-A phase	0.20451	0.3080	0.2446	0.8752
S_5-B phase	0.44067	0.3380	0.3970	0.2476
S_9-C phase	0.18596	0.2588	0.2345	0.4858
Magnitude Error, A (average)				
S_1-A phase	-0.0099	-0.0045	0.0053	0.0046
S_5-B phase	0.00302	-0.0040	0.0117	0.0067
S_9-C phase	-0.00141	0.0002	0.0073	-0.0057
Angle Error, Degrees (average)				
S_1-A phase	0.00015	0.0003	-0.0001	0.0002
S_5-B phase	-0.00013	-0.0003	-0.0001	-0.0007
S_9-C phase	0.00012	0.0001	0.0004	-0.0004

Table 6.2 Errors for three-phase CTs in triangular structure

	Distance of sensors from the conductor of each phase			
	d_1 = 7 mm	**d_2 = 15 mm**	**d_3 = 25 mm**	**d_4 = 35 mm**
% TVE (average)				
CT-A phase	0.6480	0.648	0.6528	0.639
CT-B phase	0.3607	0.360	0.3579	0.354
CT-C phase	0.3687	0.366	0.3690	0.373
Magnitude Error, A (average)				
CT-A phase	-0.0643	-0.064	-0.0647	-0.063
CT-B phase	-0.0354	-0.035	-0.0348	-0.035
CT-C phase	-0.0363	-0.035	-0.0365	-0.037
Angle Error, Degrees (average)				
CT-A phase	0.00001	0.00001	0.00001	0.000007
CT-B phase	0.00001	0.00001	0.00001	0.000007
CT-C phase	-0.03632	0.00001	0.00001	0.000007

6.3.2 Lab Test Results of Two Sensors per Phase at Various Distances

The laboratory tests were performed with sensors S_1, S_2 for A-phase, S_5, S_6 for B-phase and S_9, S_{10} for C-phase. The outputs of each sensor for each case of source current in the circuit were estimated using the algorithm. These outputs were converted to rectangular and polar components for the purpose of comparison. For demonstration purpose, random cases are chosen, and their results are shown in the figures in this section. Figure 6.16 shows the rectangular components of the output of six sensors for the case of 14 A and distance of 7 mm. For the same case, the errors in the magnitude and the angles are shown in the Figure 6.17 and 6.18 for sensors as well as CTs. The magnitude errors show highest values provided by sensor, S_{10} and are in the range of 0.08A to 0.09A as shown in Figure 6.17 (a). The CTs show consistently lower values below zero for each phase for this current and is evident from the Figure 6.17 (b). The sensor S_5 shows a large variation in the angle errors and can be observed from the Figure 6.18 (a), whereas all other sensors are having less variation. The angle errors for CTs are below 0.0015^0 with C-phase CT showing larger variations as compared to the other two CTs as shown in Figure 6.18 (b).

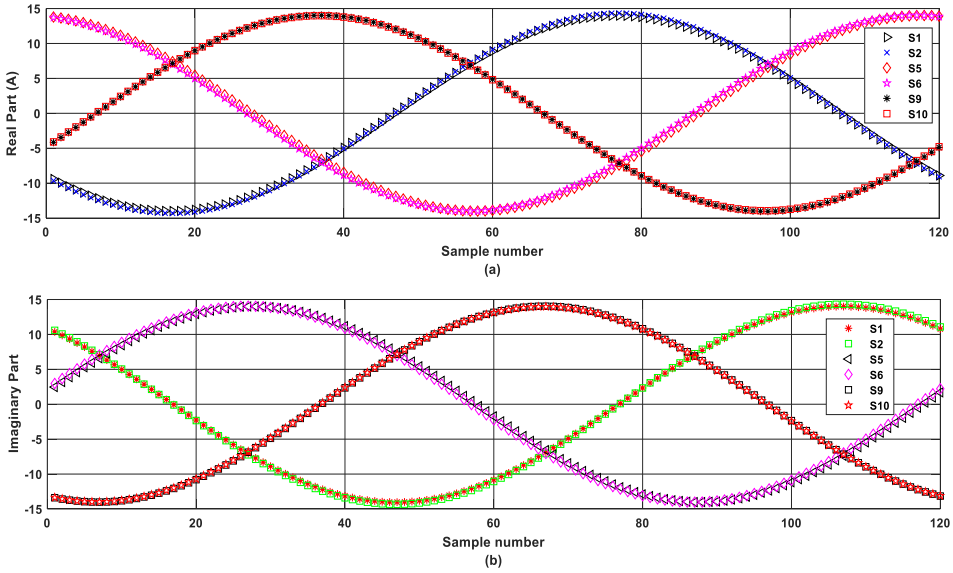

Figure 6.16 (a) Real parts and (b) Imaginary parts of estimated current outputs of sensors S_1, S_2, S_5, S_6, S_9 and S_{10} at 7 mm for 14 A in triangular structure

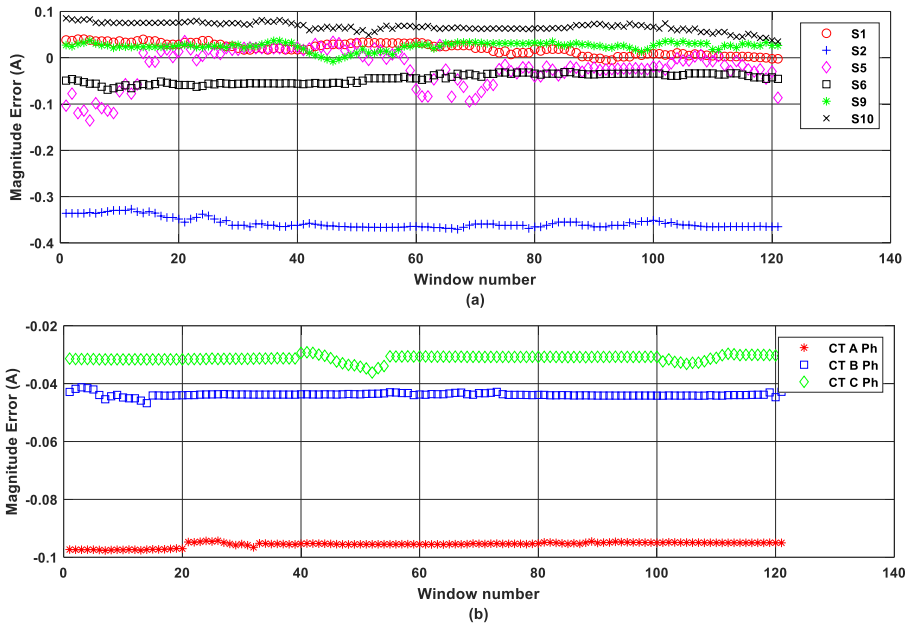

Figure 6.17 Magnitude errors in estimated phasors of 14 A for (a) two sensors per phase at 7 mm and (b) three-phase CTs in triangular structure

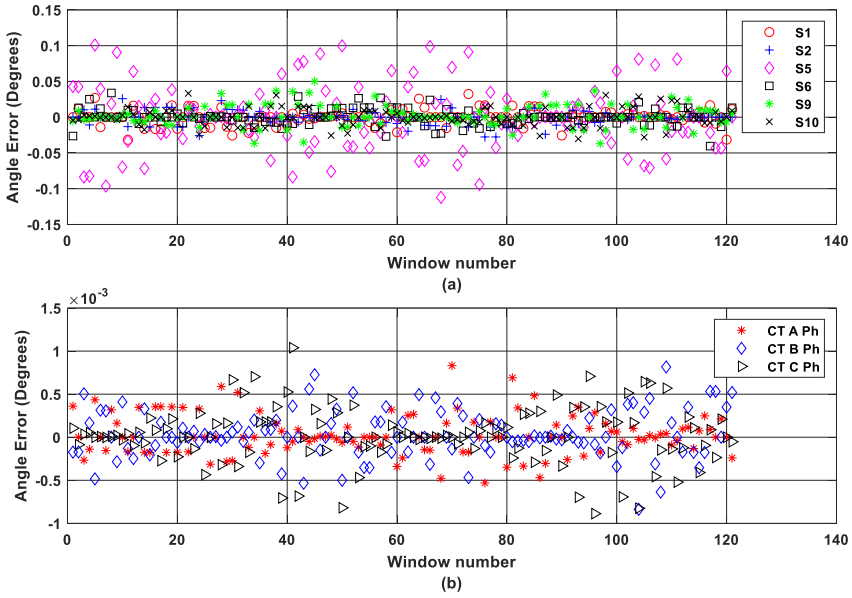

Figure 6.18 Angle errors in estimated phasors of 14 A for (a) two sensors per phase at 7 mm and (b) three-phase CTs in triangular structure

The rectangular components of six sensors for 15 A when sensors are placed at 25 mm are shown in Figure 6.19. The outputs of the sensors show an increase in the errors when their distance is increased from the source for each phase. It can be observed from Figure 6.20 (a) that the magnitude errors are larger as compared to those for the 7 mm case. Sensor S_5 shows a higher variation in the range from -0.32 A to 0.38 A for 15 A current. The error in the angle for the same current is also higher for this sensor varying up to 0.38^0 and is evident from Figure 6.21 (a).

The C-phase sensor, S_9 show a higher error of 0.28 A for the case of 10 A current sensed from 35 mm distance as shown in the Figure 6.22 (a) whereas the angle error is the highest for sensor S_5 in this case and can be seen in the Figure 6.23(a). The CTs showed less varying performance for all currents and can be seen from Figure 6.20 (b), 6.21 (b), 6.22 (b), and 6.23 (b) for magnitude and angle errors respectively.

Table 6.3 presents the average values of the errors in the outputs obtained by the algorithm for all sensors deployed for obtaining three-phase currents. The test results for each sensor are calculated individually and using the average MF for each sensor. From the Table 6.3, it is observed that the sensor S_2 yields highest TVE for all distances as compared to the other five sensors, whereas the sensors, S_1 and S_9 show minimum value of TVE for all distances.

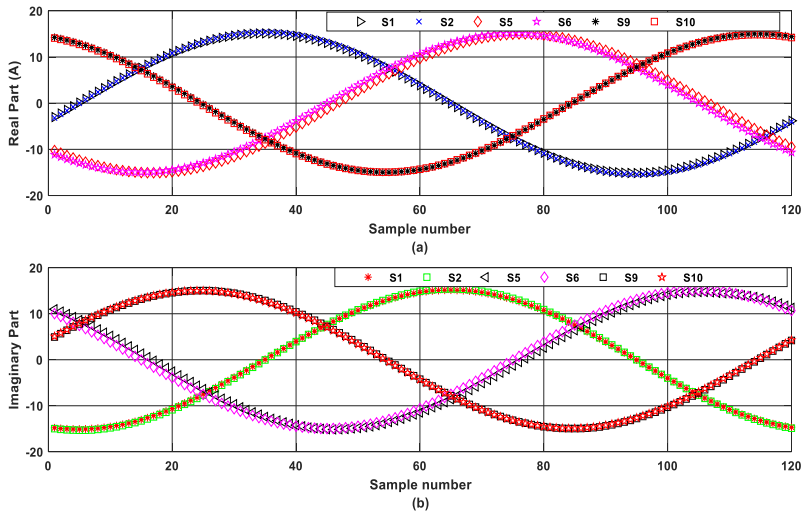

Figure 6.19 (a) Real parts and (b) Imaginary parts of estimated current outputs of sensors S_1, S_2, S_5, S_6, S_9, and S_{10} placed at 25 mm for 15 A in triangular structure

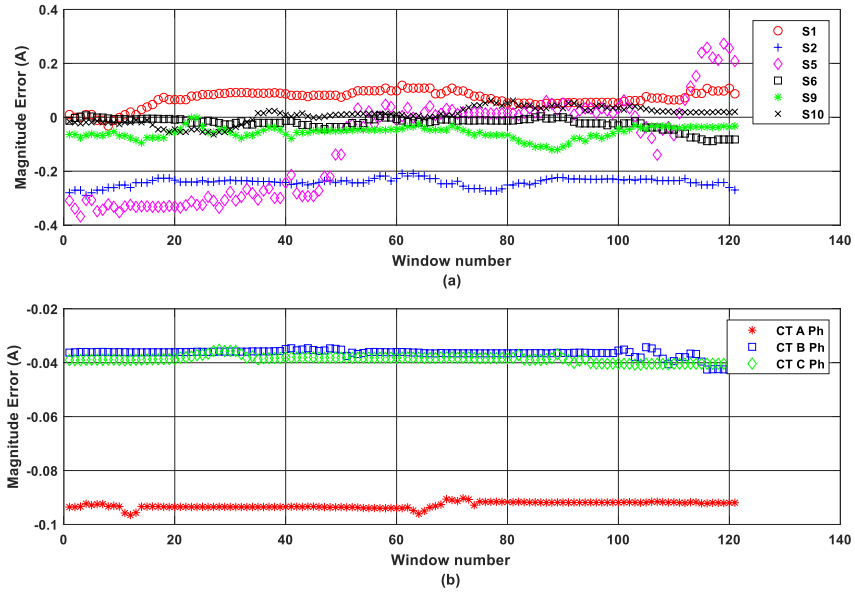

Figure 6.20 Magnitude errors in estimated phasors of 15 A for (a) two sensors per phase at 25 mm (b) three-phase CTs in triangular structure

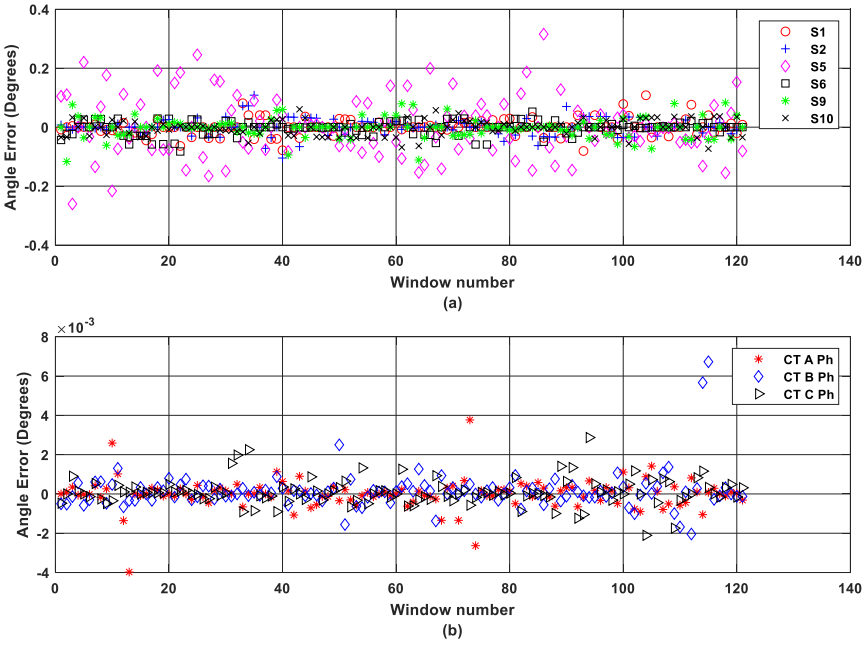

Figure 6.21 Angle errors in estimated phasors of 15 A for (a) two sensors per phase at 25 mm and (b) three-phase CTs in triangular structure

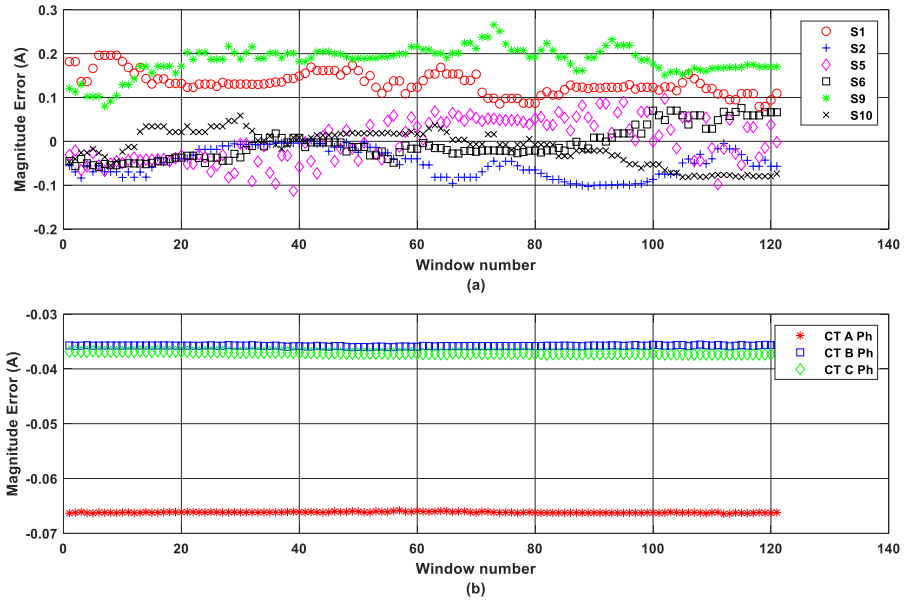

Figure 6.22 Magnitude errors in estimated phasors of 10 A for (a) two sensors per phase at 35 mm and (b) three-phase CTs in triangular structure

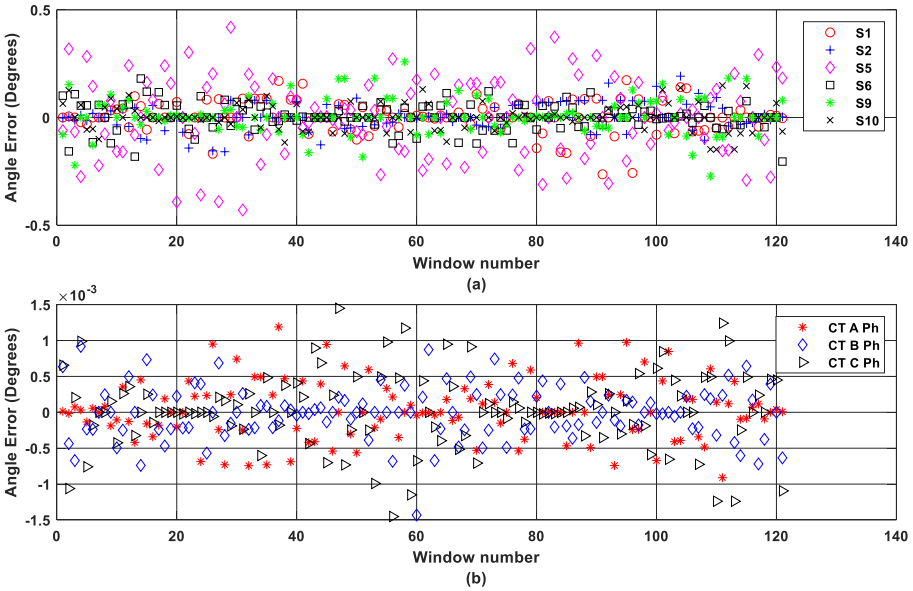

Figure 6.23 Angle errors in estimated phasors of 10 A for (a) two sensors per phase at 35 mm and (b) three-phase CTs in triangular structure

Table 6.3 Errors for two sensors per phase at all distances and CTs in triangular structure

	Distance of sensors from the conductor of each phase			
	d_1 = 7 mm	**d_2 = 15 mm**	**d_3 = 25 mm**	**d_4 = 35 mm**
% TVE (average)				
S_1-A phase	0.1621	0.3957	0.4070	0.7795
S_2-A phase	0.8007	0.8333	1.0319	1.0432
S5-B phase	0.2357	0.4997	0.5124	0.5464
S_6-B phase	0.2425	0.4797	0.3318	0.3313
S_9-C phase	0.0959	0.3013	0.2809	0.5701
S_{10}-C phase	0.2185	0.4005	0.1798	0.3322
CT-A	0.6499	0.6517	0.6471	0.6596
CT-B	0.3534	0.3527	0.3507	0.3594
CT-C	0.3655	0.3735	0.3703	0.3794
Magnitude Error, A (average)				
S_1-A phase	0.0042	-0.0021	-0.1338	0.0269
S_2-A phase	-0.1823	-0.0785	-0.1338	-0.0885
S_5-B phase	-0.0121	-0.0091	-0.0169	-0.0205
S_6-B phase	-0.0071	-0.0123	-0.0080	-0.0071
S_9-C phase	0.0023	0.0109	-0.00987	-0.0074
S_{10}-C phase	0.0067	0.0303	-0.0007	-0.0096
CT-A	-0.0646	-0.0650	-0.064	-0.0661
CT-B	-0.0344	-0.0344	-0.034	-0.0353
CT-C	-0.0357	-0.0369	-0.036	-0.0377
Angle Error, Degrees (average)				
S_1-A phase	0.00011	0.00013	0.0002	0.0007
S_2-A phase	0.00006	0.00017	0.0001	0.0005
S_5-B phase	0.00054	0.00056	0.00007	-0.0002
S_6-B phase	0.00007	0.00013	0.00027	-0.00015
S_9-C phase	0.00002	0.00040	-0.00007	-0.00004
S_{10}-C phase	0.00009	0.00065	-0.0005	0.00037
CT-A	0.00007	0.000074	0.00001	0.00001
CT-B	0.00005	0.00007	0.00001	0.00001
CT-C	0.00005	0.00092	0.00001	0.00001

6.3.3 Test Results of Three Sensors per Phase at Various Distances

This part of the test included S_1, S_2, S_3 sensors for A-phase, S_5, S_6, S_7 sensors for B-phase and S_9, S_{10} and S_{11} sensors for C-phase along with one single CT per phase. The current phasors were estimated for the case of three sensors per phase by applying the average MFs. The algorithm processed individual sensor's output data and estimated the current outputs without any data fusion to study the performance of sensors. As an initial step, it was decided to study the performance of individual sensors per phase and obtain the variation in the percentage errors in TVE, magnitude and angle. The following analysis shows the results of the individual performance of sensors. Random cases were selected to show the rectangular components of the calculated outputs, the magnitude errors, and the angle errors. Figure 6.24 (a) and (b) present the rectangular components of the nine sensors utilized in this experiment for 7 mm distance and 8 A current.

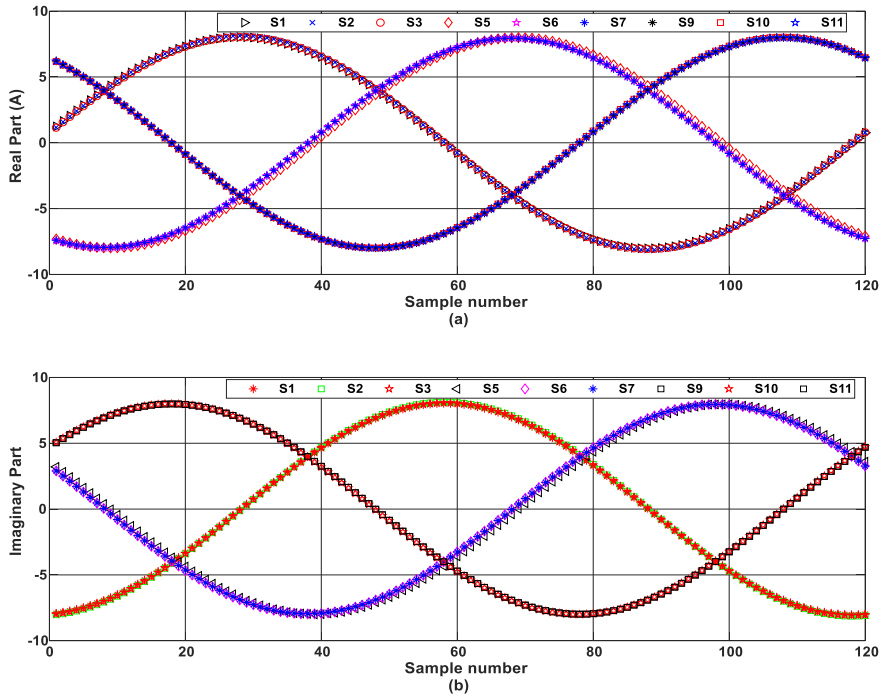

Figure 6.24 (a) Real parts and (b) Imaginary parts of calculated current outputs of sensors S_1, S_2, S_3, S_5, S_6, S_7, S_9, S_{10}, S_{11} placed at 7 mm for 8 A in triangular structure

The magnitude and angle errors for the same configuration is shown in the Figure 6.25 and Figure 6.26. The magnitude errors for all nine sensors are less than 0.065 A as shown in the Figure 6.25 (a) and the angle errors are below 0.001^0 except for the sensor S_5 as shown in the Figure 6.26 (a). The CTs provide similar results as that of previous cases and can be seen in Figure 6.25 (b) and Figure 6.26 (b).

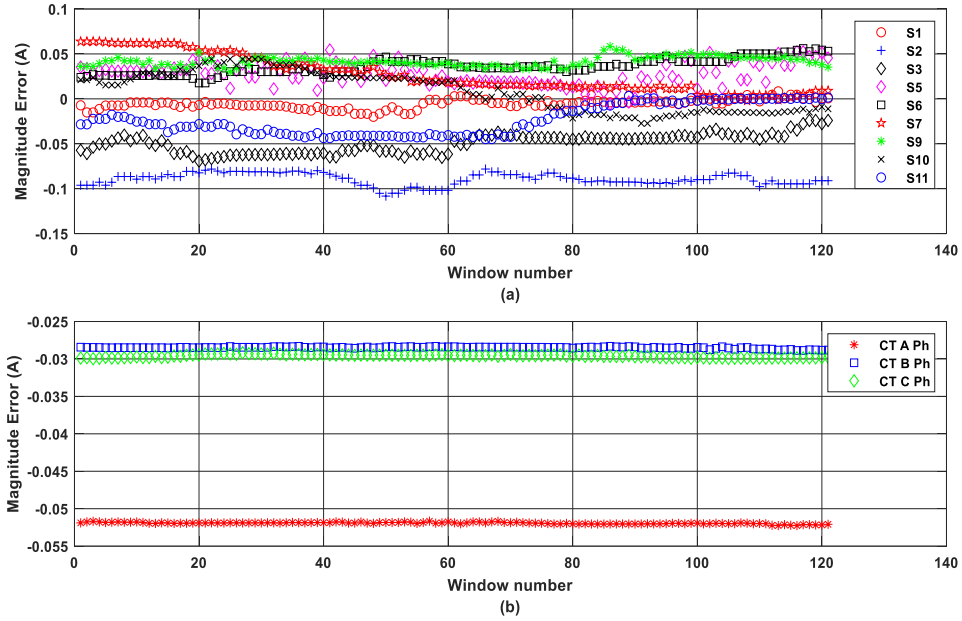

Figure 6.25 Magnitude errors in calculated phasors of 8 A for (a) three sensors per phase at 7 mm and (b) three-phase CTs in triangular structure

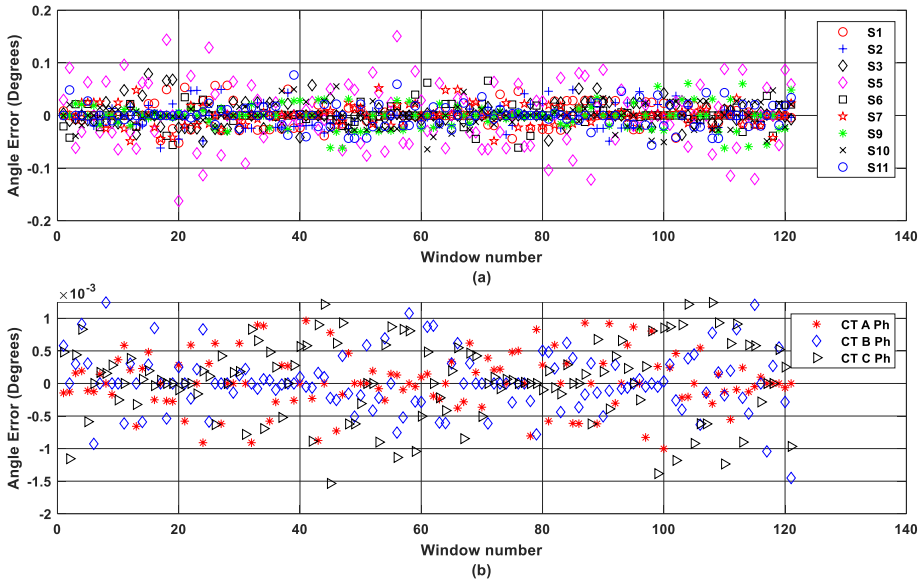

Figure 6.25 Angle errors in calculated phasors of 8 A for (a) three sensors per phase at 7 mm and (b) three-phase CTs in triangular structure

The outputs of the nine sensors for various distances and current outputs are presented in the Appendix D. The average values calculated from the percentage TVE for all current phasors for each sensor are shown in the Table 6.4. The table shows that the sensor S_2 has highest vector errors for all distances when compared with other eight sensors. Sensor S_3 exhibited 1.520% of TVE for 35 mm distance, whereas sensor S_1 proved to be efficient for all distances for A-phase current sensing with maximum TVE of 0.4443%. For B-phase, all three sensors S_5, S_6 and S_7 showed consistently good performance. Sensors S_9, S_{10} and S_{11} showed the best performance by giving minimum percentage TVEs for all distances when compared to other sensors of A-phase and B-phase. The percentage TVE of CTs of all phases were higher than the sensors.

Table 6.5 presents the magnitude errors for all sensors when placed at four distances. The maximum error is contributed by sensor S_2 for all distances. All sensors of C-phase consisted lowest errors in the magnitude among all sensors. Table 6.6 presents the average values of errors in the angle calculated for phasors of various currents when the sensors are placed at four distances. All sensors have very good accuracy in the calculated phase angles for all currents and can be verified from this table.

Table 6.4 Percentage TVE for three sensors per phase at all distances and three CTs in triangular structure

	Distance of sensors from the conductor of each phase			
	d_1 = 7 mm	**d_2 = 15 mm**	**d_3 = 25 mm**	**d_4 = 35 mm**
% TVE (average)				
S_1-A phase	0.2026	0.1915	0.4443	0.348
S_2-A phase	1.4746	0.8515	0.7901	1.229
S_3-A phase	0.2802	0.7902	1.0061	1.520
S_5-B phase	0.5726	0.5218	0.6345	0.526
S_6-B phase	0.4644	0.2864	0.5565	0.330
S_7-B phase	0.3301	0.2632	0.3787	0.437
S_9-C phase	0.1298	0.2801	0.3819	0.544
S_{10}-C phase	0.2014	0.3238	0.3045	0.285
S_{11}-C phase	0.1562	0.3019	0.2593	0.335
CT-A	0.6500	0.6504	0.6505	0.6449
CT-B	0.6500	0.3521	0.6505	0.6449
CT-C	0.6500	0.3742	0.6505	0.6449

Table 6.5 Magnitude errors for three sensors per phase and three CTs at all distances in triangular structure

	Distance of sensors from the conductor of each phase			
	d_1 = 7 mm	**d_2 = 15 mm**	**d_3 = 25 mm**	**d_4 = 35 mm**
Magnitude Error, A (average)				
S_1-A phase	0.0044	0.0112	-0.0162	-0.0141
S_2-A phase	-0.1516	-0.0764	-0.0477	-0.0654
S_3-A phase	0.0009	0.0187	-0.0102	-0.0028
S_5-B phase	0.0339	0.0030	-0.0252	-0.0073
S_6-B phase	0.0070	-0.0065	-0.0174	-0.0234
S_7-B phase	0.0091	-0.0012	-0.0006	-0.0166
S_9-C phase	-0.0093	-0.0010	0.0099	-0.0024
S_{10}-C phase	0.0057	0.0081	-0.0055	-0.0023
S_{11}-C phase	-0.0093	0.0003	0.0099	-0.0024
CT-A	-0.0648	-0.0648	-0.0646	-0.0639
CT-B	-0.0346	-0.0344	-0.0353	-0.0346
CT-C	-0.0357	-0.0373	-0.0386	-0.0358

Table 6.6 Angle errors for three sensors per phase at all distances and three CTs in triangular structure

	Distance of sensors from the conductor of each phase			
	d_1 = 7 mm	**d_2 = 15 mm**	**d_3 = 25 mm**	**d_4 = 35 mm**
Angle Error, Degrees (average)				
S_1-A phase	0.000090	0.00007	0.000262	0.00026
S_2-A phase	-0.000080	0.00007	-0.000041	-0.00017
S_3-A phase	0.000030	0.0001	0.000227	-0.00011
S_5-B phase	-0.000040	-0.00021	-0.000003	-0.00014
S_6-B phase	0.000010	-0.00008	-0.000138	0.00006
S_7-B phase	0.000120	-0.00001	-0.000050	0.00011
S_9-C phase	0.000130	0.00016	0.000088	-0.00055
S_{10}-C phase	-0.000080	-0.00005	-0.000080	-0.00016
S_{11}-C phase	-0.000006	0.00001	-0.000192	-0.00007
CT-A	0.000008	0.00001	0.000007	0.00001
CT-B	0.000006	0.00001	0.000007	0.00001
CT-C	0.000007	0.00001	0.000007	0.00001

6.4 Test Results and Performance Analysis of TMR Sensors for Three-Phase Horizontal Structure

The second part of the three-phase current measurement experiment was to install the TMR sensors on a three-phase horizontal structure in which all three phase conductors remain in the horizontal plane as shown in the Figure 6.1 (b). The objective of this experiment is to study any variation in the capability of the sensors as compared to their performance where three-phase conductors were arranged in a triangular structure. The arrangement of three-phase conductors and sensors by keeping the remaining equipment from the arrangement of triangular structure is as shown in the Figure 6.27. It shows three-phase conductors are in horizontal plane and the sensors are placed on the left side of each phase at equal height and distance from phase conductors. The stands on which the sensors are installed are arranged in a manner to adjust the distance from the individual phase conductor from 7 mm to 35 mm. Although there are four sensors per phase installed and connected to the data acquisition system, only two groups of sensors per phase utilized for this experiment. There are two sensors per phase and three sensors per phase. This is because, in the first part of

the triangular structure it was observed that, the output of sensors was very similar for all three groups, one-, two- and three- sensors per phase. Moreover, the outputs were estimated using the average MF of individual sensors and, therefore, it was concluded that the use of one sensor per phase is not necessary. Hence, in this case the tests were performed with only two-sensors per phase and three-sensors per phase with combinations of four distances.

The tests were performed with the first combination of two-sensors per phase placed at 7 mm distance from each phase conductor. Three-phase input currents of 60 Hz starting from 5 A were injected using the Omicron CMC356 test set. The outputs of sensors were recorded for four seconds period by using the data acquisition system. The input currents were increased in the steps of 1 A until they reached the maximum limit of the test set at 15 A, and the outputs were measured each step. Similar steps were followed for the remaining options of distances and the entire procedure was repeated for the set of three-sensors per phase. Further steps for estimation of three-phase currents from the measured data were followed using the algorithm explained in the Figure 6.4. The results for various cases are explained in detail in the following sections.

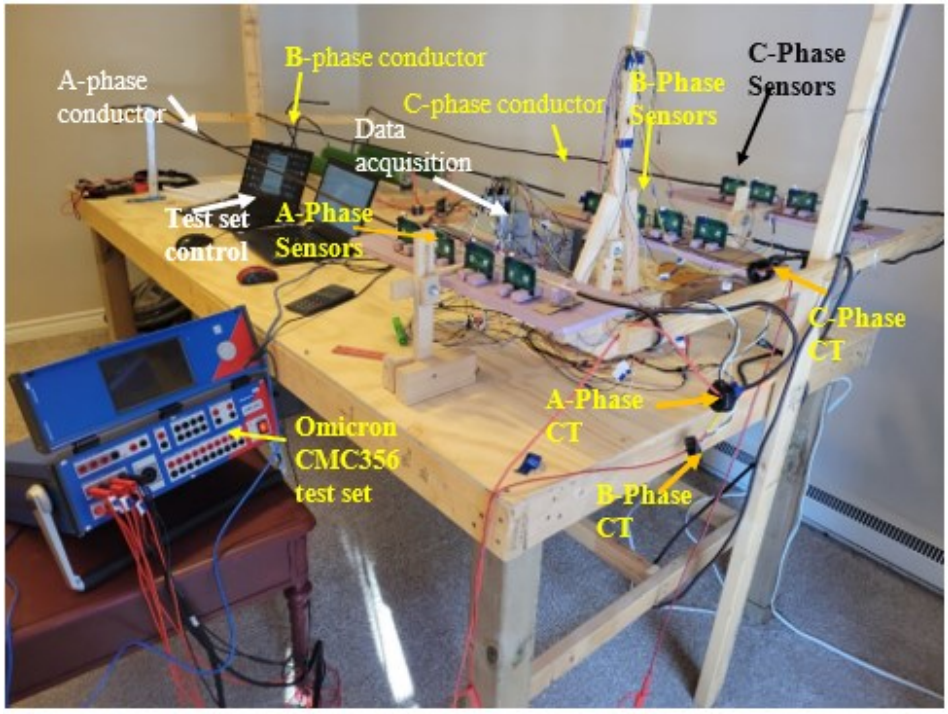

Figure 6.26 Three-phase experiment setup for horizontal structure with sensors and CTs

6.4.1 Results of Two Sensors per-Phase at Various Distances

Test results of the sensors for random cases such as 15 mm and for 14 A are discussed in detail in this section. The results of the remaining cases are presented in the Appendix D and 7 along with the tables for each sensor and for each combination of the distance and current. Figure 6.28 shows the rectangular components of the output of six sensors. Figure 6.29 (a) shows the magnitude errors of S_1, S_2, S_5, S_6, S_9 and S_{10} for 15 mm and 14 A case. It is evident from this figure that the errors are very low and consistent for all windows for the sensors S_6, S_9, S_{10}, whereas the sensors S_2 and S_5 show a larger variation in the performance with the increments in window per sample. These two sensors also showed similar performance for the previous case when they were installed in the triangular structure. The errors for three CTs as shown in Figure 6.29 (b) are observed to contribute similar values as observed before for all cases. The angel errors in estimated output for 14 A for six sensors are presented in the Figure 6.30 (a) and for CTs in Figure 6.30 (b). The angle errors for S_2, S_5 and S_9 showed variation, but the average values are very low for all sensors throughout the complete set of currents.

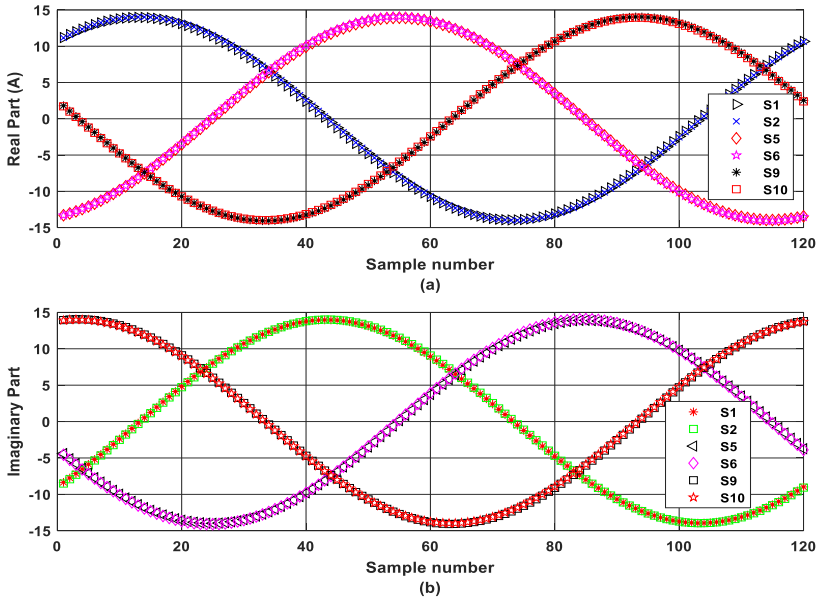

Figure 6.27 (a) Real parts and (b) Imaginary parts of estimated current outputs of sensors S_1, S_2, S_5, S_6, S_9, and S_{10} placed at 15 mm for 14 A in horizontal structure

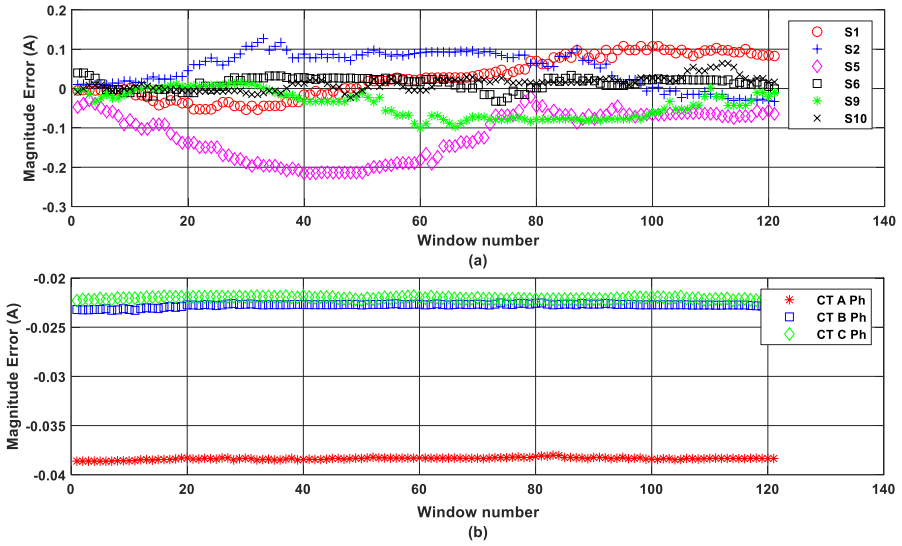

Figure 6.28 Magnitude errors in estimated phasors of 14 A for (a) two sensors per phase at 15 mm and (b) three-phase CTs in horizontal structure

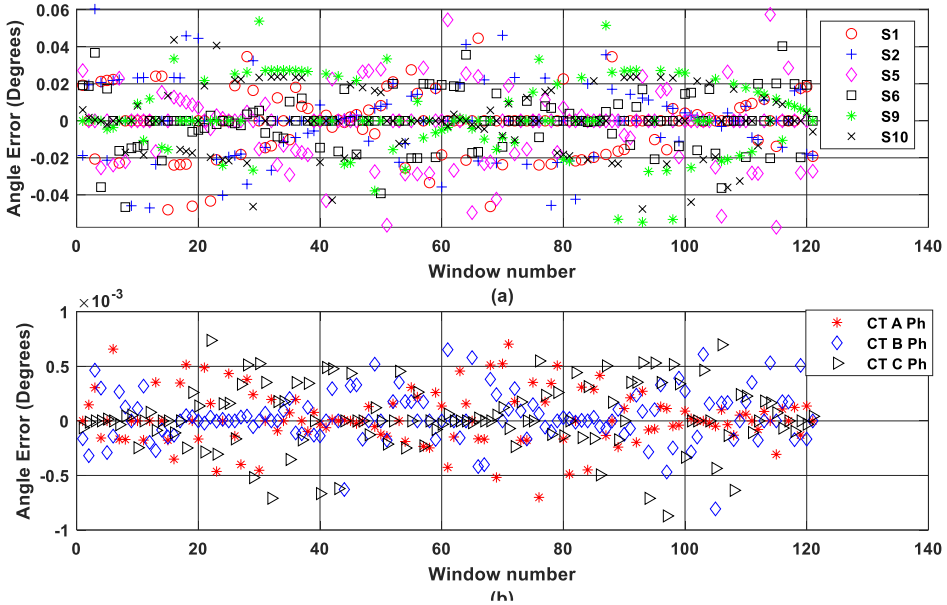

Figure 6.29 Angle errors in estimated phasors of 14 A for (a) two sensors per phase at 15 mm and (b) three-phase CTs in horizontal structure

Table 6.7 provides the performance parameters, such as the percentage TVE, the magnitude errors and the angle errors for six sensors and three CTs. The average values of the percentage TVE for all currents show that the sensor S_2 has highest errors for all distances as compared to other five sensors. The highest error of S_2, 1.007 % was observed for the distance 7 mm and 0.903% when the sensor was placed at 35 mm. The sensor S_9 showed minimum errors for all combinations of distances and currents as compared to other sensors and CTs. Similarly, Sensor S_1 showed minimum errors in the percentage TVE as compared to those of CTs with 0.272% for 7 mm and 0.307% for 35 mm. This is the most consistent performance as compared to other sensors. The magnitude errors for S_1, S_9 and S_{10} were observed to be the lowest as compared to other sensors. The magnitude errors of three CTs for all distances were observed to be higher than those of all sensors proving a better performance of sensors. The angle errors for all sensors and CTs as shown in the Table 6.7 are very low and therefore contributing positively to the accuracy of current phasor calculations.

Table 6.7 Errors for two sensors per phase at all distances in horizontal structure

	Distance of sensors from the conductor of each phase, HORIZONTAL Structure			
	d_1 = 7 mm	**d_2 = 15 mm**	**d_3 = 25 mm**	**d_4 = 35 mm**
% TVE (average)				
S_1-A phase	0.272	0.291	0.314	0.307
S_2-A phase	1.007	0.410	0.317	0.903
S_5-B phase	0.234	0.196	0.338	0.487
S_6-B phase	0.203	0.343	0.388	0.684
S_9-C phase	0.126	0.169	0.317	0.337
S_{10}-C phase	0.227	0.245	0.206	0.626
CT-A	0.644	0.636	0.645	0.641
CT-B	0.357	0.348	0.350	0.347
CT-C	0.339	0.358	0.342	0.336
Magnitude Error, A (average)				
S_1-A phase	0.0002	-0.003	0.007	-0.005
S_2-A phase	-0.019	-0.107	0.005	-0.080
S_5-B phase	-0.002	0.003	0.008	-0.007
S_6-B phase	-0.008	-0.001	-0.008	-0.002
S_9-C phase	-0.001	-0.001	-0.006	-0.011
S_{10}-C phase	0.006	-0.001	0.009	-0.002
CT-A	-0.063	0.644	-0.064	-0.064
CT-B	-0.034	0.357	-0.034	-0.034
CT-C	-0.036	-0.033	-0.033	-0.033
Angle Error, Degrees (average)				
S_1-A phase	0.00006	-0.00018	-0.00013	0.03705
S_2-A phase	-0.00005	-0.00002	0.00012	-0.00005
S_5-B phase	0.00010	0.00017	0.00027	0.00023
S_6-B phase	-0.00005	-0.00002	-0.00006	0.00010
S_9-C phase	0.00016	-0.00002	0.00007	0.00014
S_{10}-C phase	0.00033	0.00002	0.00026	0.00077
CT-A	0.00001	0.00001	0.00001	0.00001
CT-B	0.00001	0.00001	0.00001	0.00001
CT-C	0.00001	0.00001	0.00001	0.00001

6.4.2 Results of Three Sensors per Phase at Various Distances

This test became the last phase of the experiment with three-sensors per phase in horizontal structure arrangement. The current phasors of the sensors were estimated by using their individual average MF values. The results for the random cases are presented in the Appendix D which consists of the rectangular components of the estimated current phasors of the outputs of the sensors for various cases as well as the magnitude and the angle errors for the same configuration of distances and the sensors per phase. In addition, the results of each sensor output for all values of input currents and for all combinations of distances are provided in the Appendix D and Appendix E.

Table 6.8 presents the TVE for nine sensors deployed in the horizontal structure for three-phase current measurement with a combination of three-sensors per phase placed at various distances. It is evident that the sensor S_2 presented 1.574 % of TVE when placed at 7 mm distance and 0.966% when placed at 35 mm for measuring the A-phase current. This performance is found similar in other cases discussed in the previous sections. Sensor S_1 showed increased %TVE of 1.040% for distance of 25 mm and 1.626% for 35 mm. This is in contrast with its results for the previous experiments. In this experiment, the errors were found to increase when the distance increased from 15 mm to 35 mm for S_1, S_3 and S_5, whereas these errors were varying less for the rest of the sensors with the exception of S_2 where the errors decreased with the increase in the distance. A detail analysis on the output of S_2 for each current showed consistently higher error (above 1.5%) for all currents from 5 A to 15 A for 7 mm case and it decreased to below 1.5% for other three distances. For S_1, the values of the TVE increased from 1.654% at 15 mm, 2.226% at 25 mm to 4.051% at 35 mm for 5A. This affected the average value of the %TVE for this sensor. The details can be seen in the Appendix D where all results are given in separate tables for each sensor. The magnitude errors for all sensors and for all distances were very less except for S_2 for 7 mm case. The angle errors were also observed to be very less in degrees and therefore overall performance of the sensors was satisfactory.

Table 6.8 Percentage TVE errors for sensors per phase: Three sensors per phase in horizontal structure

	Distance of sensors from the conductor of each phase			
	d_1 = 7 mm	d_2 = 15 mm	d_3 = 25 mm	d_4 = 35 mm
% TVE (average)				
S_1-A phase	0.533	0.565	1.040	1.626
S_2-A phase	1.574	0.557	0.639	0.966
S_3-A phase	0.239	0.495	0.550	0.738
S_5-B phase	0.258	0.190	0.495	0.463
S_6-B phase	0.136	0.235	0.343	0.311
S_7-B phase	0.088	0.210	0.225	0.385
S_9-C phase	0.193	0.238	0.349	0.398
S_{10}-C phase	0.255	0.358	0.330	0.442
S_{11}-C phase	0.161	0.290	0.360	0.291
CT-A	0.649	0.641	0.649	0.647
CT-B	0.353	0.641	0.649	0.647
CT-C	0.336	0.641	0.649	0.647

Table 6.9 Magnitude errors for sensors per phase: Three sensors per phase in horizontal structure

	Distance of sensors from the conductor of each phase			
	d_1 = 7 mm	d_2 = 15 mm	d_3 = 25 mm	d_4 = 35 mm
Magnitude Error, A (average)				
S_1-A phase	-0.011	-0.004	0.001	-0.019
S_2-A phase	-0.157	-0.047	-0.039	-0.067
S_3-A phase	-0.002	-0.014	-0.010	-0.010
S_5-B phase	-0.005	0.001	0.005	0.012
S_6-B phase	-0.003	-0.001	-0.013	-0.003
S_7-B phase	-0.001	-0.002	0.0008	-0.008
S_9-C phase	-0.009	-0.004	-0.010	0.001
S_{10}-C phase	-0.002	0.010	-0.006	-0.028
S_{11}-C phase	0.002	-0.004	-0.010	0.001
CT-A	-0.064	-0.064	-0.065	-0.064
CT-B	-0.035	-0.034	-0.034	-0.034
CT-C	-0.033	-0.034	-0.035	-0.033

Table 6.10 Angle errors for sensors per phase: Three sensors per phase in horizontal structure

	Distance of sensors from the conductor of each phase			
	d_1 = 7 mm	**d_2 = 15 mm**	**d_3 = 25 mm**	**d_4 = 35 mm**
Angle Error, Degrees (average)				
S_1-A phase	-0.00002	0.0001	-0.0003	-0.00001
S_2-A phase	0.00015	0.0002	-0.0001	-0.00014
S_3-A phase	0.00018	0.0000	-0.0003	0.00003
S_5-B phase	-0.00003	0.0002	-0.0001	0.00001
S_6-B phase	0.00000	0.0000	0.0002	0.00019
S_7-B phase	0.00002	0.0001	0.0004	0.00027
S_9-C phase	0.00007	0.0002	-0.0001	0.00009
S_{10}-C phase	-0.00006	0.0002	0.0000	0.00019
S_{11}-C phase	0.00006	0.0002	-0.0001	0.00002
CT-A	0.00001	0.00001	0.00001	0.00001
CT-B	0.00001	0.00001	0.00001	0.00001
CT-C	0.00001	0.00001	0.00001	0.00001

6.5 Field Experiment for Three-Phase High Currents Measurement

The field experiment was performed at the General Motors Climatic Wind Tunnel (CWT) facility by installing the sensors on the solar simulation system's three-phase power supply conductors. This solar simulation system can generate solar intensity from 600 to 1200 kW/m2 from the light produced by metal halide lamps. The AC power distribution panel of this system is supplied by a three-phase 225 kVA delta-star connected transformer with 575 V on primary and 400/231 V on the secondary side. There are 21 metal halide lamps in the circuit which are powered by three-phase source through this distribution panel. The intensity of all lamps is varied simultaneously by a rectifiers and inverters system when the AC power is supplied to them. Each lamp also has the electronic ballast. A set of two sensors were installed on each phase inside the distribution panel as shown in Figure 6.30 and Figure 6.31 (a).

During the experiment, the intensity of all lamps was varied simultaneously from 50% to 100% in stages of 5% by a controller which reflected in the increased load current at every stage. The sampling rate of the data acquisition system was set to 7200 samples/second. The outputs of sensors were recorded at every stage for 5 seconds. For reference, the current flowing in the conductor of each phase for every stage was also measured by using true rms clamp-on type ammeters, one Etekcity ammeter for A-phase and, a FLUKE 325 ammeter for B-phase and, a FLUKE 374 FC ammeter for C-phase. It was observed that phase-A, phase-B and phase-C loads were not evenly distributed, resulting in unequal currents flowing in each phase and were measured by the ammeters. This is evident from Figure 6.31 (b), which shows 92.6 A in A-phase, and 113.5 A in B-phase and C-phase respectively. For B-and C-phase, the measured currents were 83.9A for 50% intensity of lamps and, 155.4A for the 100% intensity. Similarly, for A-phase, the currents were 67.8 A and 130.2 A for 50% and 100% intensity respectively.

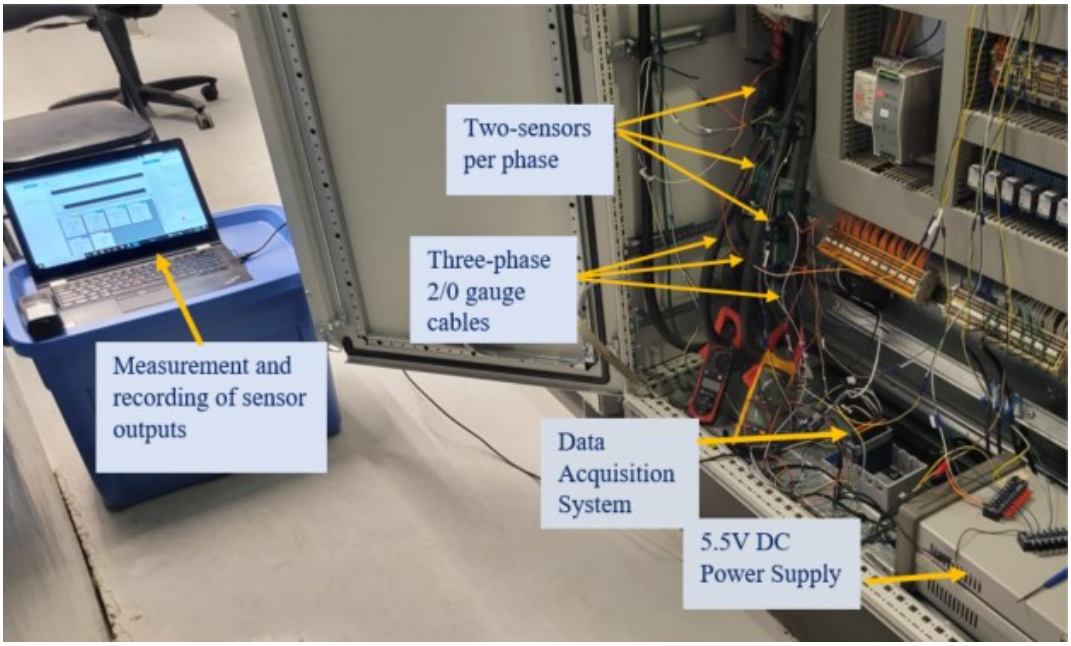

Figure 6.30 Three-phase current measurement experimental setup at CWT

After the completion of measuring sensor outputs for all stages, the recorded data was checked for verification and, it was observed that, the measured outputs of sensors had

sinusoidal waveform with multiple harmonics. The reason being the electronic devices installed in each lamp circuit which generated large amount of harmonics.

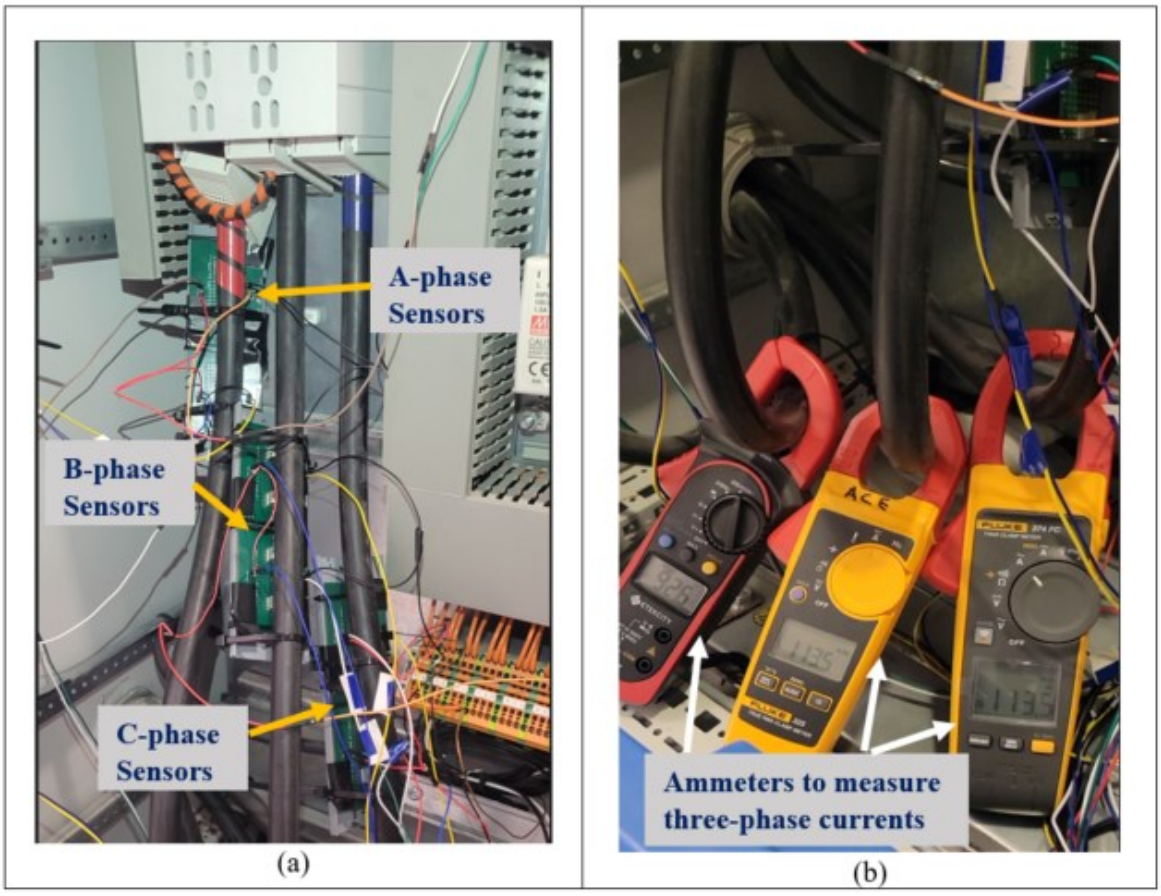

Figure 6.31 Experimental setup at CWT, (a) Installation of two-sensors on each phase (b) Three clamp-on ammeters for reading three-phase currents

6.5.1 Performance of Sensors in Measuring Three-Phase Currents

The sensors per phase deployed in the field experiment were, S_1, S_2 for A-phase, S_3, S_4 for B-phase and S_5, S_6 for C-phase. These sensors were calibrated during the single-phase experiment explained in the Chapter 4. Therefore, their multiplying factors were readily available for the performance analysis. A computational program was developed in MATLAB that utilized these multiplying factors and the measured data for each sensor and, estimated the True RMS (TRMS) currents from a set of 1200 samples recorded with a sampling rate of 7200 samples/second for each sensor. The program in MATLAB also

estimated the errors in percentage between the TRMS currents obtained from the measured data for sensors and the measured values obtained using clamp-on ammeters for each phase.

The results of sensor S_2 for measuring A-phase currents for all stages are given in the Table 6.11. The load on this phase consumed currents different than B- and C-phase. The percentage errors between the ammeter measurements and estimated current outputs vary from 0.22% for 110.8 A to 0.62% for 85.8 A. The sensor showed error of 0.25% in measuring the input current of 130.2 A.

Table 6.11 Sensor S_2 results of measuring A-phase currents

A-phase current true RMS values recorded from ammeter (A)	**True RMS value estimated for S_2 (A)**	**Percentage error (%) between recorded RMS value and estimated RMS value**
67.8	67.60	0.30
73.4	73.59	0.26
79.4	78.93	0.59
85.8	85.27	0.62
92.1	91.84	0.29
98.7	98.38	0.33
104.8	104.18	0.59
110.8	110.55	0.22
117.2	116.53	0.57
123.8	123.35	0.37
130.2	129.88	0.25

The estimated output of S_2 for 130.2 A of input current is shown in the Figure 6.32. This figure clearly indicates presence of multiple harmonics in addition to the fundamental frequency in the load currents. These harmonics are generated because of the gas discharge lamp circuit arcing, negative resistance characteristics and electronic ballasts with rectifier circuit and inverter.

Similarly, the estimated output of the sensor S_4 of B-phase for an input current of 91.2 A is shown in the Figure 6.33. The output shows harmonics, and the peak value of the output

is close to 110 A. Figure 6.34 shows the output obtained for S_4 for input current of 155.4A showing similar pattern in the sine wave with peak value close to 250 A. Therefore, the reason for using True RMS values in the algorithm to estimate the output of sensors is justified and provides more accurate results in case of measuring currents with harmonics in a three-phase circuit.

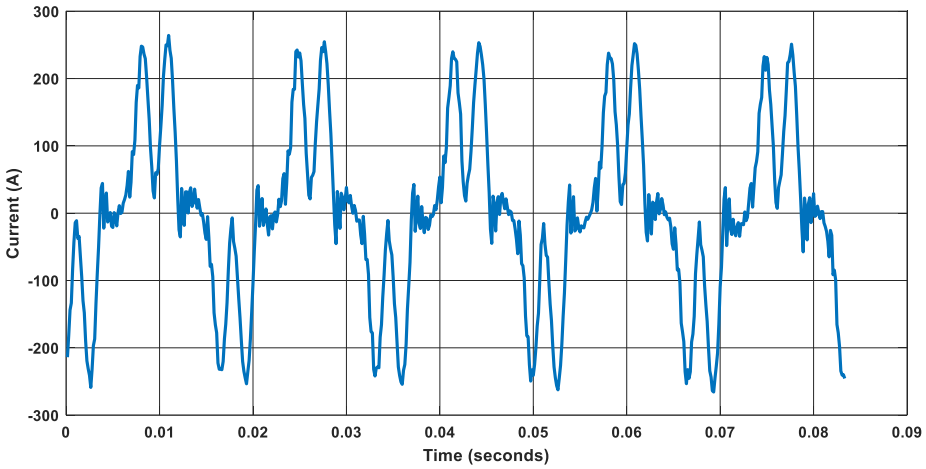

Figure 6.32 A-phase current measurement: S_2 output for 130.2 A

The performance of sensor, S_4 is illustrated in terms of percentage errors for the B-phase load currents during various stages and is shown in the Table 6.12.

Table 6.12 Sensor S_4 results of measuring B-phase currents

B-phase current true RMS values recorded from ammeter (A)	**True RMS value estimated for S_4 (A)**	**Percentage error (%) between recorded RMS value and estimated RMS value**
84.4	84.17	0.27
91.2	91.07	0.14
98.3	97.70	0.61
106.2	105.62	0.55
113.6	112.99	0.54
121.4	120.62	0.64
128.8	128.36	0.34
134.8	134.56	0.18
141.7	140.52	0.83
148.5	147.85	0.44
155.6	148.10	0.59

This table shows minimum error of 0.14% in estimating the input current of 91.2 A and maximum error of 0.83% in estimating the input current of 141.7 A. In this case, the MF used for computing the outputs for S_4 was obtained for a distance of 1.5 cm from the previous calibration process. The errors increasing with the input current indicate that the distance is not 1.5 cm during the experiment.

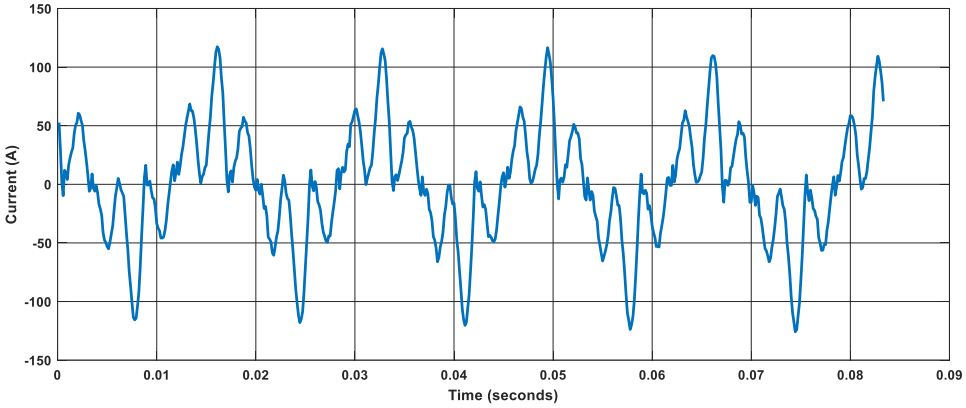

Figure 6.33 B-phase current measurement: S_4 output for 91.2 A

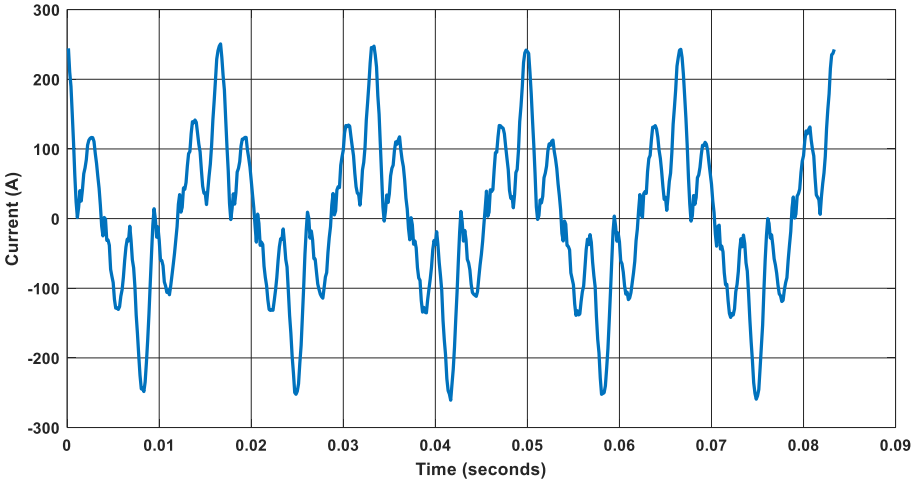

Figure 6.34 B-phase current measurement: S_4 output for 155.6 A

The load on B- and C-phase was balanced and therefore, provided matching current readings on ammeters for all stages during the experiment. The results of the sensor S_6 installed on the C-phase cable are illustrated in Table 6.13. The first column of the table provides the input current measured by the C-phase clamp-on type ammeter, the second column provides the estimated output of S_6 and, the last column provides the percentage

error between the values of first and second column for each stage. S_6 demonstrated zero error for measuring 113.6 A and maximum error of 0.37% for measuring 148.5 A. The output of S_6 for input current of 155.4 A is shown in the Figure 6.35 with its performance similar to that of S_4. The waveform shows presence of harmonics introduced by the electronic components in the intensity control circuit of metal halide lamps.

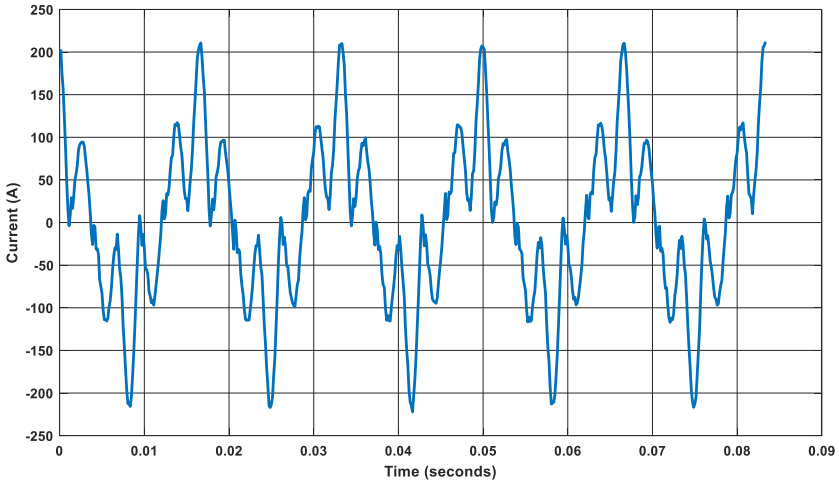

Figure 6.35 C-phase current measurement: S_6 output for 155.6 A

Table 6.13 Sensor S_6 results of measuring C-phase currents

C-Phase current true RMS values recorded from ammeter (A)	**True RMS value estimated for S_6 (A)**	**Percentage error (%) between recorded RMS value and estimated RMS value**
83.9	84.25	0.41
90.6	90.31	0.32
97.8	97.89	0.09
106.2	106.09	0.10
113.6	113.60	0.00
121.4	121.58	0.15
128.8	128.90	0.08
135	135.43	0.32
141.6	141.83	0.16
148.5	149.05	0.37
155.4	155.77	0.24

6.6 Summary

The TMR sensors are successfully tested for the three-phase current measurement with various combinations of groups and for two types of overhead three-phase structures that are in practice in Canada for AC power distribution system. The tests were performed using the balanced three-phase currents which yield equal magnitudes for all phases and a constant phase difference of 120^0 between each phase. The comparison of sensors for all combinations in triangular structure arrangement showed that S_1 and S_2 had variations in their vector errors with change at different times during various combinations. Sensors S_9 and S_{10} showed consistently low errors for all distances and when applied in groups of two- and three-sensors per phase. The highest error was observed for S_1 with the average value of 1.621% and it is the highest value among all combinations for the triangular structure. The other sensors showed very less variation in the percentage TVE for all combinations. For horizontal structure, the maximum %TVE was noted for S_1 for the distance of 35 mm and for sensor S_1 with a value of 1.626% when utilized for the combination of three-sensors per phase. The distance did not affect the performance of the sensors to a large extent.

From the comparison of the performance of nine sensors after applying them to triangular and horizontal structure, it was observed that the distance affected their performance only for 25 mm and 35 mm. The sensors of B-phase and C-phase in horizontal structure provided lower errors as compared those for triangular structure for both 25 mm and 35 mm distances. However, A-phase sensors for horizontal structure contributed higher errors as compared to those in triangular structure for the 25 mm and 35 mm. Overall the highest error was observed to be 1.63% for S_1 with remaining all sensors showing errors in the range from 0.1% to 0.7% for all combinations. The errors were observed to be decreasing for higher magnitudes of source current. The CTs showed consistent performance with 0.65% of TVE for all fundamental frequency currents. The percentage TVE average values of almost all sensors in all cases were observed to be better than those of the CTs applied to each phase. The detail analysis proved that the sensors could impart even better results when applied to measure higher values of three-phase currents. Moreover, the application of sensor data fusion was unessential for the measurement accuracy of the sensors for measuring individual phase currents unless one needs to reach a value below 0.02%.

For three-phase field experiment, the results of one sensor per phase are demonstrated in the performance analysis. A slight variation of the sensor placement from its respective phase conductor resulted in the errors and is shown in the table for each sensor. The MFs obtained for each RMS input current for each sensor were proportional to the distance, resulted in errors. This concludes that the calibration of sensor depends on the distance and therefore, it is recommended that for future field applications, the sensors are needed to be calibrated based on the distance and need to be firmly placed at that distance if the accuracy is to be maintained.

Chapter 7. Detection of Unbalanced Three-Phase and Neutral Currents by using TMR Sensors

7.1 Introduction

The AC power delivery to widespread geographical areas and growing cities is mostly happening through the overhead transmission and distribution lines. In a multi-grounded distribution system with a large variation of soil type there is a high probability of undetected high-impedance faults leading to difficulty in detection of fault location. Different geographic conditions and weather conditions add up to the difficulty in sensing high-impedance ground faults. These undetected faults can reoccur and cause damage to the power system equipment as well as pose life safety hazard. Installation of the protection relays at the substations may not always prove successful in detecting the exact location of incipient faults caused due to neutral unbalance or ground faults. Moreover, the installation of conventional CTs is not a practical and economical solution for transmission and generation utilities to cater the need of accurate detection of these faults. The conventional core wound current transformers undergo saturation under symmetrical and asymmetrical fault condition and thus limiting the fault detection capability of protection relays.

A detail analysis on the performance of TMR sensors for measuring single-phase currents and balanced three-phase currents is demonstrated in the previous chapters. The work presented in this chapter is a further step to pursue the experimental results of three-phase and neutral current measurement in an unbalanced three-phase AC power system with the help of TMR sensors. The accuracy of the sensor for single-phase and three-phase current measurement is successfully proved by testing, calibrating, and validating the sensors for various scenarios such as, current with a range of magnitudes and, various distances from the current carrying conductor. The experiment and testing for a three-phase setup in this chapter is also aimed at comparing the performance of TMR sensors with conventional CTs in AC currents measurement.

7.2 Experimental Setup

A three-phase overhead conductor triangular arrangement was selected for this experiment where the spacing between two horizontal phase conductors is 103 cm and the height of the third conductor from the horizontal plane of two conductors is 98cm as shown in Figure 7.1. A multi-strand XLPE aluminum cables of size AWG # 4 with insulation were chosen for each phase in the experiment. The insulation was removed from all conductors for a length of 50 cm. A three-phase star-connected resistive load was designed for this experiment using a resistance of 1 kW per phase and was connected in series with each phase conductor to represent a resistive load. The other end of each resistance was connected using an AWG # 8 wire to a common point. This point was the neutral point of the circuit. The experiment was performed for a range of magnitudes of current at a fixed distance of 7 mm for all sensors from each phase conductor.

The circuit diagram along with the sensor's location is similar to that explained in the previous chapter in Figure 6.2 except for number of sensors. In this experiment two sensors were placed near the bare part of each conductor with an orientation of 90^0 to the conductor plane and on the same side for all phases as shown in the Figure 7.1. To measure the neutral current one TMR sensor (#S_{11}) was installed on the neutral conductor as shown in the Figure 7.2 (a).

For comparing the performance of TMR sensors, three conventional core wound donut type CTs with a 0.15% accuracy and ratio 100 A: 100 mA were utilized in this experiment. These CTs were installed on each phase conductor, and on the neutral conductor of the circuit as shown in Figure 7.2 (b). Thus, four identical CTs were used in this experiment.

The experiment was performed in two parts, first for balanced three phase currents and the second, for three-phase unbalanced currents. In Part I, all six sensors were placed at 7 mm from the respective phase conductors with no-insulation part. The neutral sensor was also placed at 7 mm distance from the AWG#8 conductor that was connected to the current source. For part I, three-phase currents of frequency 60 Hz with variation from 5 A to 17 A with a step of 0.5 A were injected in the three-phase circuit using Omicron CMC356 current injection set. The sensor outputs and the CT outputs were recorded using NI cDAQ-

9174 data acquisition system. The specified timing resolution of this A/D converter is 1ns and timing accuracy of 50 ppm of sample rate. It has 16 channels with the maximum sampling rate of 500 kHz and each channel to have 45 kHz. Eleven channels were used for this experiment and the sampling rate for each channel was kept at 7.2 kHz. From each set of three-phase current injected, 10000 samples were recorded by using each channel input. Thus, for the symmetrical three phase system the outputs were recorded for each value of current from 5 A to 17 A. For Part II, the current inputs were changed from balanced to unbalanced as shown in the Table 7.1 and, the output of the sensor and CT on the neutral were recorded in addition to the sensors and CTs on three phases.

Two sets of three-phase currents selected for the second part of the experiment. First set included unbalanced components and, was introduced by changing the angles of each phase for example, case#1 has $9<80^0$, $13<-170^0$ and $4<150^0$ whereas for the second set of unbalanced currents, these angles were changed to a different value. For example, the case#1 parameters become $2<120^0$, $9<-40^0$ and $13<20^0$. For both sets, there were five cases of three-phase currents with magnitude and phase angle chosen as shown in the Table 7.1 to measure the outputs of each sensor for respective phase and neutral current.

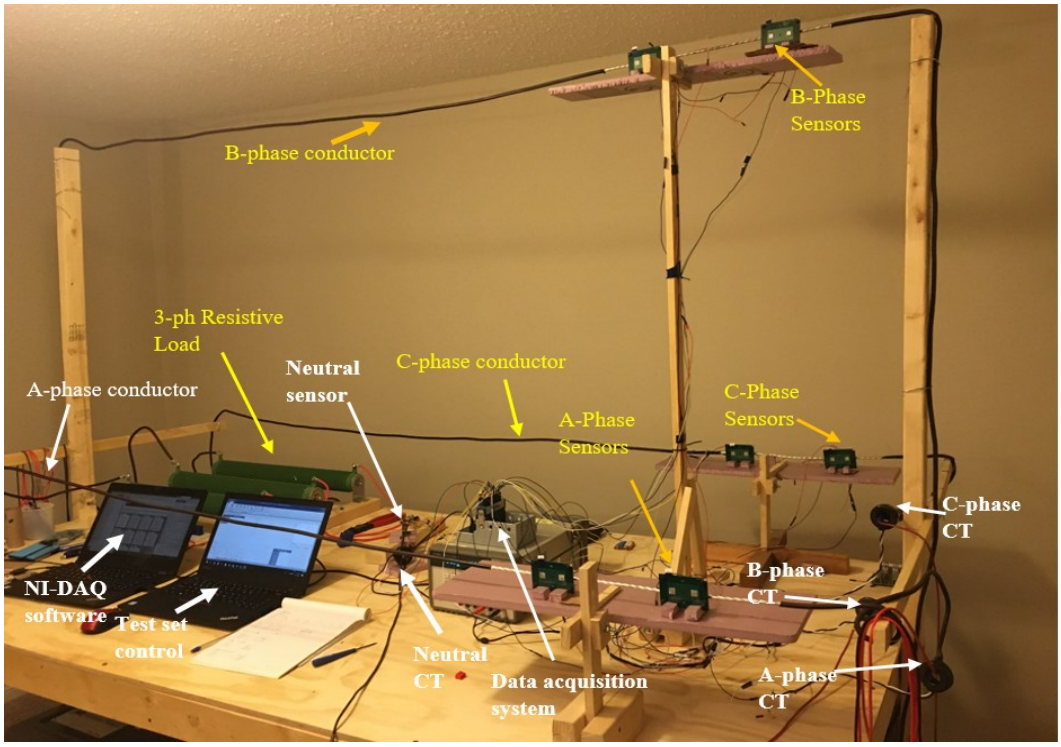

Figure 7.1 Experimental setup for neutral current measurement

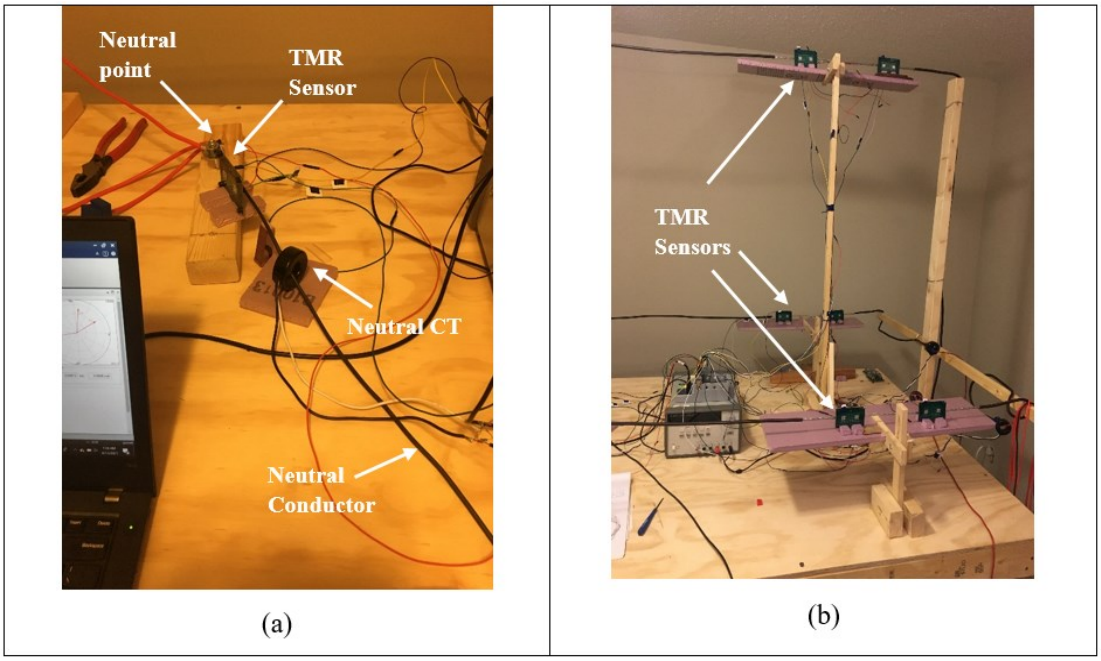

Figure 7.2 TMR Sensors and CTs installed on (a) neutral and (b) three-phases

Table 7.1 Test cases for three-phase current injection

Test Sets	**Balanced set of three-phase currents (A)**		
SET # 1	**A-Phase**	**B-Phase**	**C-Phase**
Case # 1	$9\angle 80^0$	$13\angle -170^0$	$4\angle 150^0$
Case # 2	$12\angle 80^0$	$4\angle -170^0$	$9\angle 150^0$
Case # 3	$2\angle 80^0$	$7\angle -170^0$	$12\angle 150^0$
Case # 4	$4\angle 80^0$	$9\angle -170^0$	$14\angle 150^0$
Case # 5	$5\angle 80^0$	$10\angle -170^0$	$2\angle 150^0$
SET # 2	**Unbalanced set of three-phase currents (A)**		
	A-Phase	**B-Phase**	**C-Phase**
Case # 6	$2\angle 120^0$	$9\angle -40^0$	$13\angle 20^0$
Case # 7	$6\angle 120^0$	$12\angle -40^0$	$2\angle 20^0$
Case # 8	$3\angle 120^0$	$13\angle -40^0$	$8\angle 20^0$
Case # 9	$13\angle 120^0$	$4\angle -40^0$	$8\angle 20^0$
Case # 10	$3\angle 120^0$	$9\angle -40^0$	$14\angle 20^0$

The amplification gains of the Wheatstone bridge and other components in the sensor circuit are combined to give the sensitivity of the sensor as 20 mV output for 1mT at 1VDC power supply. Thus, the outputs from sensors were directly connected to the A/D converter and further analysis performed to estimate the current from the measured magnetic field. The circuit diagram of the setup is shown in Figure 6.2 in the previous chapter and, it gives an idea of three stages: first the sensors and CTs, second, the A/D converter and third, the computer for application of algorithms and analysis. The TMR sensors named and calibrated in the previous experiment were utilized for this experiment with specific allocation of S_1, S_2 for A-phase, S_5 and S_6 for B-phase, S_9, S_{10} for C-phase and S_{11} for the neutral current.

7.3 Computation of Current Phasors

The outputs of all sensors were measured and recorded in terms of discrete samples with a sampling rate of 120 samples per cycle. The algorithm for calibration and estimation of the current magnitudes and phasors for sensors is similar to that explained in the previous chapter and illustrated in Figure 6.4. The algorithm and computation were repeated for the outputs recorded for symmetrical as well as asymmetrical current input sets designed for this experiment and the MFs were estimated and verified during this experiment for all sensors. It was observed that the MFs obtained for sensors S_1, S_2, S_5, S_6, S_9, S_{10} and S_{11} in previous experiments were utilized for the analysis in this experiment including the calibration factors of CTs. For analysis, the data samples were divided into two parts; first, 5000 samples were utilized for obtaining the multiplying factor and the current phasors both, using the orthogonal functions and then, the remaining 5000 samples were used for the validation. The multiplying factors obtained during the testing and validation steps were used for verification of the results of seven sensors deployed in this experiment. The algorithm estimated the magnitude errors in percentage for phase currents and neutral currents for sensors and CTs. In this case, the output of CT installed on the neutral was considered as the reference for comparing the accuracy of the TMR sensor installed on the neutral.

7.4 Test Results

Computational results were obtained for both symmetrical and asymmetrical input currents applied during the test. The behavior of the sensor for both types of input currents is shown in the Figure 7.3 and Figure 7.4. The outputs of sensor S_5 obtained for symmetrical B-phase current magnitudes for 5 A, 10 A and 15 A are shown in Figure 7.3 (a), (b) and (c) respectively. It is evident from this figure that the estimated magnitudes of current phasors vary in the range of -0.064 to +0.034 A for the first two cases of 5 A, and 10 A and from -0.082 A to +0.093 A for the 15 A case. The estimated results for asymmetrical currents are shown in Figure 7.4 (a) for sensor S_1, Figure 7.4 (b) for sensor S_5 and Figure 7.4 (c) for sensor S_9 respectively. The asymmetric currents injected for this case are from the test case#7 where $I_A = 6\angle 120^0$, $I_B = 12\angle -40^0$ and $I_C = 2\angle 20^0$. From the variation range of the

outputs for each case of sensor shown in Figure 7.4, it is observed that the accuracy of the algorithm for estimation of sensor outputs for asymmetrical input currents is satisfactory and, matches with that for the symmetrical input currents.

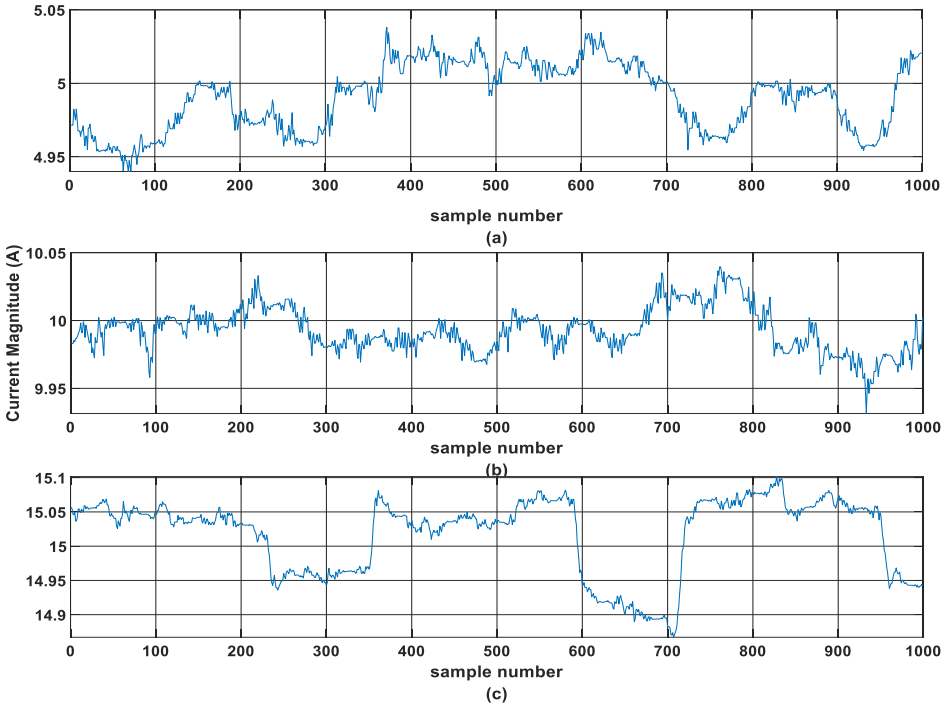

Figure 7.3 Magnitudes of current outputs of sensor S_5 calculated for 5 A, 10 A and 15 A

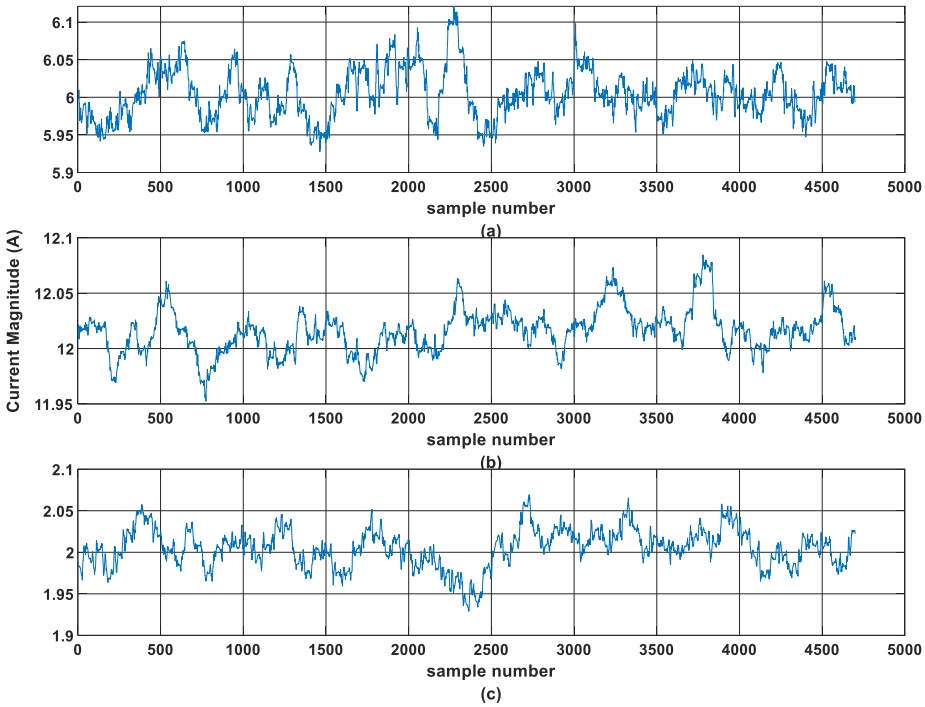

Figure 7.4 Estimated currents for (a) sensor S_1 (b) sensor S_5 and (c) sensor S_9

7.4.1 Results for Symmetrical Three-phase Currents for Phase Sensors

The first part of the test was to inject a set of three-phase balanced currents where the angle between each phase is 120^0. There were 17 sets of input currents from 1 A to 17 A injected in the three-phase circuit at a time interval of 5 minutes. The results of all cases were obtained using the computation program based on the algorithm developed in MATLAB and discussed in the previous chapter. Figure 7.5 shows the estimated output of sensor S_1 for A-phase, 10 A current and compared with the output of CT on the same phase. It is observed that the relative percentage error in magnitude for this output was 0.754%. Figure 7.6 shows the output of sensor S_5 for Phase B as compared to the B-phase CT output for 15 A.

Similarly, for the input current of 15 A on C-phase, sensor S_9 shows the output comparison with C-phase CT as shown in Figure 7.7. From all these figures, it is evident that the sensors have same accuracy. The advantage of digital sensors is that there is no saturation effect,

or hysteresis involved in the operating characteristics as compared to the conventional CT. The relative errors in the outputs for the balanced phase currents for all sensors were found to be very low, with minimum error of 0.0013% and maximum error of 1.19.

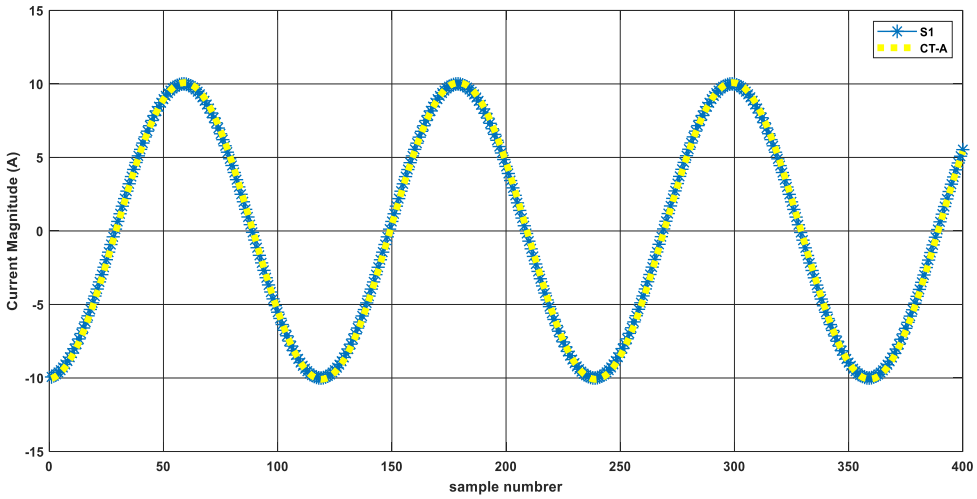

Figure 7.5 Calculated output of sensor S_1 and CT for A-phase, 10 A

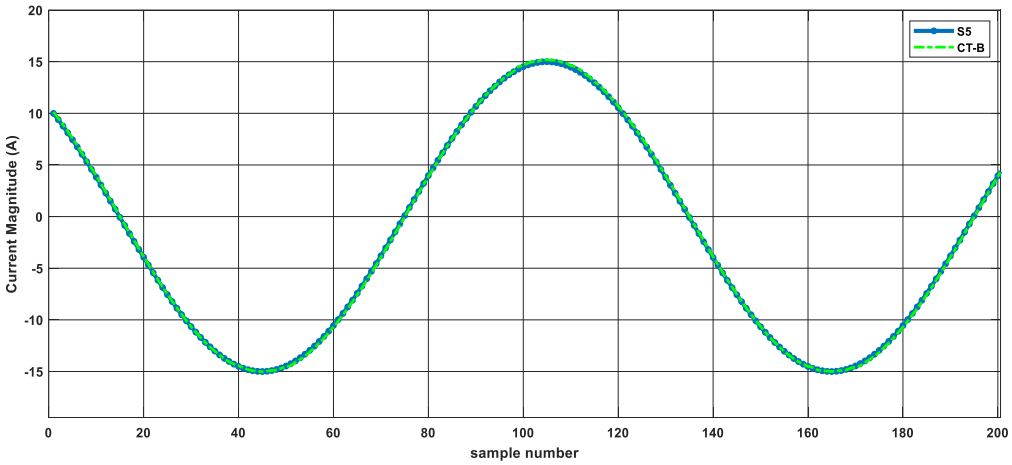

Figure 7.6 Calculated output of sensor S_5 and CT for B-phase, 15 A

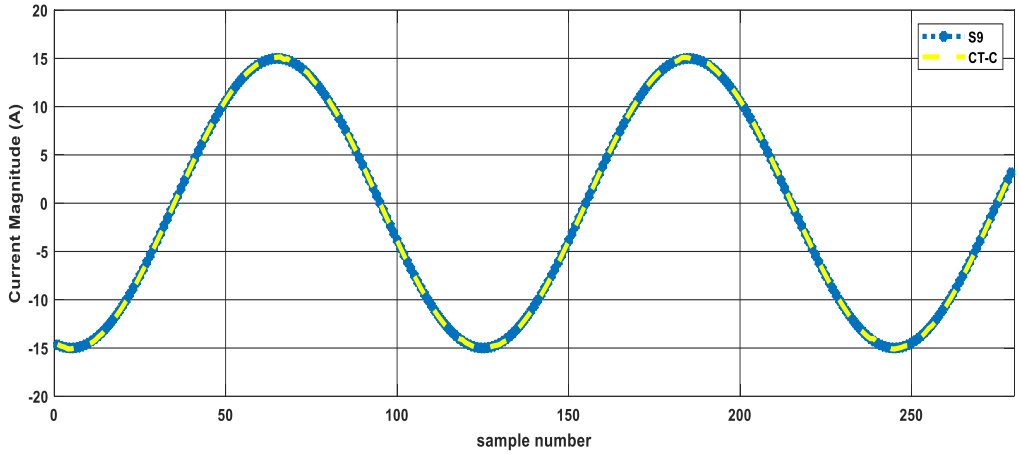

Figure 7.7 Calculated output of sensor S_9 and CT for C-phase, 15 A

It is observed that the sensor performances are more accurate than those of CTs. This is evident from the comparison of the A-phase CT and S_2 output for 15 A where the CT-A's peak output exceeded the magnitude of 15 A whereas, the sensor S_2 shows exact 15A magnitude with a relative error of 1.29%. By considering the 15A input current as a reference, the sensor showed relative error of 0.0032%.

7.4.2 Results for Neutral Currents

The unbalanced three-phase currents result in the neutral current. The generation of the neutral current was created for this experiment with the help of four cases of unbalanced currents from case#6 to case#9 shown in the Table 7.1. The output of the phase sensors as well as neutral sensor and respective CTs were recorded for each case. The measurements were used to estimate phase currents as well as neutral current using the algorithm programmed in MATLAB. Figure 7.8 shows the output of the sensor S_{11} for the test case#6 of asymmetrical currents.

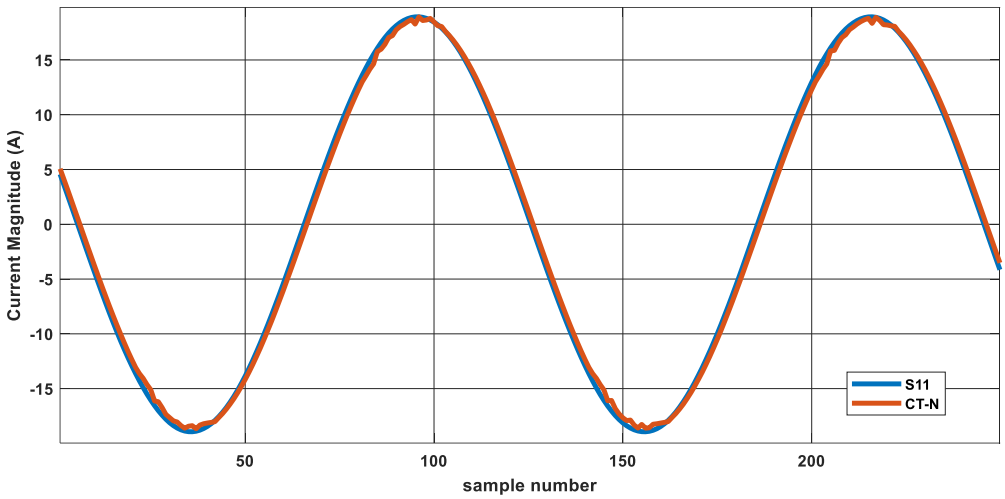

Figure 7.8 Output of sensor S_{11} for neutral current, case#6

The relative error in the magnitude for the case#6 is 0.0581%. The magnetic field generated by the resultant neutral current that has occurred because of the unbalanced three-phase currents is measured by sensor S_{11} in all cases from case#6 to case#10. Figure 7.9 shows the output of the sensor S_{11} for case # 7 and in this case the magnitude error is 0.0133%.

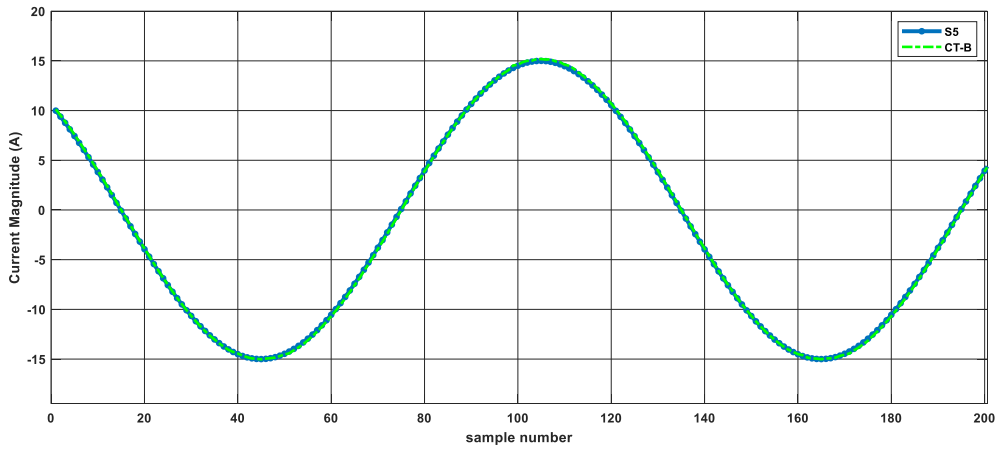

Figure 7.9 Calculated output of sensor S_5 and CT for B-phase, 15 A

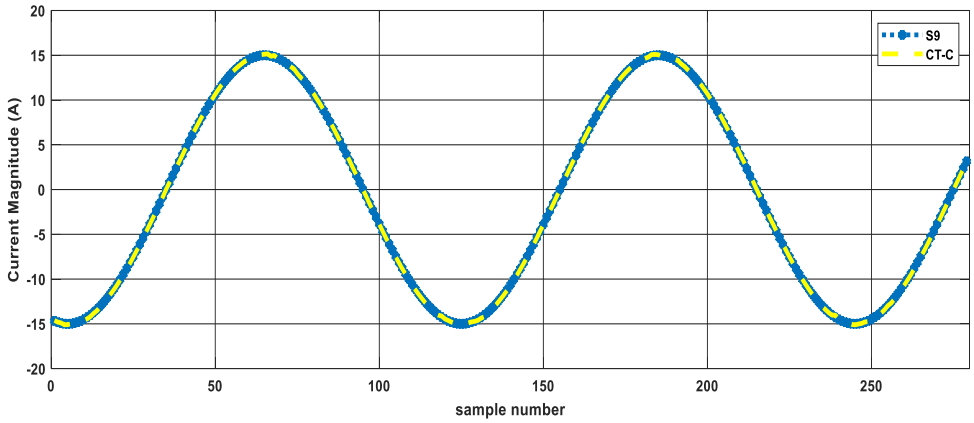

Figure 7.10 Calculated output of sensor S_9 and CT for C-phase, 15 A

Figure 7.10 shows its output for case#3 with the error between the neutral sensor and CT-N to be 0.0964%. The output of the S_{11} for case # 4 is shown in the Figure 7.11 with an error of 0.1626%. The estimated neutral current using the multiplying factors obtained using DFT method show high accuracy with the minimum relative error of 0.0581% and maximum error of 0.1626%. The output of S_{11} for the last case, i.e., case # 10 resulted with an error of 0.07321% as compared to that of the CT-N magnitude. From all these cases it is inferred that for each case, there was a high accuracy in calculating this current by the TMR sensor as compared to the neutral CT and is evident from all figures shown above.

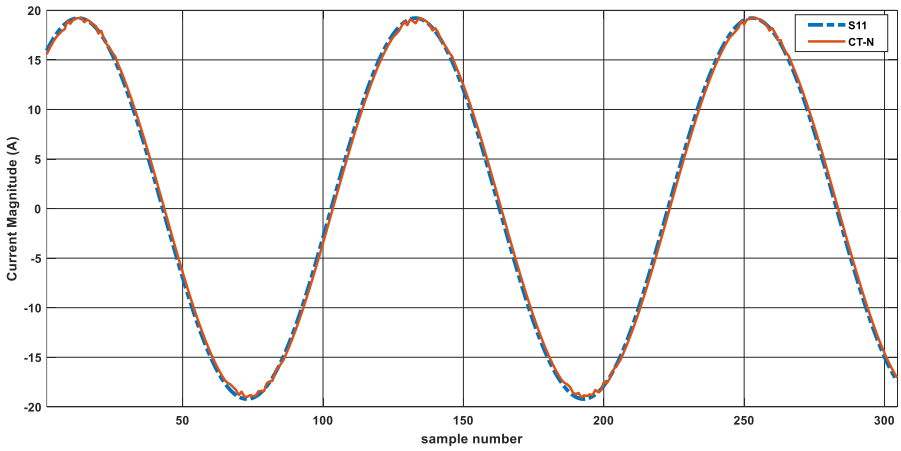

Figure 7.11 Output of sensor S_{11} and CT-N for neutral current, case#9

7.5 Summary

The performance of TMR sensor pairs in measuring three-phase current as well as neutral current using one TMR sensor is studied for a fixed distance of 7 mm from the bare conductor and for a frequency of 60Hz. For balanced system, the maximum relative error of 1.29% was noted in sensor S_2 as compared to the output of high accuracy CT and, the minimum error of 0.0013% was observed for sensor S_9. This proves that the DFT technique provided accurate multiplying factors to convert the sensor magnetic field output in terms of voltage to current. This also helped in estimating the neutral current as well as unbalanced three-phase currents. Generally, the sensors show better performance for a higher magnetic field which can be produced by higher magnitude of AC currents. In this study, a three-phase current range was chosen up to 17 A per phase. The TMR sensors chosen for this experiment have range up to 200 A AC. From the accuracy of sensors for lower currents, it is expected that the performance of these sensors will be even more accurate for higher three-phase currents. The HV laboratory test results shown in the Chapter 4 proved their ability to successfully measure single phase currents. The valuable outcome of this study is that the sensors were able to obtain the neutral current even more accurately than the conventional high accuracy CT as observed from the figures and, the relative errors between actual currents, the outputs of CTs and, the outputs of TMR sensors.

Chapter 8. Conclusions and Future Work

8.1 Research Findings from the Present Work

The application of traditional instrument transformers has been in practice for more than a century and accepted as the simplest technique for measuring alternating current in the power systems applications. The manufacturers of power system protection relays have been using computationally expensive microprocessor-based algorithms to overcome the drawbacks of CTs and provide accurate protection logic. Therefore, an attempt of solving the main problem is made through this thesis. The magnetic field sensing technique using magnetoresistance has been established since 1980s but never was referred for current applications. A high-quality magnetic sensor based on TMR effect can sense currents up to 200 A in both DC and AC applications. Such sensors are definitely advantageous towards achieving the goal of current measurement in low and medium voltage power distribution system.

This thesis introduces an innovative current measurement technique with a comprehensive study on non-invasive current sensing for singe-phase and three-phase power systems applications. A theoretical study and literature survey was conducted to formulate the main objectives and define the challenges in this endeavor. This thesis successfully addressed the major issues such as the effect of distance on the strength of measured magnetic field, effect of harmonics, effect of magnitude of source currents, sensor quality and interference of neighboring magnetic field on the measurement accuracy.

Proposed technique was investigated through theoretical simulation and modeling of the magnetic field generated in a medium and high voltage overhead system with the help of MATLAB computational software. An algorithm was developed using least square technique for overcoming the interference of neighboring magnetic field in three-phase system to estimate accurate single-phase currents. This simulation study also provided the most favorable locations in a three-phase conductor system for sensing magnetic field with less errors.

The selection of suitable sensor was performed by conducting initial laboratory tests on a few types of sensors available in the market. TMR sensor passed the initial screening tests such as linearity, sensitivity for lower currents etc. and was taken for the further stages of research. Twelve TMR sensors were successfully calibrated and tested for their response to various factors such as, sensing low and high frequency currents, effect of distance on their sensitivity through laboratory experiments with overall measurement error to be 0.0013% in current measurement.

The verification of sensors performance during single-phase experiment for various distances indicated that there was a need to calibrate each sensor separately to achieve a better accuracy in current measurement that is independent of the distance from source or the magnitude of source current.

Verification of sensors for measuring high currents up to 1500 A was a noticeable achievement in this research. The HV laboratory tests showed that the sensors can measure the magnetic field density from a distance of 15 cm with a good accuracy and limit the %TVE below 0.05%. The results of six sensors showed consistent performance even though their individual MFs used for calibration were different for each sensor. One interesting conclusion obtained from this experiment that the MFs obtained for 15 cm distance from the HV laboratory tests were 10 times greater than those obtained for 1.5 cm in the low current laboratory tests. This proved that the sensors can be calibrated successfully for any distance without testing if, their MFs are known for one distance. However, their performance depends on the distance from the current carrying conductors. The sensors are calibrated for a particular distance selected prior to the measurement application. Therefore, a slight variation in the distance may introduce the errors in the measurement. However, the change in the distance will not affect the measurement accuracy if the sensors are installed very close to the conductors and tied to them using proper means, such as tie wraps. The investigation of the sensors when installed in triangular and horizontal structure led to the results that all sensors had percentage total vector error in the range of 0.1% to 0.7% except for S1 which had 1.63% error. The application of sensor data fusion technique improved their measurement accuracy and reduced the error in all combinations of four sensor pairs to 0.02%.

The field experiment on a three-phase unbalanced load which was also a source of generating harmonics provided practical scenarios to test the performance of sensors. The outputs of the sensors for each phase were estimated using the multiplying factors that were obtained from the laboratory test results of single-phase experiment explained in the previous chapters. The clamp-on type ammeter readings were used in the analysis as a reference to compare the accuracy of the estimated currents from the outputs of the sensors. The readings of the meter were true RMS values and, therefore, in this case, the true RMS values of the currents were estimated for each sensor and for each stage. The sensors performed satisfactory in measuring three-phase currents. Moreover, it is proven that the harmonics present in the input current did not affect the measurement accuracy of the sensors. The results obtained for each sensor show that their performance varies based on the distance they are placed at, and their calibration needs to be done separately when deployed in the field to measure three-phase currents. This experiment also proves a practical condition that the three-phase loads may not necessarily be balanced always and have pure sinusoidal load. The quality of the current is always defined by the load and proved by this experiment. In addition, this experiment also illustrated the fact about space constraint inside AC power distribution panel with practical difficulties to install conventional CTs.

8.2 Research Contributions of the Present Work

The sensors have been repeatedly tested and validated by conducting experiments at various times and with the same test procedures. Moreover, the standard deviation in the %TVE, magnitude error, and the angle error obtained for each sensor was observed to be very low for all test currents, which indicate that these sensors have a very good repeatability.

The verification of sensors on the horizontal and triangular types of structures also ensures that their accuracy will remain unaffected for any other type of structure if they are placed not more than 15 cm.

The novel technique for estimating the angle error for all measured samples in absence of time-stamped data proved very efficient in calculating the accurate current phasors for three-phases from the measured data for all sensors.

These sensors also showed better accuracy in obtaining three-phase and neutral current when faced to asymmetrical source currents. The distance factor didn't affect to a large extent to the accuracy of current measurement for all sensors because of the effective calibration.

The sensors were able to faithfully produce the currents in presence of harmonics. The outputs of sensors matched with the true RMS value shown by each meter accurately to the accuracy of 1%. In case, the instantaneous samples known and recorded for the input current using CTs, it could be used to prove that the sensors perform better than the CTs using DFT technique.

The major contributions of this research are to overcome all drawbacks of the core-wound current transformers (CTs). There are four major drawbacks of the CTs; the first being the saturation issue because of its iron-core. The higher accuracy CTs means a higher CT ratio which requires a greater number of copper windings resulting in higher size, bigger diameter and more weight. Therefore, they are difficult to install on a busbar or a circuit breaker phase conductors inside the medium voltage or high voltage switchgear. In addition, a higher ratio CT means higher cost. A TMR sensor overcomes all these issues because of its tiny size, and its ease of installation at any place indoor or outdoor in the substation or switchgear or on the overhead conductors on poles.

The second major advantage of the magnetic sensors is that they are free of any hysteresis, giving a fully linear response to the primary current. Another drawback of CTs is their dependence on the burden which decides their accuracy class. In case of TMR sensors, there's no requirement of designing any burden and therefore these sensors are free of any external element for their accuracy.

The medium and high voltage CTs are oil filled in order to withstand the temperature. They are prone to explosion because of high temperature, open secondary circuit, and damage to their insulation due to lightening. Therefore, they pose very high risk due to safety hazard

during operation. In contrary, the TMR sensors have no requirement of oil-filled insulation, can be isolated from the circuit if damaged without any safety hazard, because they have no physical contact with the live circuit and have no possibility of developing immensely high potential across their output terminals in case their circuit is open.

Another contribution of this research is to introduce a device for current measurement which is economically cheaper as compared to core-wound CTs for low and medium voltage applications. The price of CTs is driven by the price of copper. The higher the accuracy, higher the price. In contrary, the size of TMR sensors is very small which makes them economically feasible for installation, wiring, and operation for any application.

The most valuable contribution of this research is to identify, investigate, test and verify the application of TMR sensors for contactless installation and measurement current with a proven accuracy of 99.68% for low and medium voltage application.

To conclude finally, the TMR sensors can be successfully deployed in the field for measuring three-phase currents up to 1500 A. From the investigation results presented in this thesis it can be concluded that the sensors reached to a level of qualification where, they can function as a reliable backup to the conventional CTs that are present in the existing industrial, and utility establishments for measuring three-phase currents or can also be used as a primary source of current measurement at any upcoming distributed generation facility.

8.3 Limitations of the Present Work:

There are a few limitations of the present research work. The range of voltage up to which these sensors can perform better is not tested above 44 kV. The currents in that range will be more than 2000 A and, in that case, proper safety procedures are needed to investigate their performance safely. The impact of the extreme temperatures during winter and summer are not tested during this research. The laboratory and field work conducted during indoor conditions that had controlled temperatures. The prototype built for the experimentation work during this research was not waterproof. Therefore, the performance of sensors was not tested for rainy conditions either. The range of current inside the laboratory was limited because of the technical specifications of the current inject test set.

The higher currents up to 300A could have given more data for analyzing and calibration of the sensors for a wide range of currents.

8.4 Future Work

There are a few tasks that still need to be investigated and experimented with to make this technique more useful for implementation in industrial and utility applications. The following are suggested to undertake in the future:

1) Field testing for performance verification.

The sensors can be tested for sensing three-phase higher currents from 50 A to 300 A typically observed in a medium voltage power system distribution substation feeding to assigned subdivision load. The field test will require installation of these sensors on each phase conductor or copper bus of a 15 kV distribution feeder inside the switchgear panel of a feeder breaker. The installation task needs the outage of the substation to safely install the sensors inside the switchgear panel. After installation, the substation can be switched back in the service and the feeder currents can be measured using the TMR sensors per phase. To achieve redundancy in measurement, two sensors per phase can be utilized for this application. The current phasors estimated from recorded data using DFT can be compared with the actual phasors recorded either through the CTs that are installed on the feeder or through the phasor measurement units installed on the feeder protection panel.

The field testing can also be performed on the outdoor three-phase medium voltage overhead structures with arrangement other than triangular and horizontal to prove the versatility of sensor field applications.

2) Field tests for short circuit current sensing

The sensors were tested in the laboratory for low frequency currents to simulate the fault current that inhibits DC decay by injecting currents of very low frequencies. The results showed satisfactory performance with good accuracy in measuring the low frequency currents whereas the CT of high accuracy (0.15%) failed to measure

them and instead, showed saturation. The verification of this laboratory test can be achieved by conducting field experiments, in which, the sensors can be installed on a three-phase feeder inside a substation for a longer period to sense fault currents. Generally, the single phase-to-ground faults mostly occur in the summer due to trees touching the overhead lines or due to animal contact. These scenarios can give a real fault sensing opportunity to test the performance of sensors. This will also need a long-term data recording function and data access facility while the sensors are installed on the live feeder conductors inside the substation.

3) **Testing effect of rain and cold weather on the performance of TMR sensors**

This test is important to validate the sensors for outdoor current sensing application in various geographical locations and varying weather conditions. The tests can be performed by preparing a weatherproof case for the sensors and installing them in an outdoor setup for current measurement during the winter and rainy seasons. A weatherproof harness of wires and DC power supply is necessary for this experiment. Further possible issues need to be investigated before setting up the outdoor experiment.

REFERENCES

[1] L. Moslehi, R. Kumar, “A Reliability Perspective of the Smart Grid”, IEEE Transactions on Smart Grid, Vol.1, No. 1, June 2010, pp.57-64.

[2] Campbell, R. J., “Weather-related power outages and electric system resiliency,” CRS report for congress, Congressional Research Service, 7-5700, Websource: www.crs.gov, R42696, 3–14, 2012.

[3] “MIT Energy Initiative: Utility of the Future”, an MIT Energy Initiative Response to an Industry in Transition, 2016 Massachusetts Institute of Technology. Websource: www.energy.mit.edu/uof

[4] “The Future of the Electric Grid, An Interdisciplinary MIT Study”, https://energy.mit.edu/wp-content/uploads/2011/12/MITEI-The-Future-of-the-Electric-Grid.pdf, ISBN 978-0-9828008-6-7

[5] M. C. Schmidt, Electric power research trends. New York: Nova Science Publishers, 2007.

[6] V. Terzija, G. Valverde, C. Deyu, P. Regulski, V. Madani, J. Fitch, et al., "Wide-Area Monitoring, Protection, and Control of Future Electric Power Networks," Proceedings of the IEEE, vol. 99, pp. 80-93, 2011.

[7] IEEE Guide for Electric Power Distribution Reliability Indices, IEEE 1366-2012.

[8] “Blackout Tracker, Canada Annual Report 2017”, Power Outage Annual Report by Eaton, https://www.eaton.com/content/dam/eaton/products/backup-power-ups-surge-it-power-distribution/backup-power-ups/blackout-tracker-/eaton-blackout-tracker-annual-report-canada-2017.pdf

[9] J. L. Blackburn, T. J. Domin, “Protective Relaying: Principles and Applications,” Third Edition. CRC Press, Taylor and Francis Group. pp 144-269.

[10] Electrical Distribution-System Protection, Cooper Power Systems, Jan 1, 2005. pp 27-69.

[11] G. Benmouyal and S.E. Zocholl, “Impact of high fault current and CT rating limits on overcurrent protection,” presented at the 29th Annual Western Protective Relay Conference, Spokane, WA, 2002.

[12] IEEE Std. C37.110-2007, IEEE Guide for the Application of Current Transformers Used for Protective Relaying Purposes.

[13] A. Hargrave, M. Thompson, B. Heilman, “Beyond the knee point: A practical guide to CT saturation”, 2018 71st Annual Conference for Protective Relay Engineers (CPRE), pp. 1-23

[14] IEEE Std. C57.152-2013, IEEE Guide for Diagnostic Field Testing of Fluid-Filled Power Transformers, Regulators, and Reactors.

[15] D. M. Robilino, “Power Transformer Demagnetization”, 2016 IEEE 36th Central American and Panama Convention (CONCAPAN XXXVI), pp. 1-5, 2016.

[16] DEM60R-Transformer Demagnetizer DEM Series, DVPower, (https:// www.dv-power.com/product/transformer-demagnetizer/demagnetizer-dem/)

[17] S.E. Zocholl, G. Benmouyal, and J. Roberts, “Selecting CTs to optimize relay performance,” presented at the 23rd Annual Western Protective Relay Conference, Spokane, WA, 1996.

[18] R.A. Pfuntner, “The accuracy of current transformers adjacent to high current buses,” AIEE Trans., vol. 70, 1951.

[19] S. Ziegler, R. C. Woodward, H. Lu, L. J. Borle, “Current Sensing Techniques: A Review,” IEEE Sensors Journal, vol. 9, no. 4, pp 354-376, April 2009.

[20] J.A.Ferreria, W.A.Cronje, and W.A.Relihan, “Integration of high frequency current shunts in power electronic circuits.” IEEE Transactions on Power Electronics, vol. 10, pp.32-37, 1995

[21] F. Costa, P. Poulichet, F. Mazaleyrat, and E. Labaoure, “The current sensors in power electronics, a review,” EPE Journal, vol. 11, pp. 7-18, 2001.

[22] W.F. Ray and C.R. Hewson, “High Performance Rogowski Current Transducers”, Proceedings of IEEE Industrial Applications Conference, Rome, Italy, pp. 3083-3090, 2000.

[23] P. Ripka, “Electric Current Sensors: A Review,” Measurement Science Technology. Vol.21 112001, pp.1-23, 2010

[24] S. Ziegler, R.C. Woodward, H.H.C. Lu, and L.J. Borle, “Investigation into static and dynamic performances of the copper trace current sense method,” IEEE Sensors J., 2009.

[25] Hall Effect sensing and application, Honeywell book. Online source

[26] P. Ripka, “Advances in fluxgate sensors,” Sensors and Actuators A, vol. 106, pp. 8–14, 2003.

[27] Binasch, G.; Grünberg, P.; Saurenbach, F.; Zinn, W. Enhanced magnetoresistance in layered magnetic structures with antiferromagnetic interlayer exchange. Phys. Rev. B 1989, 39, 4828–4830

[28] P. Mlejnek, M. Voplensky, P. Ripka, “AMR current measurement device”, Sens. Actuators A, vol. 141, pp 649-653, 2008.

[29] C. Reig, M. Dolores, C. Beltran, D. Munoz, “Magnetic Field Sensors Based on Giant Magnetoresistance (GMR) Technology: Applications in Electrical Current Sensing”, MDPI Journal of Sensors, Vol. 9, pp. 7919-7942, 2009.

[30] J. Lenz and A. S. Edelstein, “Magnetic sensors and their applications,” IEEE Sensors J., vol. 6, pp. 631–649, 2006.

[31] P. P. Freitas, R. Ferreira, S. Cardoso, F. Cardoso, “Magnetoresistive Sensors”, Journal of Physics: Condensed Matter, 2007, Vol. 19, 165221, pp. 1-21.

[32] M. Volmer, J. Neamtu, “Micromagnetic Analysis and development of high sensitivity spin-valve magnetic sensors,” Journal of Physics Conf. Ser., vol. 268, 012032, 2011.

[33] Z. Li, S. Dixon, “A Closed-Loop Operation to Improve GMR Sensor Accuracy”, IEEE Sens. Journal, vol. 16, pp. 6003-6007, 2016.

[34] G. Grandi, M. Landini, “Magnetic-field Transducer based on closed-loop operation of magnetic sensors”, IEEE Trans. Ind. Electron. vol. 53, pp. 880-885, 2006.

[35] X. Yang, C. Xie, Y. Wang, W. Yang, G. Dong, “Optimization Design of a Giant Magneto Resistive Effect Based Current Sensor with a Magnetic Field Shielding,” IEEE Transactions on Applied Superconductivity, vol. 24, pp.1-4.

[36] I. Jedlicska, R. Weiss, R. Weigel, “Linearizing the Output Characteristics of GMR Current Sensors through Hysteresis Modeling”, IEEE Trans. Ind. Electron. vol. 57, pp. 1728-1734, 2010.

[37] E.G. Vidal, D.R. Munoz, S.I.R. Arias, J.S. Moreno, R. Ferreira, P. Freitas, “Electronic Energy Meter Based on a Tunnel Magnetoresistive Effect (TMR) Current Sensor”, Materials, vol.10, pp. 1134-1143, 2017.

[38] C. Ye, Y. Wang, Y. Tao, "High-Density Large-Scale TMR Sensor Array for Magnetic Field Imaging," IEEE Trans. Instrumentation and Measurement, vol. 68, No. 7, pp. 2594-2602, 2019.

[39] M. Shafiq, G. A. Hussain, L. Kutt, M. Lethonen, "Electromagnetic Sensing for Predictive Diagnostics of Electrical Insultaion Defects in MV Power Lines", 2015 Elsevier Journal of Measurement, Vol. 73, pp.480-493, 2015.

[40] J. P. Sebastia, J. A. Lluch, J.R.L. Vizcaino, J. S. Bellon, "Vibration detector based on GMR Sensors", IEEE Trans. Instrum. Meas. vol. 58, pp. 707-712, 2009.

[41] N. McNeil, N. K. Gupta, S.G. Burrow, D. Holliday, P.H. Mellor, "Applications of reset voltage feedback for droop minimization in the unidirectional current pulse transformer", IEEE Transactions on Power Electronics, vol. 23, pp. 591-599, 2008.

[42] R. S. Popovic, P. M. Drljaca, C. Schott, "Bridging the gap between AMR, GMR, and Hall magnetic sensors", Proceedings of the 23rd International Conference on Microelectronics (MIEL2002), Nis, Yugoslavia, pp. 55-58, 2002.

[43] H. S. Dhani, A. Aminudin and Waslaluddin, "Characterization of AC current sensor based on giant magnetoresistance and coil for power meter design", IOP Conf. Series: Journal of Physics: Conf. series 1013 012177, pp 1-8, 2018.

[44] F. Xie, R. Weiss, and R. Weigel, "Giant-Magnetoresistance-Based Galvanically Isolated Voltage and Current Measurements," IEEE Trans. On Instrumentation and Measurement, Vol. 64, NO. 8, pp 2048-2054, Aug.2015

[45] A. D. Xu, L. C. Li, P. Li, Z. M. Wang, Z. B. Wu, C. J. Hao, "Application of Current Sensor Based on Giant Magnetoresistive Effect in Distribution Network", Intern. Conf. New Energy and Future Energy Systems, IOP. Conf. Series: Earth and Environment Science, vol.354, 12058, pp. 1-6, 2019.

[46] T. Y. Poon, N. C. F. Tse, R. W. H. Lau, "Extending the GMR Current Measurement Range with a Counteracting Magnetic Field", MDPI Journal of Sensors, Vol. 13, pp. 8042-8059, 2013.

[47] O. Yong, J. He, J. Hu, S. X. Wang, "A Current Sensor Based on the Giant Magnetoresistance Effect: Design and Potential Smart Grid Applications", Sensors, vol. 12, pp. 15520-15541, 2012.

[48] L. Bi, M. Wu, L. Xu, S. Sun, K. Yu, X. Zeng, "Power Systems Transient Current Sensor Based on Magnetoresistance Effect", IOP Conf. Series: Earth and Environmental Science, Vol. 668 012081, pp. 1- 7, 2021.

[49] M. Vopalensky, A. Platil, and P. Kaspar, "Wattmeter with AMR sensor," Sens. Actuators A, Phys., pp. 303–307, 2005, 123-124.

[50] X. Sun, K. S. Lui, K. K. Y. Wong, W. K. Lee, Y. Hou, Q. Huang and P.W.T. Pong, "Novel Application of Magneto-resistive Sensors for High-Voltage Transmission-Line Monitoring,"IEEE Trans. Magn., vol.47, no.10, pp.2608-2611, Oct. 2011.

[51] Qi Huang, W. Zhen, P.W. T. Pong," A Novel Approach for Fault Location of Overhead Transmission Line with Noncontact Magnetic-Field Measurement", IEEE Transactions on Power Delivery, Vol. 27, No. 3, July 2012, pp. 1186-1196.

[52] X. Li, J. You, X. Shu, R. Kang, "Electric Current Measurement using AMR Sensor Array", Proceedings of the 2009 IEEE International Conf. on Mechatronics and Automation, China, pp. 1-5, Aug.9,2012,

[53] L. Meng, P. Gao, M. M. Haji, W. Xu, "Magnetic Sensor Array-Based AC Current Measurement for Multiconductor Cables Using Evolutionary Computation Method", IEEE Transactions on Instrumentation and Measurement, Vol. 64, No. 10, pp. 2747-2759, October 2015.

[54] G. D'Antona, L. Di Rienzo, R. Ottoboni, A. Manara. "Processing Magnetic Sensor Array Data for AC Current Measurement in Multiconductor Systems", IEEE Transactions on Instrumentation and Measurement, Vol. 50, No. 5, pp. 1289-1296, October 2001.

[55] B. L. Theraja, A.K. Theraja, "A Textbook of Electrical Technology," S. Chand Publishing, Vol. I, pp. 140-147.

[56] Wiliam H Hyat, Jr., John A. Buck, "Engineering Electromagnetics", Eigth Edition. McGraw-Hill Higher Education. pp. 164-269.

[57] A. Greenwood, "Electrical Transients in Power Systems", Hoboken, NJ: Wiley, 1991, pp. 118–230.

[58] USF Section 01-17 January 2017, Overhead Primary Framing, Utility Standards Forum, Ontario, Canada.

[59] USF Section 2 April 2017, Voltages, Line Locations and Clearances for Distribution Circuits, Utility Standards Forum, Ontario, Canada.

[60] Tupsie, S., "Analysis of Electromagnetic Field using FEM for Transmission Lines Transposition," Journal Title Abbreviation, Vol. 34, No. 10, pp. 1064–1076, 2013.

[61] Pao-La-Or, P., Isaramongkolrak, P., Pao-La-Or, P., "Title of the journal paper," International Journal of Electrical and Computer Engineering, Vol. 3, No. 05, pp. 1174–1178, 2009.

[62] Hamayer, K., Mertens, R., Belmans, R., "Computation and measurement of electromagnetic fields of AC-high voltage transmission lines," Sixth International Conference on AC and DC Power Transmission, pp. 52–57, 1996.

[63] Farah, A. A. M., Afonso, M. M., Vasconcelos, J. A., Schroeder, M. A. O., "A Finite-Element Approach for Electric Field Computation at the Surface of Overhead Transmission Line Conductors," IEEE Transactions on Magnetics, Vol. 54, No. 03, pp. 1 – 4, 2018.

[64] Pao-La-Or, P., Kulworawanichpong, T., Sujitjorn, S., "Distributions of flux and electromagnetic force In Induction Motors: A Finite Element Approach," WSEAS Transactions on systems, Vol. 5, No. 3, pp. 617 – 624, 2006.

[65] Mismar, M., "Numercial Simulation of Maxwell's Equations," IOSR Journal of Engineering, Vol. 7, No. 03, pp. 01 – 10, 2017.

[66] M.N. O. Sadiku, "Numerical Techniques in Electromagnetics with MATLAB", Third Edition, CRC Press, pp 384-395

[67] *ABB Digital Switchgear* (https://library.e.abb.com/public/0510ff0f8dd442098a275ca0091ac184/UniGear%20Digital_Brochure_RevG_1VLC000058.pdf)

[68] FOCS – Fiber-Optic Current Sensor make light work of DC current measurement" (https://search.abb.com/library/Download.aspx?DocumentID=3BHS362996E01&LanguageCode=en&DocumentPartId=&Action=Launch).

[69] ACS37003: 400kHz, High Accuracy Current sensor with 5kV isolation, https://www.allegromicro.com/en/products/sense/current-sensor-ics/fifty-to-two-hundred-amp-integrated-conductor-sensor-ics/acs37003

[70] ACS724, ACS725 High accuracy, isolated current sensor with stray field rejection, https://www.allegromicro.com/en/products/sense/current-sensor-ics/zero-to-fifty-amp-integrated-conductor-sensor-ics/acs724-5

[71] ACS772: 200 kHz, 1.5% Max Tolerance, 100 μΩ IR Module 200A AC/DC current sensor IC, source: https://www.allegromicro.com/en/Products/Sense/current-sensor-ics/Fifty-To-Two-Hundred-Amp-Integrated-Conductor-Sensor-ICs/ACS772

[72] MLX90215 programmable linear Hall-Effect sensor IC with ratiometric analog output, Melexis. Source: https://www.melexis.com/en/product/MLX90215/Precision-Programmable-Linear-Hall-Effect-IC.

[73] HMR2300 Magnetometer sensors by Honeywell, source: chrome-extension://efaidnbmnnnibpcajpcglclefindmkaj/https://aerospace.honeywell.com/content/dam/aerobt/en/documents/learn/products/sensors/datasheet/SmartDigitalMagnetometerHMR2300_ds.pdf.

[74] R M Faradzhaev, Yu A Trofimov, E E Lupar, V N Yurov, "Performances investigation and material selection of PMT magnetic shields for the space experiments with GRIS and PING-M instruments", Journal of Physics: Conference Series 675 (2016) 042008, pp. 1-6. 2016.

[75] H. K. Kuga, and V. Carrara, "Attitude Determination with Magnetometers and Accelerometers to Use in Satellite Simulator", Mathematical Problems in Engineering Volume 2013, Article ID 401282, pp.1-6, 2013.

[76] X. Li, Ji. Hu, W. Chen, L. Yin, X. Liu, "A Novel High-Precision Digital Tunneling Magnetic Resistance-Type Sensor for the Nanosatellites' Space Application", Journal of Micromachines, MDPI, 2018, Vol. 9, No. 121, pp. 1-18, 2018.

[77] AG903B-07E: 0.75A/5A/50A GMR Current Sensor evaluation kit.

[78] AG905-07E: ALT025, source: https://www.nve.com/webstore/catalog/ product_ info.php?cPath=27_29&products_id=721&osCsid=t58cr35t5s7h7eumeg0pll3c47

[79] Omicron Energy Website. Available online: https://www.omicronenergy. com/en/products/cmc-356/ (accessed on 14 Sept. 2020).

[80] National Instruments Website: Available Online: https://www.ni.com/pdf/ manuals /371931/pdf (accdessed on 8 Aug 2019).

[81] Miyazaki, T.; Jin, H. The Physics of Ferromagnetism; Springer series in Material Science: New York, NY, USA, 2009; Volume 158, pp. 204–249.

[82] National Instruments Website: Available Online: https://www.ni.com/pdf/manuals/372838/pdf (accessed on 14 Jan 2020).

[83] IEEE Standard for Synchrophasor Measurement for Power Systems, IEEE C37.118.1-2011.

[84] J. R. S. Cristobal, "Multi-Criteria Decision-making in the Selection of a Renewable Energy Project in Spain: The Vikor Method", Elsevier Journal of Renewable Energy, Vol. 36 (2011), pp.498-502.

[85] Q. L. Zeng, D. D. Li, Y.B. Yang, "VIKOR Method with Enhanced Accuracy for Multiple Criteria Decision Making in Healthcare Management", J. of Medical Systems, Vol. 27:9908, 2013, pp. 1-9.

[86] R. Valliant, J. A. Dever, F. Kreuter, "Practical Tools for Designing and Weighting Survey Samples", 2nd ed. New York, NY, USA: Springer, 2018, ch. 13, ch. 14, pp. 321-414.

[87] D. Zhang, J. Liu, Y. Lv, X. Wei, "A Weighted Fusion Algorithm for Multi-Sensors", Sixth International Conference on Instrumentation and Measurement, Computer and Control, 2016, pp. 808-811.

[88] F. Xie, R. Weiss, R. Weigel, "Simple Mathematical Operation-Based Calibration Method for Giant Magnetoresistive Current Sensor Applying B-Spline Modelling", IEEE Sensors Journal, Vol. 16, No. 12, June15, 2016, pp.4733-4739.

[89] Ontario Electrical Safety Code (OESC), 28th Edition – 2021.

[90] TMR sensor Bipolar Analog Sensor, 20kOhm, x-axis, TDFN6, ALT025-10E: 0-1mT, Websource: https://www.nve.com/webstore/catalog/product_info.php?products_id=718.

[91] Ontario Electrical Safety Code, 28th Edition, 2021, Section 12-104, 12-106, 12-110, 12-118, 12-204, 12-302, Appendix B.

Appendix A. Results of Theoretical Simulation of Three-Phase system

A.1 Results of Average Estimation error (A) for Group I: One Measurement Point per Phase

Case	PhA	PhB	PhC	I_A_error (A)	I_B_error (A)	I_C_error (A)
a1: 90N_90N_90N	N1	N13	N25	0.8178	2.1789	2.0386
a2: 90N_90N_90N	N2	N14	N26	1.2900	4.7883	4.9244
a3: 90N_90N_90N	N3	N15	N27	0.8462	2.6952	2.6006
a4: ZE_ZE_ZE	E4	E16	E28	1.6001	2.0659	2.0077
a5: ZE_ZE_ZE	E5	E17	E29	3.7130	1.4897	5.9332
a6: ZE_ZE_ZE	E6	E18	E30	8.4936	2.5597	10.2796
a7: 90S_90S_90S	S7	S19	S31	3.2152	0.6997	1.3858
a8: 90S_90S_90S	S8	S20	S32	6.3336	2.2482	3.0033
a9: 90S_90S_90S	S9	S21	S33	18.1449	22.4477	21.4370
ia10: ZW_ZW_ZW	W10	W22	W34	2.7160	1.7843	0.5507
a11: ZW_ZW_ZW	W11	W23	W35	0.4727	0.5498	0.1597
a12: ZW_ZW_ZW	W12	W24	W36	6.5407	7.9907	2.5842
a13:90N_ZE_ZW	N1	E16	W34	0.8155	2.1442	0.5937
a14:90N_ZE_ZW	N2	E17	W35	1.1017	1.5046	1.2988
a15:90N_ZE_ZW	N3	E18	W36	1.3931	2.2330	2.1043
a16: 90N_90S_90S	N1	S19	S31	**0.7848**	**0.7346**	**1.4061**
a17: 90N_90S_90S	N2	S20	S32	0.9798	2.3060	3.0474
a18: 90N_90S_90S	N3	S21	S33	2.4267	2.2453	2.9262
a19: 90N_90S_ZW	N1	S19	W34	**0.0848**	**0.0795**	**0.0630**
a20: 90N_90S_ZW	N2	S20	W35	0.9639	2.2260	1.3962
a21: 90N_90S_ZW	N3	S21	W36	1.1082	3.5119	2.3558
a22: ZE_90S_ZW	E4	S19	W34	1.6299	0.7247	0.6042
a23: ZE_90S_ZW	E5	S20	W35	3.7904	2.2915	1.4883
a24: ZE_90S_ZW	E6	S21	W36	10.1594	6.7085	3.3902

A.1 Results of Minimum Estimation error (A) for Group I: One Measurement Point per Phase

Case	PhA	PhB	PhC	I_A_error (A)	I_B_error (A)	I_C_error (A)
a1: 90N_90N_90N	N1	N13	N25	0.0912	0.2428	0.2260
a2: 90N_90N_90N	N2	N14	N26	0.1427	0.5315	0.5464
a3: 90N_90N_90N	N3	N15	N27	0.0938	0.2976	0.2875
a4: ZE_ZE_ZE	E4	E16	E28	0.1771	0.2299	0.2219
a5: ZE_ZE_ZE	E5	E17	E29	0.4103	0.1646	0.6565
a6: ZE_ZE_ZE	E6	E18	E30	0.9428	0.2826	1.1353
a7: 90S_90S_90S	S7	S19	S31	0.3560	0.0775	0.1541
a8: 90S_90S_90S	S8	S20	S32	0.7025	0.2493	0.3316
a9: 90S_90S_90S	S9	S21	S33	2.0197	2.4751	2.4850
a10: ZW_ZW_ZW	W10	W22	W34	0.3001	0.1978	0.0612
a11: ZW_ZW_ZW	W11	W23	W35	0.4727	0.5498	0.1597
a12: ZW_ZW_ZW	W12	W24	W36	0.7220	0.8859	0.2872
a13:90N_ZE_ZW	N1	E16	W34	0.0906	0.2382	0.0660
a14:90N_ZE_ZW	N2	E17	W35	0.1220	0.1658	0.1436
a15:90N_ZE_ZW	N3	E18	W36	0.1542	0.2467	0.2330
a16: 90N_90S_90S	N1	S19	S31	**0.0869**	**0.0815**	**0.1551**
a17: 90N_90S_90S	N2	S20	S32	0.1089	0.2566	0.3372
a18: 90N_90S_90S	N3	S21	S33	2.4267	2.2453	2.9262
a19: 90N_90S_ZW	N1	S19	W34	**0.0848**	**0.0795**	**0.0630**
a20: 90N_90S_ZW	N2	S20	W35	0.1065	0.2457	0.1549
a21: 90N_90S_ZW	N3	S21	W36	0.1234	0.3892	0.2622
a22: ZE_90S_ZW	E4	S19	W34	0.1798	0.0804	0.0668
a23: ZE_90S_ZW	E5	S20	W35	0.4195	0.2546	0.1649
a24: ZE_90S_ZW	E6	S21	W36	1.1302	0.7435	0.3759

A.2 Average Estimation Errors (A) for Group II: Two Measurement Points per Phase

Case	PhA	PhB	PhC	Ia_Error	Ic_Error	Ic_Error
b1:90N_90N_90N	N1,N2	N13, N14	N25,N26	0.8702	2.699	2.6177
b2:90N_90N_90N	N2,N3	N14,N15	N26,N27	1.4244	5.5561	5.7446
b3:90N_90N_90N	N1,N3	N13,N15	N25,N27	0.8462	2.6952	2.6006
b4: ZE_ZE_ZE	E4,E5	E16,E17	E28,E29	2.0024	1.7566	2.7833
b5: ZE_ZE_ZE	E5,E6	E17,E18	E29,E30	4.3043	1.7553	6.8522
b6: ZE_ZE_ZE	E4,E6	E16,E18	E28,E30	1.9748	1.8994	2.6911
b7: 90S_90S_90S	S7,S8	S19,S20	S31,S32	3.8337	0.9912	1.7006
b8: 90S_90S_90S	S8,S9	S20,S21	S32,S33	7.1015	2.6424	3.5510
b9: 90S_90S_90S	S7,S9	S19,S21	S31,S33	3.7687	0.9641	1.7142
b10: ZW_ZW_ZW	W10,W11	W22,W23	W34,W35	3.0299	2.4206	0.6817
b11: ZW_ZW_ZW	W11,W12	W23,S24	W35,W36	4.9642	5.8842	1.7595
b12: ZW_ZW_ZW	W10,W12	W22,W24	W34,W36	3.1013	2.4049	0.6790
b13:90N_ZE_ZW	N1,N2	E16,E17	W34,W45	0.8531	1.8512	0.7007
b14:90N_ZE_ZW	N2,N3	E17,E18	W35,W36	1.1753	1.7168	1.5433
b15:90N_90S_90S	N1,N2	S19,S20	S31,S32	0.8144	1.0258	1.7214
b16:90N_90S_90S	N2,N3	S20,S21	S32,S33	1.0156	2.7136	3.6067
b17:90N_90S_ZW	N1,N2	S19,S20	W34,W35	**0.7877**	**1.0013**	**0.6879**
b18:90N_90S_ZW	N2,N3	S20,S21	W35,W36	1.0040	2.6139	1.6774
b19:90U_90S_ZW	N1,N2	S19,S21	W34,W36	**0.7894**	**0.9747**	**0.6828**
b20:90N_90S_90S	N2,N3	S19,S20	S31,S32	1.0333	1.0207	1.7175
b21: ZE_90S_ZW	E4,E5	S19,S20	W34,W35	4.7584	0.6580	0.7035
b22: ZE_90S_ZW	E5,E6	S20,S21	W35,W36	4.4153	2.6964	1.7851
b23: ZE_90S_ZW	E4,E6	S19,S21	W34,W36	2.0209	0.9844	0.7188
b24: ZE_90S_90D	E4,E5	S19,S20	S31,S32	2.0020	1.0404	1.6781

A.3 Minimum Estimation Errors (A) for Group II: Two Measurement Points per Phase

Case	PhA	PhB	PhC	Ia_Error	Ic_Error	Ic_Error
b1:90N_90N_90N	N1,N2	N13, N14	N25,N26	*0.0964*	*0.2982*	*0.2890*
b2:90N_90N_90N	N2,N3	N14,N15	N26,N27	*0.1572*	*0.6184*	*0.6383*
b3:90N_90N_90N	N1,N3	N13,N15	N25,N27	*0.0938*	*0.2976*	*0.2875*
b4: ZE_ZE_ZE	E4,E5	E16,E17	E28,E29	*0.2210*	*0.1955*	*0.3087*
b5: ZE_ZE_ZE	E5,E6	E17,E18	E29,E30	*0.4794*	*0.1942*	*0.7572*
b6: ZE_ZE_ZE	E4,E6	E16,E18	E28,E30	*0.2184*	*0.2097*	*0.2995*
b7: 90S_90S_90S	S7,S8	S19,S20	S31,S32	*0.4242*	*0.1093*	*0.1877*
b8: 90S_90S_90S	S8,S9	S20,S21	S32,S33	*0.7868*	*0.2915*	*0.4681*
b9: 90S_90S_90S	S7,S9	S19,S21	S31,S33	*0.4172*	*0.1070*	*0.1863*
b10: ZW_ZW_ZW	W10,W11	W22,W23	W34,W35	*0.3353*	*0.2672*	*0.0758*
b11: ZW_ZW_ZW	W11,W12	W23,S24	W35,W36	*0.5489*	*0.6556*	*0.1944*
b12: ZW_ZW_ZW	W10,W12	W22,W24	W34,W36	*0.3424*	*0.2655*	*0.0749*
b13:90N_ZE_ZW	N1,N2	E16,E17	W34,W45	*0.0950*	*0.2046*	*0.0774*
b14:90N_ZE_ZW	N2,N3	E17,E18	W35,W36	*0.1305*	*0.1900*	*0.1716*
b15:90N_90S_90S	N1,N2	S19,S20	S31,S32	*0.0901*	*0.1133*	*0.1910*
b16:90N_90S_90S	N2,N3	S20,S21	S32,S33	*0.1140*	*0.3016*	*0.4564*
b17:90N_90S_ZW	N1,N2	S19,S20	W34,W35	***0.0874***	***0.1108***	***0.0760***
b18:90N_90S_ZW	N2,N3	S20,S21	W35,W36	*0.1110*	*0.2888*	*0.1861*
b19:90U_90S_ZW	N1,N2	S19,S21	W34,W36	***0.0876***	***0.1079***	***0.0751***
b20:90N_90S_90S	N2,N3	S19,S20	S31,S32	*0.1142*	*0.1130*	*0.1910*
b21: ZE_90S_ZW	E4,E5	S19,S20	W34,W35	*0.5268*	*0.0726*	*0.0779*
b22: ZE_90S_ZW	E5,E6	S20,S21	W35,W36	*0.4893*	*0.3000*	*0.1978*
b23: ZE_90S_ZW	E4,E6	S19,S21	W34,W36	*0.2231*	*0.1088*	*0.0791*
b24: ZE_90S_90D	E4,E5	S19,S20	S31,S32	*0.2218*	*0.1151*	*0.1867*

A.4 Average Estimation Errors (A) for Group III: Three Measurement Point per Phase

Case	PhA	PhB	PhC	Ia_Error	Ic_Error	Ic_Error
c1	N1,N2,N3	N13,N14,N15	N25,N26,N27	0.8991	3.0764	3.0275
c2	E4,E5,E6	E16,E17,E18	E28,E29,E30	2.2825	1.6652	3.2812
c3	S7,S8,S9	S19,S20,S21	S31,S32,S33	4.2381	1.1879	1.9447
c4	W10,W11,W12	W22,W23,W25	W34,W35,W36	3.3176	2.8742	0.7931
c5	N1,N2,N3	E16,E17,E18	W34,W35,W36	0.8770	1.7606	0.7950
c6	N1,N2,N3	S19,S20,S21	S31,S32,S33	0.8316	1.2233	1.9663

A.5 Minimum Estimation Errors (A) for Group III: Three Measurement Points per Phase

Case	PhA	PhB	PhC	Ia_Error	Ic_Error	Ic_Error
c1	N1,N2,N3	N13,N14,N15	N25,N26,N27	0.0998	0.3410	0.3342
c2	E4,E5,E6	E16,E17,E18	E28,E29,E30	0.2535	0.1843	0.3632
c3	S7,S8,S9	S19,S20,S21	S31,S32,S33	0.4677	0.1317	0.2035
c4	W10,W11,W12	W22,W23,W25	W34,W35,W36	0.3666	0.3175	0.0876
c5	N1,N2,N3	E16,E17,E18	W34,W35,W36	0.0969	0.1952	0.0881
c6	N1,N2,N3	S19,S20,S21	S31,S32,S33	0.0924	0.1355	0.2051

Appendix B. Report on Magnetic Field Sensing for Single-phase Using Honeywell's GMR Sensors

B.1 Experimental Setup

The experimental setup consists of a single-phase conductor, one resistor and one inductor. The current source has a range of variation from 1A to 15A with unit incremental adjustment knob. So, the values could be set at a particular value and then the magnetic field could be sensed, or the magnetic field can be sensed by varying the current from 1A to 15 A with a time lapse of 10 seconds and duration of 30seconds.

B.2 Combinations for Measuring Magnetic Field

It was observed that there were quite a few factors to be considered for combinations while measuring the magnetic field such as the current magnitude, Baud rate of sensors, sampling rate, and distance from conductor and orientation of the sensors. Following set of combinations were applied for measuring magnetic field:

Sr. #	Configurations and Combinations	Range of Variation of parameter
1	Distance from Conductor	0.5cm, 1cm, 1.5cm, 2.5cm
2	Direction from Conductor	East, West and South
3	Baud Rate	9600 and 19200
4	Sampling Rate (samples/sec)	30,40,50 (samples per second)
5	Orientation of Sensor	Configuration A, Configuration B Configuration C and Configuration D
6	Magnitude of Current Fixed	5A, 8A, 10A, 15A
7	Current Varied Gradually	1A to 15A with values gradually increased to: 1A, 5A, 8A, 10A, 12A, 15A
8	Sensors Grouping /Location	1) Close to each other: E & WE B. 2) Separate Location: South
9	Time Duration	1) 2 Min to 10min for One Fixed Current Value 2) 30seconds for each value for Gradually Increasing Current Value

The gradual increase of current and periods of measurement are as shown in the Fig.1 below. There was a gap of 10 seconds inserted between each recording, and each current value was set for 30seconds to sense and record the data using TeraTerm Software. This sequence was followed only for the gradual increase and sensing of the current. There was another set of experiment where the currents were set for a particular value and the measurements were taken for a period of 2minutes. The values set for this set were 5A, 8A and 10A.

There could not be a good record of measurements for 15A, because the current test set could not withstand the temperature increase and would switch off. For further experiment of three-phase combinations, it is suggested to use Omicron CMC356 test set which can inject 30A for a period of 5minutes without reset because of increased temperature.

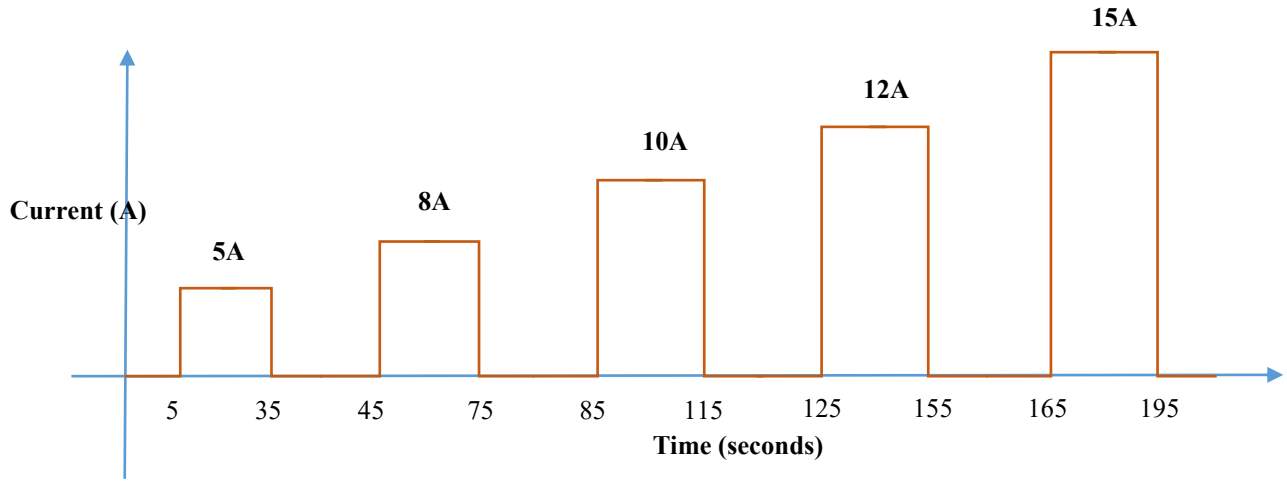

Figure B.1 Combination of time duration and incremental current values

B.3 Programming and Settings of Sensors

The transmitted output data of HMR2300 sensor is a 16bit value and it can be either 16-bit signed binary value or Binary coded decimal (BCD) ASCII characters. The output sampling rate depended on the Baud Rate for this sensor. There is a standard table provided in the instruction manual for the sensing speed and rate and it was tried for combinations of Baud rate and sampling rate to decide which combination contributes more correct values and larger quantity of samples.

The Table B.1 below shows the parameter section versus output sampling rate.

Table B.1 Parameter Selection Chart of Honeywell GMR Sensor

Sample Rate (sps)	ASCII		Binary		f_{3dB} (Hz)	Notch (Hz)	Command Input Rate - min. (msec)
	9600	19200	9600	19200			
10	*yes*	*yes*	*yes*	*yes*	17	50/60	20
20					17	50/60	20
25					21	63/75	16
30					26	75/90	14
40					34	100/120	10
50					42	125/150	8
60					51	150/180	7
100	DATA				85	250/300	4
123	INVALID				104	308/369	3.5
154					131	385/462	3

From above table, we decided to set maximum number of samples per second. This is because we want a greater number of samples per cycle to compare them with the industry standards. The industrial existing relays use 4 samples per cycle. In this case, the maximum number we could go was 50 samples per second.

For conversion of the recorded values to actual magnetic field, there is a table of conversion included in the instruction manual. It is presented below as Table B.2. As per this table, to obtain the real value of the magnetic field, for exa 1Gauss is equivalent to 15000 of the BCD ASCII value.

Thus, measured values from the experiment, we need to use the conversion factor of 1/15,000 to obtain the magnetic fields in Bx, By and Bz components.

Table B.2 Conversion of Magnetic Field into Binary

Field (Gauss)	BCD ASCII Value	Binary Value (Hex) High Byte	Low Byte
+2.0	30,000	75	30
+1.5	22,500	57	E4
+1.0	15,000	3A	98
+0.5	7,500	1D	4C
0.0	00	00	00
-0.5	- 7,500	E2	B4
-1.0	-15,000	C3	74
-1.5	-22,500	A8	1C
-2.0	-30,000	8A	D0

B.4 Orientation and Configuration of Sensors

Configuration A: As seen in the figure, the arrow of the Bx is in the direction of the flow of current. By is perpendicular to the direction of the Bx and therefore the direction of current.

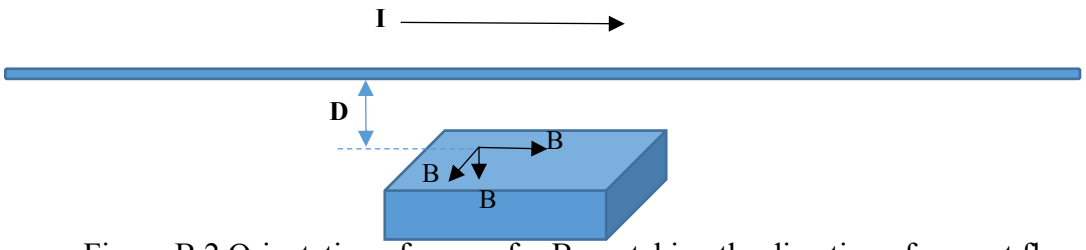

Figure B.2 Orientation of sensor for B_x matching the direction of current flow

Configuration B: As seen in the figure, the arrow of the B_y is in the direction of the flow of current, I. B_x is perpendicular to the direction of the B_y and therefore the direction of current.

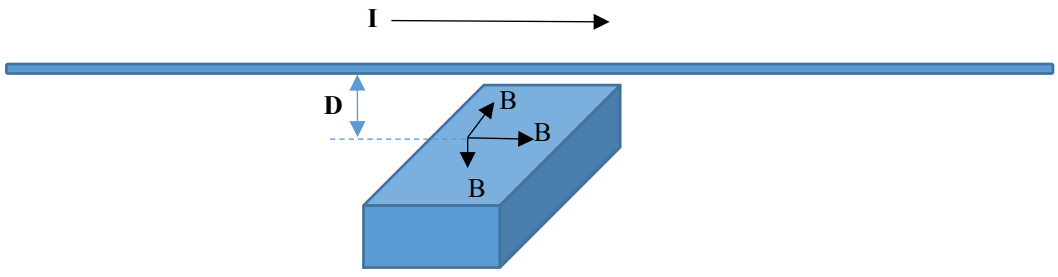

Figure B.3 Orientation of sensor for B_y matching the direction of current flow

Configuration C: As seen in the figure, the arrow of the B_y is in the opposite direction of the flow of current, I. B_x is perpendicular to the direction of the B_y and therefore the direction of current but in opposite direction of that of the configuration B.

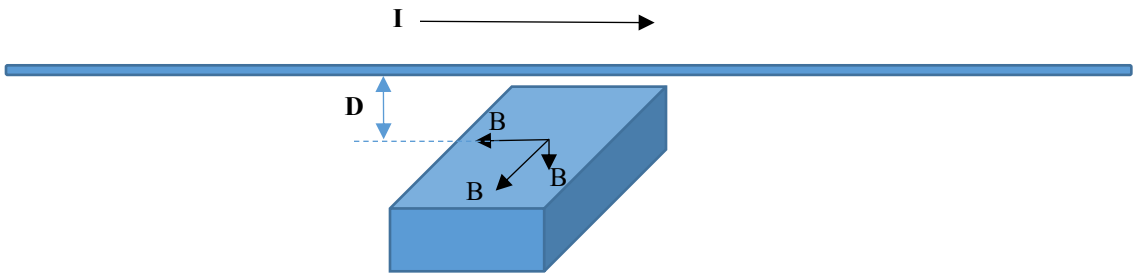

Figure B.4 Orientation of sensor for B_y in parallel to the current flow but opposite in direction

Configuration D: As seen in the figure, the arrow of the B_x is in the opposite direction of the flow of current, I. B_y is perpendicular to the direction of the B_y and therefore the direction of current but in opposite direction of that of the configuration A.

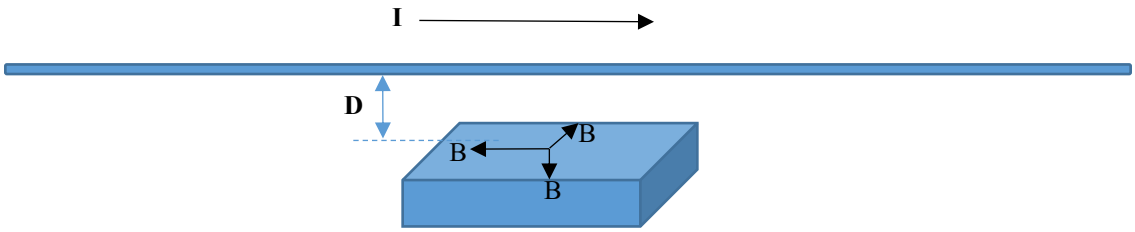

Figure B.5 Orientation of sensor for B_x in parallel to the current flow but opposite in direction.

B.5 Experiment Procedure

Following factors were considered for setting up the sensors.

1. Circuit connections for the R-L series circuit with 3/0 XLPE conductor were performed.
2. DC power supply to the sensors and connections for RS-232 communication using DB9 Pin configuration.

3. Programming of the sensor for Baud Rate and SPS.
4. Number of sensors: Assigned address to each sensor in TeraTerm: Sensor 1 ID= 22 and Sensor 2 ID is 44.
5. There were Four Configurations considered for placing the sensor below the conductor, Configuration A, B, C and D as mentioned in the Table B.2 above.

   These configurations were decided based on the directional vector diagram on the sensor faceplate indicating B_x, B_y and B_z. The very first question was how to decide which direction to be considered correct? From simulation, it was obvious that the field which is perpendicular and tangent to the circular lines of magnetic field surrounding the conductor carrying current should be considered as a correct value for the magnetic field.

   For a two-dimensional field, we will have two components B_x, and B_y but only one component will be the correct value.
6. The test set for current injection was chosen as AVO Multi-AMP SR-98 Relay Test Set. This test set works on 120Vac, and the output has a range of current from 1A to 40A.
7. The Read command was applied to both sensors once the current injection started. The variation of current and time duration was followed as mentioned in the Fig.1
8. Values recorded and stored as log files in TeraTerm and later transferred to MATLAB for conversion from BCD ASCII to integer values and stored as column vectors.

The photo of the experimental setup is as shown below. The first photo shows the location of two sensors away from each other with 50cm. There was also a combination of sensors considered where both sensors were placed at the same location but East and West of the sides of the conductor. This combination of two sensors was used for sensing same current.

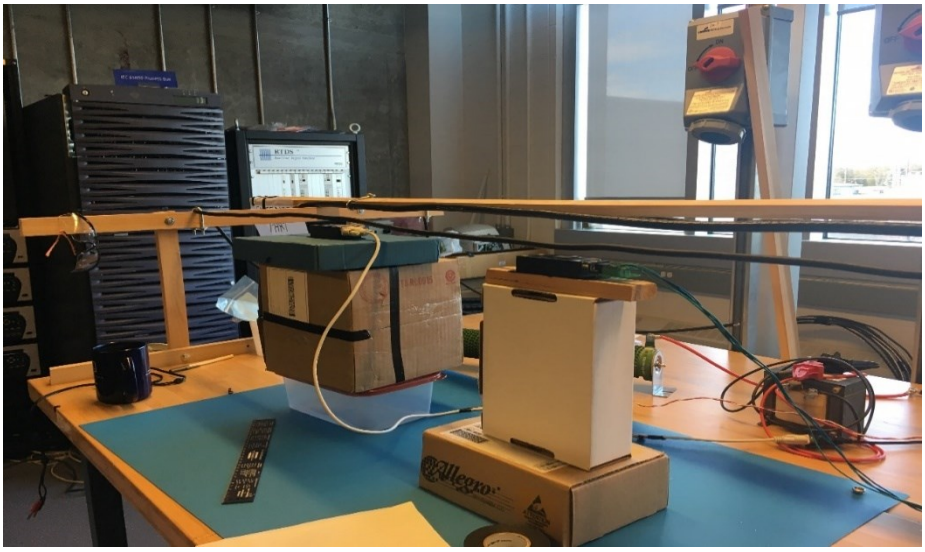

Figure B.6 Experimental setup for GMR sensor, S_3 at laboratory

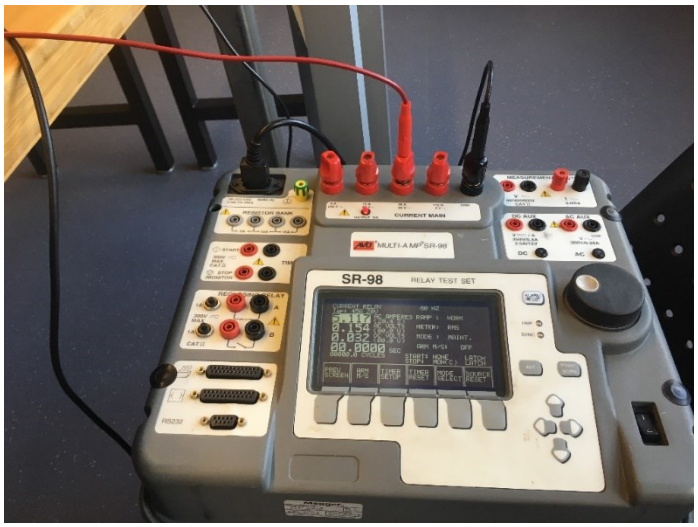

Figure B.7 Current Injection set AVO SR98

The photo of AVO SR-98 test set shows the main screen and the current variation knob that is used to vary and set a particular value of the current. The current value setting can be adjusted till third decimal.

B.6 Interpretation of Data Stored in B_x, B_y and B_z Columns for Magnetic Fields

Following test were performed on the column vectors of Bx, By and Bz obtained after conversion from ASCII to integer values.

1. Comparison of Bx and By for Configuration A

2. Comparison of B_x and B_y for Configuration A and Configuration B
3. Comparison of B_x and B_y obtained using setting one value for 2minutes, and those obtained from the gradual incremented current value experiments
4. Checking the pattern of the data collected from sensors.
5. Comparison of magnitudes for both sensors to verify whether the sensors have any location issues.
6. Interpretation of magnetic fields for all negative and varying negative and positive values.

   It is expected that out of three parameters B_x, B_y and B_z, there will be one parameter that show the variation of the field from positive to negative based on the sinusoidal varying current.

The polarities on the output measured during this experiment as observed from the results are shown in the Table B.3

1. Baud Rate of 19200 gave good results from the point of view of correlation and uniform variation pattern for each value of current. The baud rate of 9600 gave all random values with no correlation.
2. Configuration A seemed to be appropriate and B_y was the magnetic field to be considered that varies both positive and negative for each value of the current.

   Table B.3: Polarities of the Magnetic Field recorded for various configurations.

Sr. #	Configuration	B_x	B_y	B_z
1	Configuration A	-Ve	+ve and –Ve	-Ve
2	Configuration B	+ve	-ve	-ve
3	Configuration C	-ve	+ve	-ve
4	Configuration D	+ve	+Ve and –VE	-ve

B.7 Experiment Results and Observations for Sensor 1 and Sensor 2 Combinations for a Single Phase.

The combinations of one sensor for measuring the magnetic field in three directions are shown in the figures previously from Figure B.3 to Figure B.6. In addition, the experiment using 2 sensors was performed with placement of each sensor at a horizontal distance of

3.5feet. The combination used both sensors in the Configuration A where both of the sensors had their Bx in the same direction as that of the flow of the current. Therefore, the combination looks as shown in the figure below.

Figure B.8 Use of two sensors with measuring field, B_x in the direction of current flow

Results and figures of the Magnetic Fields in three directions for one of the combinations are given below.

B. 8 Results of Case: S1_1_10to15_AS_TBF_50.m

In this case, the sensor is kept at the South side of the conductor. The other combinations have the sensor placed at the East of the conductor and at the West of the Conductor as we considered for the combinations for the simulations. This was considered to get the maximum magnetic field from the conductor. Therefore, south of the conductor averages it is kept 1cm below the conductor.

The distance was precisely kept as 1cm by measuring scale and the Vernier calipers. The Baud rate was kept fast and the number of samples per second were kept as 50 using the TeraTerm command and programming the sensor using TeraTerm. The results of the magnetic field are stored in the database using B_x, B_y and B_z as three columns. The results are as shown in the figures below.

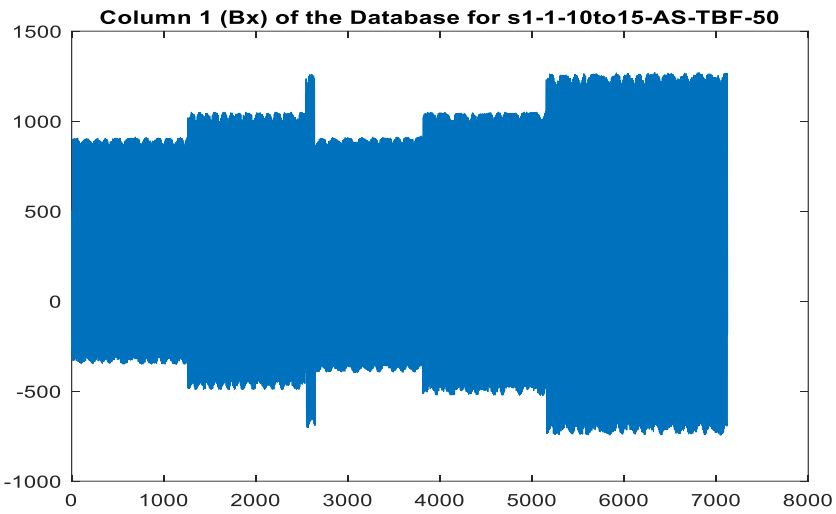

Figure B.9 Measured B_x component of the field in Tesla for inputs currents from 10A to 15A.

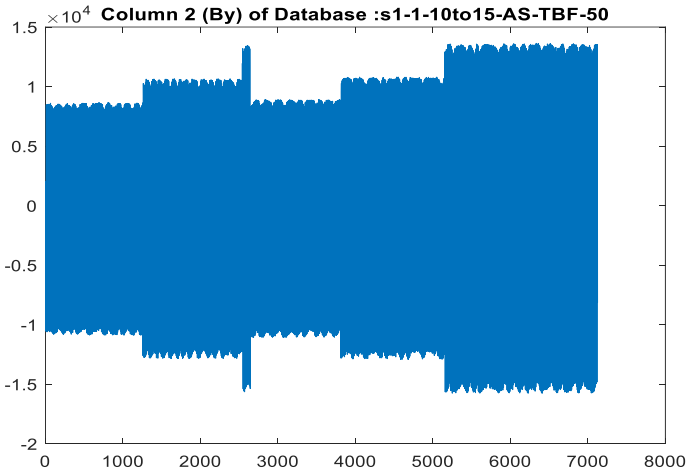

Figure B.10 Measured B_y component of the field in Tesla for inputs currents from 10A to 15A.

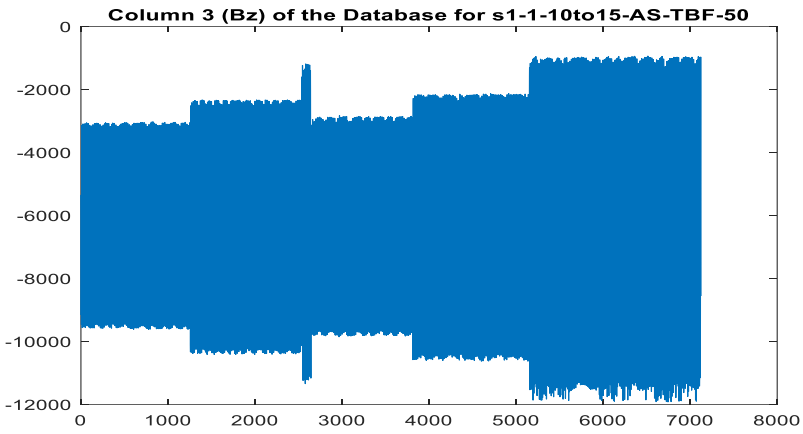

Figure B.11 Measured B_z component of the field in Tesla for inputs currents from 10A to 15A.

With the first 350 samples for the Figure B.3, the results show that there is a sinusoidal variation of the field

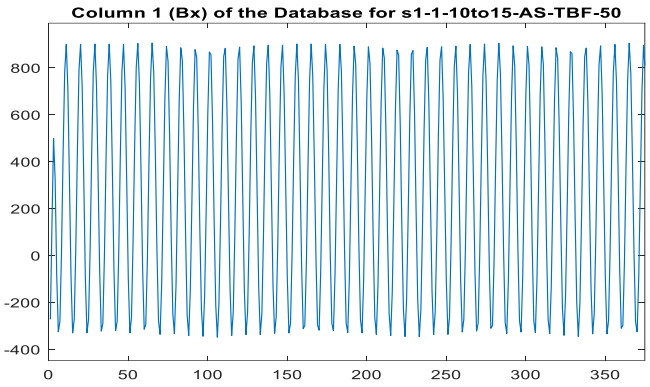

Figure B.12 First 350 samples of the measured B_x component of the field in milliTesla for 10 A inputs currents.

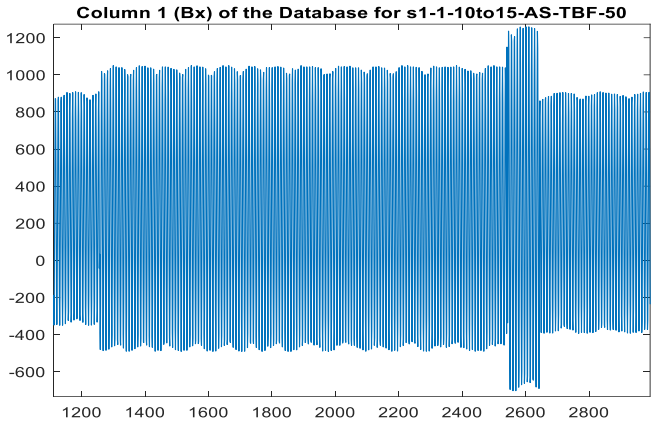

Figure B.13 Measured B_x component of the field in Tesla for 11 A input current for the same number of samples, the By is found to be very higher value

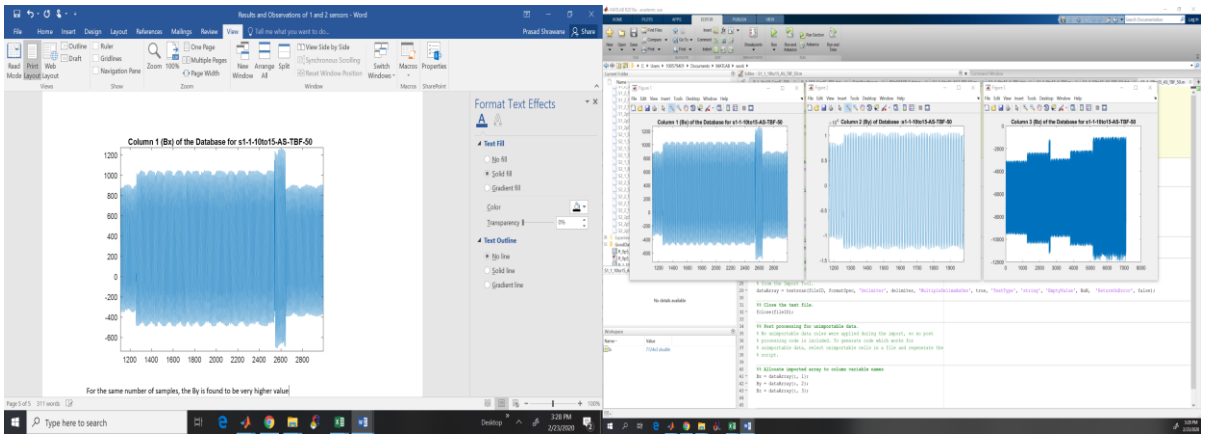

Figure B.14 Comparison of B_x, B_y and B_z components in the TeraTerm software window

Appendix C. Results of Sensors for High Current Testing

C.1 Performance Results of Sensor S_1 for High Currents

Current	Magnitude Error			Phase Error			TVE		
	Avg	Max	S.D.	Avg	Max	S.D.	Avg	Max	S.D.
50A	0.21	0.71	0.30	0.0015	0.0137	0.0077	0.425	1.41	0.59
100A	0.04	0.50	0.25	0.0011	0.0043	0.0031	0.039	0.50	0.25
200A	0.31	0.75	0.26	0.0009	0.0048	0.0016	0.153	0.38	0.13
300A	0.35	0.58	0.14	0.0000	0.0014	0.0006	0.117	0.19	0.05
400A	0.22	0.87	0.40	0.0012	0.0006	0.0008	0.055	0.22	0.10
500A	0.39	0.26	0.39	0.0014	0.0003	0.0005	0.078	0.05	0.08
600A	0.03	0.41	0.29	0.0015	0.0004	0.0003	0.004	0.07	0.05
700A	0.07	0.46	0.30	0.0015	0.0007	0.0003	0.009	0.07	0.04
800A	0.09	0.62	0.28	0.0005	0.0004	0.0004	0.012	0.08	0.03
900A	0.36	0.30	0.33	0.0001	0.0006	0.0004	0.040	0.03	0.04
1000A	0.71	0.94	0.15	0.0012	0.0017	0.0002	0.071	0.09	0.02
1100A	0.40	0.89	0.26	0.0012	0.0019	0.0003	0.037	0.08	0.02
1200A	0.26	0.75	0.29	0.0007	0.0011	0.0002	0.022	0.06	0.02
1300A	0.90	1.30	0.27	0.0003	0.0001	0.0002	0.069	0.10	0.02
1400A	0.45	1.09	0.27	0.0010	0.0005	0.0003	0.032	0.08	0.02
1500A	0.10	0.46	0.25	0.0001	0.0003	0.0002	0.007	0.03	0.02

C.2 Performance Results of Sensor S_2 for High Currents

Current	Magnitude Error			Phase Error			TVE		
	Avg	Max	S.D.	Avg	Max	S.D.	Avg	Max	S.D.
50A	0.151	0.797	0.299	0.0003	0.0116	0.0064	0.302	1.59	0.60
100A	0.035	0.561	0.301	0.0001	0.0105	0.0034	0.035	0.56	0.30
200A	0.384	1.211	0.376	0.0008	0.0047	0.0017	0.192	0.61	0.19
300A	0.682	1.529	0.418	0.0002	0.0029	0.0012	0.227	0.51	0.14
400A	0.134	0.417	0.324	0.0012	0.0010	0.0009	0.034	0.10	0.08
500A	0.013	0.569	0.342	0.0012	0.0008	0.0008	0.003	0.11	0.07
600A	0.381	0.447	0.278	0.0016	0.0004	0.0007	0.063	0.07	0.05
700A	0.406	0.230	0.311	0.0014	0.0002	0.0005	0.058	0.03	0.04
800A	0.043	0.607	0.351	0.0005	0.0004	0.0004	0.005	0.08	0.04
900A	0.732	0.092	0.466	0.0000	0.0011	0.0006	0.081	0.01	0.05
1000A	0.230	1.454	0.687	0.0011	0.0017	0.0003	0.023	0.15	0.07
1100A	0.286	1.039	0.501	0.0013	0.0022	0.0005	0.026	0.09	0.05
1200A	0.539	0.179	0.231	0.0007	0.0013	0.0002	0.045	0.01	0.02
1300A	1.105	1.821	0.401	0.0003	0.0002	0.0002	0.085	0.14	0.03
1400A	0.379	1.291	0.503	0.0010	0.0002	0.0003	0.027	0.09	0.04
1500A	0.116	0.176	0.223	0.0001	0.0003	0.0002	0.008	0.01	0.01

C.3 Performance Results of Sensor S_4 for High Currents

Current	Magnitude Error			Phase Error			TVE		
	Avg	Max	S.D.	Avg	Max	S.D.	Avg	Max	S.D.
50A	0.06	0.33	0.20	0.00121	0.01097	0.00458	0.118	0.662	0.394
100A	0.06	0.84	0.37	0.00086	0.00449	0.00172	0.064	0.837	0.371
200A	0.31	0.99	0.41	0.00093	0.00290	0.00083	0.156	0.496	0.204
300A	0.01	0.35	0.16	0.00010	0.00151	0.00062	0.004	0.118	0.054
400A	0.51	0.81	0.14	0.00119	0.00019	0.00036	0.128	0.203	0.035
500A	0.13	0.66	0.29	0.00137	0.00066	0.00030	0.026	0.132	0.059
600A	0.17	0.68	0.32	0.00148	0.00065	0.00022	0.028	0.113	0.053
700A	0.09	0.33	0.22	0.00143	0.00046	0.00036	0.012	0.048	0.032
800A	0.05	1.28	0.37	0.00046	0.00000	0.00017	0.007	0.160	0.047
900A	0.50	0.05	0.28	0.00008	0.00071	0.00036	0.055	0.006	0.031
1000A	0.47	0.91	0.25	0.00119	0.00160	0.00018	0.047	0.091	0.025
1100A	0.29	0.61	0.24	0.00133	0.00202	0.00030	0.026	0.055	0.022
1200A	0.08	0.51	0.24	0.00066	0.00109	0.00019	0.006	0.042	0.020
1300A	0.54	0.99	0.31	0.00029	0.00034	0.00019	0.042	0.076	0.024
1400A	0.56	1.27	0.31	0.00100	0.00053	0.00024	0.040	0.091	0.022
1500A	0.28	0.87	0.32	0.00005	0.00021	0.00014	0.018	0.058	0.021

C.4 Performance Results of Sensor S_5 for High Currents

Current	Magnitude Error			Phase Error			TVE		
	Avg	Max	S.D.	Avg	Max	S.D.	Avg	Max	S.D.
50A	0.13	0.46	0.35	0.00024	0.01020	0.00401	0.26	0.91	0.70
100A	0.14	0.92	0.40	0.00046	0.00629	0.00327	0.14	0.92	0.40
200A	0.12	0.83	0.48	0.00115	0.00460	0.00158	0.06	0.42	0.24
300A	0.13	0.93	0.56	0.00009	0.00213	0.00089	0.04	0.31	0.19
400A	0.26	1.08	0.41	0.00135	0.00142	0.00099	0.07	0.27	0.10
500A	0.27	0.84	0.33	0.00128	0.00007	0.00064	0.05	0.17	0.07
600A	0.41	0.14	0.12	0.00130	0.00001	0.00057	0.07	0.02	0.02
700A	0.58	0.05	0.27	0.00143	0.00036	0.00058	0.08	0.01	0.04
800A	0.13	0.71	0.36	0.00042	0.00013	0.00025	0.02	0.09	0.05
900A	0.35	0.18	0.43	0.00016	0.00084	0.00037	0.04	0.02	0.05
1000A	0.71	1.74	0.72	0.00120	0.00166	0.00020	0.07	0.17	0.07
1100A	0.30	1.09	0.39	0.00128	0.00221	0.00043	0.03	0.10	0.04
1200A	0.03	1.16	0.52	0.00061	0.00138	0.00035	0.00	0.10	0.04
1300A	0.74	1.23	0.26	0.00026	0.00017	0.00018	0.06	0.09	0.02
1400A	0.49	1.06	0.32	0.00107	0.00053	0.00022	0.03	0.08	0.02
1500A	0.12	0.71	0.32	0.00003	0.00053	0.00032	0.01	0.05	0.02

C.5 Performance Results of Sensor S_6 for High Currents

Current	Magnitude Error			Phase Error			TVE		
	Avg	Max	S.D.	Avg	Max	S.D.	Avg	Max	S.D.
50A	0.23	0.06	0.16	0.0005	0.0108	0.0056	0.469	0.118	0.314
100A	0.07	0.47	0.22	0.0005	0.0030	0.0020	0.070	0.468	0.219
200A	0.43	1.03	0.33	0.0011	0.0036	0.0010	0.217	0.513	0.165
300A	0.16	0.70	0.26	0.0000	0.0012	0.0005	0.052	0.234	0.086
400A	0.13	0.79	0.29	0.0012	0.0003	0.0005	0.033	0.198	0.074
500A	0.16	0.39	0.19	0.0013	0.0005	0.0004	0.033	0.077	0.038
600A	0.36	0.10	0.34	0.0014	0.0007	0.0004	0.060	0.016	0.057
700A	0.38	0.02	0.23	0.0014	0.0010	0.0002	0.054	0.003	0.033
800A	0.16	0.68	0.33	0.0005	0.0002	0.0003	0.020	0.086	0.041
900A	0.21	0.21	0.29	0.0002	0.0004	0.0002	0.024	0.023	0.032
1000A	0.40	1.00	0.28	0.0012	0.0019	0.0003	0.040	0.100	0.028
1100A	0.29	0.64	0.18	0.0012	0.0016	0.0002	0.027	0.058	0.017
1200A	0.05	0.31	0.18	0.0006	0.0011	0.0002	0.004	0.026	0.015
1300A	0.77	1.08	0.30	0.0003	0.0002	0.0002	0.059	0.083	0.023
1400A	0.55	0.72	0.09	0.0010	0.0006	0.0002	0.039	0.051	0.006
1500A	0.02	0.47	0.34	0.0001	0.0003	0.0002	0.001	0.032	0.023

Appendix D. Phasor Measurement Results for Chapter 6

D.1 Test Results of Three Sensors per Phase at Various Distances, Triangular Structure

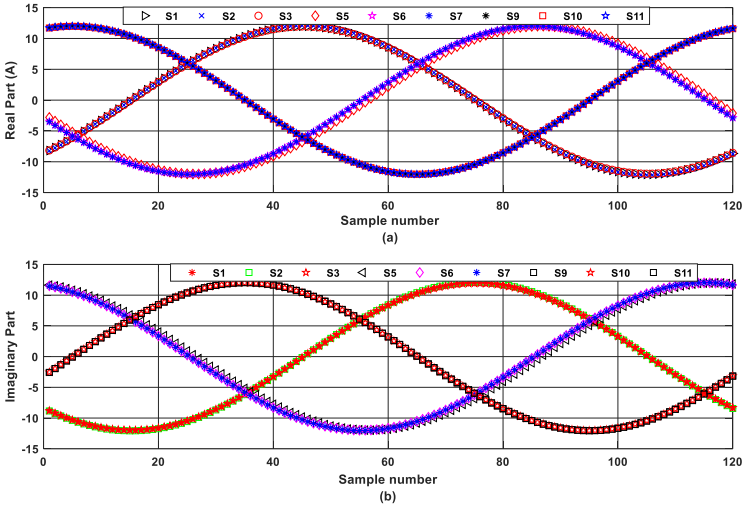

Figure D.1 (a) Real parts and (b) Imaginary Parts of calculated current outputs of sensors S_1, S_2, S_3, S_5, S_6, S_7, S_9, S_{10}, S_{11} placed at 15mm for 12 A in triangular structure

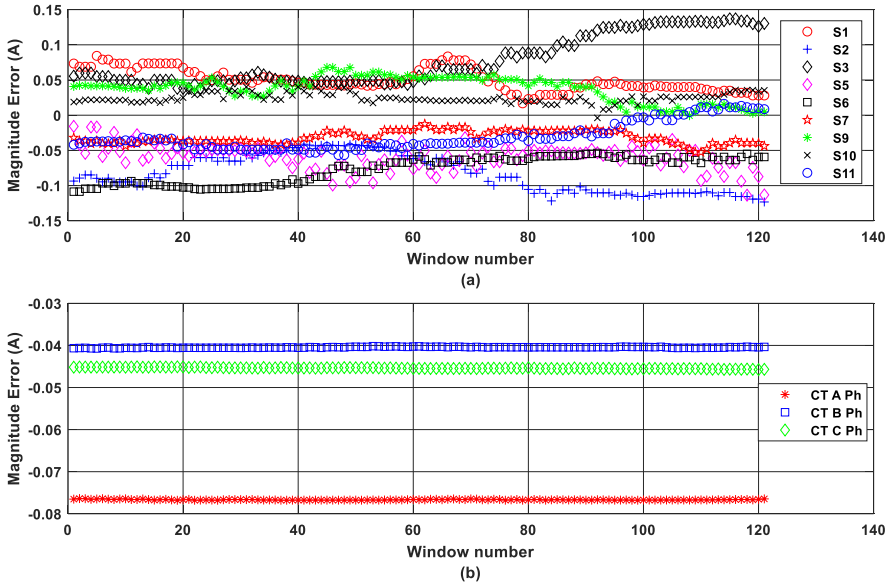

Figure D.2 Magnitude errors in calculated phasors of 12A for (a) three sensors per phase at 15mm and (b) three-phase CTs in triangular structure

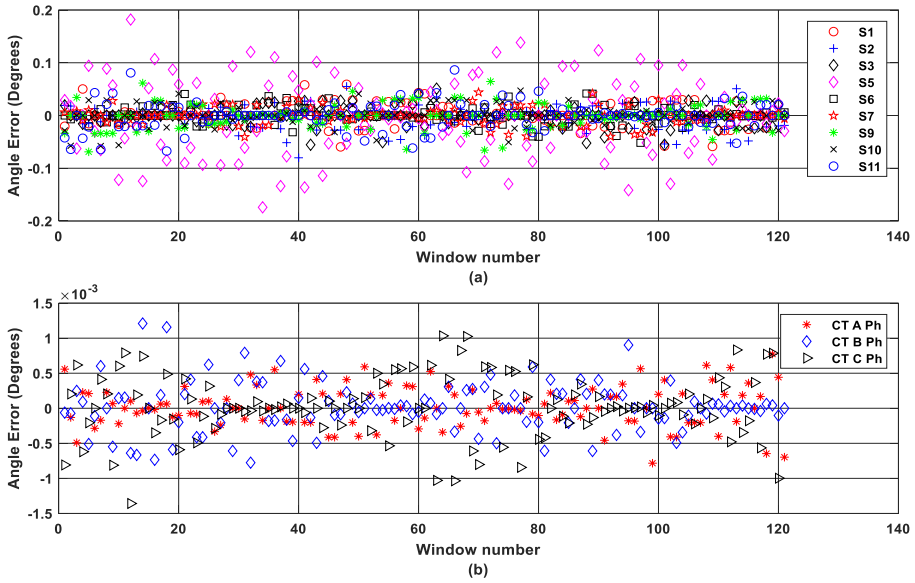

Figure D.3 Angle errors in calculated phasors of 12A for (a) three sensors per phase at 15 mm and (b) three-phase CTs in triangular structure

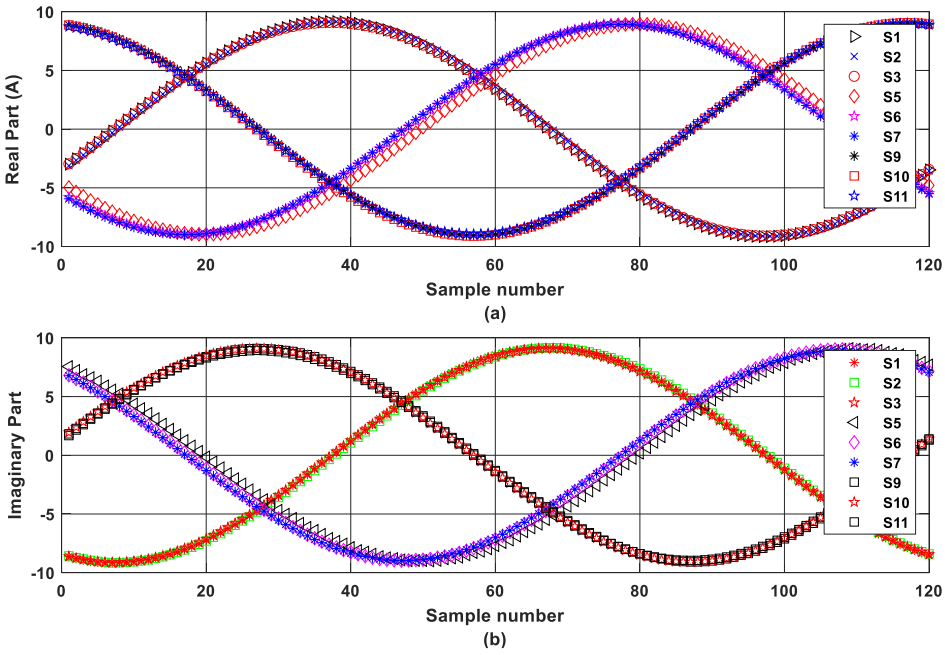

Figure D.4 (a) Real parts and (b) Imaginary Parts of calculated current outputs of sensors S_1, S_2, S_3, S_5, S_6, S_7, S_9, S_{10}, S_{11} placed at 25 mm for 9 A in triangular structure

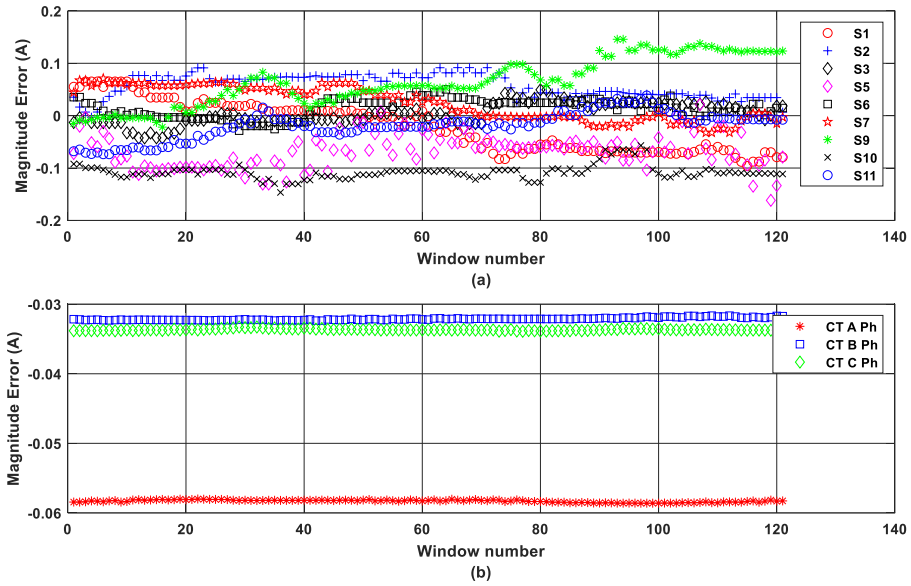

Figure D.5 Magnitude errors in calculated phasors of 9 A for (a) three sensors per phase at 25 mm and (b) three-phase CTs in triangular structure

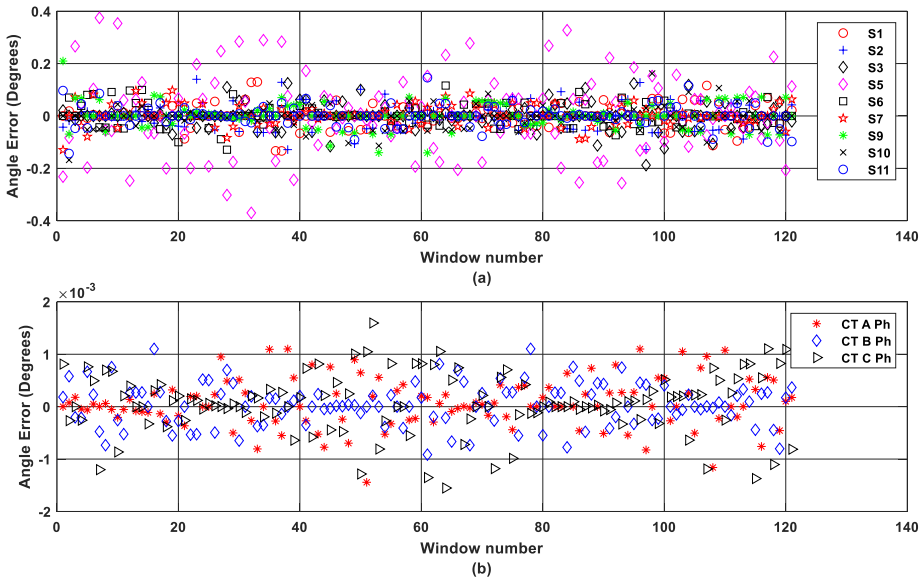

Figure D.6 Angle errors in calculated phasors of 9 A for (a) three sensors per phase at 25 mm and (b) three-phase CTs in triangular structure

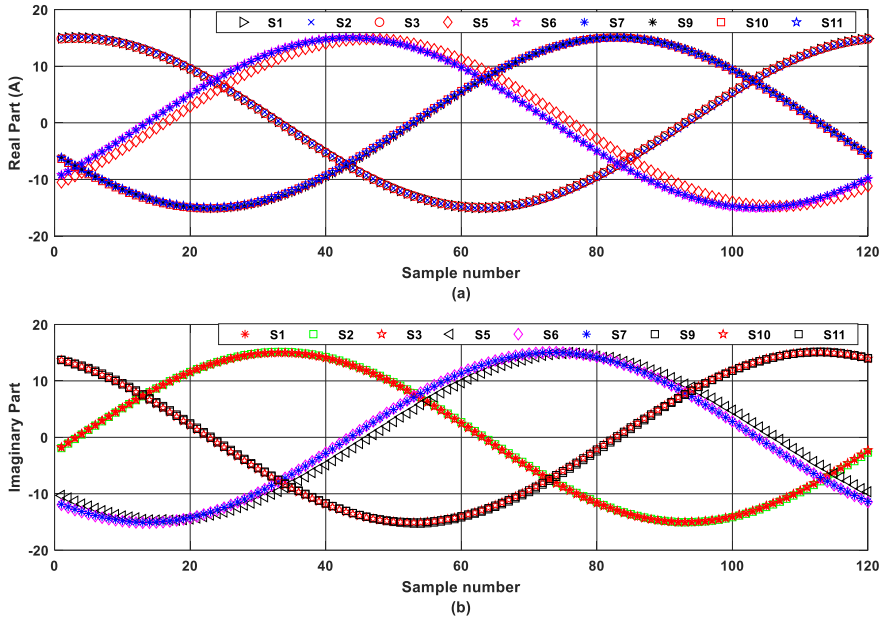

Figure D.7 (a) Real parts and (b) Imaginary Parts of calculated current outputs of sensors S_1, S_2, S_3, S_5, S_6, S_7, S_9, S_{10}, S_{11} placed at 35 mm for 15 A in triangular structure

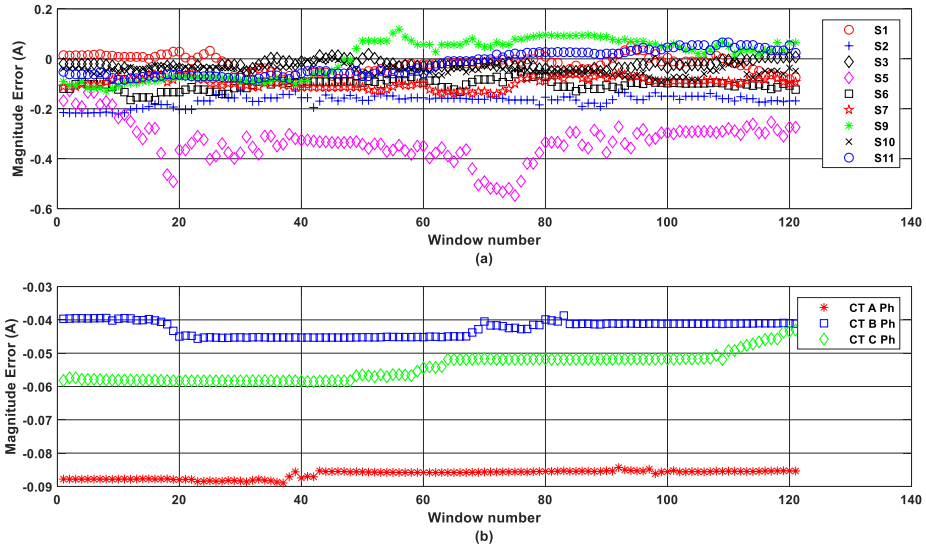

Figure D.8 Magnitude errors in calculated phasors of 15 A for (a) three sensors per phase at 35 mm and (b) three-phase CTs in triangular structure

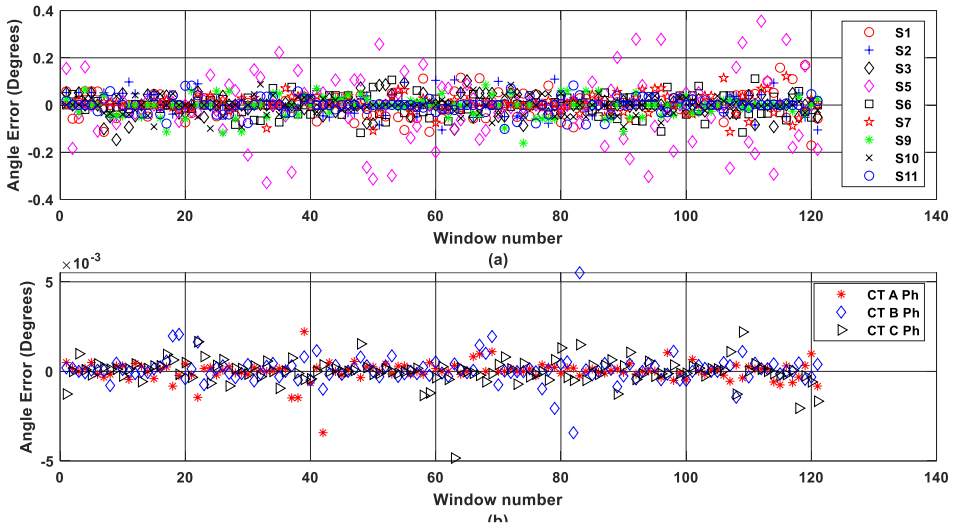

Figure D.9 Angle errors in calculated phasors of 15 A for (a) three sensors per phase at 35 mm and (b) three-phase CTs in triangular structure

D.2 Results of Two Sensors per Phase at Various Distances in Horizontal Structure

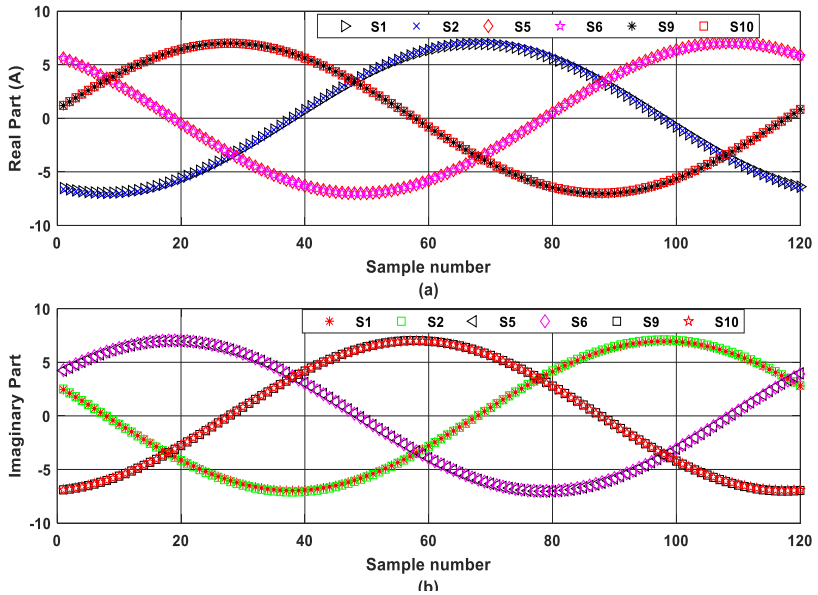

Figure C.10 (a) Real parts and (b) Imaginary Parts of calculated current outputs of sensors S_1, S_2, S_5, S_6, S_9, and S_{10} placed at 7 mm for 7 A in horizontal structure

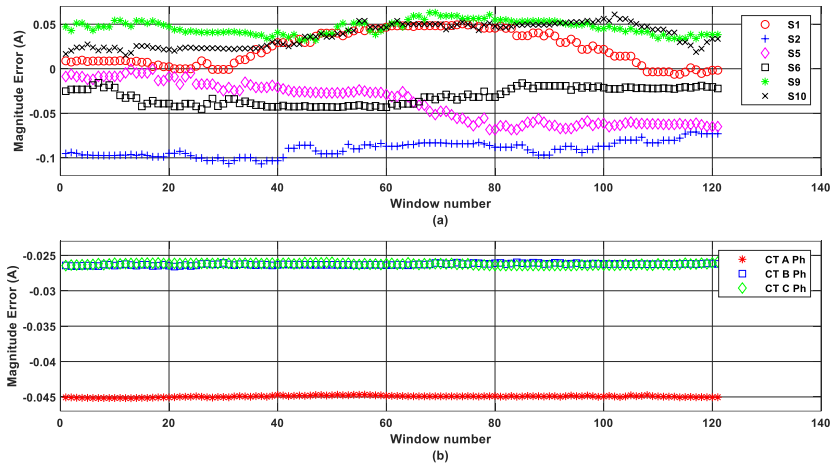

Figure D.11 Magnitude errors in calculated phasors of 7 A for (a) two sensors per phase at 7 mm and (b) three-phase CTs in Horizontal structure

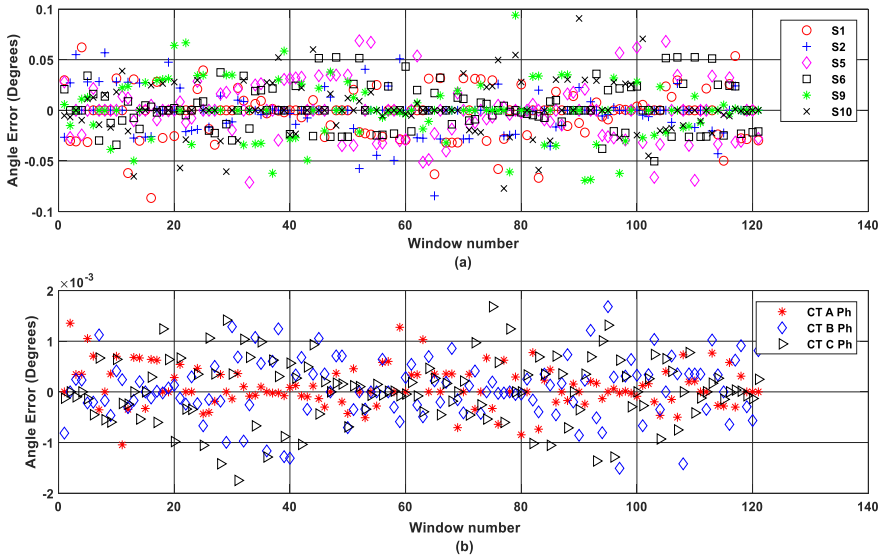

Figure D.12 Angle errors in calculated phasors of 7 A for (a) two sensors per phase at 7 mm and (b) three-phase CTs in Horizontal structure

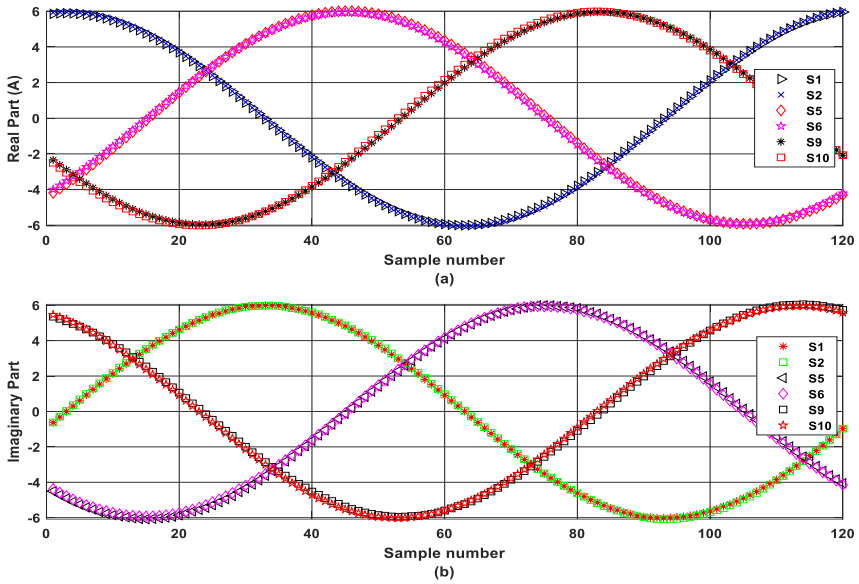

Figure D.13 (a) Real parts and (b) Imaginary Parts of calculated current outputs of sensors S_1, S_2, S_5, S_6, S_9, and S_{10} placed at 25 mm for 6 A in horizontal structure

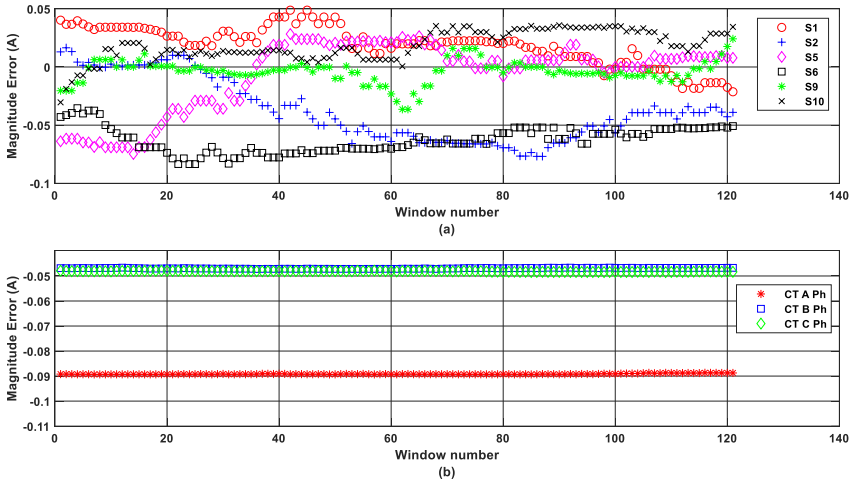

Figure D.14 Magnitude errors in calculated phasor of 6 A for (a) two sensors per phase at 25 mm and (b) three-phase CTs in horizontal structure

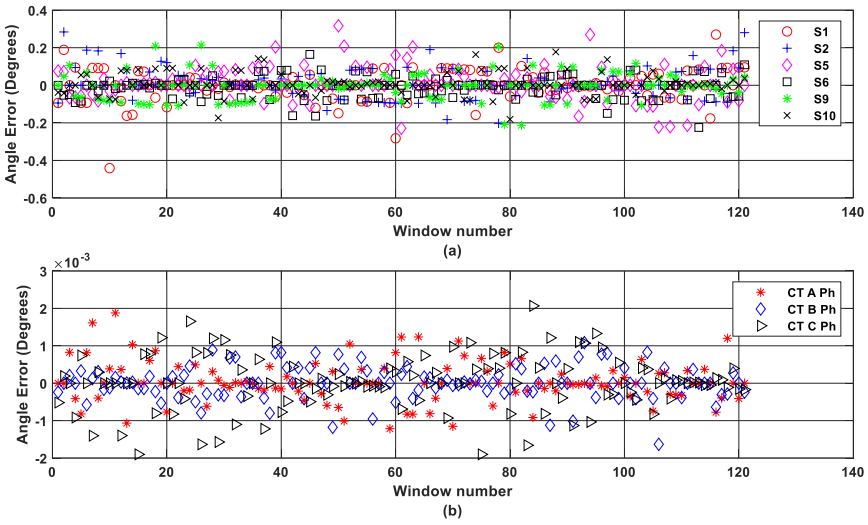

Figure D.15 Angle errors in calculated phasor of 6 A for (a) two sensors per phase at 25 mm and (b) three-phase CTs in horizontal structure

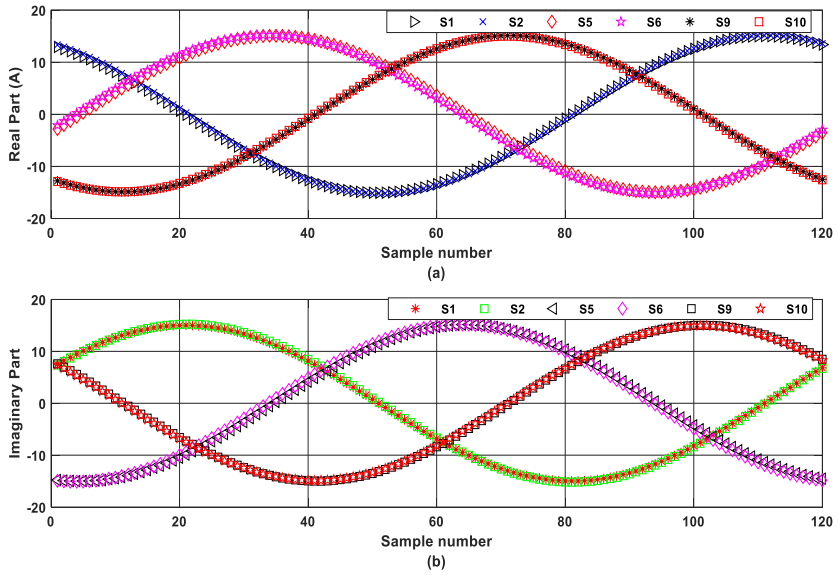

Figure D.16 (a) Real parts and (b) Imaginary Parts of calculated current outputs of sensors S_1, S_2, S_5, S_6, S_9, and S_{10} placed at 35 mm for 15 A in horizontal structure

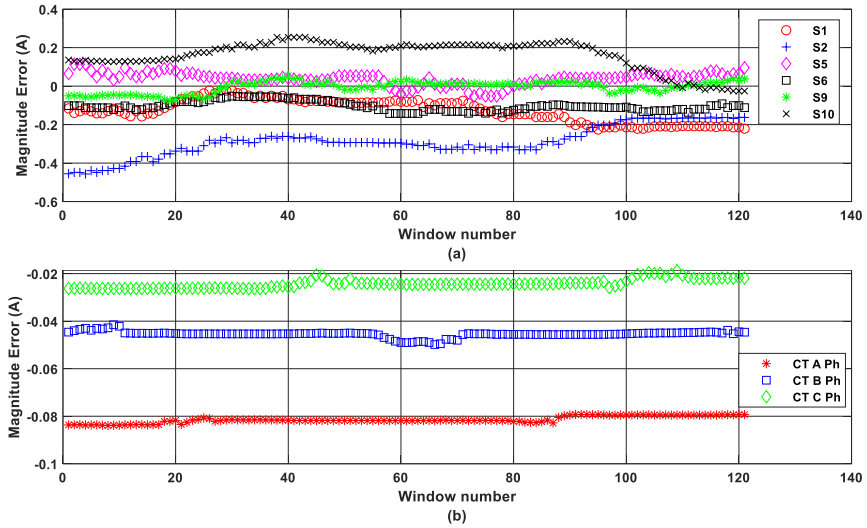

Figure D.17 Magnitude errors in calculated phasor of 15 A for (a) two sensors per phase at 35 mm and (b) three-phase CTs in horizontal structure

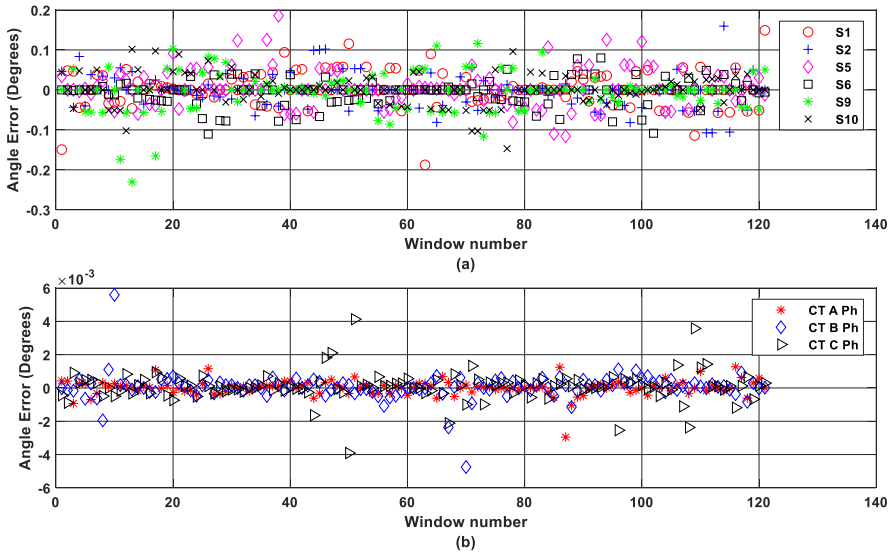

Figure D.18 Angle errors in calculated phasor of 15 A for (a) two sensors per phase at 35 mm and (b) three-phase CTs in horizontal structure

D.3 Results of Three Sensors per Phase at Various Distances in Horizontal Structure

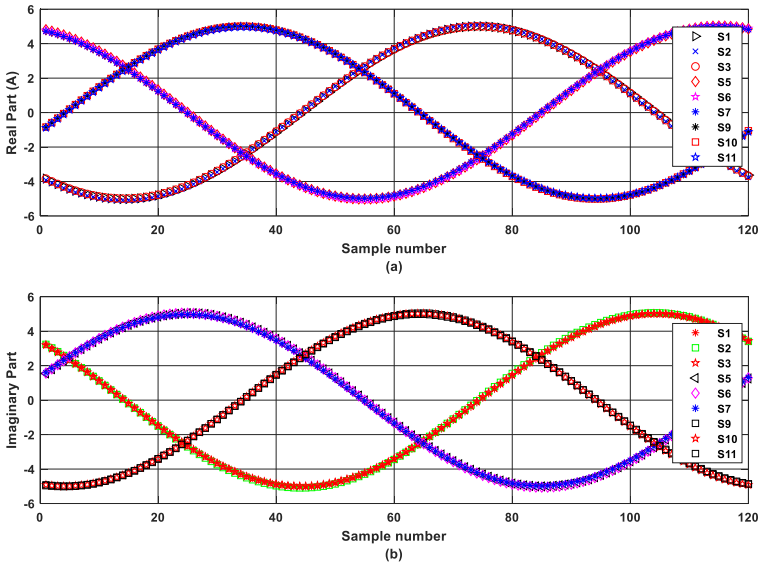

Figure D.19 (a) Real parts and (b) Imaginary Parts of calculated current outputs of sensors S_1, S_2, S_3, S_5, S_6, S_7, S_9, S_{10}, and S_{11} placed at 7 mm for 5 A in horizontal structure

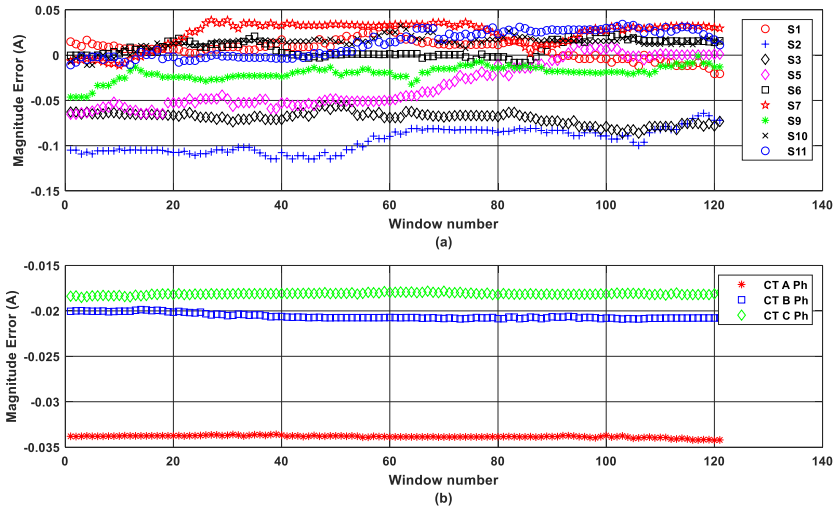

Figure D.20 Magnitude errors in calculated phasors of 5 A for (a) three sensors per phase at 7 mm and (b) three-phase CTs in horizontal structure

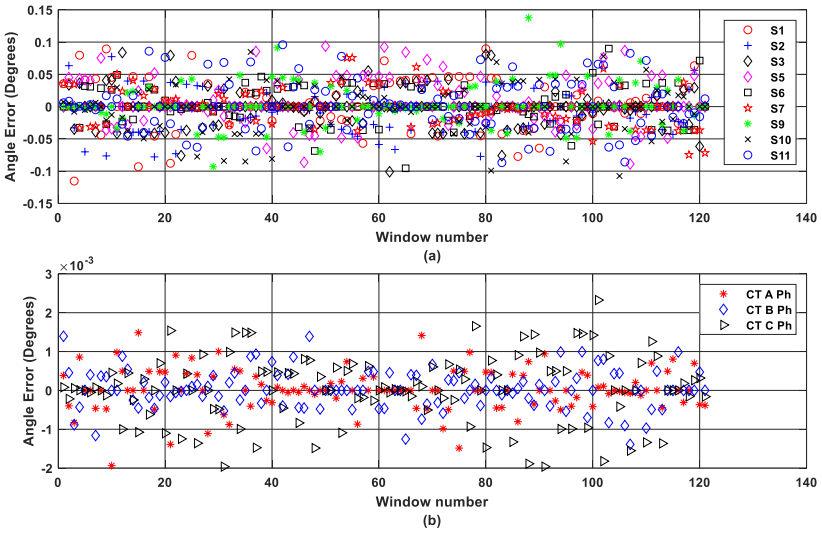

Figure D.21 Angle errors in calculated phasors of 5 A for (a) three sensors per phase at 7 mm and (b) three-phase CTs in horizontal structure

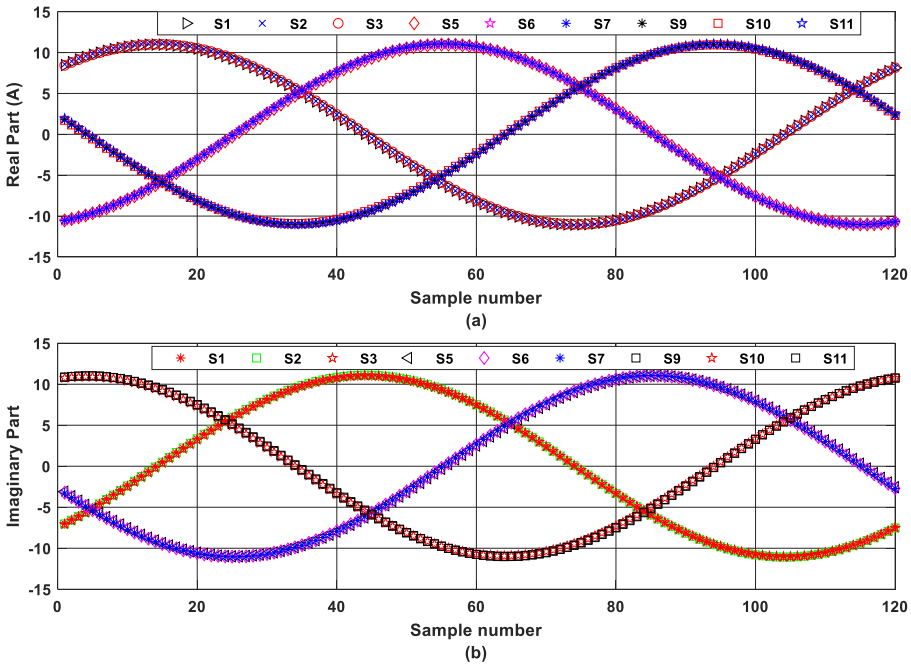

Figure D.22 (a) Real parts and (b) Imaginary Parts of calculated current outputs of sensors S_1, S_2, S_3, S_5, S_6, S_7, S_9, S_{10}, S11 placed at 15 mm for 11 A in horizontal structure

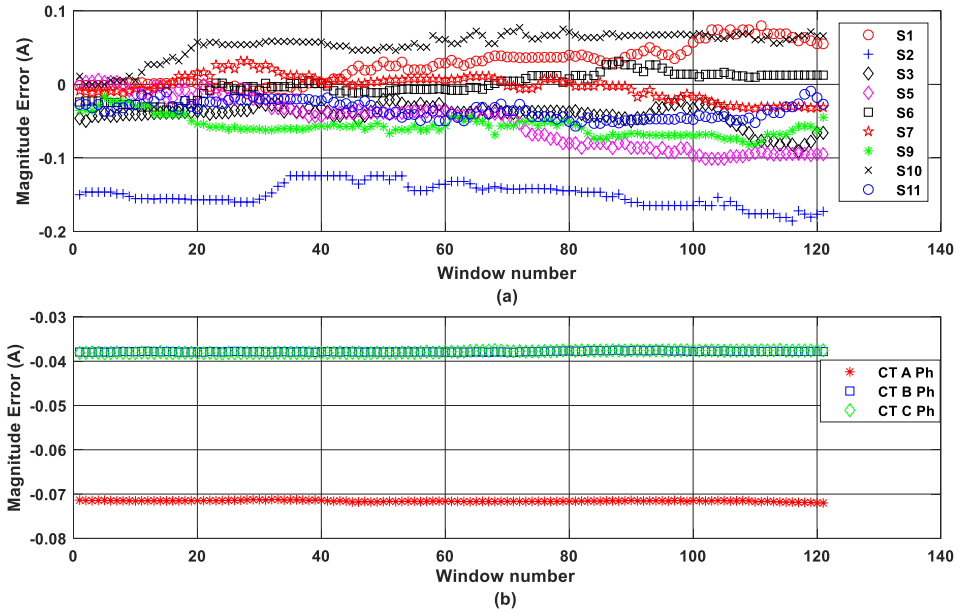

Figure D.23 Magnitude errors in calculated phasors of 11 A for (a) three sensors per phase at 15 mm and (b) three-phase CTs in horizontal structure

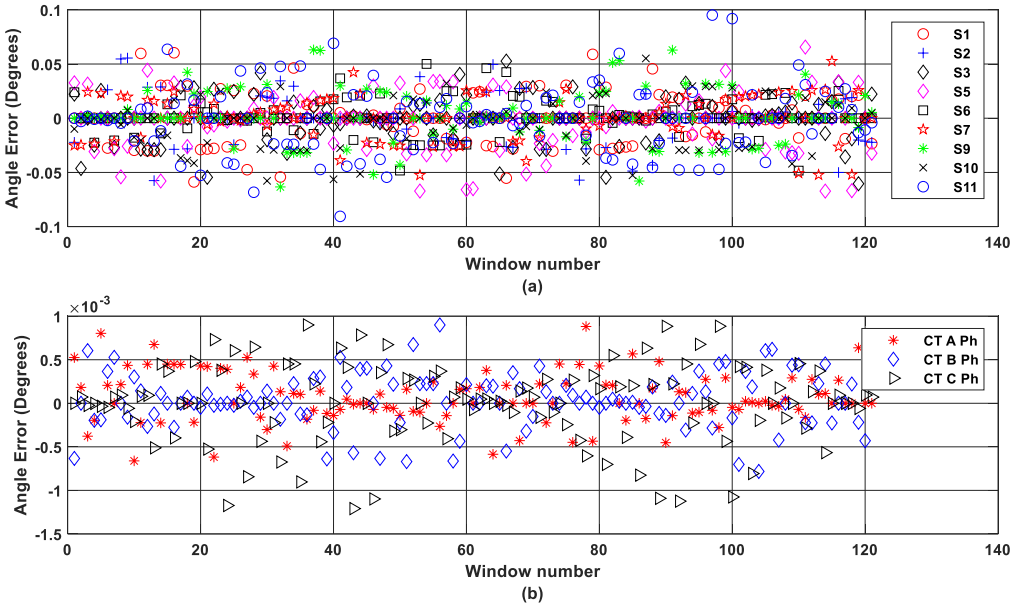

Figure D.24 Angle errors in calculated phasors of 11 A for (a) three sensors per phase at 15 mm and (b) three-phase CTs in horizontal structure

Appendix E. Performance Parameters of Three-Phase Phasor Calculation Algorithm

E.1 Results for Various Combinations in Triangular Structure

Percentage TVE: Triangular Structure, One sensors per phase at 7mm

Amp / Sensor	5A	6A	7A	8A	9A	10A	11A	12A	13A	14A	15A
S1	0.350	0.266	0.613	0.011	0.063	0.012	0.325	0.235	0.054	0.246	0.085
S5	0.187	0.645	0.752	0.345	0.307	0.383	0.504	0.922	0.019	0.297	0.487
S9	0.101	0.114	0.037	0.586	0.013	0.166	0.241	0.070	0.216	0.369	0.134
CT_A	0.6783	0.6754	0.6521	0.6414	0.6578	0.6450	0.6595	0.6432	0.6509	0.6401	0.5847
CT_B	0.4149	0.3984	0.3720	0.3578	0.3585	0.3451	0.3540	0.3432	0.3520	0.3486	0.3232
CT_C	0.4020	0.3777	0.3708	0.3842	0.3674	0.3760	0.3697	0.3773	0.3702	0.3697	0.2907

Magnitude Error: Triangular Structure, One sensors per phase at 7mm

Amp / Sensor	5A	6A	7A	8A	9A	10A	11A	12A	13A	14A	15A
S1	0.018	0.016	-0.043	-0.001	-0.006	-0.001	-0.036	-0.028	-0.007	-0.035	0.013
S5	-0.009	-0.039	-0.053	-0.028	-0.028	-0.038	0.055	0.111	-0.003	0.042	0.022
S9	0.005	0.007	0.003	0.047	0.001	0.017	-0.027	-0.008	-0.028	-0.052	0.020
CT_A	-0.0339	-0.0405	-0.0456	-0.0513	-0.0592	-0.0645	-0.0725	-0.0772	-0.0846	-0.0896	-0.0877
CT_B	-0.0207	-0.0239	-0.0260	-0.0286	-0.0323	-0.0345	-0.0389	-0.0412	-0.0458	-0.0488	-0.0485
CT_C	-0.0201	-0.0227	-0.0260	-0.0307	-0.0331	-0.0376	-0.0407	-0.0453	-0.0481	-0.0518	-0.0436

Angle Error: Triangular Structure, One sensors per phase at 7mm

Amp / Sensor	5A	6A	7A	8A	9A	10A	11A	12A	13A	14A	15A
S1	0.00018	0.00012	0.00033	0.00015	0.00037	0.00018	-0.00017	0.00029	4.5E-05	0.00012	0.00001
S5	-0.0003	0.0003	-0.0011	0.0002	0.0008	-0.0004	-0.0002	-0.0003	0.0002	-0.0005	1.3E-05
S9	0.00093	0.00050	0.00014	-0.00030	-0.00002	-0.00004	0.00024	0.00012	-0.00004	-0.00013	-0.00014
CT_A	6.6E-06	7.1E-06	6.2E-06	6.9E-06	7.1E-06	7.2E-06	7.6E-06	7.6E-06	7.4E-06	6.4E-06	5.6E-06
CT_B	4.7E-06	8.0E-06	7.6E-06	7.5E-06	6.0E-06	7.5E-06	5.9E-06	6.7E-06	6.9E-06	6.4E-06	7.4E-06
CT_C	-0.0201	-0.0227	-0.0260	-0.0307	-0.0331	-0.0376	-0.0407	-0.0453	-0.0481	-0.0518	-0.0436

Percentage TVE: Triangular Structure, One sensors per phase at 15mm

Amp / Sensor	5A	6A	7A	8A	9A	10A	11A	12A	13A	14A	15A
S1	0.885	0.168	0.428	0.391	0.202	0.298	0.135	0.562	0.128	0.017	0.174
S5	0.2732	0.2129	0.5402	0.8704	0.3685	0.3071	0.0967	0.4791	0.1118	0.1892	0.2685
S9	0.505	0.323	0.370	0.411	0.125	0.091	0.381	0.067	0.183	0.160	0.231
CT_A	0.691	0.647	0.647	0.657	0.651	0.655	0.653	0.640	0.644	0.636	0.607
CT_B	0.412	0.385	0.385	0.364	0.353	0.356	0.351	0.346	0.348	0.335	0.328
CT_C	0.385	0.401	0.401	0.368	0.372	0.368	0.370	0.380	0.368	0.377	0.232

Magnitude Error: Triangular Structure, One sensors per phase at 15mm

Amp / Sensor	5A	6A	7A	8A	9A	10A	11A	12A	13A	14A	15A
S1	-0.044	0.010	-0.030	-0.031	-0.018	-0.030	0.015	0.067	-0.017	0.002	0.026
S5	-0.0137	0.0128	-0.0378	-0.0696	-0.0332	-0.0307	-0.0106	0.0575	0.0145	0.0265	0.0403
S9	-0.025	0.019	-0.026	0.033	0.011	-0.009	-0.042	0.008	-0.024	0.022	0.035
CT_A	-0.035	-0.039	-0.039	-0.053	-0.059	-0.065	-0.072	-0.077	-0.084	-0.089	-0.091
CT_B	-0.021	-0.023	-0.023	-0.029	-0.032	-0.036	-0.039	-0.042	-0.045	-0.047	-0.049
CT_C	-0.019	-0.024	-0.024	-0.029	-0.033	-0.037	-0.041	-0.046	-0.048	-0.053	-0.035

Angle Error: Triangular Structure, One sensors per phase at 15mm

Amp / Sensor	5A	6A	7A	8A	9A	10A	11A	12A	13A	14A	15A
S1	0.0016	0.0007	-0.0006	0.0003	0.0003	-0.0001	0.0002	-0.0002	0.0003	0.0001	0.0004
S5	-0.00167	-0.00150	-0.00080	-0.00017	0.00018	0.00068	0.00035	0.00007	-0.00047	0.00036	0.00018
S9	0.00073	0.00032	-0.00021	-0.00030	0.00021	0.00030	0.00025	0.00020	-0.00039	-0.00027	-0.00009
CT_A	7.4E-06	7.0E-06	7.0E-06	6.1E-06	7.1E-06	6.5E-06	7.0E-06	7.8E-06	7.1E-06	6.2E-06	8.0E-06
CT_B	6.2E-06	6.1E-06	6.1E-06	6.1E-06	8.1E-06	7.4E-06	7.8E-06	7.4E-06	6.8E-06	6.9E-06	5.4E-06
CT_C	8.7E-06	6.7E-06	6.7E-06	7.3E-06	8.3E-06	7.4E-06	6.4E-06	7.0E-06	6.0E-06	7.6E-06	6.5E-06

Percentage TVE: Triangular Structure, One sensors per phase at 25mm

Amp / Sensor	5A	6A	7A	8A	9A	10A	11A	12A	13A	14A	15A
S1	0.0623	0.1425	0.1728	0.1796	0.0239	0.1941	0.4009	0.0499	0.1057	0.6994	0.6600
S5	0.5823	0.3550	0.0304	0.2967	0.3240	0.5230	0.0402	0.3362	0.2101	0.2233	1.4463
S9	0.4515	0.1480	0.3008	0.1229	0.0912	0.4913	0.1946	0.0476	0.3552	0.2512	0.1253
CT_A	0.697	0.682	0.663	0.637	0.657	0.646	0.648	0.652	0.652	0.639	0.608
CT_B	0.4169	0.3992	0.3825	0.3505	0.3640	0.3559	0.3538	0.3529	0.3516	0.3371	0.2719
CT_C	0.3743	0.3769	0.3733	0.3829	0.3757	0.3827	0.3792	0.3680	0.3721	0.3749	0.2994

Magnitude Error: Triangular Structure, One sensors per phase at 25mm

Amp / Sensor	5A	6A	7A	8A	9A	10A	11A	12A	13A	14A	15A
S1	0.0031	0.0086	0.0121	0.0144	0.0022	-0.0194	0.0441	0.0060	-0.0137	-0.0979	0.0990
S5	-0.0291	-0.0213	0.0021	-0.0237	-0.0292	0.0523	0.0044	-0.0403	0.0273	-0.0313	0.2169
S9	-0.0226	-0.0089	0.0211	0.0098	0.0082	0.0491	0.0214	-0.0057	-0.0462	0.0352	0.0188
CT_A	-0.035	-0.041	-0.046	-0.051	-0.059	-0.065	-0.071	-0.078	-0.085	-0.089	-0.091
CT_B	-0.0208	-0.0240	-0.0268	-0.0280	-0.0328	-0.0356	-0.0389	-0.0424	-0.0457	-0.0472	-0.0408
CT_C	-0.0187	-0.0226	-0.0261	-0.0306	-0.0338	-0.0383	-0.0417	-0.0442	-0.0484	-0.0525	-0.0449

Angle Error: Triangular Structure, One sensors per phase at 25mm

Amp / Sensor	5A	6A	7A	8A	9A	10A	11A	12A	13A	14A	15A
S1	-0.00056	0.00041	-0.00100	0.00056	-0.00162	-0.00077	0.00044	-0.00052	0.00108	0.00032	0.00004
S5	0.0010	-0.0002	-0.0018	0.0005	-0.0001	-0.0005	0.0010	-0.0005	0.0004	-0.0003	-0.0002
S9	0.0001	-0.0008	0.0012	0.0015	0.0002	0.0006	0.0008	0.0011	-0.0001	0.0002	-0.0001
CT_A	7.8E-06	5.2E-06	5.7E-06	7.8E-06	6.7E-06	6.7E-06	6.6E-06	6.4E-06	7.5E-06	6.3E-06	6.1E-06
CT_B	5.47E-06	7.32E-06	5.32E-06	7.75E-06	6.70E-06	6.39E-06	6.75E-06	5.67E-06	7.42E-06	6.49E-06	5.86E-06
CT_C	4.7E-06	8.7E-06	8.3E-06	7.8E-06	7.3E-06	8.5E-06	6.2E-06	7.0E-06	7.4E-06	7.5E-06	7.7E-06

Percentage TVE: Triangular Structure, One sensors per phase at 35mm

Amp / Sensor	5A	6A	7A	8A	9A	10A	11A	12A	13A	14A	15A
S1	1.079	1.763	1.821	0.998	0.479	0.242	1.022	0.703	1.201	0.075	0.245
S5	0.1821	0.2012	0.3989	0.0380	0.3668	0.3812	0.7231	0.1377	0.2000	0.0799	0.0152
S9	1.131	0.436	1.065	0.348	0.323	0.053	0.229	0.547	0.417	0.042	0.752
CT_A	0.6589	0.6552	0.6400	0.6456	0.6367	0.6572	0.6472	0.6432	0.6348	0.6488	0.5576
CT_B	0.3882	0.3889	0.3657	0.3551	0.3491	0.3593	0.3551	0.3495	0.3369	0.3498	0.2995
CT_C	0.3941	0.3954	0.3830	0.3759	0.3850	0.3708	0.3797	0.3763	0.3734	0.3677	0.3052

Magnitude Error: Triangular Structure, One sensors per phase at 35mm

Amp / Sensor	5A	6A	7A	8A	9A	10A	11A	12A	13A	14A	15A
S1	0.0540	0.1058	0.1274	-0.0798	0.0431	-0.0242	0.1124	-0.0843	-0.1562	-0.0105	-0.0368
S5	-0.0091	0.0121	0.0279	-0.0030	0.0330	-0.0381	0.0795	-0.0165	-0.0260	0.0112	0.0023
S9	0.0565	0.0262	0.0745	0.0279	-0.0291	-0.0053	0.0252	-0.0656	-0.0543	-0.0058	-0.1128
CT_A	-0.0329	-0.0393	-0.0448	-0.0516	-0.0573	-0.0657	-0.0712	-0.0772	-0.0825	-0.0908	-0.0836
CT_B	-0.0194	-0.0233	-0.0256	-0.0284	-0.0314	-0.0359	-0.0391	-0.0419	-0.0438	-0.0490	-0.0449
CT_C	-0.0197	-0.0237	-0.0268	-0.0301	-0.0347	-0.0371	-0.0418	-0.0452	-0.0485	-0.0515	-0.0458

Angle Error: Triangular Structure, One sensors per phase at 35mm

Amp / Sensor	5A	6A	7A	8A	9A	10A	11A	12A	13A	14A	15A
S1	0.0017	-0.0020	0.0012	-0.0018	0.0002	0.0011	-0.0002	0.0021	0.0003	0.0001	-0.0005
S5	-0.0026	-0.0020	-0.0008	-0.0008	-0.0008	-0.0006	0.0003	0.0005	0.0002	-0.0009	-0.0001
S9	-0.0018	-0.0009	-0.0004	-0.0021	-0.0007	-0.0010	0.0011	-0.0004	0.0010	0.0011	0.0000
CT_A	7E-06	7E-06	6E-06	9E-06	7E-06	8E-06	8E-06	7E-06	7E-06	7E-06	9E-06
CT_B	9E-06	8E-06	7E-06	7E-06	6E-06	7E-06	7E-06	7E-06	6E-06	7E-06	5E-06
CT_C	6E-06	6E-06	9E-06	6E-06	7E-06	6E-06	7E-06	6E-06	7E-06	7E-06	4E-06

Percentage TVE: Triangular Structure, Two sensors per phase at 7mm

Amp / Sensor	5A	6A	7A	8A	9A	10A	11A	12A	13A	14A	15A
S1	0.0880	0.1099	0.1773	0.0939	0.2684	0.2467	0.0209	0.2448	0.4049	0.1140	0.0151
S2	2.256	1.944	1.328	1.466	1.662	1.726	1.617	1.639	1.736	2.139	2.294
S5	0.0257	0.2480	0.2449	0.0767	0.0363	0.1580	0.2712	0.0508	0.1058	0.4690	0.9061
S6	0.498	0.712	0.010	0.162	0.063	0.056	0.020	0.206	0.227	0.385	0.328
S9	0.0507	0.1434	0.1432	0.1644	0.0090	0.0912	0.1329	0.0177	0.0813	0.1951	0.0260
S10	0.198	0.302	0.425	0.257	0.207	0.208	0.122	0.092	0.031	0.189	0.373
CT_a	0.6895	0.6831	0.6379	0.6379	0.6583	0.6494	0.6402	0.6376	0.6430	0.6506	0.6209
CT_b	0.4117	0.4021	0.3648	0.3546	0.3561	0.3545	0.3413	0.3379	0.3409	0.3451	0.2783
CT_c	0.3834	0.3740	0.3881	0.3875	0.3750	0.3822	0.3825	0.3853	0.3807	0.3701	0.2113

Angle Error: Triangular Structure, Two sensors per phase at 7mm

Amp / Sensor	5A	6A	7A	8A	9A	10A	11A	12A	13A	14A	15A
S1_ang	-0.0003	-0.0005	0.0004	0.0003	0.0002	0.0007	0.0002	-0.0001	0.0000	0.0001	0.0001
S2_ang	-6.3E-05	0.00037	0.0007	6.9E-05	-0.0002	3.9E-05	-0.0002	-3.7E-05	-4.2E-05	0.00011	-3.83E-05
S5_ang	0.0003	-0.0003	0.0003	0.0003	0.0001	-0.0004	-0.0002	-0.0002	0.0002	0.0006	-0.0001
S6_ang	-0.00064	0.00060	-0.00028	-6.1-05	0.0003	-0.0001	-0.0002	0.0002	-0.0003	-8.9E-05	-0.00011
S9_ang	0.0005	-0.0007	-0.0003	0.0005	4.2E-05	0.0001	-0.0002	0.0004	-0.0002	-0.0001	8.7E-05
S10_ang	-1.5E-05	-0.0004	8.4E-05	-0.0001	-0.0002	-0.0001	5.6E-06	-1.3E-04	3.0E-04	-2.7E-04	-6.5E-05
CT_a_ang	8.7E-06	6.2E-06	6.8E-06	5.7E-06	8.3E-06	6.9E-06	6.8E-06	7.9E-06	7.7E-06	8.1E-06	7.1E-06
CT_b_ang	5.7E-06	6.4E-06	7.3E-06	7.9E-06	5.5E-06	6.8E-06	7.8E-06	6.4E-06	6.0E-06	6.5E-06	5.8E-06
CT_c_ang	7.4E-06	7.5E-06	7.2E-06	5.3E-06	7.0E-06	6.6E-06	6.8E-06	6.1E-06	7.1E-06	7.3E-06	4.5E-06

Magnitude Error: Triangular Structure, Two sensors per phase at 7mm

Amp / Sensor	5A	6A	7A	8A	9A	10A	11A	12A	13A	14A	15A
S1_mag	-0.0044	0.0066	-0.0124	0.0075	-0.0242	-0.0247	-0.0023	0.0294	0.0526	0.0160	0.0023
S2_mag	-0.113	-0.117	-0.093	-0.117	-0.150	-0.173	-0.178	-0.197	-0.226	-0.299	-0.344
S5_mag	0.0013	0.0149	0.0171	0.0061	0.0033	0.0158	0.0298	-0.0061	-0.0138	-0.0657	-0.1359
S6_mag	0.025	0.043	0.001	0.013	0.006	-0.006	-0.002	-0.025	-0.030	-0.054	-0.049
S9_mag	0.0025	-0.0086	0.0100	0.0132	-0.0008	0.0091	0.0146	-0.0021	0.0106	-0.0273	0.0039
S10_mag	-0.010	0.018	-0.030	-0.021	0.019	0.021	-0.013	0.011	-0.004	0.026	0.056
CT_a_mag	-0.0345	-0.0410	-0.0447	-0.0510	-0.0592	-0.0649	-0.0704	-0.0765	-0.0836	-0.0911	-0.0931
CT_b_mag	-0.0206	-0.0241	-0.0255	-0.0284	-0.0320	-0.0354	-0.0375	-0.0406	-0.0443	-0.0483	-0.0417
CT_c_mag	-0.0192	-0.0224	-0.0272	-0.0310	-0.0337	-0.0382	-0.0421	-0.0462	-0.0495	-0.0518	-0.0317

Percentage TVE: Triangular Structure, Two sensors per phase at 15mm

Amp / Sensor	5A	6A	7A	8A	9A	10A	11A	12A	13A	14A	15A
S1	0.703	1.067	0.821	0.225	0.662	0.263	0.222	0.132	0.049	0.009	0.200
S2	0.4469	1.8872	0.1948	0.9912	0.0681	1.1117	1.0672	0.8815	0.9191	0.7406	0.8580
S5	0.8909	0.0179	0.9387	1.4195	0.4602	0.6894	0.1464	0.3331	0.1522	0.0915	0.3573
S6	0.9060	0.6149	1.1563	0.1120	0.2951	0.9457	0.0602	0.2572	0.1733	0.4364	0.3204
S9	0.2402	0.4669	0.7601	0.3314	0.6211	0.2379	0.1884	0.1979	0.0621	0.1376	0.0718
S10	0.7817	0.4861	0.4778	0.5614	0.0954	0.1721	0.0923	0.5114	0.6120	0.3661	0.2498
CT_a	0.6523	0.6711	0.6486	0.6608	0.6442	0.6578	0.6551	0.6474	0.6506	0.6390	0.6418
CT_b	0.3903	0.3983	0.3726	0.3646	0.3505	0.3564	0.3517	0.3454	0.3474	0.3351	0.2673
CT_c	0.4051	0.3842	0.3863	0.3682	0.3838	0.3723	0.3747	0.3742	0.3695	0.3790	0.3115

Magnitude Error: Triangular Structure, Two sensors per phase at 15mm

Amp / Sensor	5A	6A	7A	8A	9A	10A	11A	12A	13A	14A	15A
S1_mag	-0.035	-0.064	0.057	-0.018	0.060	-0.026	0.024	0.016	-0.006	-0.001	-0.030
S2_mag	0.0223	-0.1132	-0.0136	-0.0793	0.0061	-0.1112	-0.1174	-0.1058	-0.1195	-0.1037	-0.1287
S5_mag	0.0445	0.0011	0.0657	-0.1136	0.0414	-0.0689	0.0161	-0.0400	0.0198	-0.0128	-0.0536
S6_mag	0.0453	0.0369	0.0809	-0.0090	-0.0266	-0.0946	-0.0066	-0.0309	-0.0225	-0.0611	-0.0481
S9_mag	0.0120	-0.0280	0.0532	0.0265	0.0559	-0.0238	-0.0207	0.0237	-0.0081	0.0193	0.0108
S10_mag	-0.0391	0.0292	0.0334	0.0449	0.0086	0.0172	0.0102	0.0614	0.0796	0.0513	0.0375
CT_a_mag	-0.0326	-0.0403	-0.0454	-0.0529	-0.0580	-0.0658	-0.0721	-0.0777	-0.0846	-0.0895	-0.0963
CT_b_mag	-0.0195	-0.0239	-0.0261	-0.0292	-0.0315	-0.0356	-0.0387	-0.0414	-0.0452	-0.0469	-0.0401
CT_c_mag	-0.0203	-0.0231	-0.0270	-0.0295	-0.0345	-0.0372	-0.0412	-0.0449	-0.0480	-0.0531	-0.0467

Angle Error: Triangular Structure, Two sensors per phase at 15mm

Amp / Sensor	5A	6A	7A	8A	9A	10A	11A	12A	13A	14A	15A
S1_ang	0.0012	-0.0004	0.0000	-0.0002	0.0006	-0.0005	0.0006	0.0002	-0.0002	0.0004	0.0000
S2_ang	0.0013	-0.0003	0.0006	0.0005	-0.0001	-0.0005	0.0001	3.30E-05	0.00010	0.00020	3.43E-05
S5_ang	-0.0002	0.0005	-0.0006	0.0013	-0.0010	-0.0001	-1.98E-05	0.00018	0.00034	0.0001	8.95E-05
S6_ang	-0.00112	0.00004	-0.00042	0.00026	-0.00058	0.00045	0.00026	0.00026	-0.00046	-0.00023	0.00004
S9_ang	0.0010	-0.0006	-0.0007	-0.0004	0.0012	1.08E-05	0.0003	-0.0003	0.0002	-0.0002	-0.0002
S10_ang	-0.00122	0.00008	-0.00008	0.00094	0.00083	0.00003	-0.00002	0.00026	0.00003	-0.00013	0.00001
CT_a_ang	6.52E-06	7.02E-06	7.88E-06	7.42E-06	7.55E-06	7.43E-06	7.77E-06	6.49E-06	7.02E-06	7.92E-06	8.55E-06
CT_b_ang	6.52E-06	6.14E-06	8.36E-06	6.74E-06	7.24E-06	5.68E-06	8.03E-06	6.77E-06	7.63E-06	6.39E-06	5.66E-06
CT_c_ang	3.1E-06	6.1E-06	6.3E-06	7.1E-06	7.9E-06	6.8E-06	6.3E-06	6.5E-06	6.7E-06	7.3E-06	9.2E-06

Percentage TVE: Triangular Structure, Two sensors per phase at 25mm

Amp / Sensor	5A	6A	7A	8A	9A	10A	11A	12A	13A	14A	15A
S1	0.133	0.213	0.949	0.312	0.291	0.444	0.422	0.449	0.544	0.435	0.284
S2	0.6057	0.0309	0.4391	1.8410	1.1474	2.4111	1.9368	1.7251	1.2159	1.2607	1.9027
S5	0.157	1.020	1.292	0.946	0.029	0.604	0.009	0.493	0.248	0.516	0.322
S6	0.3493	0.5112	1.0468	0.0108	0.0825	0.0088	0.0777	0.5687	0.1796	0.4591	0.3556
S9	0.1742	0.5398	0.2605	0.6118	0.2073	0.3907	0.0458	0.0641	0.0806	0.2994	0.4167
S10	0.0960	0.7128	0.0464	0.0950	0.0149	0.1903	0.1149	0.2240	0.0772	0.0672	0.3391
CT_a	0.659	0.648	0.638	0.663	0.654	0.659	0.652	0.643	0.640	0.646	0.614
CT_b	0.3916	0.3869	0.3681	0.3697	0.3611	0.3558	0.3528	0.3391	0.3396	0.3357	0.2481
CT_c	0.403	0.401	0.390	0.372	0.374	0.371	0.374	0.373	0.377	0.377	0.261

Magnitude Error: Triangular Structure, Two sensors per phase at 25mm

Amp / Sensor	5A	6A	7A	8A	9A	10A	11A	12A	13A	14A	15A
S1_mag	-0.007	0.013	0.066	-0.025	0.026	-0.044	0.046	-0.054	-0.071	-0.061	-0.043
S2_mag	0.0303	-0.0019	0.0307	-0.1473	-0.1033	-0.2411	-0.2130	-0.2070	-0.1581	-0.1765	-0.2854
S5_mag	0.008	0.061	0.090	-0.076	0.003	-0.060	-0.001	-0.059	-0.032	-0.072	-0.048
S6_mag	0.0175	0.0307	0.0733	-0.0009	-0.0074	-0.0009	0.0086	-0.0682	-0.0234	-0.0643	-0.0533
S9_mag	-0.0087	0.0324	0.0182	-0.0489	0.0187	-0.0391	0.0050	0.0077	0.0105	-0.0419	-0.0625
S10_mag	-0.0048	-0.0428	0.0033	0.0076	-0.0013	0.0190	-0.0126	-0.0269	-0.0100	0.0094	0.0509
CT_a_mag	-0.033	-0.039	-0.045	-0.053	-0.059	-0.066	-0.072	-0.077	-0.083	-0.090	-0.092
CT_b_mag	-0.0196	-0.0232	-0.0258	-0.0296	-0.0325	-0.0356	-0.0388	-0.0407	-0.0442	-0.0470	-0.0372
CT_c_mag	-0.020	-0.024	-0.027	-0.030	-0.034	-0.037	-0.041	-0.045	-0.049	-0.053	-0.039

Angle Error: Triangular Structure, Two sensors per phase at 25mm

Amp / Sensor	5A	6A	7A	8A	9A	10A	11A	12A	13A	14A	15A
S1_ang	-0.0002	0.0001	0.0014	-0.0011	0.0019	0.0008	-0.0002	0.0007	0.0003	-0.0005	-0.0004
S2_ang	0.0002	-0.0002	0.0005	-0.0016	0.0009	0.0005	-0.0005	0.0004	0.0010	0.0003	-0.0001
S5_ang	0.001	0.001	-0.001	0.001	0.000	0.000	0.000	0.000	-0.001	0.000	0.001
S6_ang	-0.0003	-0.0007	0.0010	0.0001	0.0010	0.0007	-0.0003	0.0006	0.0007	-0.0001	0.0003
S9_ang	0.0019	-0.0005	0.0005	-0.0014	-0.0004	-0.0004	-0.0002	-0.0006	-0.0001	-0.0002	0.0006
S10_ang	-0.0025	-0.0008	0.0012	-0.0001	-0.0004	-0.0003	-0.0018	0.0006	-0.0005	-0.0008	-0.0005
CT_a_ang	5.61E-06	4.60E-06	7.38E-06	8.24E-06	7.36E-06	6.29E-06	8.33E-06	6.17E-06	7.92E-06	8.88E-06	1.08E-05
CT_b_ang	5.7E-06	6.2E-06	7.3E-06	6.1E-06	6.2E-06	6.1E-06	7.4E-06	6.5E-06	7.1E-06	6.3E-06	3.9E-06
CT_c_ang	7.2E-06	7.1E-06	6.2E-06	6.9E-06	7.1E-06	7.1E-06	6.1E-06	7.8E-06	6.9E-06	7.2E-06	9.0E-06

Percentage TVE: Triangular Structure, Two sensors per phase at 35mm

Amp / Sensor	5A	6A	7A	8A	9A	10A	11A	12A	13A	14A	15A
S1	0.32036	1.53699	2.16118	1.01952	0.89426	0.66386	0.98777	0.52502	0.01879	0.36629	0.08091
S2	0.4424	1.2483	0.8481	0.7368	1.6339	1.0653	0.6599	0.4173	1.5357	1.3987	1.4899
S5	0.4393	1.2193	0.5292	0.0548	0.8384	0.7282	0.5872	0.1735	0.4140	0.2910	0.7363
S6	0.490	0.423	0.279	0.412	0.413	0.460	0.297	0.008	0.034	0.300	0.530
S9	0.366	0.518	0.567	0.919	1.206	0.178	0.938	0.320	0.029	0.594	0.637
S10	0.281	0.360	0.400	0.745	0.099	0.542	0.135	0.544	0.413	0.057	0.079
CT_a	0.665	0.672	0.644	0.644	0.662	0.659	0.646	0.647	0.651	0.651	0.714
CT_b	0.400	0.397	0.371	0.356	0.365	0.361	0.348	0.342	0.344	0.344	0.326
CT_c	0.408	0.383	0.382	0.385	0.370	0.369	0.380	0.373	0.371	0.369	0.383

Angle TVE: Triangular Structure, Two sensors per phase at 35mm

Amp / Sensor	5A	6A	7A	8A	9A	10A	11A	12A	13A	14A	15A
S1_ang	0.00246	-0.00007	0.00073	0.00047	0.00132	0.00085	0.00027	0.00039	0.00032	0.00119	-0.00009
S2_ang	-0.0016	0.0018	0.0006	0.0008	0.0001	-0.0014	0.0012	-0.0005	0.0001	-0.0002	-0.0004
S5_ang	0.0011	-0.0019	0.0002	-0.0001	-0.0005	0.0002	-0.0020	0.0009	-0.0007	0.0001	0.0000
S6_ang	-0.003	-0.001	-0.001	0.001	0.000	0.001	0.001	0.000	0.000	-0.001	0.000
S9_ang	0.000	0.002	0.000	-0.001	0.000	-0.001	-0.001	0.000	0.000	0.000	0.000
S10_ang	0.002	-0.002	0.001	0.000	0.002	-0.001	0.002	-0.001	0.000	0.001	0.001
CT_a_ang	4.66E-06	7.45E-06	6.87E-06	8.20E-06	8.04E-06	7.33E-06	7.14E-06	8.09E-06	7.79E-06	8.03E-06	8.99E-06
CT_b_ang	9.81E-06	5.05E-06	6.77E-06	6.31E-06	5.99E-06	7.85E-06	6.62E-06	6.49E-06	6.18E-06	6.68E-06	4.19E-06
CT_c_ang	8.08E-06	7.08E-06	7.42E-06	7.39E-06	6.57E-06	5.85E-06	6.93E-06	6.86E-06	7.03E-06	7.67E-06	4.10E-06

Magnitude TVE: Triangular Structure, Two sensors per phase at 35mm

Amp / Sensor	5A	6A	7A	8A	9A	10A	11A	12A	13A	14A	15A
S1_mag	-0.01602	0.09222	0.15128	-0.08156	0.08048	0.06639	0.10866	-0.06300	-0.00244	-0.05128	0.01214
S2_mag	-0.0221	-0.0749	0.0594	0.0589	-0.1470	-0.1065	-0.0726	-0.0501	-0.1996	-0.1958	-0.2235
S5_mag	-0.0220	0.0732	0.0370	-0.0044	-0.0755	-0.0728	0.0646	-0.0208	-0.0538	-0.0407	-0.1105
S6_mag	0.024	0.025	-0.020	-0.033	0.037	0.046	-0.033	-0.001	-0.004	-0.042	-0.080
S9_mag	-0.018	0.031	0.040	0.074	-0.108	0.018	0.103	-0.038	-0.004	-0.083	-0.096
S10_mag	-0.014	-0.022	-0.028	-0.060	0.009	0.054	-0.015	-0.065	0.054	-0.008	-0.012
CT_a_mag	-0.033	-0.040	-0.045	-0.051	-0.060	-0.066	-0.071	-0.078	-0.085	-0.091	-0.107
CT_b_mag	-0.020	-0.024	-0.026	-0.029	-0.033	-0.036	-0.038	-0.041	-0.045	-0.048	-0.049
CT_c_mag	-0.020	-0.023	-0.027	-0.031	-0.033	-0.037	-0.042	-0.045	-0.048	-0.052	-0.058

Percentage TVE: Triangular Structure, Three sensors per phase at 7mm

Amp / Sensors	5A	6A	7A	8A	9A	10A	11A	12A	13A	14A	15A
1	0.489	0.173	0.076	0.208	0.210	0.289	0.048	0.104	0.192	0.089	0.351
2	1.109	1.576	1.503	1.383	1.132	1.628	1.498	1.152	1.742	1.735	1.764
3	0.005	0.144	0.454	0.350	0.261	0.517	0.127	0.205	0.357	0.350	0.313
5	0.996	0.588	0.345	0.482	1.027	1.039	0.033	0.890	0.117	0.629	0.152
6	0.531	0.476	0.204	0.469	0.866	0.959	0.057	0.287	0.355	0.207	0.697
7	0.567	0.100	0.529	0.538	0.555	0.507	0.020	0.186	0.167	0.086	0.380
9	0.294	0.122	0.060	0.220	0.163	0.118	0.056	0.033	0.260	0.052	0.049
10	0.758	0.186	0.114	0.183	0.032	0.273	0.139	0.025	0.234	0.104	0.168
11	0.297	0.265	0.165	0.061	0.045	0.065	0.107	0.253	0.193	0.232	0.034
CTa	0.659	0.674	0.656	0.646	0.640	0.656	0.642	0.636	0.647	0.641	0.653
CTb	0.393	0.395	0.371	0.355	0.346	0.356	0.344	0.340	0.341	0.343	0.304
CTc	0.396	0.379	0.364	0.372	0.376	0.362	0.376	0.374	0.373	0.370	0.257

Magnitude Error: Triangular Structure: Three sensors per phase, 7mm

Sensor \ Amp	5	6	7	8	9	10	11	12	13	14	15
S1 Mag	0.0244	0.0104	-0.0053	-0.0166	-0.0189	-0.0289	0.0053	-0.0125	0.0249	0.0125	0.0527
S2 Mag	-0.0555	-0.0946	-0.1052	-0.1106	-0.1019	-0.1628	-0.1647	-0.1382	-0.2264	-0.2429	-0.2646
S3 Mag	0.0002	-0.0086	-0.0318	-0.0280	-0.0235	-0.0517	-0.0139	0.0246	0.0464	0.0489	0.0469
S5 Mag	-0.0498	-0.0353	0.0241	0.0386	0.0924	0.1039	-0.0036	0.1068	-0.0153	0.0880	0.0229
S6 Mag	-0.0265	-0.0285	0.0143	0.0375	0.0780	0.0959	-0.0063	0.0345	-0.0462	0.0290	-0.1046
S7 Mag	-0.0283	-0.0060	0.0370	0.0430	0.0499	0.0507	-0.0022	0.0223	-0.0217	0.0120	-0.0569
S9 Mag	0.0149	-0.0159	0.0115	-0.0049	0.0040	-0.0065	-0.0118	-0.0304	-0.0251	-0.0325	-0.0051
S10 Mag	-0.0379	-0.0112	0.0080	-0.0146	0.0029	0.0273	0.0153	0.0031	0.0304	0.0145	0.0252
S11 Mag	0.0149	-0.0159	0.0115	-0.0049	0.0040	-0.0065	-0.0118	-0.0304	-0.0251	-0.0325	-0.0051
CTA Mag	-0.0329	-0.0404	-0.0459	-0.0517	-0.0576	-0.0656	-0.0707	-0.0763	-0.0841	-0.0898	-0.0979
CTB Mag	-0.0196	-0.0237	-0.0260	-0.0284	-0.0312	-0.0356	-0.0378	-0.0408	-0.0443	-0.0480	-0.0456
CTC Mag	-0.0198	-0.0227	-0.0255	-0.0298	-0.0338	-0.0362	-0.0414	-0.0449	-0.0485	-0.0518	-0.0385

Angle Error: Triangular Structure: Three sensors per phase, 7mm

Amp / Sensors	5	6	7	8	9	10	11	12	13	14	15
S1_Ang	-0.0002	0.0003	0.0007	0.0001	-0.0002	0.0001	0.0004	0.0001	-0.0002	7.18E-06	-2E-05
S2_Ang	0.0006	-0.0001	-0.0006	-0.0002	-0.0003	0.0001	-0.0001	-0.0002	-0.0001	1.71E-05	8E-06
S3_Ang	0.0001	0.0003	0.0000	0.0002	0.0002	-0.0003	0.0002	-0.0002	-0.0001	-0.0002	0.0000
S5_Ang	0.0000	0.0000	-0.0008	-0.0001	0.0000	0.0000	-0.0002	0.0004	0.0001	0.0004	-0.0003
S6_Ang	-0.0004	0.0003	-0.0001	0.0003	0.0000	-0.0002	-0.0001	0.0002	0.0002	-0.0002	0.0002
S7_Ang	-0.0001	0.0002	0.0001	0.0004	-0.0001	0.0002	0.0004	0.0002	0.0001	-3.4E-05	-1.4E-05
S9_Ang	0.0005	-0.0001	0.0001	0.0005	0.0005	-0.0004	-0.0001	0.0002	0.0002	7.36E-07	4.9E-05
S10_Ang	-0.0005	0.0001	-0.0007	0.0000	0.0002	-0.0003	-0.0003	0.0003	0.0002	-8.6E-05	3.5E-05
S11_Ang	-0.0005	0.0000	-0.0001	0.0004	0.0001	0.0000	-0.0003	0.0001	0.0003	1.83E-05	-2.5E-05
CTA_Ang	7.8E-06	5.9E-06	7.8E-06	6.6E-06	8.2E-06	9.3E-06	7.1E-06	8.1E-06	8.6E-06	7.8E-06	9.7E-06
CTB_Ang	6.3E-06	4.3E-06	7.1E-06	7.3E-06	6.1E-06	6.5E-06	7.0E-06	5.9E-06	7.1E-06	6.7E-06	5.5E-06
CTC_Ang	6.2E-06	9.4E-06	5.8E-06	7.2E-06	6.9E-06	6.9E-06	6.8E-06	7.4E-06	7.7E-06	6.7E-06	9.6E-06

Triangular Structure, Three Sensors per Phase 15mm distance from source

Percentage TVE

Amp / Sensors	5A	6A	7A	8A	9A	10A	11A	12A	13A	14A	15A
1	0.080	0.338	0.162	0.339	0.091	0.097	0.416	0.296	0.075	0.062	0.151
2	0.536	1.983	0.774	1.235	0.047	1.404	0.182	0.553	1.301	0.826	0.527
3	1.387	0.742	1.269	0.897	0.787	0.845	0.715	0.743	0.139	0.554	0.613
5	1.026	0.259	0.323	0.102	0.707	0.755	0.636	0.270	0.367	0.461	0.834
6	0.298	0.127	0.339	0.222	0.144	0.332	0.516	0.362	0.482	0.165	0.164
7	0.392	0.470	0.377	0.401	0.216	0.006	0.056	0.316	0.412	0.074	0.175
9	0.539	0.402	0.249	0.002	0.346	0.298	0.234	0.112	0.197	0.226	0.476
10	0.577	0.111	0.442	0.311	0.429	0.167	0.114	0.014	0.053	0.796	0.548
11	0.529	0.149	0.211	0.142	0.308	0.213	0.183	0.592	0.267	0.041	0.687
CTa	0.657	0.674	0.651	0.664	0.640	0.656	0.645	0.639	0.642	0.642	0.644
CTb	0.394	0.397	0.366	0.369	0.351	0.352	0.345	0.339	0.338	0.341	0.281
CTc	0.403	0.372	0.369	0.364	0.381	0.366	0.365	0.376	0.373	0.371	0.377

Triangular Structure, Three Sensors per Phase 15mm distance from source

Magnitude Error

Amp / Sensors	5A	6A	7A	8A	9A	10A	11A	12A	13A	14A	15A
1	0.004	-0.020	0.011	0.027	0.008	-0.010	0.046	0.036	-0.010	0.009	0.023
2	0.027	-0.119	-0.054	-0.099	-0.004	-0.140	-0.020	-0.066	-0.169	-0.116	-0.079
3	0.069	-0.045	-0.089	-0.072	0.071	-0.085	0.079	0.089	0.018	0.078	0.092
5	0.051	-0.016	-0.023	-0.008	0.064	-0.075	-0.070	-0.032	-0.048	0.065	0.125
6	0.015	0.008	0.024	0.018	0.013	-0.033	-0.057	-0.043	-0.063	0.023	0.025
7	-0.020	0.028	0.026	0.032	-0.019	0.001	-0.006	-0.038	-0.054	0.010	0.026
9	0.027	-0.024	-0.017	0.000	0.031	-0.030	-0.026	0.013	-0.026	-0.032	0.071
10	-0.029	-0.007	-0.031	0.025	-0.039	-0.017	-0.012	-0.002	0.007	0.111	0.082
11	0.026	-0.009	-0.015	0.011	0.028	-0.021	-0.020	-0.071	-0.035	0.006	0.103
CTa	-0.033	-0.040	-0.046	-0.053	-0.058	-0.066	-0.071	-0.077	-0.083	-0.090	-0.097
CTb	-0.020	-0.024	-0.026	-0.030	-0.032	-0.035	-0.038	-0.041	-0.044	-0.048	-0.042
CTc	-0.020	-0.022	-0.026	-0.029	-0.034	-0.037	-0.040	-0.045	-0.049	-0.052	-0.057

Triangular Structure, Three Sensors per Phase 15mm distance from source

Angle Error

Amp / Sensors	5A	6A	7A	8A	9A	10A	11A	12A	13A	14A	15A
1	-0.0008	0.0002	0.0002	0.0006	-0.0001	0.0001	0.0003	0.0005	-0.0003	0.0003	-0.0003
2	0.0009	0.0000	-0.0013	0.0000	0.0003	0.0002	-0.0006	0.0003	0.0004	0.0004	0.0002
3	0.0002	-0.0003	0.0002	0.0001	0.0005	0.0000	0.0003	0.0002	0.0005	-0.0001	-0.0005
5	-0.0004	-0.0005	-0.0006	0.0008	-0.0005	-0.0006	0.0001	-0.0004	0.0002	-0.0001	-0.0003
6	-0.0007	0.0001	-0.0005	0.0005	-0.0002	0.0001	0.0002	-0.0002	0.0001	-0.0003	0.0000
7	-0.0006	0.0006	-0.0004	0.0002	-0.0006	0.0004	0.0000	0.0002	-0.0003	-0.0001	0.0003
9	0.0004	0.0013	0.0009	-0.0002	-0.0006	-0.0009	0.0008	0.0001	0.0001	0.0001	-0.0002
10	-0.0013	0.0002	-0.0002	0.0006	0.0001	0.0001	0.0001	-0.0001	-0.0002	-0.0001	0.0002
11	-9E-05	0.00019	0.00029	0.00066	-0.00020	-0.00007	-0.00001	-0.00042	-0.00049	0.00032	-0.00004
Cta	7.0E-06	7.1E-06	9.2E-06	9.2E-06	7.8E-06	6.7E-06	7.1E-06	7.8E-06	7.8E-06	7.9E-06	7.0E-06
CTb	8.3E-06	7.2E-06	7.2E-06	6.5E-06	6.2E-06	6.3E-06	7.2E-06	6.1E-06	6.9E-06	6.5E-06	7.0E-06
CTc	7.9E-06	7.1E-06	7.5E-06	6.6E-06	7.3E-06	8.2E-06	7.8E-06	6.5E-06	7.6E-06	6.6E-06	6.6E-06

Triangular Structure, Three Sensors per Phase 25mm distance from source

Percentage TVE Error

Amp / Sensor	5	6	7	8	9	10	11	12	13	14	15
S1_TVE	1.382	0.602	0.577	0.156	0.632	0.253	0.592	0.315	0.019	0.242	0.118
S2_TVE	1.525	1.840	0.705	0.242	0.154	1.131	0.902	0.844	0.633	0.546	0.168
S3_TVE	3.094	1.704	0.451	0.921	0.339	0.630	1.203	1.315	0.242	0.755	0.413
S5_TVE	1.936	0.355	0.801	0.384	0.235	0.082	0.375	1.037	0.184	0.161	1.430
S6_TVE	0.849	1.035	0.580	0.549	0.067	0.269	0.792	0.859	0.350	0.366	0.405
S7_TVE	0.343	0.923	0.835	0.236	0.260	0.212	0.265	0.094	0.305	0.155	0.538
S9_TVE	0.365	0.685	0.915	0.566	0.115	0.274	0.054	0.290	0.264	0.069	0.604
S10_TVE	0.893	0.509	0.195	0.325	0.866	0.111	0.165	0.165	0.006	0.058	0.057
S11_TVE	0.027	0.157	0.367	0.278	0.193	0.507	0.193	0.108	0.198	0.340	0.484
CTA_TVE	0.666	0.679	0.658	0.659	0.644	0.650	0.649	0.648	0.642	0.633	0.627
CTB_TVE	0.666	0.679	0.658	0.659	0.644	0.650	0.649	0.648	0.642	0.633	0.627
CTC_TVE	0.666	0.679	0.658	0.659	0.644	0.650	0.649	0.648	0.642	0.633	0.627

Triangular Structure, Three Sensors per Phase 25mm distance from source

Magnitude Error

Amp / Sensor	5	6	7	8	9	10	11	12	13	14	15
S1_Mag	0.0691	-0.0361	0.0404	-0.0125	-0.0568	-0.0253	-0.0651	-0.0378	-0.0024	-0.0339	-0.0177
S2_Mag	0.0763	-0.1104	-0.0494	0.0193	-0.0138	-0.1131	-0.0992	-0.1012	-0.0823	-0.0765	0.0253
S3_Mag	0.1547	-0.1023	0.0316	0.0737	-0.0305	0.0630	-0.1323	-0.1578	0.0314	-0.1057	0.0620
S5_Mag	0.0968	-0.0213	0.0561	0.0307	-0.0212	0.0082	-0.0412	-0.1244	-0.0239	-0.0225	-0.2146
S6_Mag	0.0425	0.0621	0.0406	0.0439	-0.0060	-0.0269	-0.0872	-0.1031	-0.0454	-0.0512	-0.0607
S7_Mag	-0.0172	0.0554	0.0584	0.0189	0.0234	-0.0212	0.0292	-0.0113	-0.0397	-0.0217	-0.0807
S9_Mag	-0.0014	0.0094	-0.0257	0.0222	0.0174	-0.0507	-0.0212	0.0129	0.0258	0.0477	0.0725
S10_Mag	-0.0447	0.0305	0.0137	0.0260	-0.0780	-0.0111	-0.0181	0.0198	0.0008	-0.0081	0.0085
S11_Mag	-0.0014	0.0094	-0.0257	0.0222	0.0174	-0.0507	-0.0212	0.0129	0.0258	0.0477	0.0725
CTA_Mag	-0.033	-0.041	-0.046	-0.053	-0.058	-0.065	-0.071	-0.078	-0.083	-0.089	-0.094
CTB_Mag	-0.020	-0.024	-0.027	-0.030	-0.032	-0.035	-0.038	-0.041	-0.045	-0.047	-0.051
CTC_Mag	-0.020	-0.022	-0.026	-0.030	-0.034	-0.038	-0.041	-0.044	-0.049	-0.052	-0.070

Triangular Structure, Three Sensors per Phase 25mm distance from source

Angle Error

Amp / Sensor	5	6	7	8	9	10	11	12	13	14	15
S1_Ang	0.0025	0.0004	0.0008	-0.0008	-0.0001	-0.0006	0.0010	-0.0005	0.0006	-0.0005	0.0000
S2_Ang	-0.0003	0.0018	0.0006	-0.0005	-0.0011	-0.0002	-0.0004	0.0000	-0.0004	0.0000	0.0001
S3_Ang	-0.0013	0.0004	0.0009	0.0019	0.0011	-0.0010	0.0001	0.0007	-0.0004	0.0003	-0.0001
S5_Ang	0.0031	-0.0005	-0.0005	-0.0003	-0.0004	-0.0002	-0.0001	-0.0007	0.0003	-0.0009	0.0002
S6_Ang	0.0000	0.0003	-0.0010	-0.0003	-0.0003	-0.0006	0.0002	-0.0004	0.0009	-0.0001	-0.0002
S7_Ang	-0.0015	0.0005	0.0006	-0.0013	0.0005	0.0006	0.0006	-0.0004	-0.0005	0.0000	0.0004
S9_Ang	0.0003	0.0012	-0.0008	0.0012	-0.0006	0.0005	-0.0003	-0.0005	0.0001	-0.0002	0.0000
S10_Ang	0.0010	-0.0005	0.0001	-0.0003	-0.0011	0.0004	-0.0006	-0.0003	0.0004	-0.0007	0.0006
S11_Ang	-0.0001	-0.0013	0.0005	-0.0013	0.0002	0.0002	-0.0004	0.0003	0.0001	-0.00004	-0.0002
CTA_Ang	7.6E-06	6.3E-06	7.9E-06	6.5E-06	7.8E-06	7.4E-06	7.1E-06	9.1E-06	7.6E-06	6.6E-06	8.2E-06
CTB_Ang	6.4E-06	6.5E-06	6.4E-06	6.9E-06	6.3E-06	6.8E-06	6.7E-06	5.7E-06	6.4E-06	7.4E-06	7.9E-06
CTC_Ang	8.6E-06	6.3E-06	7.9E-06	7.8E-06	6.5E-06	6.8E-06	6.5E-06	8.7E-06	7.0E-06	7.2E-06	6.7E-06

Triangular Structure, Three Sensors per Phase 35mm distance from source,

Percentage TVE

Amp / Sensor	5	6	7	8	9	10	11	12	13	14	15
S1_TVE	0.307	0.740	0.039	0.465	0.060	0.065	0.130	0.567	0.175	0.805	0.481
S2_TVE	3.922	2.268	0.741	1.356	0.342	0.252	0.978	0.937	1.204	0.172	1.351
S3_TVE	6.007	0.927	2.425	1.759	1.643	1.305	0.659	1.209	0.660	0.051	0.070
S5_TVE	1.119	0.794	0.948	0.006	0.541	0.004	0.281	0.299	0.172	0.115	1.509
S6_TVE	0.256	0.162	0.268	0.187	0.094	0.307	0.045	0.253	0.547	1.027	0.484
S7_TVE	0.398	1.082	0.121	0.218	0.131	0.394	0.556	0.129	0.392	0.903	0.488
S9_TVE	1.170	0.914	1.140	0.699	0.641	0.110	0.512	0.267	0.016	0.434	0.086
S10_TVE	0.690	0.233	0.160	0.044	0.236	0.507	0.019	0.179	0.577	0.119	0.367
S11_TVE	0.743	0.922	0.350	0.292	0.145	0.141	0.282	0.104	0.135	0.333	0.237
CTA_TVE	0.679	0.671	0.650	0.641	0.653	0.652	0.644	0.653	0.644	0.635	0.572
CTB_TVE	0.679	0.671	0.650	0.641	0.653	0.652	0.644	0.653	0.644	0.635	0.572
CTC_TVE	0.679	0.671	0.650	0.641	0.653	0.652	0.644	0.653	0.644	0.635	0.572

Triangular Structure, Three Sensors per Phase 35mm distance from source

Magnitude Error

Amp / Sensor	5	6	7	8	9	10	11	12	13	14	15
S1 Mag	0.015	0.044	-0.003	0.037	0.005	0.006	0.014	-0.068	-0.023	-0.113	-0.072
S2 Mag	-0.196	-0.136	-0.052	0.108	-0.031	-0.025	0.108	-0.112	-0.157	-0.024	-0.203
S3 Mag	-0.300	0.056	0.170	0.141	0.148	-0.130	-0.072	-0.145	0.086	0.007	0.011
S5 Mag	0.056	0.048	0.066	0.000	0.049	0.000	-0.031	-0.036	-0.022	0.016	-0.226
S6 Mag	0.013	0.010	0.019	-0.015	0.008	0.031	-0.005	-0.030	-0.071	-0.144	-0.073
S7 Mag	0.020	0.065	-0.008	0.017	0.012	0.039	-0.061	-0.015	-0.051	-0.126	-0.073
S9 Mag	0.037	-0.055	-0.025	-0.023	0.013	0.014	0.031	-0.012	-0.018	0.047	-0.036
S10 Mag	0.035	0.014	-0.011	-0.004	-0.021	-0.051	-0.002	-0.022	0.075	0.017	-0.055
S11 Mag	0.037	-0.055	-0.025	-0.023	0.013	0.014	0.031	-0.012	-0.018	0.047	-0.036
CTA Mag	-0.034	-0.040	-0.045	-0.051	-0.059	-0.065	-0.071	-0.078	-0.084	-0.089	-0.086
CTB Mag	-0.021	-0.024	-0.026	-0.028	-0.032	-0.035	-0.037	-0.041	-0.045	-0.047	-0.043
CTC Mag	-0.018	-0.023	-0.027	-0.031	-0.034	-0.037	-0.042	-0.044	-0.048	-0.053	-0.039

Triangular Structure, Three Sensors per Phase 35mm distance from source

Angle Error

Amp / Sensor	5	6	7	8	9	10	11	12	13	14	15
S1_Ang	-0.0019	0.0002	0.0015	-0.0010	0.0030	0.0015	-0.0010	0.0022	0.0002	-0.0008	-0.0009
S2_Ang	-0.0009	0.0019	0.0006	-0.0014	0.0007	-0.0002	-0.0016	0.0011	-0.0013	-0.0009	0.0002
S3_Ang	-0.0006	-0.0002	-0.0006	-0.0009	0.0000	0.0001	0.0003	-0.0002	0.0004	0.0005	0.0001
S5_Ang	0.0020	0.0000	0.0017	0.0003	-0.0022	-0.0007	-0.0003	-0.0006	-0.0004	0.0000	-0.0013
S6_Ang	0.0019	0.0008	0.0000	0.0002	-0.0004	-0.0009	-0.0004	-0.0005	-0.0004	0.0004	0.0001
S7_Ang	-0.0007	0.0019	0.0005	-0.0007	-0.0008	0.0010	0.0007	-0.0003	0.0005	-0.0003	-0.0006
S9_Ang	-0.0018	0.0005	-0.0003	-0.0016	-0.0001	-0.0002	-0.0004	-0.0011	-0.0009	0.0007	-0.0009
S10_Ang	-0.0006	-0.0008	-0.0013	0.0014	0.0003	0.0005	-0.0002	0.0008	-0.0002	-0.0012	-0.0005
S11_Ang	0.0002	0.0010	0.0011	-0.0004	-0.0003	-0.0010	0.0003	-0.0010	0.0003	-0.0009	-0.0001
CTA_Ang	7.4E-06	6.5E-06	5.7E-06	8.9E-06	6.0E-06	8.1E-06	8.1E-06	7.1E-06	6.3E-06	8.2E-06	1.4E-05
CTB_Ang	9.6E-06	6.9E-06	6.4E-06	6.7E-06	7.0E-06	6.5E-06	6.0E-06	6.8E-06	7.0E-06	6.4E-06	5.9E-06
CTC_Ang	6.2E-06	6.9E-06	6.7E-06	4.2E-06	7.5E-06	7.0E-06	5.7E-06	7.0E-06	7.1E-06	6.7E-06	8.9E-06

E.2 Results for Various Combinations in Horizontal Structure

HORIZONTAL STRUCTURE: Two Sensors per Phase 7mm distance from source, Percentage TVE

Amp / Sensor	5	6	7	8	9	10	11	12	13	14	15
S1_TVE	0.929	0.411	0.380	0.218	0.296	0.284	0.048	0.103	0.056	0.163	0.110
S2_TVE	0.717	0.979	1.156	0.418	0.830	0.698	0.920	1.278	1.326	1.213	1.537
S5_TVE	0.144	0.737	0.710	0.064	0.098	0.149	0.219	0.208	0.024	0.038	0.187
S6_TVE	0.126	0.497	0.087	0.266	0.200	0.241	0.284	0.058	0.191	0.113	0.173
S9_TVE	0.211	0.078	0.214	0.203	0.121	0.053	0.176	0.139	0.006	0.046	0.138
S10_TVE	0.190	0.115	0.332	0.541	0.289	0.312	0.084	0.014	0.187	0.235	0.201
CTA_TVE	0.652	0.665	0.640	0.644	0.650	0.639	0.638	0.646	0.645	0.635	0.628
CTB_TVE	0.398	0.411	0.378	0.364	0.366	0.354	0.354	0.356	0.352	0.342	0.255
CTC_TVE	0.401	0.336	0.376	0.355	0.337	0.357	0.350	0.328	0.334	0.346	0.207

Horizontal Structure: Two Sensors per Phase 7mm distance from source

Angle Error

Amp / Sensor	5	6	7	8	9	10	11	12	13	14	15
S1_Ang	-0.00025	-0.00019	-0.00051	-0.00030	-0.00040	-0.00041	0.00007	0.00009	0.00031	-0.00008	-0.00030
S2_Ang	-0.001	0.001	0.000	0.000	0.000	0.000	0.000	0.000	0.000	0.000	0.000
S5_Ang	0.0002	0.0006	0.0006	0.0002	0.0001	-0.0002	0.0001	-0.0001	0.0003	0.0000	0.0001
S6_Ang	-0.0002	-0.0003	-0.0003	0.0006	-0.0002	-0.0001	0.0002	0.0001	0.0000	0.0001	-0.0001
S9_Ang	-0.0012	-0.0004	0.0007	-0.0003	0.0006	0.0001	0.0001	0.0001	-0.0001	0.0000	0.0003
S10_Ang	-0.0001	0.0004	0.0001	-0.0002	0.0000	0.0002	-0.0002	-0.0001	-0.0001	-0.0001	0.0002
CTA_Ang	7.6E-06	6.5E-06	7.4E-06	7.5E-06	6.9E-06	7.3E-06	7.5E-06	7.4E-06	7.2E-06	7.1E-06	9.9E-06
CTB_Ang	5.54E-06	6.72E-06	5.50E-06	7.07E-06	7.64E-06	8.06E-06	7.03E-06	6.75E-06	6.99E-06	5.78E-06	5.49E-06
CTC_Ang	5.45E-06	8.31E-06	5.17E-06	7.56E-06	7.51E-06	8.23E-06	6.71E-06	6.89E-06	6.37E-06	6.77E-06	7.34E-06

Horizontal Structure: Two Sensors per Phase 7mm distance from source

Magnitude Error

Amp / Sensor	5	6	7	8	9	10	11	12	13	14	15
S1_Mag	0.046	-0.025	0.027	-0.017	-0.027	-0.028	0.005	-0.012	-0.007	0.023	-0.017
S2_Mag	-0.036	-0.059	-0.081	-0.033	-0.075	-0.070	-0.101	-0.153	-0.172	-0.170	-0.231
S5_Mag	-0.007	0.044	-0.050	0.005	-0.009	0.015	-0.024	0.025	-0.003	0.005	0.028
S6_Mag	-0.006	0.030	0.006	0.021	0.018	0.024	-0.031	-0.007	-0.025	-0.016	-0.026
S9_Mag	0.011	0.005	-0.015	-0.016	-0.011	-0.005	0.019	-0.017	0.001	-0.006	0.021
S10_Mag	-0.010	-0.007	0.023	-0.043	0.026	-0.031	0.009	0.002	0.024	-0.033	0.030
CTA_Mag	0.652	0.665	0.640	0.644	0.650	0.639	0.638	0.646	0.645	0.635	0.628
CTB_Mag	0.398	0.411	0.378	0.364	0.366	0.354	0.354	0.356	0.352	0.342	0.255
CTC_Mag	-0.020	-0.020	-0.026	-0.028	-0.030	-0.036	-0.038	-0.039	-0.043	-0.048	-0.031

Horizontal Structure: Two Sensors per Phase 15mm distance from source

Percentage TVE

Amp / Sensor	5	6	7	8	9	10	11	12	13	14	15
S1_TVE	0.686	0.170	0.868	0.317	0.045	0.382	0.077	0.184	0.270	0.147	0.058
S2_TVE	0.807	0.852	0.108	0.571	0.404	0.526	0.573	0.217	0.101	0.190	0.156
S5_TVE	0.595	0.228	0.148	0.584	0.001	0.044	0.119	0.044	0.167	0.070	0.157
S6_TVE	0.760	0.670	0.569	0.073	0.172	0.281	0.057	0.338	0.270	0.275	0.314
S9_TVE	0.609	0.148	0.339	0.119	0.022	0.028	0.138	0.150	0.004	0.145	0.155
S10_TVE	0.163	0.363	0.238	0.358	0.123	0.178	0.136	0.140	0.252	0.252	0.494
CTA_TVE	0.661	0.633	0.634	0.640	0.632	0.637	0.657	0.650	0.641	0.634	0.579
CTB_TVE	0.388	0.369	0.363	0.354	0.350	0.346	0.349	0.341	0.339	0.334	0.296
CTC_TVE	0.374	0.380	0.362	0.359	0.363	0.359	0.347	0.347	0.347	0.344	0.356

Horizontal Structure: Two Sensors per Phase 15mm distance from source

Angle Error

Amp / Sensor	5	6	7	8	9	10	11	12	13	14	15
S1_Ang	0.0004	0.0009	-0.0002	-0.0003	-0.0005	0.0002	0.0002	0.0001	0.0002	0.0002	-0.0003
S2_Ang	-0.0004	-0.0014	-0.0003	-0.0002	0.0004	0.0007	0.0001	0.0002	0.0003	0.0002	-0.00008
S5_Ang	0.0012	0.0002	0.0003	-0.0006	-0.0009	0.0004	0.0004	-0.0001	0.0001	-0.0002	0.0003
S6_Ang	-0.0008	-0.0002	0.0005	-0.0007	0.0001	0.0001	0.0003	0.0001	-0.0004	0.0001	0.0004
S9_Ang	0.0005	-0.0003	0.0008	0.0002	0.0003	0.0000	0.0003	-0.0001	-0.0002	0.0002	0.0000
S10_Ang	0.0015	0.0011	-0.0003	0.0004	0.0006	-0.0003	-0.0001	0.0006	-0.0004	0.0003	0.0003
CTA_Ang	7.23E-06	7.67E-06	5.42E-06	5.67E-06	6.71E-06	7.26E-06	7.89E-06	8.33E-06	7.02E-06	8.18E-06	8.23E-06
CTB_Ang	7.70E-06	7.18E-06	7.91E-06	7.09E-06	6.42E-06	6.01E-06	5.96E-06	7.87E-06	6.16E-06	7.03E-06	7.08E-06
CTC_Ang	5.8E-06	6.8E-06	7.5E-06	7.9E-06	6.3E-06	6.2E-06	6.1E-06	6.0E-06	7.5E-06	7.4E-06	8.4E-06

Horizontal Structure: Two Sensors per Phase 15mm distance from source

Magnitude Error

Amp / Sensor	5	6	7	8	9	10	11	12	13	14	15
S1_Mag	-0.034	0.001	0.061	-0.025	0.004	-0.038	-0.009	-0.022	0.035	0.021	0.009
S2_Mag	0.040	0.001	0.008	-0.046	-0.036	-0.053	-0.063	-0.026	0.013	-0.027	-0.023
S5_Mag	-0.030	0.014	0.010	-0.047	0.000	-0.004	-0.013	-0.005	0.022	0.010	0.024
S6_Mag	-0.038	0.040	0.040	-0.006	0.016	0.028	-0.006	-0.041	-0.035	-0.038	-0.047
S9_Mag	0.030	-0.009	0.024	-0.010	-0.002	0.003	0.015	-0.018	0.001	-0.020	-0.023
S10_Mag	-0.008	-0.022	-0.017	-0.029	-0.011	-0.018	0.015	0.017	0.033	0.035	0.074
CTA_Mag	-0.0331	-0.0380	-0.0444	-0.0512	-0.0569	-0.0637	-0.0722	-0.0780	-0.0833	-0.0887	-0.0869
CTB_Mag	-0.0194	-0.0222	-0.0254	-0.0283	-0.0315	-0.0346	-0.0384	-0.0409	-0.0441	-0.0468	-0.0443
CTC_Mag	-0.0187	-0.0228	-0.0253	-0.0288	-0.0327	-0.0359	-0.0382	-0.0417	-0.0451	-0.0482	-0.0533

Horizontal Structure: Two Sensors per Phase 25mm distance from source

Percentage TVE

Amp / Sensor	5	6	7	8	9	10	11	12	13	14	15
S1_TVE	0.9906	0.0926	0.3577	0.1830	0.0648	0.3186	0.3409	0.0092	0.4691	0.2402	0.3888
S2_TVE	0.0744	0.2580	0.2059	0.6071	0.4630	0.4265	0.1721	0.2686	0.1937	0.3461	0.4713
S5_TVE	0.7982	0.1311	0.2871	0.4135	0.1668	0.2692	0.5128	0.3416	0.2807	0.1614	0.3610
S6_TVE	0.0738	0.9421	0.9359	0.5694	0.1679	0.4228	0.2812	0.0108	0.2128	0.4605	0.1893
S9_TVE	0.8119	0.1296	0.6219	0.7513	0.3696	0.1171	0.1061	0.0520	0.0365	0.2726	0.2187
S10_TVE	0.2852	0.0324	0.1496	0.0148	0.7294	0.0576	0.0960	0.1256	0.2481	0.0436	0.4805
CTA_TVE	0.6828	0.6385	0.6621	0.6500	0.6324	0.6385	0.6374	0.6320	0.6340	0.6393	0.6474
CTB_TVE	0.4104	0.3835	0.3719	0.3644	0.3473	0.3425	0.3380	0.3366	0.3373	0.3372	0.2762
CTC_TVE	0.3647	0.3697	0.3473	0.3500	0.3574	0.3522	0.3506	0.3538	0.3491	0.3454	0.2210

Horizontal Structure: Two Sensors per Phase 25mm distance from source

Angle Error

Amp / Sensor	5	6	7	8	9	10	11	12	13	14	15
S1_Ang	-2.8E-05	-0.00085	0.00043	-0.00082	0.00112	-0.00019	-0.00004	0.00011	0.00007	-0.00049	-0.00081
S2_Ang	-0.0007	-0.0002	-0.0001	0.0007	-0.0005	-0.0001	0.0010	0.0010	-0.0003	0.0003	0.0002
S5_Ang	0.0020	0.0012	-0.0012	-0.0011	0.0003	0.0000	0.0007	0.0007	0.0000	0.0005	-0.0002
S6_Ang	0.0020	0.0002	-0.0010	-0.0009	-0.0002	-0.0003	-0.0006	-0.0002	-0.0001	-0.0004	0.0008
S9_Ang	0.0004	-0.0024	0.0011	0.0007	0.0001	0.0002	0.0008	0.0002	-0.0005	-0.0003	0.0004
S10_Ang	0.0012	-0.0001	0.0010	0.0009	0.0004	-0.0006	0.0003	-0.0001	-0.0003	-0.0001	0.0004
CTA_Ang	5.94E-06	7.59E-06	6.76E-06	7.40E-06	7.13E-06	7.29E-06	6.78E-06	8.43E-06	8.21E-06	7.89E-06	9.39E-06
CTB_Ang	6.11E-06	6.75E-06	7.03E-06	5.98E-06	6.46E-06	6.62E-06	6.37E-06	5.94E-06	7.17E-06	6.79E-06	9.04E-06
CTC_Ang	7.15E-06	6.67E-06	2.90E-06	5.01E-06	6.97E-06	7.26E-06	7.02E-06	5.98E-06	6.46E-06	7.09E-06	7.27E-06

Horizontal Structure: Two Sensors per Phase 25mm distance from source

Magnitude Error

Amp / Sensor	5	6	7	8	9	10	11	12	13	14	15
S1_Mag	0.0495	-0.0056	0.0250	-0.0146	0.0058	-0.0319	-0.0375	0.0011	0.0610	-0.0336	0.0583
S2_Mag	-0.0037	-0.0155	-0.0144	-0.0486	0.0417	0.0427	0.0189	0.0322	0.0252	0.0484	-0.0707
S5_Mag	0.0399	0.0079	-0.0201	0.0331	-0.0150	0.0269	-0.0564	-0.0410	0.0365	0.0226	0.0542
S6_Mag	-0.0037	0.0565	-0.0655	0.0455	0.0151	-0.0423	-0.0309	-0.0013	0.0277	-0.0645	-0.0284
S9_Mag	0.0406	-0.0078	-0.0435	-0.0601	0.0333	-0.0117	-0.0117	0.0062	-0.0047	-0.0382	0.0328
S10_Mag	-0.0143	0.0019	0.0105	0.0012	0.0656	-0.0058	0.0106	-0.0151	-0.0323	0.0061	0.0721
CTA_Mag	-0.0341	-0.0383	-0.0463	-0.0520	-0.0569	-0.0639	-0.0701	-0.0758	-0.0824	-0.0895	-0.0971
CTB_Mag	-0.0205	-0.0230	-0.0260	-0.0292	-0.0313	-0.0343	-0.0372	-0.0404	-0.0438	-0.0472	-0.0414
CTC_Mag	-0.0182	-0.0222	-0.0243	-0.0280	-0.0322	-0.0352	-0.0386	-0.0425	-0.0454	-0.0484	-0.0332

Horizontal Structure: Two Sensors per Phase 35mm distance from source

Percentage TVE

Amp / Sensor	5	6	7	8	9	10	11	12	13	14	15
S1_TVE	0.256	0.374	0.263	0.189	0.113	0.455	0.293	0.281	0.024	0.613	0.519
S2_TVE	0.505	0.219	1.945	0.125	1.012	0.931	0.155	1.460	1.053	1.462	1.062
S5_TVE	1.835	0.659	0.215	0.215	0.290	0.188	0.941	0.411	0.010	0.317	0.272
S6_TVE	2.536	1.244	0.485	0.175	0.721	0.353	0.347	0.700	0.189	0.280	0.498
S9_TVE	0.199	0.521	0.716	0.451	0.332	0.201	0.199	0.392	0.214	0.147	0.330
S10_TVE	0.2696	0.6659	0.6303	1.4433	1.2549	0.3233	0.2337	0.3947	0.6729	0.5233	0.4720
CTA_TVE	0.680	0.630	0.661	0.638	0.637	0.655	0.634	0.640	0.649	0.654	0.566
CTB_TVE	0.396	0.374	0.376	0.350	0.344	0.343	0.338	0.341	0.340	0.341	0.269
CTC_TVE	0.364	0.373	0.348	0.356	0.354	0.351	0.352	0.348	0.341	0.339	0.170

Horizontal Structure: Two Sensors per Phase 35mm distance from source, Angle Error

Amp / Sensor	5	6	7	8	9	10	11	12	13	14	15
S1_Ang	0.4044	0.0000	0.0001	0.0021	0.0006	-0.0003	0.0003	-0.0003	0.0008	-0.0001	0.0001
S2_Ang	-0.00089	-0.00219	0.00102	-0.00050	0.00147	-0.00031	-0.00060	0.00060	-0.00009	-0.00028	0.00125
S5_Ang	0.00070	0.00191	0.00132	0.00030	-0.00194	-0.00050	-0.00109	0.00107	0.00103	-0.00023	-0.00009
S6_Ang	0.00167	-0.00086	0.00026	0.00029	-0.00011	-0.00066	0.00021	-0.00003	0.00083	-0.00015	-0.00039
S9_Ang	-0.00030	-0.00010	-0.00123	0.00125	0.00173	-0.00047	0.00180	0.00011	0.00011	-0.00050	-0.00083
S10_Ang	0.0026	0.0016	-0.0005	0.0011	0.0009	0.0006	0.0006	0.0007	-0.0001	0.0003	0.0006
CTA_Ang	9.3E-06	8.0E-06	8.5E-06	8.0E-06	7.0E-06	7.9E-06	6.5E-06	7.7E-06	7.4E-06	9.3E-06	4.4E-06
CTB_Ang	6.4E-06	7.6E-06	6.0E-06	6.9E-06	7.2E-06	5.9E-06	6.5E-06	6.0E-06	7.3E-06	7.3E-06	7.4E-06
CTC_Ang	6.5E-06	7.1E-06	5.4E-06	6.9E-06	7.2E-06	7.7E-06	7.7E-06	6.6E-06	5.8E-06	6.8E-06	5.0E-06

Horizontal Structure: Two Sensors per Phase 35mm distance from source, Magnitude Error

Amp / Sensor	5	6	7	8	9	10	11	12	13	14	15
S1_Mag	0.013	0.022	0.018	-0.015	0.010	-0.046	-0.032	-0.034	-0.003	0.086	-0.078
S2_Mag	-0.025	-0.013	-0.136	-0.010	0.091	-0.093	-0.017	-0.175	-0.137	-0.205	-0.159
S5_Mag	-0.092	0.040	-0.015	-0.017	-0.026	-0.019	0.103	-0.049	0.001	-0.044	0.041
S6_Mag	-0.127	0.075	0.034	-0.014	0.065	-0.035	0.038	0.084	-0.025	-0.039	-0.075
S9_Mag	-0.010	0.031	0.050	-0.036	-0.030	-0.020	-0.022	-0.047	0.028	-0.021	-0.049
S10_Mag	0.0135	-0.0400	0.0441	-0.1155	-0.1129	0.0323	-0.0257	-0.0474	0.0875	0.0733	0.0708
CTA_Mag	-0.034	-0.038	-0.046	-0.051	-0.057	-0.066	-0.070	-0.077	-0.084	-0.092	-0.085
CTB_Mag	-0.020	-0.022	-0.026	-0.028	-0.031	-0.034	-0.037	-0.041	-0.044	-0.048	-0.040
CTC_Mag	-0.018	-0.022	-0.024	-0.028	-0.032	-0.035	-0.039	-0.042	-0.044	-0.047	-0.025

Horizontal Structure: Three Sensors per Phase 7mm distance from source, Percentage TVE

Amp / Sensor	5A	6A	7A	8A	9A	10A	11A	12A	13A	14A	15A
1	0.056	2.126	0.571	0.549	0.083	0.078	0.261	0.670	0.228	0.466	0.771
2	1.768	1.525	1.746	1.618	1.665	1.169	1.199	1.561	1.843	1.689	1.527
3	0.787	0.201	0.271	0.287	0.237	0.010	0.086	0.265	0.188	0.107	0.187
5	0.745	0.630	0.124	0.313	0.216	0.163	0.260	0.003	0.163	0.148	0.077
6	0.051	0.282	0.178	0.070	0.114	0.062	0.215	0.169	0.008	0.075	0.276
7	0.027	0.001	0.241	0.098	0.026	0.039	0.165	0.183	0.089	0.020	0.080
9	0.566	0.312	0.057	0.099	0.231	0.056	0.105	0.043	0.400	0.240	0.010
10	0.360	0.807	0.112	0.186	0.243	0.273	0.233	0.105	0.016	0.070	0.397
11	0.034	0.182	0.221	0.120	0.227	0.285	0.105	0.134	0.109	0.190	0.170
Cta	0.685	0.652	0.662	0.654	0.659	0.633	0.632	0.635	0.647	0.638	0.638
CTb	0.409	0.379	0.370	0.362	0.357	0.344	0.342	0.336	0.342	0.344	0.295
CTc	0.362	0.354	0.347	0.352	0.342	0.355	0.349	0.338	0.339	0.344	0.208

Horizontal Structure: Three Sensors per Phase 7mm distance from source: Angle Error

Amp / Sensor	5A	6A	7A	8A	9A	10A	11A	12A	13A	14A	15A
1	0.0004	0.0007	-0.0007	-0.0002	-0.0001	-0.0001	-0.0002	-0.0002	0.0001	0.0002	-5E-05
2	0.0002	0.0002	0.0003	0.0001	0.0003	0.0001	0.0005	-0.0001	-0.0001	0.0001	-1E-06
3	0.0004	0.0008	0.0003	0.0001	0.0001	0.0006	-0.0001	0.0002	-0.0002	0.0000	-8E-05
5	0.0002	-0.0003	-0.0001	0.0001	-0.0004	-0.0002	0.0001	0.0003	-0.0001	-0.0002	0.00030
6	0.0000	0.0001	-0.0001	0.0002	0.0000	-0.0001	0.0000	-0.0001	0.0000	0.0001	-0.00011
7	0.0008	0.0001	-0.0001	0.0003	-0.0002	-0.0002	-0.0003	0.0000	-0.0001	0.0000	5.16E-05
9	0.0005	-0.0001	-0.0005	0.0001	0.0000	0.0003	-0.0001	0.0000	0.0000	-0.0001	0.0005
10	-0.0003	-0.0007	0.0003	-0.0002	0.0003	0.0000	-0.0002	0.0001	-0.0001	-0.0001	0.0002
11	0.0001	0.0000	0.0003	-0.0003	0.0000	-0.0001	0.0000	0.0001	0.0003	0.0002	0.0002
Cta	0.00001	8.31E-06	7.13E-06	9.25E-06	6.95E-06	7.39E-06	7.45E-06	8.45E-06	7.57E-06	7.54E-06	7.7E-06
CTb	0.00001	7.19E-06	8.54E-06	7.41E-06	5.56E-06	6.75E-06	6.52E-06	6.61E-06	6.83E-06	6.58E-06	4.7E-06
CTc	0.00001	7.62E-06	4.83E-06	7.42E-06	5.89E-06	6.69E-06	7.67E-06	6.65E-06	7.09E-06	7.02E-06	6.79E-06

Horizontal Structure: Three Sensors per Phase 7mm distance from source: Magnitude Error

Amp / Sensor	5A	6A	7A	8A	9A	10A	11A	12A	13A	14A	15A
1	-0.003	0.128	-0.040	-0.044	0.008	-0.008	-0.029	0.080	-0.030	-0.065	-0.116
2	-0.088	-0.091	-0.122	-0.129	-0.150	-0.117	-0.132	-0.187	-0.240	-0.236	-0.229
3	-0.039	0.012	0.019	-0.023	-0.021	0.001	0.009	0.032	-0.024	-0.015	0.028
5	-0.037	-0.038	-0.009	-0.025	-0.019	0.016	0.029	0.000	0.021	0.021	-0.012
6	-0.003	-0.017	0.012	0.006	0.010	0.006	0.024	-0.020	0.001	-0.010	-0.041
7	0.001	0.000	0.017	0.008	0.002	-0.004	0.018	-0.022	-0.012	-0.003	-0.012
9	-0.028	0.019	-0.004	0.008	-0.021	0.006	0.012	-0.005	-0.052	-0.034	0.001
10	-0.018	-0.048	0.008	0.015	0.022	-0.027	-0.026	-0.013	-0.002	0.010	0.060
11	0.002	0.011	-0.015	0.010	-0.020	0.028	0.012	0.016	-0.014	-0.027	0.025
Cta	-0.034	-0.039	-0.046	-0.052	-0.059	-0.063	-0.070	-0.076	-0.084	-0.089	-0.096
CTb	-0.020	-0.023	-0.026	-0.029	-0.032	-0.034	-0.038	-0.040	-0.045	-0.048	-0.044
CTc	-0.018	-0.021	-0.024	-0.028	-0.031	-0.035	-0.038	-0.041	-0.044	-0.048	-0.031

Horizontal Structure: Three Sensors per Phase 15mm distance from source, Percentage TVE

Amp / Sensor	5A	6A	7A	8A	9A	10A	11A	12A	13A	14A	15A
1	1.654	1.163	0.176	0.562	0.342	0.353	0.055	0.219	0.811	0.435	0.441
2	0.142	0.790	0.187	0.275	0.471	0.582	0.969	0.259	1.073	0.834	0.538
3	0.566	1.156	0.124	0.323	0.564	0.860	0.660	0.266	0.228	0.530	0.172
5	0.551	0.112	0.134	0.179	0.158	0.067	0.110	0.281	0.131	0.134	0.235
6	0.123	0.430	0.231	0.260	0.100	0.356	0.401	0.056	0.326	0.232	0.076
7	0.057	0.616	0.203	0.161	0.189	0.186	0.015	0.172	0.275	0.065	0.371
9	0.143	0.236	0.162	0.075	0.299	0.444	0.289	0.099	0.345	0.375	0.155
10	0.577	0.174	0.813	0.423	0.446	0.092	0.239	0.004	0.154	0.437	0.574
11	0.444	0.404	0.422	0.137	0.413	0.079	0.216	0.318	0.179	0.266	0.307
Cta	0.655	0.662	0.628	0.642	0.653	0.636	0.650	0.628	0.639	0.639	0.617
CTb	0.655	0.662	0.628	0.642	0.653	0.636	0.650	0.628	0.639	0.639	0.617
CTc	0.655	0.662	0.628	0.642	0.653	0.636	0.650	0.628	0.639	0.639	0.617

Horizontal Structure: Three Sensors per Phase 15mm distance from source: Angle Error

Amp / Sensor	5A	6A	7A	8A	9A	10A	11A	12A	13A	14A	15A
1	0.00032	0.00071	-0.00033	-0.00004	-0.00013	0.00052	0.00044	0.00027	0.00009	-0.00012	-0.00062
2	0.00120	0.00040	0.00068	0.00013	-0.00063	0.00013	0.00017	-0.00012	0.00006	0.00044	0.00005
3	0.00006	0.00054	-0.00028	0.00022	-0.00014	-0.00003	0.00031	-0.00017	0.00005	-0.00007	0.00003
5	0.00125	0.00111	-0.00029	0.00049	0.00048	-0.00089	-0.00010	0.00006	0.00006	-0.00003	0.00028
6	-0.00038	0.00041	-0.00030	0.00039	-0.00036	0.00049	-0.00003	0.00008	-0.00066	-0.00004	0.00000
7	0.00032	-0.00073	0.00070	0.00010	0.00043	0.00026	-0.00044	0.00037	-0.00033	0.00031	-0.00028
9	0.00016	0.00076	0.00036	-0.00037	0.00064	0.00032	0.00007	-0.00093	0.00026	0.00032	0.00036
10	0.00150	-0.00059	0.00060	-0.00008	0.00018	0.00008	0.00047	-0.00037	0.00009	0.00005	-0.00004
11	0.00053	0.00131	-0.00009	-0.00042	-0.00033	0.00044	0.00013	0.00010	0.00032	-0.00004	0.00036
Cta	7.77E-06	7.53E-06	7.31E-06	5.91E-06	6.68E-06	7.13E-06	7.31E-06	7.46E-06	7.51E-06	7.67E-06	7.07E-06
CTb	5.42E-06	5.28E-06	7.38E-06	5.25E-06	6.13E-06	6.51E-06	6.62E-06	7.25E-06	7.14E-06	7.85E-06	8.93E-06
CTc	6.13E-06	6.22E-06	8.09E-06	7.37E-06	6.84E-06	6.45E-06	7.13E-06	6.57E-06	5.9E-06	7.64E-06	1.09E-05

Horizontal Structure: Three Sensors per Phase 15mm distance from source, Magnitude Error

Amp / Sensor	5A	6A	7A	8A	9A	10A	11A	12A	13A	14A	15A
1	0.083	-0.070	-0.012	-0.045	-0.031	0.035	-0.006	0.026	0.105	-0.061	-0.066
2	-0.007	-0.047	0.013	-0.022	-0.042	0.058	-0.107	-0.031	-0.140	-0.117	-0.081
3	0.028	-0.069	-0.009	-0.026	-0.051	0.086	-0.073	0.032	0.030	-0.074	-0.026
5	-0.028	0.007	-0.009	-0.014	-0.014	0.007	-0.012	0.034	-0.017	0.019	0.035
6	0.006	0.026	0.016	0.021	0.009	0.036	-0.044	0.007	-0.042	-0.032	-0.011
7	-0.003	0.037	0.014	0.013	0.017	0.019	0.002	-0.021	-0.036	-0.009	-0.056
9	0.022	0.024	0.030	-0.011	-0.037	0.008	-0.024	-0.038	-0.023	-0.037	0.046
10	-0.029	0.010	-0.057	-0.034	0.040	-0.009	0.026	-0.001	0.020	0.061	0.086
11	0.022	0.024	0.030	-0.011	-0.037	0.008	-0.024	-0.038	-0.023	-0.037	0.046
Cta	-0.033	-0.040	-0.044	-0.051	-0.059	-0.064	-0.072	-0.075	-0.083	-0.089	-0.093
CTb	-0.019	-0.023	-0.025	-0.029	-0.032	-0.035	-0.038	-0.040	-0.043	-0.047	-0.043
CTc	-0.018	-0.022	-0.026	-0.029	-0.031	-0.036	-0.038	-0.042	-0.044	-0.049	-0.036

Horizontal Structure: Three Sensors per Phase 25mm distance from source, Percentage TVE

Amp / Sensor	5A	6A	7A	8A	9A	10A	11A	12A	13A	14A	15A
1	2.226	1.555	0.008	2.224	1.942	0.685	0.337	0.299	0.608	0.752	0.802
2	1.706	0.702	0.985	0.309	0.130	0.334	0.289	0.011	0.372	0.911	1.279
3	1.641	0.117	0.966	1.405	0.563	0.568	0.059	0.025	0.393	0.269	0.043
5	1.838	0.045	0.291	0.618	0.315	0.223	0.035	0.118	0.575	0.397	0.994
6	0.138	0.437	0.022	0.922	0.865	0.348	0.241	0.038	0.111	0.106	0.545
7	0.606	0.013	0.299	0.543	0.247	0.205	0.152	0.140	0.005	0.129	0.136
9	0.118	0.900	0.621	0.274	0.446	0.229	0.182	0.315	0.409	0.150	0.196
10	0.714	0.320	0.604	0.281	0.011	0.519	0.295	0.283	0.043	0.391	0.169
11	0.225	0.536	0.485	0.629	0.438	0.453	0.491	0.333	0.193	0.122	0.052
Cta	0.672	0.651	0.659	0.649	0.645	0.637	0.634	0.624	0.629	0.639	0.696
CTb	0.672	0.651	0.659	0.649	0.645	0.637	0.634	0.624	0.629	0.639	0.696
CTc	0.672	0.651	0.659	0.649	0.645	0.637	0.634	0.624	0.629	0.639	0.696

Horizontal Structure: Three Sensors per Phase 25mm distance from source, Angle Error

Amp / Sensor	5A	6A	7A	8A	9A	10A	11A	12A	13A	14A	15A
1	-0.0021	0.000907	-0.0008	-0.00101	0.000914	-0.00016	0.000771	-0.00013	-0.00023	2.21E-05	-0.00111
2	-0.0016	0.001098	0.000755	-0.0004	-0.00042	8.17E-05	-0.00015	-1.4E-05	0.000104	-0.00066	-9E-05
3	-0.00322	-0.00017	0.000917	-3.9E-05	-0.00031	0.000381	0.000147	-0.00066	0.000169	0.000372	-0.00045
5	0.00162	0.000726	-0.00088	-0.00076	-0.0004	-0.00181	0.000782	-0.00021	-0.0005	0.000791	-0.00054
6	0.001615	-0.00014	0.000369	-0.00077	-0.00072	0.000137	0.000974	0.000257	-0.00034	0.000502	-9.5E-06
7	0.000695	0.001868	0.000439	-2.4E-07	0.000294	0.000754	-0.00029	-6.1E-05	-0.00036	0.000349	0.000343
9	-3.3E-05	-0.00228	-0.00064	-0.00014	0.000255	-0.00036	0.000738	0.000409	0.000695	9.72E-05	-9E-06
10	-0.00048	-0.00082	-0.0003	0.000223	-9.4E-05	-0.00034	-0.00043	0.000449	0.00056	0.000145	0.000619
11	-0.00063	-5E-05	-0.00092	0.000492	0.000186	0.000115	-0.00012	0.000288	0.000256	-0.00028	-0.00022
Cta	7.36E-06	6.64E-06	6.48E-06	7.14E-06	8.01E-06	7.53E-06	7.42E-06	6.87E-06	6.94E-06	7.82E-06	7.77E-06
CTb	6.94E-06	7.41E-06	7.38E-06	6.44E-06	6.82E-06	6.01E-06	6.76E-06	6.11E-06	6.72E-06	6.84E-06	8.05E-06
CTc	6.05E-06	7.6E-06	6.2E-06	4.93E-06	5.67E-06	8.05E-06	6.78E-06	6.83E-06	6.93E-06	6.65E-06	4.24E-06

Horizontal Structure: Three Sensors per Phase 25mm distance from source, Magnitude Error

Amp / Sensor	5A	6A	7A	8A	9A	10A	11A	12A	13A	14A	15A
1	-0.111	-0.093	0.001	0.178	0.175	-0.068	-0.037	0.036	-0.079	-0.105	0.120
2	0.000	0.042	-0.069	-0.025	-0.012	-0.033	0.032	-0.001	-0.048	-0.128	-0.192
3	-0.082	0.007	-0.068	0.112	0.051	-0.057	0.006	0.003	-0.051	-0.038	0.006
5	0.092	-0.003	0.020	-0.049	-0.028	0.022	0.004	0.014	0.075	0.056	-0.149
6	0.007	0.026	-0.002	-0.074	-0.078	0.035	0.027	-0.005	0.014	-0.015	-0.082
7	0.030	0.001	-0.021	-0.043	-0.022	0.020	0.017	0.017	0.001	0.018	-0.020
9	-0.011	-0.032	0.034	0.050	0.039	-0.045	-0.054	-0.040	-0.025	-0.017	-0.008
10	-0.036	-0.019	0.042	-0.022	-0.001	-0.052	-0.032	-0.034	0.006	0.055	0.025
11	-0.011	-0.032	0.034	0.050	0.039	-0.045	-0.054	-0.040	-0.025	-0.017	-0.008
Cta	-0.034	-0.039	-0.046	-0.052	-0.058	-0.064	-0.070	-0.075	-0.082	-0.090	-0.104
CTb	-0.020	-0.023	-0.026	-0.029	-0.031	-0.034	-0.037	-0.040	-0.044	-0.047	-0.045
CTc	-0.019	-0.022	-0.024	-0.028	-0.031	-0.035	-0.039	-0.042	-0.046	-0.049	-0.047

Horizontal Structure: Three Sensors per Phase 35mm distance from source, Percentage TVE

Amp / Sensor	5A	6A	7A	8A	9A	10A	11A	12A	13A	14A	15A
1	4.051	1.307	0.421	2.343	1.343	1.609	1.668	0.042	1.937	1.409	1.756
2	1.033	2.504	1.932	0.717	0.958	0.487	0.435	0.078	1.245	0.154	1.082
3	1.416	0.635	0.916	1.234	0.859	0.571	0.204	0.163	1.336	0.240	0.546
5	0.564	0.205	0.163	0.595	0.280	0.820	0.345	0.501	0.349	0.485	0.785
6	0.199	0.196	0.215	0.391	0.536	0.398	0.488	0.017	0.402	0.469	0.106
7	0.234	0.555	0.909	0.035	1.065	0.557	0.143	0.144	0.157	0.179	0.257
9	0.203	0.938	0.537	0.472	0.090	0.457	0.243	0.864	0.026	0.471	0.080
10	0.103	0.550	0.324	0.586	0.041	0.708	0.669	0.485	0.285	0.683	0.432
11	0.618	0.041	0.858	0.102	0.116	0.125	0.151	0.556	0.157	0.225	0.251
Cta	0.662	0.672	0.660	0.655	0.651	0.640	0.641	0.631	0.643	0.635	0.625
CTb	0.662	0.672	0.660	0.655	0.651	0.640	0.641	0.631	0.643	0.635	0.625
CTc	0.662	0.672	0.660	0.655	0.651	0.640	0.641	0.631	0.643	0.635	0.625

Horizontal Structure: Three Sensors per Phase 35mm distance from source, Angle Error

Amp / Sensor	5A	6A	7A	8A	9A	10A	11A	12A	13A	14A	15A
1	-0.0010	0.0019	0.0016	-0.0012	-0.0030	0.0009	0.0001	0.0003	-0.0011	0.0000	0.0013
2	-0.0011	0.0007	0.0011	-0.0013	-0.0002	-0.0009	-0.0004	0.0005	-0.0004	0.0000	0.0004
3	-0.0006	-0.0010	-0.0018	0.0004	-0.0010	0.0009	-0.0004	0.0010	0.0007	0.0011	0.0011
5	-0.0031	0.0020	0.0000	0.0000	0.0017	0.0002	-0.0001	-0.0005	-0.0003	0.0009	-0.0007
6	-0.0010	0.0021	-0.0008	0.0005	0.0006	-0.0004	0.0001	0.0007	0.0003	-0.0003	0.0003
7	-0.0004	0.0008	0.0005	0.0017	-0.0013	0.0007	-0.0010	0.0000	0.0005	0.0012	0.0001
9	-0.0024	-0.0003	0.0009	-0.0006	0.0029	0.0007	-0.0011	0.0007	0.0017	-0.0005	-0.0012
10	0.0013	-0.0005	0.0007	-0.0003	-0.0010	0.0001	0.0010	0.0008	0.0008	-0.0001	-0.0005
11	0.0005	0.0005	0.0009	-0.0017	0.0002	-0.0001	0.0008	-0.0006	-0.0002	-0.0003	0.0003
Cta	0.00001	0.00001	0.00001	0.00001	0.00001	0.00001	0.00001	0.00001	0.00001	0.00001	0.00001
CTb	0.00000	0.00001	0.00001	0.00001	0.00001	0.00001	0.00001	0.00001	0.00001	0.00001	0.00000
CTc	0.00001	0.00001	0.00001	0.00001	0.00001	0.00001	0.00001	0.00001	0.00001	0.00001	0.00001

Horizontal Structure: Three Sensors per Phase 35mm distance from source, Magnitude Error

Amp / Sensor	5A	6A	7A	8A	9A	10A	11A	12A	13A	14A	15A
1	-0.203	0.078	-0.029	0.187	0.121	0.161	0.184	0.005	-0.252	-0.197	-0.263
2	0.052	-0.150	-0.135	-0.057	-0.086	0.049	-0.048	-0.009	-0.162	-0.022	-0.162
3	-0.071	0.038	-0.064	0.099	0.077	0.057	0.022	0.020	-0.174	-0.034	-0.082
5	0.028	0.012	-0.011	-0.048	-0.025	-0.082	-0.038	0.060	0.045	0.068	0.118
6	0.010	0.012	-0.015	-0.031	-0.048	-0.040	-0.054	-0.002	0.052	0.066	0.016
7	0.012	0.033	-0.064	-0.003	-0.096	-0.056	-0.016	0.017	0.020	0.025	0.039
9	0.031	-0.002	0.060	-0.008	0.010	0.012	-0.017	-0.067	-0.020	-0.032	0.038
10	-0.005	0.033	-0.023	-0.047	0.004	-0.071	-0.074	-0.058	-0.037	-0.096	0.065
11	0.031	-0.002	0.060	-0.008	0.010	0.012	-0.017	-0.067	-0.020	-0.032	0.038
Cta	-0.033	-0.040	-0.046	-0.052	-0.059	-0.064	-0.070	-0.076	-0.084	-0.089	-0.094
CTb	-0.020	-0.024	-0.026	-0.029	-0.032	-0.034	-0.037	-0.040	-0.044	-0.047	-0.039
CTc	-0.019	-0.022	-0.024	-0.028	-0.031	-0.035	-0.038	-0.042	-0.045	-0.049	-0.030